

Flow-through Microchannel DNA Chips

A thesis submitted to
the Faculty of Engineering
of the University of Glasgow

for the degree of
Doctor of Philosophy

by

Vincent Benoit

ProQuest Number: 13833988

All rights reserved

INFORMATION TO ALL USERS

The quality of this reproduction is dependent upon the quality of the copy submitted.

In the unlikely event that the author did not send a complete manuscript and there are missing pages, these will be noted. Also, if material had to be removed, a note will indicate the deletion.



ProQuest 13833988

Published by ProQuest LLC (2019). Copyright of the Dissertation is held by the Author.

All rights reserved.

This work is protected against unauthorized copying under Title 17, United States Code
Microform Edition © ProQuest LLC.

ProQuest LLC.
789 East Eisenhower Parkway
P.O. Box 1346
Ann Arbor, MI 48106 – 1346



12394

copy 1

ABSTRACT

This work represents a contribution to the rapidly expanding field of microarray technology, which consists in the pooling of a large number of miniaturised biorecognition elements on a single solid substrate so as to allow heterogeneous bioassays to be performed in a highly multiplexed fashion. Numerous applications of life science research and pharmaceutical development, such as diagnostics and molecular medicine, are expected to greatly benefit from the increased levels of throughput provided by the microarray approach. However, most microarray platforms developed as of this writing have merely been based on a two-dimensional configuration in which the biorecognition sites are distributed on the surface of a planar, unpenetrable substrate; this format does not address the mass-transfer limitations inherent to heterogeneous ligand binding kinetics and thus does not provide optimal assay performance in terms of speed and sensitivity.

In this thesis, a novel concept is presented that has been devised to increase the intrinsic analytical performance of microarrays. The approach is based on the use of three-dimensional, uniformly porous substrates featuring a regular array of discrete, ordered, high aspect ratio microchannels. The fabrication of such microstructures, with feature sizes in the micrometre range and aspect ratios in excess of 30:1, was achieved using two subtractive silicon processing techniques, electrochemical etching and deep dry etching, whose relative merits have been assessed. Commercially available microchannel glass substrates were also used.

Nucleic acid molecules were immobilised as capture probes on the sidewalls of the microchannels, in a conformation allowing biorecognition through heterogeneous hybridisation. To that end, a chemical strategy was developed for the functional immobilisation of oligonucleotide probes onto silica-rich substrates such as glass and oxidised silicon. Nucleic acid hybridisation was chosen as the model ligand binding process due not only to the relative ease of handling of DNA (including the availability of chemically pure, synthetic oligonucleotides) but also to its relevance, through genomics, to a number of clinical, medical and pharmaceutical applications.

The particular wetting properties of microchannel substrates were characterised and subsequently taken into account in the development of a microarraying procedure based on non-contact, ink-jet dispensing technology. In this respect, the physical-chemical processes that control the formation of spots on microchannel substrates, *i.e.* the wetting properties of the substrates, as well as the main parameters involved in the arraying process, such as the concentration of the capture probe solution and volume of the aliquots dispensed, have been investigated. Medium-density microchannel oligoarrays were produced that comprised as many as 256 probe spots over a 1 cm² area. Since the effective surface area available for probe immobilisation was increased by expansion into the third dimension, a higher spatial density of probes could be achieved as compared to planar substrates with the same lateral dimensions.

Biorecognition events between the immobilised capture probes and solution-borne target molecules were allowed to take place, in a dynamic mode, by convectively pumping sample through the microchannel array. As each microchannel acted as a miniature analytical chamber, probe-target hybridisation kinetics were enhanced by spatial confinement, while recirculation of the sample provided enhanced mass transfer. The feasibility of using electrokinetic transport of the targets was also assessed.

Quantitative detection of heterogeneous hybridisation events taking place along the microchannel sidewalls was achieved through a CCD camera-based epifluorescence detection scheme. In a first instance, conventional low magnification microscope objective lenses were used as imaging optics whose depth-of-field characteristics matched the thickness of the microchannel substrate. The suitability of the approach was illustrated by the achievement of detection limits as low as a few attomoles of fluorescent dye per spot. This level of performance was made possible by the remarkable optical properties of the substrate, which were characterised both experimentally and through simulations based on ray-tracing procedures.

Since the use of microchannel chips of increased thickness provided a way of increasing the number of capture probe molecules immobilised within each spot without increasing the lateral dimensions of the spots, a range of chip thicknesses were considered in a first step towards optimisation of the substrate geometry. Potential limitations to the benefits associated with an increase in chip thickness were discussed, in terms of the effectiveness of both the fluorescence detection scheme and the process of probe immobilisation on the microchannel sidewalls.

Comparative hybridisation experiments were conducted which demonstrated the improved performance of the flow-through microchannel configuration over the conventional planar configuration, with an observed circa 5 times enhancement in hybridisation kinetics and a one to two orders of magnitude higher detectability. A few routes for further improving the performance of flow-through microchannel DNA chips are suggested, along with other possible bioanalytical applications of the microchannel biochip platform.

ACKNOWLEDGEMENTS

First and foremost, I wish to express my gratitude to Professor Jon Cooper, who gave me the opportunity to pursue this doctoral work within his Research Group, and whose ressourcefulness, consideration and leadership have been a constant source of inspiration and motivation throughout my time in Glasgow.

I am also indebted to a number of members of the Electronics Department, in particular Dr Andrew Glidle for his immense knowledge and his willingness to share it, Mary Robertson and Bill Monaghan for much-appreciated technical support, Dr Daniel Ortega and Professor Stewart Aitchinson for expanding my horizon in the field of optics, Dr Shu-Xin Wu for his dry etching skills, Linda McRobbie for help with the thermal oxidation of silicon, and all the members of staff of the Department who always did their best to help.

My most sincere acknowledgements go to Dr Tony Cass, for allowing me to spend a few productive stays at his laboratory at Imperial College, and to his post-docs Dr Catherine Haliwell and Dr Christophe Valat for stimulating collaborative work.

Gene Logic Inc. must be acknowledged for the funding of this research. I am particularly grateful to Dr Harry Yang for allowing me to spend a few months at Gene Logic's facilities in Maryland, where the presence of Dr Adam Steel, Matt Torres and Dr Yong-Yi Yu, among others, greatly helped in making my stay there both productive and enjoyable. Also to be acknowledged is Dr Xiaoyang Zhu, who kindly welcomed me to his lab at the University of Minnesota where I learned a lot about silicon surface chemistry.

I also thank all the members of the Bioelectronics Group for the friendly atmosphere in the labs, as well as all the people I got to know during my stay in Glasgow, the company of whom was greatly appreciated: Erik, for his unabated enthusiasm; Norbert, for his kindness and great wisdom; David, for the golf games and the Keilihs; Dave, for the Aussie perspective on life; Martin and Eishi, for the football games; Morten, for the Danish cooking and breakthrough political ideas; and all the others.

Finally, I would like to acknowledge the spiritual support of my parents, brothers and old friends back in France, without whom nothing would have been possible.

CONTENTS

Abstract.....	3
Acknowledgements	5
Contents	6
List of Figures	13
List of Tables	20
Glossary.....	21
 CHAPTER 1. Introduction.....	 23
1. 1. State of the art in DNA microarray technology	23
1. 1. 1. Biochips and microarrays.....	23
1. 1. 2. DNA chips	24
1. 1. 2. 1. Impetus	24
1. 1. 2. 2. Heterogeneous, multiplexed nucleic acid hybridisation assays	25
1. 1. 2. 3. DNA chip platforms.....	28
1. 1. 2. 4. Applications of DNA chips	33
1. 2. The flow-through microchannel DNA chip platform: concept and implementation	36
1. 2. 1. Introduction.....	36
1. 2. 2. Limitations of current DNA chip platforms.....	36
1. 2. 3. The flow-through microchannel DNA chip concept.....	37
1. 2. 4. Potential advantages of the flow-through microchannel DNA chip configuration	38
1. 2. 5. Technical challenges associated with the use of microchannel substrates.....	39
1. 2. 6. Implementation of the flow-through microchannel DNA chip configuration.	40
1. 2. 6. 1. Microchannel substrates.....	40
1. 2. 6. 2. Capture probe attachment chemistry	43
1. 2. 6. 3. Arraying of capture probes onto microchannel substrates	45
1. 2. 6. 4. Fluidics.....	47
1. 2. 6. 5. Assay detection by fluorescence imaging	50
 CHAPTER 2. Fabrication and characterisation of flow-through biochip substrates.....	 51
2. 1. Introduction	51
2. 2. Microchannel glass (MCG)	51
2. 2. 1. Fabrication of microchannel glass biochip substrates.....	51

2. 2. 1. 1. Fabrication of microchannel glass boules.....	51
2. 2. 1. 2. Dicing of microchannel glass boules into chips.....	52
2. 2. 2. Characterisation.....	52
2. 2. 2. 1. Physical properties.....	52
2. 2. 2. 2. Morphology.....	53
2. 2. 2. 3. Calculations of geometrical parameters of interest.....	55
2. 3. Photoelectrochemical etching of silicon.....	56
2. 3. 1. Principle and implementation.....	56
2. 3. 1. 1. Overview of the process.....	57
2. 3. 1. 2. Photoelectrochemical etching setup.....	57
2. 3. 1. 3. Etching parameters.....	59
2. 3. 1. 4. Control of the etching pattern.....	60
2. 3. 2. Fabrication of microchannel silicon (MCS) biochip substrates.....	61
2. 3. 2. 1. Adjustment of experimental parameters.....	61
2. 3. 2. 2. Substrate preparation.....	61
2. 3. 3. Results.....	62
2. 3. 4. Physical characterisation of macroporous silicon substrates.....	64
2. 3. 4. 1. Scanning electron microscopy imaging.....	64
2. 3. 4. 2. Morphology of the microchannels.....	65
2. 3. 4. 3. Calculations of geometrical parameters of interest.....	65
2. 4. Deep dry etching of silicon.....	66
2. 4. 1. The Advanced Silicon Etch (ASE) process.....	66
2. 4. 1. 1. Principle.....	66
2. 4. 1. 2. Relevance to the fabrication of flow-through silicon chips.....	67
2. 4. 2. Implementation of the process for the fabrication of microchannel silicon.....	68
2. 4. 2. 1. Materials and methods.....	68
2. 4. 2. 2. Experimental.....	69
2. 4. 3. Results and discussion.....	71
2. 5. Poly(dimethylsiloxane), PDMS.....	74
2. 5. 1. Fabrication of PDMS structures by imprinting against a master.....	74
2. 5. 2. Fabrication of masters for the production of PDMS microchannel substrates.....	74
2. 5. 2. 1. Requirements.....	74
2. 5. 2. 2. Photolithographic microstructuring of thick photoresist.....	75
2. 5. 2. 3. Deep dry etching of silicon.....	77
2. 5. 3. Master passivation.....	78
2. 5. 3. 1. Aim.....	78
2. 5. 3. 2. Experimental.....	78
2. 5. 4. PDMS molding and release.....	79
2. 5. 4. 1. Principle.....	79
2. 5. 4. 2. Experimental.....	79

2. 5. 4. 3. Results and discussion	79
2. 6. Conclusions.....	80
 CHAPTER 3. Fluorescence detection from microchannel biochips	 81
3. 1. Introduction	81
3. 2. Fluorescence as a detection scheme in bioanalytics.....	81
3. 2. 1. Physical principles of fluorescence	81
3. 2. 1. 1. Molecular photoactivation and deactivation processes.....	81
3. 2. 1. 2. Spectral characteristics of fluorescence	83
3. 2. 1. 3. Fluorescence quantum yield.....	83
3. 2. 1. 4. Fluorescence quenching and photobleaching	83
3. 2. 2. Quantitative fluorescence measurements in heterogeneous bioassays.....	84
3. 2. 2. 1. Analyte fluorescence signal	84
3. 2. 2. 2. Background signals	85
3. 2. 2. 3. Long-wavelength fluorescence measurements	86
3. 2. 2. 4. Epifluorescence microscopy imaging	86
3. 2. 3. CCD-based fluorescence imaging	88
3. 2. 3. 1. CCD cameras	88
3. 2. 3. 2. Principle of CCD photodetection	88
3. 2. 3. 3. Features and performance of CCD cameras	88
3. 3. Fluorescence detection from microchannel structures	90
3. 3. 1. Introduction.....	90
3. 3. 2. Simulation of fluorescence detection from microchannel structures.....	91
3. 3. 2. 1. Introduction	91
3. 3. 2. 2. Methods	91
3. 3. 2. 3. Results and discussion	98
3. 3. 3. Experimental characterisation of the optical properties of microchannel biochip substrates.....	109
3. 3. 3. 1. Introduction	109
3. 3. 3. 2. Experimental.....	109
3. 3. 3. 3. Results and discussion	112
3. 3. 4. Quantitative detection of fluorophores from microchannel biochip substrates	120
3. 3. 4. 1. Introduction	120
3. 3. 4. 2. Experimental.....	120
3. 3. 4. 3. Procedures	121
3. 3. 4. 4. Results and discussion	122
3. 4. Conclusions.....	129

CHAPTER 4. Functional attachment of oligonucleotide capture probes onto solid substrates	131
4. 1. Introduction	131
4. 2. Strategies for the covalent attachment of oligonucleotide capture probes onto silica-rich surfaces using organosilane chemistry.....	131
4. 2. 1. Organosilane surface chemistry.....	131
4. 2. 1. 1. Principle	131
4. 2. 1. 2. Chemical mechanisms for reactions between organosilane compounds and surface hydroxyl groups.....	132
4. 2. 1. 3. Pre-silanisation treatment of silica-rich surfaces	133
4. 2. 2. Derivatisation of oligonucleotides to be used as covalently-bound probes	134
4. 2. 2. 1. Reactive nucleophile terminal groups.....	134
4. 2. 2. 2. Spacer arms	134
4. 2. 3. Examples of oligonucleotide probe attachment to silanised surfaces	135
4. 2. 4. Optimisation of the probe coverage density.....	136
4. 2. 5. Blocking of non-specific adsorption.....	137
4. 3. Strategy for the functional immobilisation of oligonucleotide capture probes onto glass and oxidised silicon and PDMS substrates	137
4. 3. 1. Organosilane	137
4. 3. 2. Reactive nucleophile and linker on the probe	138
4. 3. 3. Cross-linking.....	139
4. 3. 4. Overall surface modification and capture probe attachment process.....	140
4. 4. Generation of reactive silanol moieties on planar substrates in preparation for silanisation	141
4. 4. 1. Surface oxidation of silicon substrates.....	141
4. 4. 1. 1. Issues	141
4. 4. 1. 2. Thermal oxidation of silicon	141
4. 4. 1. 3. Thermal oxidation of planar silicon substrates	144
4. 4. 1. 4. Chemical oxidation of silicon	146
4. 4. 2. Surface oxidation of PDMS substrates	146
4. 4. 2. 1. Introduction	146
4. 4. 2. 2. Experimental.....	147
4. 5. Validation of the strategy for the attachment of oligonucleotide capture probes onto planar substrates	147
4. 5. 1. Analysis of immobilised probe layers by fluorescence microscopy	147
4. 5. 1. 1. Introduction	147
4. 5. 1. 2. Experimental.....	148
4. 5. 1. 3. Results and discussion	151

4. 5. 2. Further characterisation and validation of the attachment strategy	154
4. 5. 3. Heterogeneous hybridisation on flat glass and oxidised silicon and PDMS substrates	154
4. 5. 3. 1. Introduction	154
4. 5. 3. 2. Experimental	155
4. 5. 3. 3. Results and discussion	156
4. 6. Conclusions.....	160
 CHAPTER 5. Arraying of microchannel substrates with oligonucleotide probes	161
5. 1. Introduction	161
5. 2. Constraints associated with the use of microchannel substrates	161
5. 2. 1. Liquid-phase treatment of microchannel glass and microchannel silicon.....	161
5. 2. 2. Thermal oxidation of microchannel silicon	162
5. 3. Piezoelectric ink-jet arraying of microchannel substrates.....	163
5. 3. 1. Experimental	163
5. 3. 1. 1. Materials and reagents	163
5. 3. 1. 2. Apparatus	163
5. 3. 1. 3. Procedures	165
5. 3. 2. Results and discussion	168
5. 3. 2. 1. Differences in wetting properties between microchannel glass and planar glass.....	168
5. 3. 2. 2. Parameters affecting the dimensions of oligonucleotide spots on microchannel glass	170
5. 3. 2. 3. Comparison of oligonucleotide spots formed on microchannel glass and on microchannel silicon	174
5. 4. Flow-through washing of microchannel chips.....	174
5. 4. 1. Experimental	175
5. 4. 1. 1. Materials	175
5. 4. 1. 2. Instrumentation	175
5. 4. 1. 3. Procedures	177
5. 4. 2. Results and discussion	178
5. 4. 2. 1. Filling of the cell and establishment of the flow	178
5. 4. 2. 2. Uniformity of flow through a microchannel glass chip	179
5. 4. 2. 3. Effectiveness of the washing procedure and uniformity of capture probe immobilisation.....	180
5. 5. Conclusions.....	181

CHAPTER 6. Microchannel oligoarray-based fluorescence hybridisation assays.....	182
6. 1. Introduction	182
6. 2. Microchannel oligoarray-based fluorescence hybridisation assays with convective sample pumping.....	182
6. 2. 1. Introduction.....	182
6. 2. 2. Experimental	182
6. 2. 2. 1. Materials	182
6. 2. 2. 2. Instrumentation	183
6. 2. 2. 3. Procedures	184
6. 2. 3. Results and discussion	186
6. 3. Relative performance of microchannel glass and planar glass oligoarrays	189
6. 3. 1. Introduction.....	189
6. 3. 2. Experimental	189
6. 3. 2. 1. Materials	189
6. 3. 2. 2. Methods	190
6. 3. 3. Results and discussion	191
6. 3. 4. Conclusions.....	193
6. 4. Electrokinetic sample transport in microchannel oligoarray hybridisation assays.....	194
6. 4. 1. Introduction.....	194
6. 4. 1. 1. Electrophoretic transport of nucleic acids.....	194
6. 4. 1. 2. Microchannel oligoarray-based hybridisation with electrophoretic pumping..	194
6. 4. 1. 3. Integrated device design	196
6. 4. 1. 4. Adjustment of the experimental parameters.....	197
6. 4. 2. Device fabrication	197
6. 4. 2. 1. Introduction	197
6. 4. 2. 2. Experimental	198
6. 4. 2. 3. Results and discussion	205
6. 4. 3. Selection of a suitable buffer.....	210
6. 4. 3. 1. Introduction	210
6. 4. 3. 2. Experimental	210
6. 4. 3. 3. Results and discussion	213
6. 4. 4. Conclusions	219
CHAPTER 7. Conclusions and future directions	221
7. 1. Achievements of this thesis	221
7. 2. Suggestions for future work	222
7. 2. 1. Improved optical detection	222

7. 2. 1. 1. Fluorescence resonance energy transfer (FRET)-based methodologies..... 222

7. 2. 1. 2. Molecular beacon technology..... 224

7. 2. 1. 3. Non-organic fluorescent labels 225

7. 2. 1. 4. Chemiluminescence detection..... 225

7. 2. 2. Optimisation of the morphology of microchannel substrates..... 227

7. 3. Further possible applications of the flow-through microchannel biochip platform 229

References 230

LIST OF FIGURES

Figure 1-1. The three-dimensional, flow-through microchannel DNA chip concept.....	37
Figure 2-1. Brightfield optical microscopy image of a 50 μm channel diameter, 0.5 mm thick microchannel glass chip.....	53
Figure 2-2. Brightfield optical microscopy images of 25 μm channel diameter, 1 mm thick microchannel glass chips.....	53
Figure 2-3. Scanning electron microscope images of a 10 μm channel diameter, 0.5 mm thick microchannel glass chip.....	54
Figure 2-4. Scanning electron microscope images of the cleaved edge of of a 10 μm channel diameter, 0.5 mm thick microchannel glass chip.....	55
Figure 2-5. Setup for the electrochemical etching of silicon.....	58
Figure 2-6. Cyclic voltammograms for a 3 $\Omega\text{ cm}$ silicon photoanode in 2.5% HF, recorded at 100 mV s^{-1} versus a Pt pseudoreference electrode, at room temperature	59
Figure 2-7. 4 μm pitch square pattern of 1 μm diameter holes produced by dry etching of a circa 1 μm thick silica layer thermally grown on the surface a n-type, {100}, 10 $\Omega\text{ cm}$ silicon wafer	63
Figure 2-8. Pyramidal recesses formed by KOH etching of a n-type, {100}, 35 $\Omega\text{ cm}$ silicon wafer, after removal of the silicon dioxide masking layer.....	63
Figure 2-9. Scanning electron microscope images of electrochemically etched microchannel silicon.	64
Figure 2-10. Approximate microchannel morphology of electrochemically etched silicon.....	65
Figure 2-11. Scanning electron microscope image of the cleaved edge of a 250 μm thick silicon wafer, etched through a 15 μm thick AZ4562 photoresist sacrificial masking layer patterned with an array of 5 x 5 μm^2 openings, for 360 minutes.....	71
Figure 2-12. Scanning electron microscope images of the cleaved edge of a 525 μm thick silicon wafer etched through a 20 μm thick SU8 photoresist sacrificial masking layer	72
Figure 2-13. Scanning electron microscope images of an array of self-standing micropillars produced by photolithographic structuring of a 380 μm thick layer of SU8-1070 negative photoresist	76
Figure 2-14. Arrays of self-standing silicon micropillars produced by Advanced Silicon Etch processing of silicon wafers patterned with AZ4562 photoresist.....	78

Figure 2-15. Stereomicroscopy images of a microchannel substrate produced by casting poly(dimethylsiloxane) against an SU8 master passivated with perfluorooctyltrichlorosilane	80
Figure 3-1. Energy-level Jablonski diagram, showing the various possible activation and deactivation processes for a hypothetical molecule	82
Figure 3-2. Schematic representation of an imaging epifluorescence microscope.....	87
Figure 3-3. Spectral responsivity curve (at room temperature) for a SITe SIA003AB back-thinned illuminated CCD	89
Figure 3-4. Propagation of electromagnetic radiations at the interface between two media with different refractive indices	91
Figure 3-5. 19-channel model cutout structure used in light propagation simulations with OptiCAD software	94
Figure 3-6. Schematic depiction of the phenomenon of inter-channel optical cross-talk in microchannel structures.....	96
Figure 3-7. Schematic representation of the epi-illumination of the front face of a microchannel chip through objective lenses of various numerical apertures, as used in simulations of the excitation of microchannel sidewall-bound fluorophores.....	97
Figure 3-8. Reflectivity of a monochromatic, unpolarised radiation at the interface between water and silicon and between water and heavy flint glass, as predicted from Fresnel's law	98
Figure 3-9. Simulated three-dimensional intensity profiles of the fraction of radiant fluorescence energy transmitted to the front face of a 19 channel model microchannel glass chip immersed in air, illustrating the phenomenon of inter-channel cross-talk of the fluorescence radiation emitted by a single model fluorophore, located close to the sidewall of the central channel and at an axial distance of 10 μm from the front face of the chip	100
Figure 3-10. Relative amount of fluorescence radiation, emitted by a single fluorophore, that is guided to the front face of different types of microchannel chips immersed in water, as a function of the position of the fluorophore with respect to the front face of the chip	102
Figure 3-11. Radiant energy in a plane perpendicular to the axis of the central channel, showing long range cross-talk across two rows of channels, in the case of a single fluorophore located at an axial distance of 100 μm from the front surface of a microchannel glass chip immersed in water.....	103
Figure 3-12. Relative amount of fluorescence, emitted by a single fluorophore, that is guided to the front surface of a microchannel glass chip immersed in air or water, as a function of the position of the fluorophore with respect to the front face of the chip	104

Figure 3-13. Fraction of fluorescence energy (emitted by a single fluorophore) that falls within a given numerical aperture, relative to the total fluorescence energy that reaches the front face of a microchannel glass chip immersed in water, as a function of the axial position of the fluorophore with respect to the front face of the chip.....	105
Figure 3-14. Schematic illustration of the propagation of radiation inside a microchannel chip, upon epi-illumination of the chip through an objective lens with the focus set on the front face of the chip	106
Figure 3-15. Axial distribution of light intensity within two types of microchannel chips immersed in water, as results from the waveguiding of light focused on the front surface of the chip through an objective lens of given numerical aperture	107
Figure 3-16. Efficiency of detection of a sidewall-bound fluorophore through epifluorescence imaging of the front face of a microchannel chip with an objective lens of given numerical aperture, as a function of the axial position of the fluorophore with respect to the front face of the chip	108
Figure 3-17. Photograph of the combination of an epifluorescence microscope and a cooled CCD camera used for the imaging of microchannel biochips.....	111
Figure 3-18. Epifluorescence imaging procedure used in the investigation of the optical properties of microchannel glass chips, with a two-dimensional, circa 260 μm diameter fluorescent TAMRA spot immobilised on the surface of a silanised planar glass substrate	111
Figure 3-19. Radial intensity profiles associated with the epifluorescence images of a two-dimensional fluorescent spot imaged with a 4x, 0.13 NA microscope objective lens at different levels of defocusing	113
Figure 3-20. Width of the out-of-focus image of a two-dimensional reference fluorescent TAMRA spot on planar glass, relative to that of the in-focus image, as a function of the level of defocusing	113
Figure 3-21. Fluorescence intensity of the out-of-focus image of a two-dimensional reference fluorescent TAMRA spot, relative to that of the in-focus image, as a function of the level of defocusing	114
Figure 3-22. Epifluorescence images A to D associated with the procedure described in Figure 3-18, for a 0.5 mm-thick microchannel glass chip.....	115
Figure 3-23. Image C, as defined in Figure 3-18, for microchannel glass chips from different manufacturers.....	115
Figure 3-24. Radial intensity profiles associated with the images of Figure 3-22	116

Figure 3-25. Characteristic ratios $S(C)/S(A)$, $S(B)/S(A)$ and $S(C)/S(D)$ for 10 μm channel diameter microchannel glass chips from Galileo Corp. and Collimated Holes Inc., as a function of the chip thickness	117
Figure 3-26. Relative intensity $S(C)/S(D)$ (as defined in Figure 3-18) for a 200 μm channel diameter, 350 μm thick PDMS chip and for 0.5 mm thick microchannel silicon chips with various channel diameters.....	119
Figure 3-27. Schematic representation of the bespoke epifluorescence microscope platform used for the imaging of microchannel biochips	121
Figure 3-28. Fluorescence microscopy image of a 4x4 array of spots, each spot resulting from the adsorption of 100 attomoles of Cy5 fluorophore at the surface of a microchannel glass substrate.....	124
Figure 3-29. Signal-to-noise ratio for fluorescent spots (produced by the dispensing of 10 nL aliquots of Cy5 solution onto 0.5 mm thick, 10 μm channel diameter MCG substrates), as a function of the CCD integration time.....	125
Figure 3-30. Dependence of the signal-to-noise ratio for fluorescent spots (300 amol Cy5 deposited onto 0.5 mm thick, 10 μm channel diameter MCG substrates) on the number of consecutive measurements, under an illumination power of 1.2 mW cm^{-2}	126
Figure 3-31. Signal-to-noise ratio for fluorescent spots (produced by the dispensing of 10 nL aliquots of Cy5 solution onto 0.5 mm thick, 10 μm channel diameter MCG substrates), as a function of the amount of fluorophore present in each spot	127
Figure 3-32. Signal-to-noise ratio for 30 amol Cy5 fluorescent spots (produced by the dispensing of 10 nL aliquots of Cy5 solution onto 0.5 mm thick, 10 μm channel diameter MCG substrates) as a function of the illumination power	128
Figure 4-1. Mechanism for the reaction between an organosilane compound and a silica-like surface, in the presence of water.....	132
Figure 4-2. Strategy used for the covalent attachment of amino-terminated oligonucleotide capture probes onto the silica-like surface of solid substrates.....	140
Figure 4-3. Setup used for the thermal oxidation of macroporous silicon chips.....	145
Figure 4-4. Fluorescence microscopy images of fluorescently-labelled oligonucleotide probes covalently attached to planar substrates: glass, thermally oxidised silicon (1 μm thick oxide layer), silicon (with native oxide only) and O_2 plasma-oxidised PDMS.....	151
Figure 4-5. Setup used to carry out heterogeneous hybridisation assays with planar DNA chips.....	156

Figure 4-6. Evolution of the signal-to-noise of spots of oligonucleotide probes immobilised on planar glass, thermally oxidised silicon and O ₂ plasma-oxidised PDMS substrates upon sequential hybridisation with FAM-labelled oligonucleotide targets	147
Figure 5-1. Photograph of the piezoelectric ink-jet spotter (Packard Biochip Arrayer 1) used to produce microchannel DNA chips	164
Figure 5-2. Spectral responsivity curve of the Hamamatsu Orca CCD camera (maufacturer's data)	165
Figure 5-3. Brightfield and epifluorescence microscopy images and associated radial intensity profiles of fluorescent spots formed by the dispensing of 5 nL aliquots from a 30 μ M solution of fluorescently-labelled probe in 1x SSC onto planar glass and microchannel glass	168
Figure 5-4. Brightfield images of 30 μ M oligonucleotide spots (in quadruplicate) on silanised microchannel glass, acquired with a 4x, 0.20 NA objective lens, prior to washing	170
Figure 5-5. Variation of the diameter of oligonucleotide probe spots (measured from the brightfield images of Figure 5-4) as a function of the dispensed volume, for various glass chips	171
Figure 5-6. Brightfield images of oligonucleotide probe spots formed on microchannel glass from solutions of variable concentration in 1x SSC	173
Figure 5-7. Brightfield images of oligonucleotide probe spots on microchannel glass and thermally oxidised macroporous silicon	174
Figure 5-8. Schematic drawing (exploded view) of the glass / PDMS flow cell used in microchannel chip-based bioassays	175
Figure 5-9. Schematic cross-sectional view of the stainless steel flow-through cell used in microchannel chip-based bioassays	177
Figure 5-10. Establishment of a flow of working solutions through a microchannel glass chip, monitored by white light imaging	178
Figure 5-11. Fluorescence images of oligonucleotide probe spots formed on microchannel glass and planar glass, before and after washing	180
Figure 6-1. Schematic representation of the setup used for the convective pumping (with recirculation) of working solutions in flow-through chip-based bioassays	183
Figure 6-2. Layout of one of 16 replicates of a 4x4 array of oligonucleotide capture probe spots (each spot produced by the dispensing of a 5 nL aliquot of a 30 μ M solution of activated probe) forming the pattern of a microchannel glass oligoarray	184

Figure 6-3. Epifluorescence image of a three-dimensional microchannel glass oligoarray, showing a pattern of FAM-labelled oligonucleotide targets hybridised to spots of complementary oligonucleotide probes	187
Figure 6-4. Layout of a 4x4 array of oligonucleotide probe spots (each spot produced by the dispensing of a 5 nL aliquot of a 30 μ M solution of activated probe) forming the pattern of microchannel glass and planar glass oligoarrays	190
Figure 6-5. Pseudo real-time kinetics curves of multiplexed heterogeneous hybridisation of oligonucleotide targets to a planar glass oligoarray and a microchannel glass oligoarray, at room temperature, upon continuous convective pumping of the sample at 0.5 mL min ⁻¹ through (<i>resp.</i> over) the microchannel (<i>resp.</i> planar) chip	192
Figure 6-6. Fluorescence images of a planar glass oligoarray and a microchannel glass oligoarray, after 230 minutes of hybridisation with 600 μ L of a mixture of oligonucleotide targets at 2 nM, 1 nM and 0.4 nM concentrations respectively, in 5x SSPE buffer, under 0.5 mL min ⁻¹ continuous flow and at room temperature	193
Figure 6-7. Schematic representation of the proposed integrated device for the implementation of electrokinetic pumping in microchannel chip-based hybridisation assays...	196
Figure 6-8. Layout of the contact photomasks used in the photolithographic steps of the device fabrication.....	199
Figure 6-9. Experimental procedure used for the fabrication of an array of planar ITO electrodes on glass.....	203
Figure 6-10. Setup used for the electroplating of planar Au microelectrodes with Pt black.....	204
Figure 6-11. Darkfield and Nomarski Differential Interference Contrast microscopy images of Au electrode arrays produced by “rapid prototyping” photolithography with plastic photomasks	205
Figure 6-12. Microphotographs of Au electrodes after removal of the NiCr sacrificial layer	206
Figure 6-13. White light darkfield microscopy images of a Au microelectrode, prior to and after Pt electroplating at 5 μ A (equivalent to 5.1 mA cm ⁻²) for 30 s.....	207
Figure 6-14. Scanning electron microscope images of Pt black grown at 40 mA cm ⁻² and 10 mA cm ⁻²	207
Figure 6-15. Surface profiles of a bare Au microelectrode and of Pt black films grown on Au microelectrodes at 20 μ A (equivalent to 20.6 mA cm ⁻²) for 30 s and 2 min	208
Figure 6-16. Cyclic voltamograms of Pt black electrodes grown at 10 mA cm ⁻² and 40 mA cm ⁻² , for 10 s	209

Figure 6-17. Photograph of a complete 4x4 electrode array device with electrical connectors, and microphotograph of a 4x4 array of thin film Au electrodes	209
Figure 6-18. Evolution of the potential difference between a Au anode and a Au cathode over time, during continuous galvanostatic biasing in two different isoelectric buffers, histidine and γ -aminobutyric acid.....	214
Figure 6-19. Epifluorescence images of a 100 nM solution of a Texas Red-labelled 29-mer oligonucleotide target in 100 mM γ -aminobutyric acid submitted to an electric field generated by the continuous application of a 1 μ A galvanostatic biasing between two Au electrodes of the device shown in Figure 6-16.....	215
Figure 6-20. Evolution over time of the fluorescence intensity over the area of the anode, the cathode and the floating electrode, measured from the images of Figure 6-18.....	216
Figure 6-21. Relative increase of fluorescence intensity at the anode over the first five seconds of galvanostatic biasing at 1 μ A, in various buffers.....	216
Figure 6-22. Time-dependence of the fluorescence intensity over an unbiased Au electrode, a biased Au electrode and a biased Pt black electrode, during electrophoretic transport of a Texas Red-labelled 29-mer oligonucleotide target present at 100 nM in 100 mM γ -aminobutyric acid buffer.....	217
Figure 6-23. Compared kinetics of mixed-phase hybridisation between a planar glass-immobilised 15-mer oligonucleotide probe and a 14-mer target present at 100 nM in different buffers: 1x SSC, 1x SSPE, 100 mM TRIS-borate, 100 mM His, and 100 mM GABA.....	219
Figure 7-1. Mechanism of action of a surface-bound "molecular beacon" oligonucleotide capture probe	224
Figure 7-2. Proposed concept of microchannel silicon chips with patches of porous areas matching the capture probe arraying pattern	228

LIST OF TABLES

Table 2-1. Expressions and numerical values for several geometrical parameters of a 10 μm channel diameter, 12 μm centre-to-centre spacing, 0.5 mm thick, 1 cm^2 microchannel glass substrate.....	56
Table 2-2. Operating conditions for the photoelectrochemical etching of silicon substrates of different doping levels in 2.5% HF	61
Table 2-3. Characteristics of the four types of silicon wafers used in photoelectrochemical etching experiments	61
Table 2-4. Expressions and numerical values for several geometrical parameters of a macroporous silicon substrate.....	66
Table 2-5. Photolithographic pattern used in Advanced Silicon Etch experiments	68
Table 2-6. Parameter settings used for the deep dry etching of silicon through the Advanced Silicon Etch process	70
Table 4-1. Equilibrium water drop contact angles for silica-rich surfaces silanised with different types of organosilane compounds.....	138
Table 4-2. Net fluorescence intensities for spots of Cy5-labelled oligonucleotide probe deposited on various planar substrates.....	152
Table 4-3. Net fluorescence intensities for spots of biotinylated oligonucleotide probe deposited on various planar substrates and stained with Cy5-labelled streptavidin.....	153
Table 5-1. Calculated ratios $V_{\text{dr}} / V_{\text{ch}}$, where V_{dr} is the volume of an aliquot of a 30 μM solution of oligonucleotide probe in 1x SSC buffer dispensed onto the microchannel substrate using the ink-jet spotter, and V_{ch} is the internal microchannel volume encompassed by the resulting spot	172
Table 5-2. Calculated numbers of binding sites and optimal spotting concentration for oligonucleotide probe spots on 0.5 mm thick, 10 μm channel diameter microchannel glass chips	173
Table 6-1. Sequence of steps involved in the conduction of a flow-through chip-based hybridisation assay in recirculation pumping mode.....	185
Table 6-2. Quantitative analysis data of a multiplexed fluorescence microchannel glass oligoarray assay.....	188
Table 6-3. Buffers tested for flow-through hybridisations in electrophoretic pumping mode.....	211

GLOSSARY

2D	Two-dimensional
3D	Three-dimensional
ADC	Analog-to-digital converter
ASE TM	Advanced silicon etch
CCD	Charge-coupled device
CE	Capillary electrophoresis
CV	Cyclic voltammetry
DMSO	Dimethylsulfoxide
DNA	Deoxyribonucleic acid
DOF	Depth-of-field
FAM	Carboxyfluorescein
FRET	Fluorescence Resonance Energy Transfer
FTIR	Fourier Transform Infra Red
GABA	γ -aminobutyric acid
His	L-histidine
IPA	Isopropyl alcohol (isopropanol)
ITO	Indium-Tin oxide
LOD	Limit of detection
MCG	Microchannel glass
MCS	Microchannel silicon
MEMS	Microelectromechanical system
MOS	Metal-oxide-semiconductor
MPTS	Mercaptopropyltrimethoxysilane
MPS	Macroporous silicon

N	Background noise (variance of the background signal)
NA	Numerical aperture
NHS	N-hydroxysuccinimide
NHE	Normal hydrogen electrode
ODN	Oligodeoxynucleotide
Ω	Ohm per square (unit of sheet resistance)
PCR	Polymerase chain reaction
PDMS	Poly(dimethylsiloxane)
PE-CVD	Plasma enhanced-chemical vapour deposition
pI	Isoionic point
PMMA	Poly(methylmetacrylate)
PVP	Polyvinylpyrrolidone
RNA	Ribonucleic acid
RI	Index of refraction
RO	Reverse osmosis
S	Analytical signal
SDS	Sodium dodecyl sulfate
SEM	Scanning electron microscopy
s-GMBS	N-(γ -maleimidobutyryloxy)sulfosuccinimide ester
S/N	Signal-to-noise ratio
SSC	Saline sodium citrate
SSPE	Saline sodium phosphate EDTA
TAMRA	Carboxytetramethylrhodamine
TIR	Total internal reflection
TRIS	Tris(hydroxymethyl)aminomethane
XPS	X-ray photoelectron spectroscopy

CHAPTER 1. INTRODUCTION

The starting point of this research was provided by the conceptual formulation of a novel biochip design (the “flow-through, microchannel” configuration) expected to offer enhanced performance in multiplexed bioassays. The work presented herein was concerned with implementing the concept into a functional platform applicable to genomic analyses, and to demonstrate the superiority of the approach over traditional DNA chip formats. The highly multidisciplinary nature of the biochip technology field is thus reflected in the contents of this work, in which a range of varied technical issues were addressed.

This introductory chapter begins with a review of the state-of-the-art in DNA chip technology, including the level of performance and limitations thereof, at the time of writing (Section 1. 1). Then, the concept of the flow-through microchannel biochip is presented in terms of its potential advantages and associated technical constraints (Section 1. 2). Finally, technical directions are suggested whose implementations and developments, which formed the bulk of this research, are reported over the next chapters.

1. 1. State of the art in DNA microarray technology

1. 1. 1. Biochips and microarrays

Over the last decade, biochip technology has emerged as a discipline that addresses the ever-increasing demand, in many bioanalytical applications, for higher levels of throughput. In this context, the term *biochip* has been coined to refer to a class of tools whose main function is to allow the multiplexing of bioassays.¹ The biochip format consists of the pooling (and possibly miniaturisation) of biorecognition sites such as nucleic acids² or antibodies³ on a single substrate, in the form of sensing elements, so as to allow as many as hundreds of thousands of assays to be performed simultaneously, in a parallel fashion, thereby dramatically increasing throughput. Initial efforts directly related to biochip technology started in 1986 with the development of miniaturised, multianalyte antibody “microspot” assays.⁴

The term *microarray* refers to a subset of the biochip group for which the density of sensing elements exceeds a certain value. One author⁵ has defined DNA microarrays as arrays of nucleic acid binding sites in which the spacing between discrete sensing elements is at most 500 μm (regardless of the support). This translates into densities in excess of 400 genes per cm^2 . Numerous applications of life science research and pharmaceutical development, such as applied genomics, diagnostics and molecular medicine, greatly benefit from being implemented in a microarray format.⁶ The main advantages associated with this approach are its higher

information content, decreased assay times, and lower unit and operating costs. These improvements in technical and commercial performance result not only from the high levels of parallelism and throughput that can be achieved, but also from a number of advantages inherent to the miniaturisation of (bio)analytical systems, such as large scale mass production, smaller working solutions (*i.e.* samples and reagents) requirements and reduced incubation times due to enhanced mass-transport kinetics, for example.

The rapid development of various biochip formats has been made possible by the combination of several disciplines: life science and technology (biochemistry, biotechnology, chemistry, molecular biology), engineering (including microfabrication and, for some microarray formats, microelectronics as well), instrumentation, automation, and computer science (bioinformatics). Automation has been, and remains, a key factor in the successful expansion of biochip technology.⁷ Although massive parallelism is an intrinsic feature of microarrays, the bottleneck to attaining high levels of throughput resides not necessarily in the assay completion stage itself, but possibly in other processing steps such as microarray fabrication, sample preparation and handling, or assay detection. Therefore, a whole range of automated instruments, based on high-speed robotics, has been developed. In this respect, a parallel can be drawn between biochip technology (for bioanalytical applications) and combinatorial chemistry (for chemical synthesis). Indeed, the manufacture of a few types of microarrays is based on a typically combinatorial approach.⁸⁻¹⁰

The fact that microarrays are essentially miniature bioanalytical tools suggests their possible coupling to, or integration with, other microfabricated devices with complementary functionalities, such as on-chip PCR¹¹⁻¹⁷ and on-chip electrophoresis¹⁸⁻²² for sample treatment; microfluidics^{23,24} and electrokinetic pumping²⁵ for fluid delivery; integrated optical modules,²⁶ *e.g.* phototransistors²⁷ and waveguides,²⁸⁻²⁹ for signal transduction and assay detection. Although still in its infancy, this field of research opens promising routes for the future development of high throughput *lab-on-a-chip* devices.^{30,31}

1. 1. 2. DNA chips

1. 1. 2. 1. Impetus

The main impetus behind the development of DNA chip technology has been the prospect of performing nucleic acid hybridisation assays in a multiplexed and *heterogeneous* format, leading to so-called *hybridisation array* assays. Here, heterogeneous is understood as the existence of two distinct phases, namely, biorecognition elements attached to a solid substrate, and sample in solution).

Microarray-based DNA / RNA analysis technologies were formally initiated in the USA in 1992 by the establishment of the Genosensor Consortium. This effort was prompted by the acknowledgement of the importance of DNA as a biological marker,³² as illustrated by the international establishment, in October 1990, of the Human Genome Project. The relative ease

with which DNA samples can be prepared and handled have also contributed to make DNA chips the most common form of biochips to date, so much so that the term *microarray* is often used to refer to *DNA microarrays*. Alternative terms used in the literature to describe DNA chips include *genosensor* and *gene array*, whilst *GeneChip*[™] is a trademark of Affymetrix, Inc.

1. 1. 2. 2. Heterogeneous, multiplexed nucleic acid hybridisation assays

1. 1. 2. 2. 1. From filters and membranes to chips

Early implementations of heterogeneous hybridisation assays were based on porous substrates such as nylon membranes and nitrocellulose filters,³³ onto which nucleic acids were attached by physisorption. This approach was made possible by the fact that single-stranded DNA molecules bound to membranes did not reanneal with each other and had the ability to hybridise with complementary RNA. The multiplexing capability of this *mixed phase* approach lay in the possibility of processing many samples simultaneously. Higher levels of multiplexing were later achieved with *dot-blot* methods, in which several different sensing elements were placed on a single support, in the form of spots.³⁴ Although assay detection still typically relied on radiolabels and autoradiography,³⁵ expediency, sensitivity and reliability were significantly improved as compared to the traditional centrifuge- and column-based techniques used hitherto in the separation of single- and double-stranded nucleic acids.³⁶

The real breakthrough in the advancement from membrane- and filter-based methodologies to microarray technology was brought about in the early nineties by the combined use of glass substrates^{8,9} and fluorescence detection.³⁷ The advantages of glass over filters and membranes are multiple. Glass is a low cost but durable material that can withstand high temperatures, high electric fields and high ionic strength washes (unlike nitrocellulose filters which can be damaged during hybridisation in aqueous solutions at 68°C or in solvents containing quaternary ammonium salts³⁸). In terms of nucleic acid immobilisation, the derivatisability of the surface silanol moieties of glass (in particular through organosilane chemistry) provides many routes for robust, covalent attachment of polynucleotides to the substrate, in a functional conformation.⁹ In addition, the non-permeable nature of glass allows for more precise, higher density spotting as compared to filters and membranes, for which spot density is limited by significant lateral diffusion within the porous structure. With glass substrates, interaction between hybridisation partners does not involve diffusion through pores, thereby enhancing hybridisation rates. Glass is also amenable to photolithographic patterning, a process through which extremely high densities of sensing elements can be achieved^{10,12} (see Section 1. 1. 2. 3. 3). Finally, the optical properties of glass make it compatible with optical detection schemes such as fluorescence imaging, including confocal fluorescence microscopy.³⁹ Alternative substrates (e.g. silicon) and transduction schemes (e.g. mass spectrometry) are now gaining importance in current DNA chip research and development, as discussed below.

1. 1. 2. 2. 2. Nucleic acid probes and targets in hybridisation array assays

Nomenclature

In this thesis, hybridisation partners are designated according to the terminology of the *reverse dot blot* approach, in which the binding sites (nucleic acids tethered to the substrate) are referred to as *capture probes* or simply *probes*, whilst the free nucleic acids contained in the sample solution that is assayed against the chip are referred to as *targets*. This terminology is now widely accepted within the microarray community.⁴⁰ The various types of probes and targets used in hybridisation array assays are described below.

Capture probes

From an analytical point of view, the DNA chip format lends itself to the use of nucleic acid probes of a wide range of complexity, from short oligonucleotides (10-100 bases) to longer DNA strands (100-2000 bases). In practice, capture probes are prepared either through chemical synthesis or by molecular cloning of genomic DNA.

*Oligoarrays*⁴¹⁻⁴³ feature 16 to 70 base-long nucleic acid oligomers (oligodeoxynucleotides, ODNs) as probes. These oligonucleotides are in most cases prepared prior to attachment to the substrate, through automated phosphoramidite chemistry synthesis,⁴⁴ although a few microarray platforms involve the *in situ* synthesis of the oligonucleotide probes, base after base, in a combinatorial approach⁸⁻¹⁰ (see Section 1. 1. 2. 3. 2). The use of such synthetic probes is valid within the framework of purely sequence-specific hybridisation pattern recognition strategies, of which *redundancy* is an important component, as further discussed in Section 1. 1. 2. 2. 3 below.

Microarrays have also been designed and manufactured that use cDNA probes as long as 2000 bases.⁴⁵⁻⁴⁷ Sample preparation involved in the construction of the relevant cDNA libraries is typically based on isolation of mRNA (e.g. from tissue) followed by reverse transcription to cDNA and amplification of the resultant cDNA using standard PCR protocols. Although this sample preparation procedure is rather labour-intensive (purification of the PCR products by precipitation and/or gel filtration is required), the approach is applicable to simultaneous *de novo* gene discovery^{45,48} and gene expression monitoring⁴⁷ (discussed in Section 1. 1. 2. 4. 2).

Targets

Although the many different applications of DNA microarrays require or entail different types of targets, as further mentioned in Section 1. 1. 2. 4, microarray-based analyses are in most cases directed to complex samples such as cellular mRNA, or RNA transcribed from genomic DNA. Since such long nucleic acid strands are prone to secondary structure rearrangements⁴⁹ (resulting from intramolecular base pairing) that are likely to adversely affect hybridisation with the probes, target complexity within the sample is usually reduced by fragmentation in order to improve mismatch discrimination and duplex formation rates. Purity of the target RNA is also

crucial to hybridisation, since cellular components (lipids, proteins, and carbohydrates) tend to promote non-specific adsorption of target molecules onto the substrate.

An important issue to consider in the preparation of the sample is the labelling of the target molecules for detection. Although detection schemes are currently in development that do not require any sample labelling (as described later), the majority of current DNA chip platforms rely on the incorporation of fluorescent tags in the target molecules. This is commonly achieved through enzymatic incorporation of fluorescently-labelled oligonucleotides into cDNA targets prepared by reverse transcription from mRNA, and by the use of fluorescent PCR primers in the case of cloned DNA fragments.

1. 1. 2. 2. 3. Kinetics and thermodynamics of hybridisation array assays

Hybridisation in solution

Nucleic acid hybridisation is a reversible, two-step process in which the two complementary stretches of DNA strands first come into contact and then “zip up” to form the duplex. The rate-limiting step is the first one, which is controlled by a bimolecular process. Thus, hybridisation between free probes and free targets in solution follows a second order kinetics.⁵⁰ Parameters which affect hybridisation include strand length and structure (*e.g.*, hairpin probes), base composition (GC content), molecular complexity, and molar concentrations of probe and target; as well as temperature, ionic strength, viscosity, pH, and presence of destabilising (*e.g.* formamide) and chaotropic (*e.g.* quaternary ammonium salts) agents in the hybridisation medium.

Mixed phase hybridisation

Overall, parameters affecting probe-target hybridisation in solution have similar effects in mixed phase systems.^{36,51} However, two-dimensional diffusion of nucleic acid target molecules over the surface of a microarray does contribute to the overall hybridisation process.⁵²⁻⁵⁴ In addition, the implementation of hybridisation assays in a mixed phase format requires consideration of the extent to which attaching probes to a substrate affects duplex formation with solution-borne targets.⁴⁸ Even when the probes are attached at one end, as is usually the case with short oligonucleotides (16-25 mers), the possibility of steric hindrance effects and electrostatic interactions between the probes and the substrate has to be taken into account. This involves consideration of the distances between adjacent probes, as well as distances from the probe nucleobases to the surface.

Since probe molecules are bound to the substrate, their abundance is characterised by a surface, rather than volume, concentration. The spacing between probe molecules is fixed, and determined by the surface coverage density. A higher surface concentration of probes permits higher levels of sensitivity and dynamic range to be attained. However, for hybridisation events to take place, target molecules must be able to gain access to the probes, a process which can

be impeded by steric hindrance if the density of probes is too high.⁴⁹ Consequently, the strategy used for the attachment of the probe molecules to the substrate should provide control over the final probe coverage density, so as to allow for optimised performance of the biorecognition layer.

Likewise, the probes should be somewhat isolated from the surface of the substrate, in order to alleviate steric constraints between the solid support and non-complementary stretches in the target strands, as well as excessive charge densities. This can be achieved by the insertion of a *spacer arm* of suitable length within the probes, between the first base and the anchoring group, as further discussed in Section 4. 2. 2. 2.

Multiplexed, mixed phase hybridisation

Issues arising from the high levels of multiplexing that characterise microarrays include possible interactions between individual spots, henceforth referred to as *cross-talk*. The latter is expected to take place when conditions ensuring perfect discrimination between non-identical targets are not met. Obviation of cross-talk requires the use of an appropriate set of probes, which has to be selected in consideration of parameters such as length, GC content and sequence.⁵⁵ For example, shorter probes allow for more efficient discrimination between perfect and mismatched duplexes, but since the probability of internal repetitions of the length of the probe within targets is increased, the length of the sample strands that can be unambiguously analysed decreases. Stringency conditions under which the hybridisation array assay is conducted are of paramount importance as well. Unless the assay is carried out on an *active* platform that enables stringency to be controlled independently at each spot (see Section 1. 1. 2. 3. 4), thermodynamics and kinetics differences between duplexes that differ in length, composition and sequence can result in biasing of the final array-wide hybridisation pattern.

These issues can be addressed in oligoarrays by resorting to *redundancy* as part of the probe set design. Redundancy consists in the use of a larger set of probes, so that the array includes, for example, several probes that are representative of several different regions of a same gene, and/or mismatched probes. Redundancy has been shown to improve affinity and specificity in hybridisation array assays, resulting in better signal-to-noise ratios (S/N), reduced cross-talk, and increased dynamic range.^{41,43}

1. 1. 2. 3. DNA chip platforms

The DNA chip concept has been translated into a whole range of platforms, based on a variety of substrates and assay transduction schemes. A brief overview of the state of the art as of this writing is given below.

1. 1. 2. 3. 1. Substrates

The many properties that make *glass* an attractive substrate material for microarrays have been described above (Section 1. 1. 2. 2. 1). The use of *ceramic* slides as biochip substrates has

also been reported.⁵⁶ *Silicon* is another commonly used biochip substrate material.^{57,58} High quality (*i.e.* chemically pure and crystallographically well-defined) wafers are readily available at relatively low cost due to the widespread use of silicon in the microelectronics industry.

In addition, the latter has contributed over the years to the development of a wide range of microfabrication techniques⁵⁹ (photolithography, wet and dry etching, metal thin film deposition methods) in the framework of very large scale integration (VLSI) strategies. These techniques are technically and economically relevant to the fabrication of microarray platforms, as illustrated by part of the work presented in this thesis (see Chapter 2). A definitive advantage in the use of silicon as a substrate is that it permits the direct interfacing of biorecognition events with microelectronic devices, resulting in truly “active” biochip platforms, as further discussed in Section 1. 1. 2. 3. 4.

Non-porous polymeric materials (*plastics*) are gaining popularity in microfabrication technology due to their low cost and versatility. A number of processing techniques such as embossing, imprinting and molding are now commonly used for the manufacture of biochemical sensing modules,⁶⁰ including integrated optics and microfluidics.^{61,62} As with silicon, further developments, in particular the possibility to modulate surface properties such as hydrophilicity, biocompatibility and electrical charge, are likely to impinge directly onto microarray technology. Medium-density arrays of oligonucleotides attached onto planar polypropylene substrates⁶³ have been shown to feature low levels of non-specific adsorption and reduced steric hindrance effects during hybridisation. Polystyrene microtitre plates⁶⁴ and poly(methylmetacrylate) (PMMA) substrates⁶⁵ derivatised with oligonucleotide probes have also been reported. An investigation into the use of poly(dimethylsiloxane) as a substrate material for planar and microchannel DNA chips is presented in this thesis (Chapters 2 and 4).

Hydrogels have also been used as substrates for the manufacture of microarrays. In this approach, nucleic acid probes are immobilised within the porous hydrophilic structure of a polyacrylamide⁶⁶⁻⁶⁸ or agarose⁶⁹ film deposited on a glass slide or a silicon wafer. Coupling moieties co-polymerised in the matrix allow for attachment of the probes by covalent or strong affinity (*e.g.* avidin-biotin) binding. The rationale behind the approach is that the large effective surface area of the porous polymer matrix permits a much greater number of probe molecules to be immobilised as compared to a planar, non-permeable substrate. In addition, the aqueous nature of the hydrogel is comparable to a bulk liquid phase, although limitations to the kinetics of hybridisation assays are introduced by the necessary diffusion of the target molecules through the polymeric matrix. The relative merits of hydrogels as compared to the flow-through, microchannel substrates on which this thesis is based are discussed in the next chapter.

1. 1. 2. 3. 2. Structured immobilisation of multiple oligonucleotide probes

In situ (on-chip) synthesis of oligonucleotide probes

As stated above, the direct combinatorial synthesis of oligonucleotide probes on a glass substrate is a well-developed process for the fabrication of oligoarrays.^{8,10} This approach is

based on the use of photolabile protecting groups for the sequential activation of selected sites, at which oligonucleotides are synthesised base after base, in an incremental fashion. The main advantage of the process results from the use of ultraviolet (UV) light illumination as the deprotection-inducing step. UV illumination of photoactive polymeric films (photoresists) through contact or close proximity photomasks, a process known as photolithography, is widely used in microelectronics for the generation of small feature size (down to a few tens of micrometers) patterns. In its current implementation, the light-directed oligoarray manufacturing technique allows individual probe features as small as $25 \times 25 \mu\text{m}^2$ to be generated on a glass substrate, so that more than 250,000 different probe sequences can be fitted on a half inch square chip surface.⁷⁰

Post-synthesis attachment

In this approach, oligonucleotide probes are first synthesised using standard techniques (usually phosphoramidite chemistry-based⁴⁴), then attached to the substrate by covalent or strong affinity binding. To that end, an appropriate moiety is incorporated into the probes (at either the 3' or the 5' end) during the synthesis process, so as to allow for subsequent coupling to the substrate. This approach benefits from the reliability, expediency and flexibility of automated solid-phase oligonucleotide synthesis techniques, and allows for quality control and assurance (QC/QA) of the probes to be carried out prior to substrate processing.

Structured attachment of a probe to the substrate is achieved either through delivery of the probe to a spatially defined area of a uniformly activated substrate, or by dispensing of the probe over the entire substrate followed by localised attachment at an actively addressable site. The former approach consists in "spotting" the substrate with probe solutions, using specially designed robots⁷¹⁻⁷³ as described in Section 1. 2. 6. 3. 1. The latter approach involves the use of a substrate featuring an array of independently and electronically activable sites, typically photolithographically-defined thin metal film microelectrodes. In one such implementation, a probe which has been derivatised so as to bear a polymerisable monomer group (pyrrole), is electrochemically co-polymerised *in situ* within a polymer film (polypyrrole).^{74,75} In another such implementation, biotinylated probes are electrophoretically transported and accumulated at electronically active sites within a streptavidin-containing hydrogel layer.⁶⁹

Compared to the *in situ* synthesis approach, post-synthesis immobilisation is characterised by lower density levels. The spotting method is limited by the minimum volume of solution that can be reproducibly dispensed as well as by the spatial resolution of the mechanical actuation stages. In the electronic addressing approach, although the electrode array is manufactured by high-resolution photolithographic techniques, the need for the electrodes to be individually addressable requires electrical wiring of each and every electrode, which eventually limits the achievable spatial resolution of sensing elements.

1. 1. 2. 3. 3. Array density

Since the multiplexing capability of a biochip is based on the spatial distribution of sensing elements, the level of multiplexing of a two-dimensional (2D), planar chip is determined by both the feature size of the spots and the lateral dimensions of the substrate. Given the advantages associated with the miniaturisation of bioanalytical devices, increasing the dimensions of the chip is not appropriate, especially in terms of mass-transport kinetics and required amounts of working solutions. As seen above, the process used in the manufacturing of a microarray ultimately determines the maximum density that can be achieved for that particular type of array. However, the highest density is often not desirable. On the contrary, it can result in a decreased performance of the DNA chip, as a smaller spot size is accompanied by a smaller number of probe molecules within each spot, which in turn limits the detectability and the dynamic range, as well as the kinetics, of the hybridisation assay.⁵

The resulting tradeoff, for a biochip of given dimensions, between the level of multiplexing and the inherent analytical performance of each sensing element underlies the need for different types of DNA chips to be used in different applications. Whereas the real-life applicability of ultra-high-density arrays is limited by the above-mentioned considerations regarding stringency control, cross-talk between probes, sensitivity, and dynamic range, lower density DNA chips are still relevant to a number of key diagnostic and therapeutic applications, in which high levels of throughput are beneficial, without the need for high levels of parallelism. This includes DNA chips specific to a few genes (tens to hundreds) relevant to one particular disease, *e.g.* breast cancer. The microarray platform presented in this thesis belongs to this category, with a few hundred sensing elements per chip, most typically 256 spots (16 x 16 array).

1. 1. 2. 3. 4. Active biochip platforms

Even though a number of microarray platforms are manufactured using microfabrication techniques borrowed or derived from the microelectronics industry, most of these platforms are *passive* in nature in that they do not take advantage of the electronic properties of the substrate. For instance, assay detection is usually based on far field optical processes (typically, molecular luminescence methodologies such as fluorescence and chemiluminescence) rather than on direct electronic or electrochemical signal transduction on the substrate (see next Section). Likewise, fluid delivery and handling most commonly rely on mechanical schemes such as convective pumping.

On the contrary, *active* biochip platforms use electronic biasing for the control of hybridisation (or at least aspects of it), thereby truly bridging the fields of microelectronics and molecular biology.^{69,76,77} This approach is made possible by the fact that polynucleic acid molecules carry a significant electrical charge over a wide range of pH, a property that can be exploited in applications such as electrokinetic pumping of fluids and electronic stringency control. The

latter allows several steps of the assay (pre-hybridisation, hybridisation, washing) to be carried out without physically changing buffers, and addresses some of the issues mentioned in Section 1.1.2.3 by permitting independent control of the stringency conditions at individual sensing elements.

1.1.2.3.5. Transduction schemes for multiplexed hybridisation assays

A variety of transduction schemes are used in hybridisation array assays. These schemes have been either adapted from the field of biosensors,⁷⁸ or developed specifically. The performance of the transducer (in terms of sensitivity, selectivity and dynamic range) must accommodate for the miniature size of the sensing elements in addition to being compatible with the high levels of multiplexing that characterise biochips.

Autoradiography, a technique in which nucleic acids are labelled with radioactive elements (most commonly ^{32}P and ^{33}P) was used extensively until the 1990s in conjunction with membrane- and filter-based assays. X-ray film now tends to be replaced by imaging plate devices or even charge couple devices (CCDs).⁷⁹ As an imaging technique, radioactive detection features some degree of multiplexing capability, in addition to its intrinsically high sensitivity and large dynamic range; however, its low spatial resolution (of the order of 100 μm), sufficient for dot-blot assays, is not appropriate for microarrays. In addition, the handling of radiolabelled compounds is complicated by the associated legal health and environmental issues, as well as their limited shelf-life.

Optical detection schemes have now superseded radiography in all but a few array-based applications, due to their exquisite sensitivity (comparable to that of radioactive labels) as well as to their versatility stemming from the availability of a wide number of labelling and detection schemes, such as FRET (fluorescence resonance energy transfer),⁵⁰ that provide high selectivity at the molecular level. Implementation of fluorescence and chemiluminescence detection in DNA chip technology is further discussed in Chapters 3 and 7 of this thesis. Far-field optical imaging techniques are particularly well suited to multiplexed detection from high-density arrays. The high spatial resolution, below 1 μm , of imaging optics such as microscope objective lenses is at least one order of magnitude higher than the density of sensing elements on the surface of a microarray. In addition, true imaging detectors such as digital CCD cameras are now available that feature high levels of sensitivity, dynamic range (16-bit digitation is available) and image resolution (with pixels down to a few micron square). The obtention of imaging data in digital format facilitates subsequent data analysis and archiving. Confocal scanning microscopy has been implemented in microarray applications that require extremely high levels of lateral and axial resolution. In this approach, a point detector (typically a PMT, photomultiplier tube) is used in conjunction with high-resolution optics, the imaging capability deriving from two-dimensional mechanical scanning of the optics relative to the array followed by digital image reconstruction.³⁹

Optical sensing has also been successfully implemented in microarray formats. Here, we refer to optical sensing as near- or far-field techniques in which the chip substrate plays an active role in the propagation of the incoming stimulus and resulting signal electromagnetic radiation. This differs from the imaging schemes mentioned above in which the substrate is not actively involved in light propagation, thereby allowing physical separation between a biochip and its imaging system. The multiplexed detection capability of optical sensing schemes comes from the multiplication of the number of sensing elements according to the pattern of biorecognition sites on the substrate. Highly sensitive DNA arrays using evanescent-field fluorescence excitation have been constructed, based on fibre optics^{29,80} and planar waveguide devices.²⁸ Also in this category are the highly multiplexed sensors based on imaging fibre optics developed by Walt *et al.*^{81,82}

Electrochemical and electronic sensing are attractive analytical detection schemes for microarray technology due to the miniaturisation and integration possibilities offered by the development of molecular electronics. A distinction can be made between *electrochemical* sensing, in which faradaic currents resulting from electron transfers occurring during redox processes are measured,⁸³ and *electronic* sensing, which is based on the measurement of changes in the properties of a biorecognition layer considered as part of an electrical circuit. Indirect electrochemical detection of DNA hybridisation based on charge transduction measurements has been demonstrated, using redox-active intercalators bound to DNA-modified Au surfaces, whose electrochemical properties are sensitive to single-base mismatches within the duplexes.⁸⁴ Examples of electronic transduction include field effect, impedance,⁸⁵ and dielectric⁸⁶ sensors. The main challenge involved in making these detection schemes suitable to microarrays concerns multiplexing, spatial resolution, and sensitivity.

Mass spectrometry has also been applied to DNA microarrays.⁸⁷ In this approach, a primer extension chemistry is used to generate gene-specific products, each with a unique molecular weight, that are subsequently arrayed onto a silicon substrate. Each spot incorporates light absorbing crystals that form a desorption / ionisation matrix specially optimised so that the primer extension products can be analysed by MALDI-TOF (matrix assisted laser desorption / ionisation - time-of-flight) mass spectrometry, in a sequential (scanning) fashion. The expediency and accuracy of the approach is well suited to high throughput screening.

1. 1. 2. 4. Applications of DNA chips

Although the analytical ability of DNA chips is based exclusively, at the molecular level, on nucleic acid hybridisation events, the importance of DNA and RNA as biological markers hints at a wealth of applications for microarrays in such varied fields as diagnostics and drug discovery. These applications can be broadly classified into two categories, sequence and polymorphism analysis on the one hand and gene expression on the other hand.

1. 1. 2. 4. 1. Sequence and polymorphism analysis

Sequencing by hybridisation (SBH) using oligoarrays has been implemented as a high-throughput alternative to the traditional Sanger sequencing method.⁸⁸ The latter, which involves PCR amplification of a target sequence of interest followed by gel-based analysis (electrophoretic separation) of PCR products, is a laborious technique hardly appropriate to large-scale efforts such as the Human Genome Project.

The limited number of complementary units involved in the process of nucleic acid hybridisation (two pairs of nucleobases) is at the source of the concept of a *universal* or *generic* array, in which all possible 4^n probes of length n are present on a single chip. Such an array theoretically allows the discrimination between targets of moderate length, and can therefore be applied to sequencing by hybridisation. An experimental validation of this approach has been demonstrated through the sequencing of 1100 base-long samples using a generic 7-mer oligoarray ($4^7 = 8,192$ different probes).⁸⁵ The power of SBH can be enhanced by contiguous stacking hybridisation (CSH),⁸⁹ which allows larger DNA strands (megabase-long) to be analysed without having to resort to prohibitively complex generic chips ($n > 13$).

Apart from its role in sequencing the genome of model organisms (human included), SBH is widely used in the analysis of genetic polymorphisms, which can be seen as a “quasi-sequencing” application.^{90,91} For example, polymorphism analysis of kilobase-long DNA has been achieved using a generic 9-mer chip⁹² featuring $4^9 = 262,144$ different probes, fabricated through the *in situ* photolithographic process described in Section 1. 1. 2. 3. 2. Besides, identification of mutations by differential hybridisation with allele-specific oligonucleotide (ASO) probes³⁷ has been employed in the diagnosis of genetic diseases, and in the detection and/or identification of infectious agents in human blood or tissue. Polymorphism analysis is also employed in forensics, in paternity testing, and for environmental protection.

1. 1. 2. 4. 2. Gene expression analysis

Principle and benefits of microarray-based gene expression analysis

The analysis of gene expression levels can be achieved by hybridisation of cellular mRNA (or cDNA representations thereof) with appropriate genetic markers, such as Expressed Sequence Tags (ESTs). Since the associated hybridisation assays can be implemented in a mixed-phase format, microarray technology provides a high-throughput route to gene expression determination; in effect, the high levels of multiplexing characteristic of microarrays make it possible to infer gene expression profiles of up to several thousands genes from a single hybridisation experiment in which a complex target sample containing many sequences in various amounts is assayed against the array.⁵ In fact, this approach allows for the whole genome of certain organisms to be analysed at once, as is the case for yeasts whose entire genome (circa 6,000 genes) has now been put on a chip.⁹³

Information concerning the function of a gene can be gained by differential expression analysis,^{45,48,94,95} in which the expression level of a gene of interest in a test or *activated* cell state (e.g. after the cell has been subjected to the action of a drug) is compared to the expression level in a reference or *resting* state. An additional dimension to multiplexing, provided by multicolor fluorescence detection, allows for mRNA from both the resting and activated cell states to be assayed against the array simultaneously,⁴⁵ in a competitive hybridisation process (a feature that is not possible with radioisotope detection). This approach requires test and reference targets to be labelled with distinct, spectrally discriminable fluorophores, and assay detection to be carried out through the two corresponding optical channels.

If randomly chosen cDNA clones, rather than ESTs, are used as probes, differential expression analysis can be the first step in a *de novo* gene discovery strategy, in which the second step involves the characterisation by sequencing of those mRNAs that exhibit differential expression. Simultaneous gene discovery and sequence determination are possible through the use of generic oligoarrays.⁹⁶

Technical requirements

The successful conduction of multiplexed gene expression analysis requires the use of a microarray platform with high intrinsic sensitivity, so that hybridisation events associated with genes with low expression levels (transcripts that represent $< 1:100,000$ (w/w) of the total mRNA sample) can be unambiguously detected. In addition, the dynamic range of the assay must be large enough to allow for the simultaneous measurements of a wide range of expression levels. For example, Schena *et al.*⁴⁵ have shown that the expression levels for heat shock and phorbol ester-regulated genes in human T (Jurkat) cells vary from $< 1:100,000$ to $> 500:100,000$, which represents 2.7 orders of magnitude. Another requirement is the ability to detect low levels of differential expression (lower than 2-fold⁴⁵).

Such high levels of intrinsic performance must be accompanied by high levels of instrumental performance, due to the experimental conditions in which hybridisation array assays are carried out. Microarray-based gene expression measurements follow the reverse dot blot approach, in which the sample consists of a complex target containing a large number of sequences at different concentrations. As the sample is prepared with mRNA extracted from tissue, a low amount of each sequence is present in the complex target (in effect, each probe sequence immobilised on the array is in large excess over its cognate target present in the sample). In addition, the simultaneous measurement of abundance levels for each of the sequences present in the complex target requires that microarray readout takes place in the initial phase of the pseudo-first order hybridisation process, when the kinetics are linear and the signals are proportional to the concentration of target molecules present in the sample (in addition to being proportional to the number of probe molecules present within each sensing element, and the hybridisation time). These conditions are only realised when a small fraction of the probe

molecules present within each sensing element is hybridised with targets.⁵ Generally, an attomole-range level of sensitivity for probe-target duplexes is required. In the case of traditional planar glass microarrays such as those used by Schena *et al.*, this level of performance is achieved through the use of two-color confocal scanning epifluorescence microscopy as the detection scheme.

1. 2. The flow-through microchannel DNA chip platform: concept and implementation

1. 2. 1. Introduction

In this section, the concept of the flow-through microchannel DNA chip is presented. The underlying rationales are discussed, in terms of potential advantages and limitations with respect to traditional planar platforms. Possible strategies for the implementation of the concept are considered.

1. 2. 2. Limitations of current DNA chip platforms

The state of the art in DNA chip technology has been presented in Section 1. 1. As stated, current platforms are based on essentially two types of configurations, namely: planar, non-permeable substrates on the surface of which probes are immobilised (two-dimensional biochip morphology); and porous substrates, such as hydrogel layers or nylon membranes, with probes immobilised inside the polymeric matrix (three-dimensional morphology).

In hybridisation assays performed in the framework of gene expression measurements, the experimental conditions used are such that signals are proportional to the number of probe molecules present within a single sensing element in the array.⁵ Therefore, the sensitivity of a DNA chip is related to the effective surface area of substrate covered by each individual spot. In the case of DNA chips based on the two-dimensional morphology, increasing the amount of probe per spot increases the effective feature size of the spots, which in turn may result in a decrease in the spot density. Likewise, the number of probe molecules present within each sensing element determines the intrinsic dynamic range of the chip. A higher dynamic range can therefore only be achieved either by lowering the spot density, and/or by increasing the lateral dimensions of the substrate.

Another limitation of planar DNA chips is concerned with the time frame of the assays. In the common implementation of static assays, in which the array is covered with a thin film of sample and capped by a coverslip to prevent evaporation,⁴⁵ hybridisation kinetics are controlled by the diffusion of a target molecule towards its cognate probe. Accordingly, for a given concentration of targets in the sample, assay times increase as the overall lateral dimensions of the array increase, since the distances over which mass transport must take place before a target reaches its cognate probe increase. Even if mass transport is enhanced by, for example, forced

convection of the sample over the array, a 10-100 μm thick stagnant layer of fluid remains through which targets must diffuse to reach the probes.⁹⁷

DNA chips based on a three-dimensional matrix feature a larger effective surface area as compared to planar, non-permeable substrates, permitting a greater number of probe molecules to be immobilised within a spot of identical lateral dimensions. However, the kinetics of hybridisation are detrimentally altered by the slower diffusion of target molecules through the polymeric matrix.

1. 2. 3. The flow-through microchannel DNA chip concept

The above-mentioned limitations of DNA microarrays have prompted the design of a novel platform, which relies on the use of microstructured solid substrates to provide increased bioanalytical performance.⁹⁸ The concept is schematically represented in Figure 1-1.

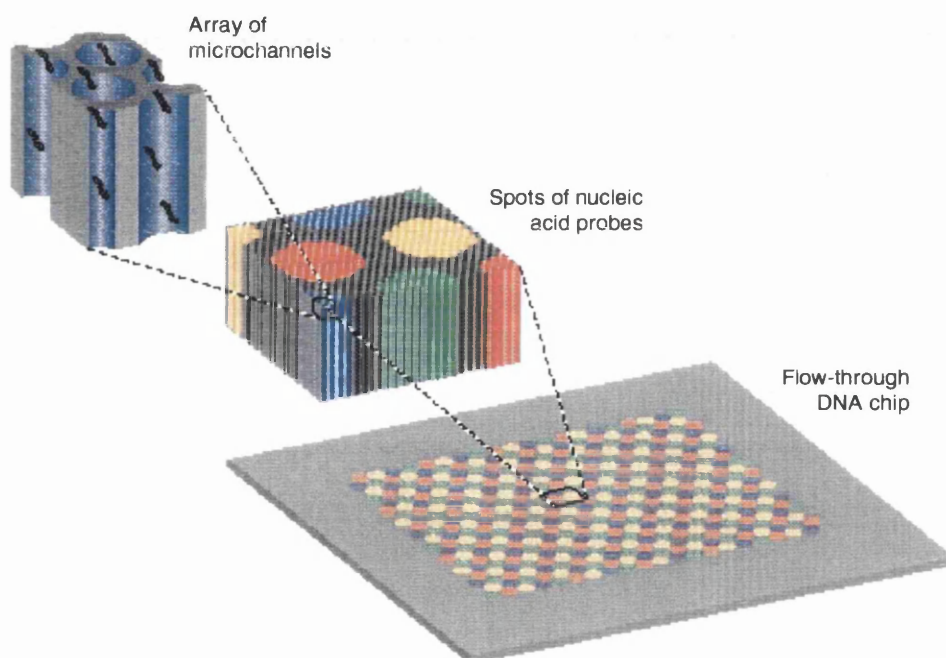


Figure 1-1. The three-dimensional, flow-through microchannel DNA chip concept. Nucleic acid probes are immobilised, in the form of discrete spots, within the microchannels of a uniformly porous substrate (each spot encompassing several microchannels). Hybridisation events take place upon flowing the sample through the chip.

This three-dimensional (3D) biochip configuration is based on uniformly porous substrates that feature an array of discrete, ordered, high aspect ratio (defined as the ratio between channel length and channel diameter) microchannels. Probe molecules (oligonucleotides or cDNA) are immobilised on the walls of the microchannels, using a post-synthesis attachment protocol. Hybridisation events between the probes and solution-borne target molecules take place whilst

flowing the sample “through” the chip, if necessary in an iterative manner. Note that, because of the typically small feature size of the microchannels (a few micrometers) as compared to the volume dispensed to produce a single spot (a few nanoliters), each spot typically encompasses tens to hundreds of channels.

Structurally speaking, a flow-through microchannel chip can be seen as a microporous membrane, such as those used in microfiltration, whose pores are cylindrical and uniform in size, *i.e.* a homoporous membrane.^{99,100} From a functional point of view, it is appropriate to consider a flow-through microchannel DNA chip as a multiplexed set of mixed phase, affinity-based separation columns. Each 3D spot, consisting of a group of microchannels within which probe molecules of identical sequence are attached, has the ability to retain a particular analyte (a target molecule that is complementary to the probe sequence of that spot) selectively to others (targets that are non-complementary to the probe). In this respect, each 3D spot or flow-through biorecognition element acts as an solid-phase extraction column. Each individual microchannel that is part of a 3D spot functions as an open-tubular capillary column. The pooling of several of these biorecognition elements on a single microchannel chip, to which a given sample is applied (in effect, “eluted” through the chip), is conceptually similar to a multiplexed capillary column analysis.

1. 2. 4. Potential advantages of the flow-through microchannel DNA chip configuration

The potential advantages that are expected to result from the use of microchannel substrates are many-fold. Firstly, in terms of intrinsic assay performance, the increase in effective surface area, brought about by extension into the third dimension, permits an increased number of probes to be immobilised within a spot of given feature size, as compared to a 2D planar substrate. The higher number of probe molecules immobilised within each spot is expected to provide a higher dynamic range, as well as a higher sensitivity (refer to Section 1. 1. 2. 4. 2 above). In addition, the high surface-to-volume ratio characteristics of the microchannel substrates can possibly result in smaller sample and reagent volume requirements.

Secondly, enhanced hybridisation kinetics are expected, due to the flow-through capability of the microchannel configuration. Forced convection of the sample within the microchannels can be used to supplement diffusion in bringing target molecules into contact with their cognate probe. In effect, each microchannel acts as a miniature analytical chamber, in which mass-transfer kinetics are enhanced by spatial confinement, a consequence of the stagnant fluid layer being reduced to the radius of the channels (typically 5 μm , versus 10-100 μm on planar substrates).

Thirdly, the microchannel configuration is expected to be beneficial to the process of probe immobilisation. Liquid dispensed onto the surface of a microchannel substrate is drawn into the microchannels by capillarity, while the non-interconnected nature of the channels prevents lateral diffusion of the spotting solution (unlike the case of porous substrates such as hydrogel

pads and nylon membranes). As a result, probe spots are expected to present a smaller footprint than on planar or porous substrates, as well as a higher uniformity of probe distribution.

Experimental demonstrations of the potential advantages provided by the use of microchannel substrates are given over the next chapters. In particular, the enhanced sensitivity and dynamic range of flow-through microchannel DNA chips with respect to planar DNA chips are demonstrated in Chapter 6.

1. 2. 5. Technical challenges associated with the use of microchannel substrates

The morphology of microchannel biochips has been designed to enhance intrinsic bioassay performance, as discussed above. However, this very morphology brings specific technical constraints as compared to traditional DNA chip configurations based on planar, non-permeable substrates.

In terms of probe attachment chemistry, photochemical methods (including photochemical immobilisation and *in situ* photoactivated oligonucleotide probe synthesis), as well as microcontact printing techniques, are obviously not implementable on high aspect ratio microchannel substrates. Mechanical spotting appears to be the only applicable approach. This has important consequences in terms of array density, as discussed later. Besides, the particular morphology of the substrate provides particular wetting properties that are likely to affect liquid-phase surface modification reactions.

In addition, the high aspect ratio microchannel structure of the substrate complicates qualitative and quantitative analysis of the biorecognition layer. The latter is not readily accessible for probing by usual surface analysis techniques, due to the active sensing layer being localised to the walls of the microchannels. Techniques commonly used in surface science, such as atomic force microscopy (AFM), X-ray photoelectron spectroscopy (XPS), goniometry, and ellipsometry, which have all been successfully applied to the characterisation of two-dimensional DNA chips,¹⁰¹ are not directly applicable to 3D microchannel substrates. Imaging methods based on the projection of particles onto a two-dimensional detector (fluorescence, autoradiography) are more readily implementable, but the information obtained is, at best, semi-quantitative.

For the same reason, a number of transduction schemes that have been successfully implemented with 2D biochips are incompatible with the 3D microchannel configuration. In particular, schemes in which the substrate plays an active role, such as near-field optical methods²⁸ and electrochemical methods,⁸⁴ can not readily be applied to microchannel chips. The use of far field optical methods (fluorescence, chemiluminescence) is *a priori* not incompatible with 3D substrates, but specific procedures have to be developed and optimised before sufficient levels of instrumental performance (as mentioned in Section 1. 1. 2. 4. 2) can be attained from these methods, when used in conjunction with microchannel chips; in particular, the bulk optical properties of the substrate have to be taken into account.

Fluidics is an important aspect of the flow-through microchannel biochip approach. Flowing the sample solution through the chip is expected to provide increased mass transport and diffusion gradient breakdowns within the microchannels, giving enhanced assay kinetics. However, the delivery of a target molecule to its cognate probe requires consideration of the fact that the non-interconnected nature of the microchannels prevents lateral diffusion of target molecules from one spot to the next within the 3D structure. As all the target molecules should be given an opportunity to interact with their respective complementary probe, some kind of external mixing process is necessary to ensure target redistribution across the array.

Overall, the morphology of the substrate is expected to play a crucial role in determining the bioanalytical performance of 3D, flow-through microchannel biochips. Assay kinetics are expected to be enhanced by a decrease in channel diameter. Sensitivity and dynamic range are likewise expected to be enhanced by a decrease in channel diameter, as well as by an increase in the thickness of the chip. However, decreasing the diameter of the channels while increasing their aspect ratio is likely to adversely affect the fluidics and detection processes, through increased resistance to sample flow, increased probability of channel blocking, and reduced optical detection efficiency.

1. 2. 6. Implementation of the flow-through microchannel configuration for DNA chip applications

In this section, technical issues regarding the implementation of the flow-through microchannel biochip concept into a functional, performant platform for nucleic acid hybridisation assays are discussed. These issues concern substrate materials and morphologies, strategies for the attachment of nucleic acid probes to the substrate, fluidics, and hybridisation detection. The technical choices that have been made regarding each of the aforementioned issues are stated and briefly justified, so as to provide the reader with an overall picture of the microchannel chip platform as well as a first insight into the various aspects of the work carried out in the framework of this thesis. Further characterisation, validation and subsequent technical developments are presented in more details in the next chapters.

1. 2. 6. 1. Microchannel substrates

1. 2. 6. 1. 1. Requirements

Materials suitable for use as substrates in the flow-through biochip approach described above have to feature a regular array of ordered, discrete microchannels. In addition, the material must be amenable to surface modification and/or derivatisation so as to permit the tethering of nucleic acid probes to the walls of the channels. As the high aspect ratio morphology translates into high surface-to-volume ratios, undesirable surface effects such as non-specific binding through physisorption have to be considered in the choice of the material. The substrate must

also be compatible with bulk liquid transport processes such as convective pumping, and thus must exhibit a low resistance to flow as well as a sufficient level of mechanical resiliency. Finally, the substrate must allow for the implementation of an analytical detection scheme suitable for mixed phase nucleic acid hybridisation assays.

1. 2. 6. 1. 2. Envisioned materials

Two existing materials have been initially identified as likely candidates for flow-through biochip substrates: microchannel glass (which is commercially available) and macroporous silicon. The applicability of deep dry etching techniques for the fabrication of microchannel silicon substrates has also been assessed in the framework of this thesis. In addition, investigations into the use of polymeric materials for flow-through DNA chip applications have been conducted, based on poly(dimethylsiloxane), PDMS.

Microchannel glass

Nanochannel glass (NCG) materials were first described by Tonucci *et al.*¹⁰² NCG materials are essentially glass structures containing a geometrically regular array of parallel channels as small as 33 nm in diameter, with packing densities in excess of 3×10^{10} channels per square centimeter, that can be fabricated in various array configurations. The initial impetus behind the development of NCG substrates stemmed from the fact that their morphology, combined with their ability to withstand temperatures in excess of 600°C without deformation, made these materials suitable as host or template structures for the development of quantum-confined semiconductor systems. The process used to fabricate NCG materials is applicable to the production of larger scale structures, with feature sizes in the 1-50 μm range and aspect ratios up to 60:1. These *microchannel glass* (MCG) structures are routinely used as in-line filters for liquids, and thus, unlike NCG substrates, exhibit the flow-through capability required for the envisioned biochip platform. The geometrical regularity of MCG implies that the surface available for the attachment of biomolecules is well defined. Other applications of MCG materials include gas-flow collimation, X-ray collimation, differential pressure barrier, and optical beam splitters.

Macroporous (photoelectrochemically etched) silicon

The formation of nanoporous silicon by anodic conversion of crystalline silicon in hydrofluoric acid (HF) was first reported by Turner in 1958.¹⁰³ In the early 80s, Beale *et al.* published systematic studies of the effects of silicon dopant type, resistivity, current density, and HF concentration on the formation and properties of nanoporous silicon.¹⁰⁴ Interest in the material widened after the discovery of the room temperature photoluminescence of porous silicon, a phenomenon resulting from the increase of the energy bandgap of silicon into the visible range by quantum confinement effects.

In 1990, Lehmann modified the photo-assisted electrochemical etching process initially developed by Turner, and achieved deep etching (several hundred microns) of vertical pores,

with feature sizes in the high nanometer - low micrometer range, arranged according to a pre-patterned array, in n-type silicon wafers. Lehmann proposed a mechanism for the formation of these photoelectrochemically etched trenches, and provided an experimental validation of his model.^{105,106} Lehmann's work has open routes towards the fabrication of highly regular structures with custom pore geometries. The latter are possible within certain limits of crystallographic orientation and doping density of the substrate,¹⁰⁷ and require the precalculation of etching parameters, namely applied electrical bias, illumination intensity, HF concentration, and pore initiation pattern. In this thesis, the term *macroporous silicon* is used to refer to photoelectrochemically etched silicon substrates featuring well-defined, regular trenches with 1-20 μm feature sizes and 30:1 to 250:1 aspect ratios.

Deep dry etched silicon

A whole range of "dry" (i.e., gas phase) subtractive processes have been available from the early 1970's onwards that allow for the transfer of photolithographic patterns into dielectric and semiconductor materials, in particular glass, quartz and silicon. Recently developed dry etch techniques provide high levels of anisotropy in the etching process, making high aspect ratio microstructuring possible. In particular, one type of process¹⁰⁸ has been shown to allow for deep ($> 300 \mu\text{m}$) and highly anisotropic (aspect ratio $> 20:1$) etching of silicon, as would be required for the fabrication of microchannel substrates to be used in flow-through DNA chip applications. This process, referred to as Advanced Silicon Etch (ASETM), relies on the alternating of etching periods and protective polymer deposition steps (for sidewall passivation) to yield highly anisotropic etching profiles.¹⁰⁸ Typically, a high-density, inductively coupled plasma (ICP) is used to drive dissociation, ionisation and attachment reactions of the fluorine reagent within the etching chamber, generating highly reactive species at moderate temperatures (between 25°C and 250°C). In addition, plasma-induced polymerisation is used to coat the sidewalls of the structures being etched with a Teflon-like $[(-\text{CF}_2-)_n]$ polymeric layer that inhibits lateral etching. The fluorine plasma process has potential capability for high aspect ratio (in excess of 40:1) etching, with highly vertical walls over large ($> 500 \mu\text{m}$) etching depths, as would be appropriate for the fabrication of microchannel DNA chip substrates.

Poly(dimethylsiloxane), PDMS

Poly(dimethylsiloxane) is an elastomeric polymer that readily lends itself to imprinting or molding into small feature size (sub-micrometer), and/or high aspect ratio, structures. A wide range of microelectromechanical, optical and microfluidics components have been realised by casting liquid siloxane prepolymer against a positive relief master, followed by heat-induced curing and release.¹⁹ The master can be made of glass, silicon or another plastic (polyurethane, PMMA).⁶⁰ Therefore, by imprinting PDMS against an array of self-standing high aspect ratio pillars (fabricated by, for example, deep dry etching of silicon), it might be possible to fabricate microchannel PDMS structures with dimensions suitable for use as flow-through DNA chip substrates. Although cured PDMS is elastomeric in nature, its bulk optical properties are similar to glass, with a very low extinction coefficient above 230 nm and a refractive index of 1.43.¹⁹

The surface properties of PDMS are characterised by an inherently low surface energy, hence a low reactivity that does not support direct surface modification. However, surface oxidation of PDMS into a silica-like material, followed by derivatisation through organosilane chemistry, has been reported.¹⁰⁹ This opens routes for the tethering of nucleic acid probes to PDMS surfaces, in particular the sidewalls of PDMS microchannel substrates.

The fabrication of macroporous silicon, imprinted PDMS and deep dry etched silicon microchannel substrates is presented in the next chapter. Methods for the derivatisation of glass, silicon and PDMS substrates to produce functional DNA chips are presented in Chapter 4.

1. 2. 6. 2. Capture probe attachment chemistry

1. 2. 6. 2. 1. Requirements

As mentioned in section 1. 2. 2. 3, the choice of an appropriate strategy for the attachment of nucleic acid capture probe molecules to the substrate is crucial to the obtention of a biorecognition layer with satisfactory, if not optimised, performance. The probes must be tethered to the substrate in a permanent and functional fashion. It is necessary to alleviate steric crowding and excessive charge densities that can hinder duplex formation, as well as minimising detrimental surface effects, such as non-specific binding of sample components. Stability of the biorecognition layer must be ensured in the operating conditions used for hybridisation, as well as upon storage and handling of the chips. In addition to these requirements pertaining to the performance of the biosensing layer, additional constraints associated with the use of microchannel substrates, as mentioned above, have to be taken into account.

1. 2. 6. 2. 2. Possible strategies

A number of strategies are reported in the literature that allow for the immobilisation of (often) derivatised nucleic acids to solid substrates, for use in mixed phase hybridisation assays.

Physisorption

Non-chemical strategies, based on *physisorption* mechanisms (*i.e.*, electrostatic, hydrophilic and hydrophobic interactions) have been used in nylon membrane-based, mixed phase hybridisation assays. Conventionally, the probes are attached to the substrates through essentially ionic interactions between the positively charged amino groups of the nylon support and the negatively charged phosphodiester backbone of the nucleic acid probes. The same mechanism has also been applied to glass surfaces coated with lysine or casein¹¹⁰ or derivatised with an aminosilane film.¹¹¹ However, these strategies only yield low probe densities and do not allow for control of strand orientation and attachment sites (giving poor biochemical functionality and resulting in relatively low hybridisation kinetics). Moreover, the significant

effect of physico-chemical parameters such as pH, ionic strength and temperature on the stability of physical bonds does not ensure long-term functionality of the immobilised probe molecules (which might leach from the surface over the course of an hybridisation assay). Therefore, probe adsorption methods are not appropriate for quantitative hybridisation assays over a reasonably wide range of experimental conditions and do not allow for repeated use of the sensing layer.

Covalent attachment

Covalent bonds are much less affected by ionic strength, temperature and pH conditions than physical bonds. Thus, chemical immobilisation via *covalent binding* is the preferred method for the permanent and functional immobilisation of biomolecules to solid substrates in biosensing applications, especially if reusability of the chip is intended. Reusability of a DNA chip requires that probe-target hybrids be dissociated without the functionality of the sensing layer to be affected. In particular, probe attachment and conformation should not be altered by the regeneration step, and tendency for non-specific binding should not increase. Alternatively, a calibration function should provide compensation for changes in the response curve over repeated use.²⁹

Covalent attachment of cDNA and genomic DNA probes onto amino group-bearing surfaces can be achieved through photoinduced cross-linking. UV-irradiation at 254 nm (at dose levels of a few hundred mJ cm⁻²) has been reported to form covalent bonds between the thymine residues of the DNA probe and the amino groups present on the surface of an aminosilane-coated substrate, due to the high reactivity of primary amino groups with light-activated thymines.¹¹² If required, the non-reacted surface amino groups can subsequently be reacted with succinic anhydride to reduce the positive charge at the surface. However, this approach has limitations, mainly possible nicking of the DNA probes by over-irradiation, and/or low functionality of the probes resulting from the nucleobases being involved in the binding to the surface.

Maximum functionality is obtained through single-point attachment, preferably end-attachment, of the nucleic acid probe molecules to the surface. Two to three orders of magnitude higher hybridisation rates have been reported, in the case of oligonucleotide probes, for strand-terminus immobilisation as compared to adsorption methods with no control over strand orientation and attachment sites.⁸⁰ The observed enhancement in performance probably results from both a higher probe coverage within each spot and a higher level of functionality for each probe molecule. One constraint of the end-attachment approach is that derivatisation of nucleic acid probes with a reactive moiety is necessary. In addition, the use of a cross-linking adduct is usually required.

Chemisorption

Gold-thiol interactions (binding of sulphur head groups as thiolates at three-fold hollow sites at the Au{111} crystal lattice) have been applied to the formation of self-assembled layers of

mercapto-terminated oligonucleotides on gold-coated surfaces, and these assembly have been used in mixed-phase hybridisations^{51,83,113,114}

Affinity binding

A viable alternative to the covalent immobilisation of probe molecules to a solid substrate is provided by antibody-hapten and vitamin-protein biochemical systems, which exhibit strong affinity and high selectivity. The pairing of (strept)avidin and biotin, with an affinity constant $K_a = 10^{15} \text{ M}^{-1}$, is widely used in bioassay design. Biotinylated probes attached to surface-bound avidin have been used successfully in hybridisation assays.^{69,115} However, this approach restricts the hybridisation procedure to experimental conditions that do not lead to degradation of the protein. Denaturation of avidin is unavoidable over a certain temperature, leading to irreversible damage of the sensor surface.¹¹⁵ This limits the possible use of heating to enhance hybridisation selectivity, as well as the use of heat-induced denaturation steps.²⁹ In addition, the use of affinity binding for probe immobilisation does not alleviate the need for immobilisation of the avidin-bearing compound to the substrate, which is usually achieved by covalent binding.

1. 2. 6. 2. 3. Approach used in this thesis

Immobilisation strategies based on gold-thiol interactions are not applicable to microchannel substrates, due to the difficulty of coating the walls of high aspect ratio structures with an appropriate thin metallic film. However, the fact that all the envisaged microchannel materials described above (glass, silicon and PDMS) can be treated to exhibit silica-like surface properties suggests the possibility of using organosilane chemistry as a route to functionalise the substrates with nucleic acid probes. The required incorporation of a nucleophile moiety at the 3' or 5' end of the oligodeoxynucleotide probes is readily achieved during synthesis.¹¹⁶ The development of a procedure for the covalent attachment of nucleic acid probe molecules to planar glass, silicon and PDMS substrates using organosilane chemistry is presented in details in Chapter 4. The extension of the procedure to microchannel substrates (taking into account the specific wetting properties of the latter) is presented in chapter 6. The biotin-avidin system was not used for probe immobilisation; instead, it was used in post-hybridisation staining schemes, with biotinylated targets, as an alternative to direct fluorescent labelling of the targets.

1. 2. 6. 3. Arraying of capture probes onto microchannel substrates

1. 2. 6. 3. 1. Requirements

As stated above, mechanical spotting is the only viable approach for the structured immobilisation of multiple biorecognition sites on microchannel substrates. In the context of this thesis, microchannel DNA chips were initially produced by manual spotting, using a micropipette to deliver droplets of probe solutions. This approach is obviously limited in terms of reproducibility and array density, because of the large dispensed volumes resulting in

accordingly large spots. A number of microarraying techniques, presented below, is available for the automated dispensing of nucleic acid probes at high densities onto biochip substrates. The microarraying of microchannel biochips requires careful selection of the printing mechanism used, due to the specificity of the 3D, high aspect ratio characteristics of the substrate.

1. 2. 6. 3. 2. State of the art in microarraying technology

A number of so-called *microarrayers* have been developed for the automated, sub-microlitre dispensing of nucleic acid probe solutions (or other biological samples) onto biochip substrates.⁷¹⁻⁷³ All consist in a computer-controlled XYZ positioning stage fitted with a print head. The positioning stage serves essentially to move the print head from a source reservoir (typically, a 96- or 384-well plate) from which a given volume of probe solution is loaded into the tip, to the precise location on the substrate where a spot is to be deposited. The performance of positioning stages is determined by a number of parameters such as repeatability, accuracy, resolution and linear velocity of positioning.

Contact vs non-contact printing

Microarray printing technologies can be broadly classified into two categories, according to the type of print head and independently of the positioning stage: contact and non-contact dispensing. The former involves direct contact between a rigid print head and the biochip substrate. Various printing devices have been developed, such as solid pins, split pins, *Pin-and-Ring*TM, capillary tubes, and tweezers. With these devices, a small volume of sample is expelled by tapping the tip onto the substrate with a force sufficient to break the meniscus of loaded sample. A more elaborate alternative is the *Micro Spotting pin* configuration, which is based on the "ink stamp" principle, whereby a small amount of liquid (between 0.25 and 2.5 nL) is withdrawn from the loaded tip by the attractive force of the substrate. The tip dimensions, as well as the relative surface energies of the pin, fluid, and substrate and the viscosity of the sample, determine the size of the spot.

In non-contact dispensing techniques, derived from the ink-jet printing industry, drops are ejected from a nozzle onto the biochip substrate, with a kinetic energy that is lower than the surface energy of the substrate, so as to avoid splashing or splitting of the drop. Two principal types of ink-jet devices are used in microarraying technology: *syringe-solenoid* devices and *piezoelectric* devices. The former combine a high-resolution syringe pump with a microsolenoid valve. Sample is loaded into the tip by withdrawing the syringe plunger, and ejection of a droplet takes place upon opening the solenoid valve after the sample has been pressurised by the syringe. The relative simplicity of this dispensing mechanism has been shown to be highly reliable for minimum dispensing volumes of the order of 4-5 nL. Piezoelectric dispensing technology relies on a piezoelectric crystal to exert radial pressure a capillary tip (into which liquid has been drawn through actuation of a syringe pump), thereby ejecting a small amount of sample. This mechanism is characterised by inherently high dispensing frequencies (up to 500

spots per second) and low dispensing volumes (down to 350 pL), due to the fast response time and small deflection characteristics of the crystal.

Microarrayer performance

While each microarraying tool is characterised by a range of spot dimensions and array densities that can be achieved (on a given type of substrate), other practical issues have to be taken into account in assessing the overall performance of a microarrayer, in particular in a large-scale production settings. For a given printing device, the loading or uptake volume determines the number of spots of identical composition that can be printed from a single sample loading. If the uptake volume is small and/or the number of arrays to be printed in a single run is large, re-loading the printing tip with the sample might be necessary. Between the printing of two sets of non-identical spots (*i.e.* two probes of different sequences), cleaning of the tip is necessary in order to alleviate contamination by carry-over. Thus, the level of throughput that can be achieved by a microarrayer, for a given number of arrays to be printed in a single run, is determined by the duration of one printing cycle, *i.e.* loading, printing, and tip washing and drying. Also to be considered is the minimum sample volume that needs to be present in the source reservoir to permit correct loading of the printing tips. Contact dispensing devices require less sample than non-contact devices (typically, 5 μL versus 20-50 μL) for a given total delivered volume and thus are more efficient in terms of sample use.

1. 2. 6. 3. 3. Microarraying of microchannel DNA chips

Among the variety of microarraying techniques available, contact printing devices are not expected to be compatible with microchannel substrates, since the latter do not present a uniformly flat surface to the printing tip (the walls of print pins are as close as 20 μm apart, whereas the diameter of microchannels is typically 10 μm), and capillary action from the microchannels can cause wicking of liquid from the dispensing tip. In addition, microchannel substrates present a lower structural rigidity and are more prone to scratches than flat glass slides. Thus, non-contact printing technology is required for the production of microchannel biochips. Implementation and experimental investigations of microchannel chip microarraying are presented in Chapter 5.

1. 2. 6. 4. Fluidics

1. 2. 6. 4. 1. Requirements

Design and implementation of an appropriate fluidics scheme is a key issue in the flow-through microchannel DNA chip approach.

For a multiplexed heterogeneous hybridisation assay to be successful, all the target molecules should be given an opportunity to interact with their respective complementary probe. Therefore, redistribution of the target molecules over the whole capillary array must be ensured.

Because of the non-interconnected nature of the channels of a flow-through chip, mixing is necessary as a means to redistribute the sample over the whole array of channels.

In addition, flowing the sample through the chip in an iterative fashion is an obvious way to enhance interactions between probes and targets. However, the delivery of target molecules to the numerous sensing elements that make up the array must respect the parallel nature of the assay, which requires that uniformity of flow be ensured over the whole microchannel chip.

1. 2. 6. 4. 2. Fluidic modes in mixed phase bioassays

Bulk liquid transport

Bulk liquid transport is an integral part of many mixed-phase and liquid-phase (bio)analytical processes. Liquid flow is particularly important in the context of process automation, as best exemplified by flow injection analysis (FIA) methodologies. In most situations, bulk liquid transport can be achieved by mechanical pumping (*i.e.*, pressure-driven convective flow). Fan *et al.*¹¹⁵ have reported a “dynamic” DNA hybridisation approach, in which pneumatic and hydrostatic pumping of probe-bearing paramagnetic beads was used to provide enhanced hybridisation kinetics, resulting from the dynamic supply of both probes and targets. Electroosmotic pumping is a possible alternative,¹¹⁷ which has been gaining importance lately due to its applicability to the rapidly growing field of miniaturised, integrated bioanalytical devices. The electro-osmotic effect requires the application of a strong electric field within channels of small cross-section that feature negatively charged walls.

Molecular transport

The selective and controlled motion of molecules and larger particles with specific electrical properties (net charge, polarisability) can be achieved, under the action of homogeneous or inhomogeneous electric fields, within a liquid medium.

Electrophoresis refers to the transport of charged molecules under the effect of a static electric field. Electrophoresis is at the core of powerful analytical separation techniques, either in its most straightforward, “free flow” implementation or in the form of more elaborate schemes such as capillary gel electrophoresis, isotachophoresis or isoelectric focusing. *Dielectrophoresis* refers to induced-dipole forces experienced by polarisable particles placed in an electric field. The formation of an induced dipole makes the particles sensitive to field gradients. Dielectrophoresis has been used for the controlled manipulation and confinement of large bioparticles (cells, bacteria, viruses) in potential energy wells, and for the characterisation and separation of species (*e.g.* viable and dead cells) by selective trapping, using positive and negative dielectric forces.¹¹⁸

As highly charged and polarisable molecules, nucleic acids lend themselves to both electrophoretic and dielectrophoretic manipulations.¹¹⁹ However, the behaviour of colloidal (sub-micrometer) particles is strongly influenced by particle-particle interactions and thermal

effects such as Brownian motion, so that strong electric fields are required to overcome these effects.¹²⁰

Mechanical vs electronic pumping

The use of electrokinetic sample pumping provides a number of potential advantages with respect to mechanical pumping. Electrokinetic pumping can be implemented in the form of a truly integrated microfluidics platform, with no mechanical moving parts, since the generation of localised and tunable electrical fields is possible through the electronic addressing of an array of microelectrodes. The associated high levels of miniaturisation and integration that can be achieved are compatible with the concept of lab-on-a-chip devices. Accordingly, a DNA chip could become part of a micro analytical platform, combining on-chip RNA extraction and reverse transcription, and/or on-chip PCR, for sample preparation, as well as integrated detection and signal transduction.^{14,18} Electrophoretic transport is at the core of one type of DNA chip.⁶⁹ In that implementation, electrophoresis is used to achieve spatial concentration of target molecules at individually addressable hybridisation sites (resulting in enhanced hybridisation kinetics) as well as electronic stringency control.

1. 2. 6. 4. 3. Sample pumping in the flow-through microchannel DNA chip configuration

Convective pumping

In terms of fluidics, it is convenient to treat a microchannel chip as a homoporous microfiltration membrane. This analogy was used to design a pressure-driven convective flow system compatible with microchannel substrates. Flow cells and fluidics circuitry have been designed that allowed fluids to be directed to and forced through microchannel DNA chips (Chapters 5 and 6).

Electrokinetic pumping

In addition to the advantages associated with miniaturisation and integration, the use of electrokinetic pumping potentially offers enhanced control of the spatial distribution of target molecules within the hybridisation volume. The main challenge associated with the use of electrokinetic pumping in microchannel chip-based hybridisation assays consists in combining target transport and probe-target hybridisation within the same medium. Also, the morphology of the substrate restricts the positioning of electrodes away from the the hybridisation sites, since the fabrication of thin film electrodes on the microchannel sidewall is not technically possible. An investigation into the feasibility of implementing electrophoretic sample transport in flow-through microchannel chip-based hybridisation assays is presented in Section 6. 4.

1. 2. 6. 5. Assay detection by fluorescence imaging

1. 2. 6. 5. 1. Suitability of fluorescence as a detection method in DNA microarray technology

Fluorescence-based methodologies are well-accepted and widely used in bioassays, including nucleic acid hybridisation assays, due to the availability of a wide range of fluorophores, labelling methods and detection schemes, from direct prompt intensity measurements to fluorescence resonance energy transfer (FRET)⁵⁰ and “molecular beacons” strategies. In addition, several levels of multiplexing are achievable through spatial and spectral discrimination (multicolor assays). These characteristics of fluorescence-based analytical methodologies provided a strong impetus for developing a fluorescence detection method compatible with the microchannel biochip concept.

1. 2. 6. 5. 2. Challenges associated with fluorescence detection in 3D microstructures

As stated in section 1. 1. 2. 3. 5, the morphology of microchannel substrates restricts the use of fluorescence to far field optical methods. In the case of 3D microstructures, fluorescence detection presents a challenge in that, since the assay takes place throughout a thick substrate, fluorescence must be detected (*i.e.*, excited and collected) over a large axial distance commensurate with the chip thickness, so as to take full advantage of the inherently higher levels of sensitivity and dynamic range provided by the 3D format. In particular, confocal epifluorescence microscopy,³⁹ which has been shown to be particularly well suited to two-dimensional DNA microarrays in terms of spatial resolution and sensitivity, is not compatible with 3D substrates.

1. 2. 6. 5. 3. Methodology for fluorescence detection of microchannel chip-based DNA hybridisation

To accommodate the technical constraints mentioned above, a specific methodology was devised for microchannel chip-based DNA hybridisation fluorescence assays. Initial efforts were directed towards the setting up of a detection system based on non-custom (*i.e.*, commercially available) elements; thus, the validity of a relatively simple approach based on a standard (non-confocal) epifluorescence microscope configuration and CCD camera imaging¹²¹ was investigated. As the optical properties of the substrate had to be taken into account for the fluorescence detection process to be characterised and optimised, the relevant optical properties of microchannel substrates were investigated, both experimentally and through simulations, as presented in Chapter 3. The suitability of the approach to gene expression measurements, whose requirements in terms of instrumental performance are described in Section 1. 1. 2. 4. 2, are reported in Chapter 6.

CHAPTER 2. FABRICATION AND CHARACTERISATION OF FLOW-THROUGH MICROCHANNEL BIOCHIP SUBSTRATES

2. 1. Introduction

As mentioned in Section 1. 2. 6. 1. 2, a range of microchannel materials have been envisaged as possible substrates for flow-through biochips. The fabrication processes involved in the production of these materials are presented below. In addition, the morphology of the materials has been characterised; knowledge of the structure of microchannel biochip substrates is important since the values for geometrical parameters such as the effective surface area of the substrate, the feature size of the microchannels and the standard of smoothness of the channel walls are directly relevant to the issues of probe immobilisation, fluidics and optical detection.

2. 2. Microchannel glass (MCG)

2. 2. 1. Fabrication of microchannel glass biochip substrates

2. 2. 1. 1. Fabrication of microchannel glass boules

The process for the fabrication of nano- and microchannel glass materials was first described by Tonucci *et al.*¹⁰² It requires the use of two dissimilar types of glasses, an acid etchable glass and an inert, acid-resistant glass. The process starts with the insertion of a cylindrical acid etchable glass rod into an inert glass tube (referred to as the matrix glass) whose inner dimensions match that of the rod. The structure is then drawn at high temperature, in a vacuum, according to a process similar to that used in the manufacture of optical fibres. The aim of this drawing step is to reduce the overall cross-section to that of a fine filament. A number of these filaments are then assembled in a predetermined configuration, most typically a hexagonal close packing. The bundle of filaments is re-fused and redrawn, and the procedure is repeated until structures with the desired number of elements and the appropriate channel diameters are obtained. Finally, the soft glass rods are etched in a suitable acidic solution.

The process allows for the production of highly regular, mechanically rigid microchannel glass structures, provided that interdiffusion of the two glass materials and structural stress be reduced, for example by annealing the structure before rod etching. Adjustment of the ratio of the diameter of the etchable glass rod to that of the outside dimension of the inert glass tubing allows for the diameters of the rods and their centre-to-centre spacing (*pitch*) to be varied independently, resulting in the production of channel arrays with a range of packing densities (or open fractions).

2. 2. 1. 2. Dicing of microchannel glass boules into chips

In the framework of this thesis, unetched microchannel boules with 5 μm to 50 μm channel diameter were purchased from several US manufacturers, namely Galileo Electro-Optics Corp. (MA), Collimated Holes, Inc. (CA) and Burle Electro-Optics (MA). The boules were wafered perpendicular to the channel axis into 0.5 to 2.0 mm thick sections, using a diamond saw (Mechanical Workshop, Electronics Department, University of Glasgow). The wafers were then cleaned in MeOH to remove surface contamination, and the soft glass core was etched in 2 M HCl. Although the selectivity in etch rate between the core and the matrix is of the order of 3 orders of magnitude, an iterative procedure was used in which etching was carried out in 5 min increments while the depth of etching was monitored by white light microscopy.

Finally, the microchannel disks were diced into 12 mm x 12 mm square self-supporting chips. These dimensions were mainly dictated by the need to ensure compatibility with CCD-based fluorescence imaging methodologies, as discussed in Chapter 3. Likewise, the standard thickness used was 0.5 mm; thinner microchannel glass chips were too brittle to be used as flow-through substrates, whereas thicker chips were less amenable to microarraying (see Chapter 5) and epifluorescence imaging (Chapter 3). The use of 10 μm channel diameter, 0.6 open fraction as standard dimensions was imposed by the wider availability and lower cost of MCG material with these dimensions. Importantly, these dimensions were found to be compatible with pressure-induced flowing of aqueous solutions through the microchannels, as demonstrated later, e.g. in Figure 5-10.

2. 2. 2. Characterisation

2. 2. 2. 1. Physical properties

The glass used for the microchannel matrix is a clear potash lead glass (Corning type 8161) containing 55% lead oxide and 35% silicon dioxide. The high lead oxide content endows the glass with a high density of 4.44 g cm⁻³, thereby providing mechanical strength to the structure. In terms of optical properties, this type of glass is characterised by a low optical absorption coefficient in the visible part of the electromagnetic spectrum, and a high index of refraction (RI) of 1.7 at wavelengths of circa 500 nm.

2. 2. 2. 2. Morphology

Figure 2-1 shows a low magnification brightfield optical microscopy image of a 50 μm channel diameter, 0.5 mm thick microchannel glass chip.

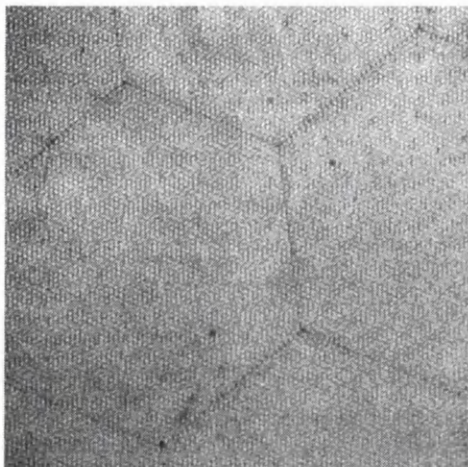


Figure 2-1. Brightfield optical microscopy image of a 50 μm channel diameter, 0.5 mm thick microchannel glass chip from Galileo Electro-Optics Corp. Magnification factor: 10x.

Even at this low level of magnification, individual microchannels can be distinguished, and the superstructure (“bundling”) that defines the hexagonal packing of the channels is apparent.

Figure 2-2 shows high magnification brightfield optical microscopy images of 25 μm channel diameter, 1 mm thick microchannel glass chips from different manufacturers.

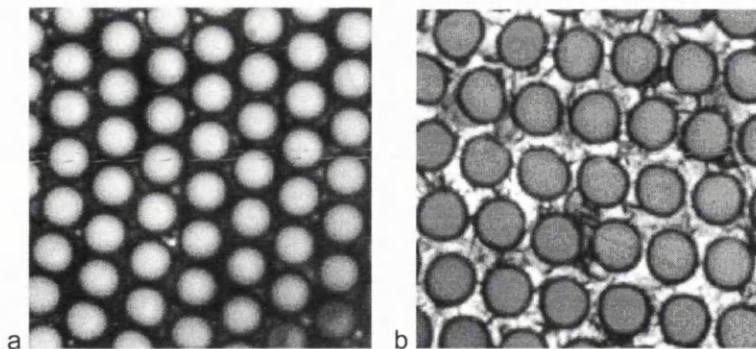


Figure 2-2. Brightfield optical microscopy images of 25 μm channel diameter, 1 mm thick microchannel glass chips from (a) Galileo Electro-Optics Corp. and (b) Collimated Holes, Inc. The two images were acquired in identical conditions of illumination and with identical camera settings. Magnification factor: 200x.

A significant difference in the levels of regularity of the two microchannel glass arrays is evidenced in Figure 2-2. Whereas microchannels of the Galileo material appear to be highly circular and uniformly arranged, the Collimated Holes substrate presents a much less uniform

array of microchannels. In addition, although the images of Figure 2-2 were acquired in identical experimental conditions, the relative levels of brightness of the channel openings and of the interstitial surface (*i.e.* the surface of the glass matrix, located on the front face of the chip, perpendicular to the sidewalls of the channels) differ greatly between the two materials. This suggests differences in optical properties, as demonstrated in the next chapter.

The morphology of the smaller diameter microchannel glass was characterised by scanning electron microscopy (SEM). Figure 2-3 shows SEM images of a 10 μm channel diameter, 0.5 mm thick microchannel glass chip from Galileo Electro-Optics Corp. acquired with a Hitachi S-800 scanning electron microscope operated at 30 kV. A circa 10 nm layer of Au-Pd was evaporated onto the substrate prior to imaging in order to prevent charging during SEM operation.

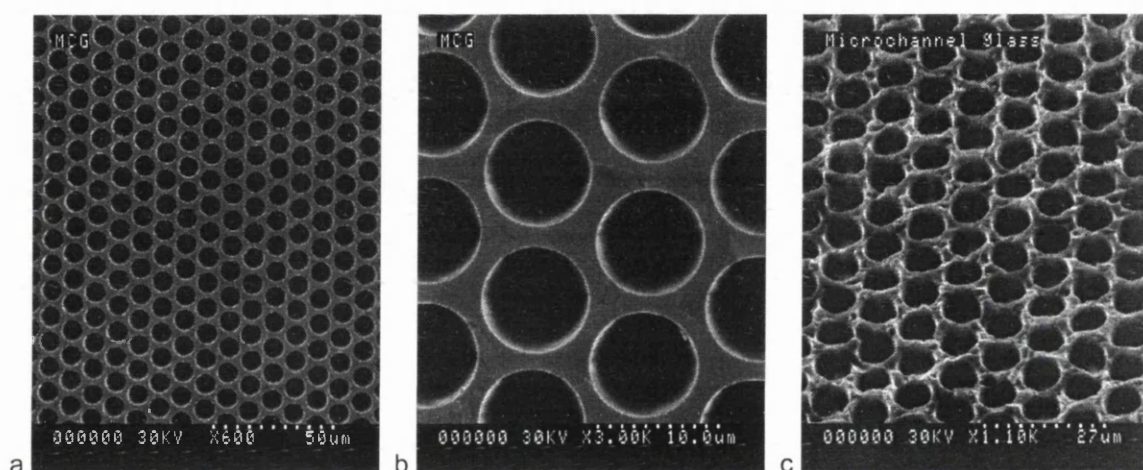


Figure 2-3. Scanning electron microscope images of a 10 μm channel diameter, 0.5 mm thick microchannel glass chip from Galileo Electro-Optics Corp. (a) Front face image, 600x magnification; (b) front face image, 3000x magnification; (c) off-axis image, 1100x magnification. The images were acquired using a Hitachi S-800 scanning electron microscope operated at 30 kV, after a circa 10 nm layer of Au-Pd was evaporated onto the substrate in order to prevent charging during SEM operation.

The high regularity of the hexagonal arrangement of the microchannels, as well as the high uniformity in their shape and dimension, are again clearly evidenced from the head-on images (a) and (b) in Figure 2-3. These images suggest that the diameter of the microchannels and the centre-to-centre spacing are circa 8.9 μm and 11.1 μm , respectively, in slight disagreement with the expected values corresponding to the manufacturer's specifications (10 μm and 12 μm , respectively). The manufacturer claims a variation in diameter of less than 1% channel-to-channel and 6% maximum between boules.

Image (c) in Figure 2-3 was taken at non-normal incidence from the surface of the chip, and shows the roughness of the interstitial surface. This roughness is a result of the diamond blade dicing of the microchannel glass boule. Individual MCG wafers polished to a high standard of surface smoothness (optical flat) with 0.5 μm diamond powder are available, at significantly

higher cost, from the manufacturer. However, this requires the polishing step to be carried out before the soft glass core is etched, because polishing of the etched wafers results in pieces of the hard matrix glass irreversibly blocking the microchannels. In the laboratory, unetched wafers could be polished to a relatively high standard of smoothness; however, subsequent etching of the soft glass core from these polished wafers was found to be impedingly slow, presumably due to the reduction in the soft glass effective area leading to reduced reactivity towards the acidic etchant. Consequently, all the microchannel glass chips used in the framework of this thesis exhibited a surface roughness comparable to that shown in Figure 2-3(c). This has important implications in terms of fluorescence imaging of MCG-based DNA chips, as described in details in Chapters 3 and 5.

Figure 2-4 shows SEM images of the cleaved edge of the same substrate, at various levels of magnification.

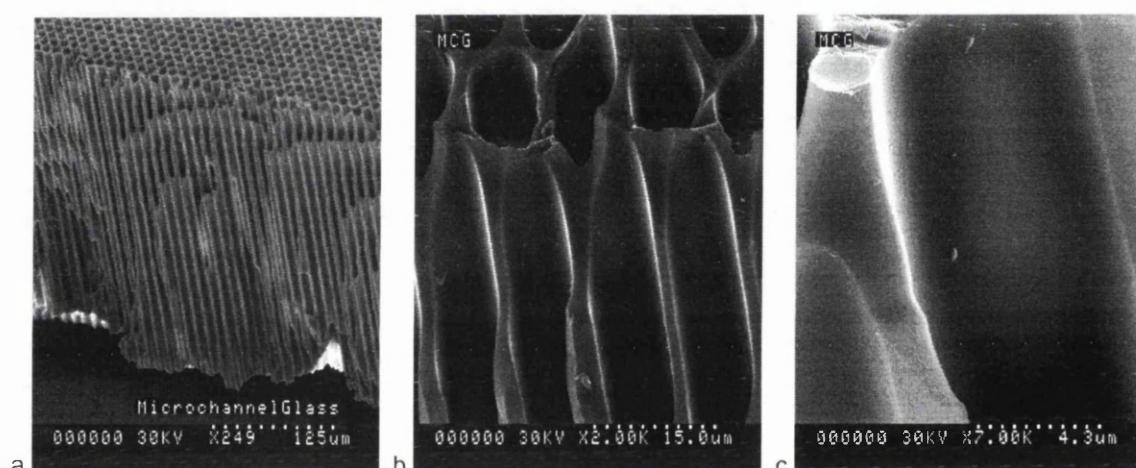


Figure 2-4. Scanning electron microscope images of the cleaved edge of a 10 μm channel diameter, 0.5 mm thick microchannel glass chip from Galileo Electro-Optics Corp. (a) 249x magnification; (b) 2000x magnification; (c) 7000x magnification.

Figure 2-4(a) shows the high levels of verticality and cross-section uniformity of the microchannels over the whole thickness of the chip. The high standard of smoothness of the microchannel walls is evidenced in Figure 2-4(b) and Figure 2-4(c).

2.2.2.3. Calculations of geometrical parameters of interest

The morphology and dimensions of microchannel glass chips, as determined from the SEM images shown above, as well as the expressions and numerical values for several geometrical parameters of interest, are given in Table 2-1.

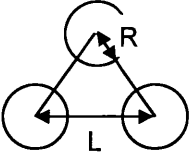
<p>Microchannel glass chip</p>  <p>Hexagonal channel packing</p> <p>Channel radius: $R = 5 \mu\text{m}$</p> <p>Centre-to-centre spacing: $L = 12 \mu\text{m}$</p> <p>Chip thickness: $T = 0.5 \text{ mm}$</p> <p>Lateral dimensions: $A^2 = 1 \times 1 \text{ cm}^2$</p>	Parameter	Expression	Value
	Open fraction	$\varepsilon = \frac{2\pi}{\sqrt{3}} \left(\frac{R}{L} \right)^2$	0.6
	Single channel surface area	$S = 2 \pi R T$	$1.6 \times 10^{-2} \text{ mm}^2$
	Single channel volume	$v = \pi R^2 T$	39.3 pL
	Density of channels	$d = \frac{\varepsilon}{\pi R^2} = \frac{2}{\sqrt{3} L^2}$	$8.0 \times 10^3 \text{ mm}^{-2}$
	Chip internal surface area	$S = \frac{4\pi}{\sqrt{3}} \frac{R}{L^2} A^2 T$	126 cm^2
	Chip internal volume	$V = \frac{2\pi}{\sqrt{3}} \left(\frac{R}{L} \right)^2 A^2 T$	$31.5 \mu\text{L}$
	Surface-to-volume ratio	$S/V = 2/R$	$0.40 \mu\text{m}^{-1}$
	Surface enlargement	$S/A^2 = \frac{2\varepsilon T}{R}$	126

Table 2-1. Expressions and numerical values for several geometrical parameters of a $10 \mu\text{m}$ channel diameter, $12 \mu\text{m}$ centre-to-centre spacing, 0.5 mm thick, 1 cm^2 microchannel glass substrate.

The last row of Table 2-1 shows that the effective surface enlargement is seen to increase in inverse proportion to the channel radius, for a given open fraction. The enhancement in effective surface area for a $10 \mu\text{m}$ channel diameter, 0.6 open fraction, 0.5 mm thick microchannel glass chip is in excess of 100 with respect to a flat chip of identical lateral dimensions.

2. 3. Photoelectrochemical etching of silicon

2. 3. 1. Principle and implementation

The silicon photoelectrochemical etching process enables the formation of regular, high aspect ratio, vertical channels in silicon wafers of appropriate doping characteristics and crystallographic orientation. Custom etching patterns (*i.e.* pitch, but also shape and dimensions

of the channels) can be obtained within limits imposed by both the doping density of the substrate and the operating conditions used during the etching process.

2. 3. 1. 1. Overview of the process

The process relies on the fact that dissolution of silicon in HF necessitates the presence of holes (or defect electrons), h^+ , in the substrate. The chemical reaction taking place is the following:^{104,105}



In the case of n-type silicon, for which majority charge carriers are electrons, generation of these holes can be achieved by illumination of the back side of the wafer with photons of energy higher than that of the band gap of silicon. In these conditions, photon absorption takes place and electrons are promoted from the valence band to the conduction band. Separation of charges in the space charge region results in the formation of mobile holes in the conduction band. Upon simultaneous application of an anodic bias voltage across the wafer, the substrate effectively acts as a photoanode, and mobile holes are attracted towards regions of high electric field strength, where dissolution of silicon can take place according to Equation 2-1.

At the surface of the electrically biased wafer, the electric field is strongest at sharp topographical discontinuities. Thus, the relative positions of the dissolution sites can be determined, prior to electrochemical etching, by the formation of pits at the surface of the wafer. Wet KOH etching of {100} silicon wafers, through a photolithographically-patterned mask of thermally grown silica or deposited silicon nitride, is particularly appropriate to that end, as it allows pyramidal recesses with sharp tips (with an angle of 54.7° with respect to the surface) to be formed at the surface of the wafer. Under suitable experimental conditions of anodic bias and illumination, the etching process is initiated at these tips. As etching progresses and the pores grow, the electric field strength remains higher at the tips of the pores than at the surface of the wafer or at the sidewalls of the pores. Thus, dissolution of silicon remains localised at the tip of the growing pores while the sidewalls are passivated against dissolution, allowing high aspect ratio microstructures to be produced.¹⁰⁴⁻¹⁰⁵

2. 3. 1. 2. Photoelectrochemical etching setup

Implementation of the electrochemical etching process required the use of an electrochemical cell whose design and setup are presented in Figure 2-5.

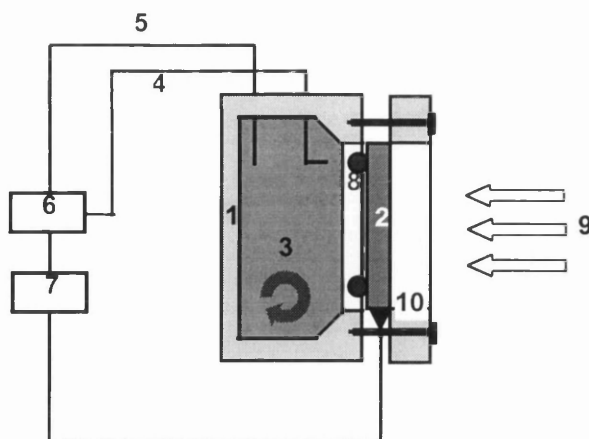


Figure 2-5. Setup for the electrochemical etching of silicon. (1) Cell body (transverse sectional view); (2) silicon wafer; (3) stirred electrolyte compartment; (4) potential reference; (5) counter electrode; (6) potentiostat; (7) am meter; (8) O-ring; (9) back-side illumination; (10) ohmic contact.

The cell body was manufactured of PTFE, so as to withstand moderately concentrated solutions of HF (< 5 %). The cell could accommodate a 18 mm x 18 mm square piece of silicon and features a 1 mm x 1 mm etching window. This small etching area ensured a low consumption of electrolyte (whose total volume available in the cell is limited to about 6 mL), while being sufficiently large (the area encompasses at least 1000 microchannels) for photoelectrochemical etching result patterns to be assessed by SEM imaging. The electrolyte consisted of a weakly concentrated (2.5 weight percent) solution of HF in water, to which a small amount of Triton X surfactant was added so as to improve the physical contact between the electrolyte and the hydrophobic silicon substrate. Sealing of the electrolyte-containing compartment was ensured by a PTFE O-ring. Stirring of the electrolyte during the course of the etching process was achieved by the use of a magnetic stirring unit. Stirring was required to keep the substrate surface free of hydrogen bubbles, which could hinder the diffusion process and lead to degenerated growth of the pores.¹⁰⁵

A potentiostat was used to apply a constant voltage of the order of a few mV across the substrate, as measured with respect to a pseudo-reference electrode consisting of a platinum wire placed close (circa 1 mm) to the surface of the wafer. To ensure a proper electrical connection between the back side of the substrate and the potentiostat, an appropriate ohmic contact had to be used. In the case of n-type silicon, the ohmic contact of choice consisted of Ga:In eutectic alloy, 75.5:24.5 (Alfa, Hertfordshire, UK) that was rubbed around the area of the wafer exposed to the electrolyte. A 1 cm² piece of Pt foil (Goodfellow, Cambridge, UK) was used as the counter electrode. An ammeter was used to measure the etching current. Illumination of the substrate from the back side was ensured by a 100 W tungsten lamp used with a IR-blocking KG 5 filter (Omega Optical, model XF 83). Since the etching current density is a direct function of the irradiance, the former could be varied by placing the lamp at various distances from the back side of the wafer.

2. 3. 1. 3. Etching parameters

2. 3. 1. 3. 1. Bias voltage

The bias voltage provides kinetic energy to the mobile holes, so that these can be transported from the bulk of the wafer to the pore tips. If the bias voltage is too low, no or uneven pore growth takes place. If the bias voltage is too high, an excess of mobile holes is generated within the bulk of the silicon, leading to etching of the sidewalls of the pores.¹⁰⁵

2. 3. 1. 3. 2. Illumination

Since a piece of silicon undergoing photoelectrochemical etching behaves as a photoanode, adjustment of the illumination intensity to appropriate values required consideration of the illumination-dependent current density versus bias voltage (I-V) plot. Figure 2-6 shows I-V plots for 3 Ω cm silicon under different levels of illumination, recorded by cyclic voltammetry, using the experimental setup of Figure 2-5.

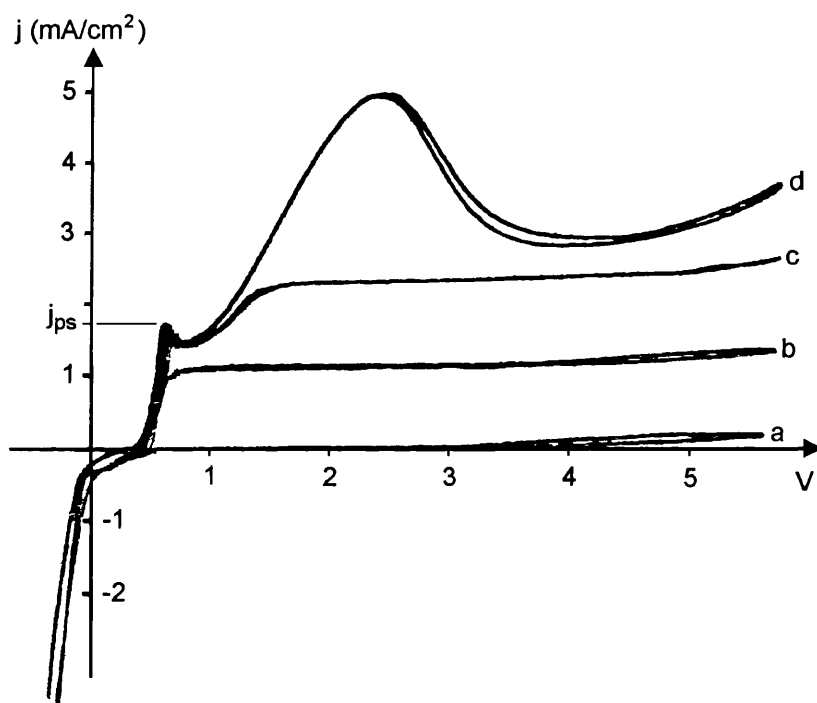


Figure 2-6. Cyclic voltammograms for a 3 Ω cm silicon photoanode in 2.5% HF, recorded at 100 mV s^{-1} versus a Pt pseudoreference electrode, at room temperature. (a) No illumination; (b)-(d) increasing illumination (a few tens of mW cm^{-2}). j_{ps} is the critical current density, below which photoelectrochemical etching takes place.

The intensity of illumination determines the level of photocurrent density, j , generated in the substrate. In the absence of illumination, a small dark current was observed (curve (a) of Figure 2-6). This residual current was ascribed to unattached pendant bonds associated with Si atoms located at the surface of the wafer.¹⁰⁶ Under illumination (curves (b)-(c) of Figure 2-6), electrochemical etching only takes place for values of j smaller than the critical current density, j_{ps} . In these conditions, the rate of the dissolution reaction is limited by the supply of holes, thereby ensuring that the mechanism of pore growth is under self-regulation conditions. If the photocurrent density is greater than j_{ps} , diffusion of chemical reactants in the Nernst diffusion layer is the limiting step of the dissolution reaction, and therefore electropolishing of the wafer surface takes place. j_{ps} was determined experimentally, by the presence of a characteristic feature in the I-V plot. For a silicon wafer of given doping and crystallographic orientation, j_{ps} depends on the concentration of the electrolyte, the temperature and the level of stirring. As shown in Figure 2-6, the critical current density for {100}, 3 Ω cm silicon in a 2.5% HF solution was found to be about 1.75 mA cm⁻².

2. 3. 1. 4. Control of the etching pattern

An array of microchannels of uniform cross-section can be characterised by the feature size and depth of the channels, and by the centre-to-centre distance between adjacent channels (the pitch). The overall volume of silicon dissolved in the course of the process determines the eventual porosity, or open fraction, of the chip. According to the etching mechanism involved, the volume of silicon dissolved is proportional to both the current density and the etching time. In addition, the channel depth is proportional to the etching time. This results in the channel diameter being proportional to the square root of the photocurrent. However, the range of possible values for the channel diameter is restricted by the doping density of the substrate, since the range of stable channel diameters scales with the width of the depletion region around the forming pore tips. Likewise, for a desired channel diameter, the pitch can only be chosen within limits imposed by the doping density, lest branching or dividing of pores takes place. Typically, possible pitch-to-diameter ratios of 1 to 10 can be achieved.¹⁰⁶

As a result of the interaction of all of these different parameters, the determination of a set of operating conditions leading to the desired etching pattern is likely to involve an iterative optimisation process. This is particularly true in the case of deep (> 200 μ m) channels, for which it is difficult to predict the photocurrent needed for a desired value of the channel diameter.

2. 3. 2. Fabrication of microchannel silicon biochip substrates

2. 3. 2. 1. Adjustment of experimental parameters

As discussed above, the successful obtention of the desired etching pattern requires all the experimental parameters to be precisely adjusted. Table 2-2 shows optimised sets of operating

conditions associated with different doping levels of the substrate, which were used as guidelines.¹⁰⁵

Substrate Resistivity (Ω cm)	Mask pattern		Bias Voltage (V)	Photocurrent density (nA/channel)	Etching time (min)	Resulting pattern	
	\varnothing (μ m)	Pitch (μ m)				\varnothing (μ m)	Depth (μ m)
1	1	4	10	0.33	30	0.6	42
20	1	4	10	1	30	2	18
80	10	30	1	13.3	100	10	60

Table 2-2. Operating conditions for the photoelectrochemical etching of silicon substrates of different doping levels in 2.5% HF (from ref. 104).

2. 3. 2. 2. Substrate preparation

Preparation of the silicon substrates for electrochemical etching consisted in thermally growing a silicon dioxide layer at the surface of the wafers, then photolithographically patterning and dry etching this layer so as to produce a sacrificial mask aimed at defining the subsequent wet etching pattern.

2. 3. 2. 2. 1. Wafers

Silicon substrates with {100} crystallographic orientation were used, for two major reasons: the anisotropic etching of silicon with wet alkali forms pyramidal holes on <100> surfaces, and photoelectrochemically etched channels grow perpendicular to the <100> direction. The characteristics of the four types of silicon wafers used are listed in Table 2-3.

Diameter (inch)	Thickness (μ m)	Doping	Resistivity (Ω cm)	Crystallographic orientation	Manufacturer
3	381 \pm 25	n type	1-5	{100}	Compart Tech Corp.
3	381 \pm 25		10		Compart Tech Corp.
4	525 \pm 15		32.2 - 37.8		Shin-Etsu Corp.
4	525 \pm 15		97.4 - 102.9		Shin-Etsu Corp.

Table 2-3. Characteristics of the four types of silicon wafers used in photoelectrochemical etching experiments.

2. 3. 2. 2. 2. Design and fabrication of contact photomasks

Several darkfield photomasks were designed and manufactured that featured arrays of clear circular holes arranged in a square packing pattern over an opaque background. The layouts of

the photomasks were designed using WaveMaker software (Barnard Microsystems, London, UK) and transferred into CATS™ software on a Sun Sparc workstation (Sun Microsystems, Palo Alto, CA). A Leica 5 electron beam writer (Leica, Cambridge, UK) was used to write 2.5 inch x 2.5 inch ferric mask plates. The following range of values were considered for the circular cross-section and pitch, according to Table 2-2: 1 μm diameter, 4 μm pitch (for 3 and 10 $\Omega\text{ cm}$ wafer); 3 μm diameter, 15 μm pitch (for 10 and 35 $\Omega\text{ cm}$ wafer); 6 μm diameter, 20 μm pitch (for 35 $\Omega\text{ cm}$ wafer); and 10 μm diameter, 30 μm pitch (for 35 and 100 $\Omega\text{ cm}$ wafer).

2. 3. 2. 2. 3. Masking and preliminary wet etching

The wafers were cleaned first by sequential 10 min sonication periods in isopropanol (IPA), acetone, methanol and RO water, then by immersion in hot Pirhana solution, 3:1 H_2SO_4 (98%): H_2O_2 (30%), for 30 min. In preparing the Pirhana solution, hydrogen peroxide was slowly added to the acid while the temperature of the solution was monitored, so as to avoid overheating. The cleaned wafers were rinsed with ample water and blow-dried. The cleaned wafers were oxidised at 1180-1200°C for 5 hours in wet O_2 (as described in Section 4. 4. 1 below), resulting in the formation of a circa 1 μm thick silicon dioxide layer on both sides. Patterns comprising sub-micron features required direct e-beam writing in 380 μm thick UVIII photoresist, whilst larger feature size patterns were transferred onto the substrates by standard UV photolithography using 2.5 x 2.5 square inch chromium mask plates. In the latter procedure, wafers were spin-coated with S1818 positive photoresist (Shipley, UK) at 4000 rpm for 30 s, baked at 90°C for 30 min, exposed for 10 s at an illumination power density of 0.52 mW cm^{-2} using a mask aligner (HTG, Oxford, UK) and developed in 1:1 Microposit: water for 75 s. Dry etching of the silica layer was carried out, using the UV-III or S1818 resist layers as a mask, by subjecting the samples to a C_2F_6 plasma in a BP80 machine (Plasma Technology, UK) for 20 min. The silica layer present on the back side of the substrate was left as a protection during subsequent wet etching in 45% KOH, at 80°C. Etching times varied from 3.5 min for a 1 μm diameter pattern to 24 min for a 10 μm diameter pattern.

Etching patterns (circular holes in the silicon dioxide superstrate, pyramidal holes in the silicon substrate) were checked using an optical microscope, under episcopic illumination, at 100x magnification, and by SEM imaging. Removal of the silicon dioxide masking layer was achieved by immersion of the substrate in 40% HF for 3 min. Figure 2-7 and Figure 2-8 show silicon substrates at different stages of the preparation.

2. 3. 3. Results

Although photoelectrochemical dissolution of silicon was clearly observed when the experimental procedure described above was implemented, it soon became apparent that the production of regular, well-defined microchannel structures would involve a much time-consuming and labour-intensive optimisation phase that would delay the development of other aspects of the microchannel biochip platform. In this respect, a collaboration was established

with Infineon Technologies AG (München, Germany), through which high-quality macroporous silicon chips were made available to us in the context of our biochip development effort.

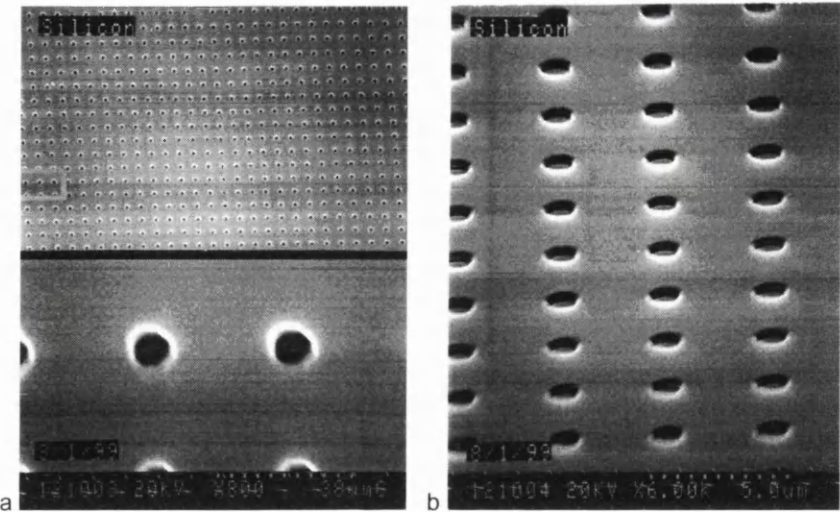


Figure 2-7. 4 μm pitch square pattern of 1 μm diameter holes produced by dry etching of a circa 1 μm thick silica layer thermally grown on the surface a n-type, {100}, 10 Ω cm silicon wafer.

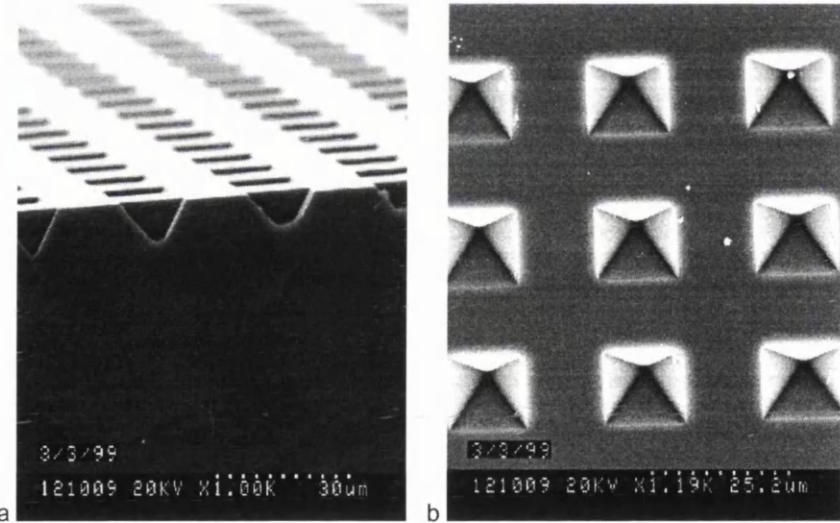


Figure 2-8. Pyramidal recesses formed by KOH etching of a n-type, {100}, 35 Ω cm silicon wafer, after removal of the silicon dioxide masking layer. Here, the wet etching process did not reach completion, as evidenced by the flat bottom of the pits.

2. 3. 4. Physical characterisation of macroporous silicon substrates

2. 3. 4. 1. Scanning electron microscopy imaging

Figure 2-9 shows SEM images of a macroporous silicon substrate, acquired with a Hitachi S-800 scanning electron microscope after coating the substrate with a circa 10 nm thick layer of Au-Pd.

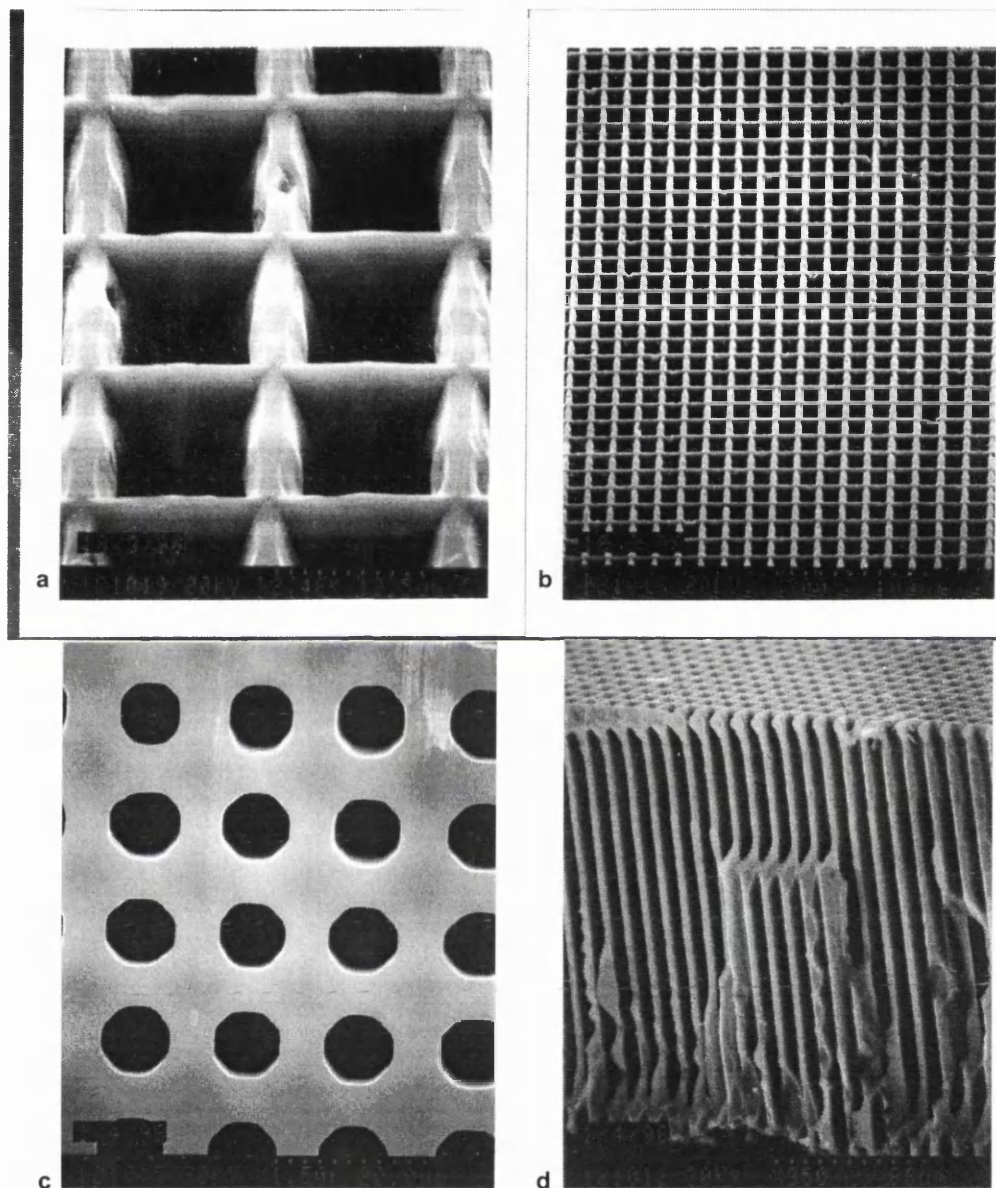


Figure 2-9. Scanning electron microscope images of electrochemically etched microchannel silicon (Infineon Technologies AG, München, Germany). (a), (b) Front face of the chip with pyramidal openings formed by KOH etching, 2480x and 200x magnification; (c) opposite face of the chip, 1500x magnification; (d) cleaved edge, 350x magnification.

Figure 2-9(a) and Figure 2-9(b) show an array of square pits, corresponding to the top of the pyramidal holes produced by anisotropic wet etching of the {100} silicon surface with KOH. The opposite side of the chip, which did not undergo the wet etching step, is shown in Figure 2-9(c)

to exhibit an array of roughly circular, almost octagonal, holes. Figure 2-9(d) is an image of a cleaved edge, from which the verticality of the microchannels is evidenced. As the feature sizes and aspect ratio of these macroporous silicon chips were comparable to those of MCG, the term microchannel silicon, MCS, is used henceforth, by analogy, to refer to these substrates.

2. 3. 4. 2. Morphology of the microchannels

By extrapolation, the morphology of the microchannels can be approximated to that depicted in Figure 2-10.

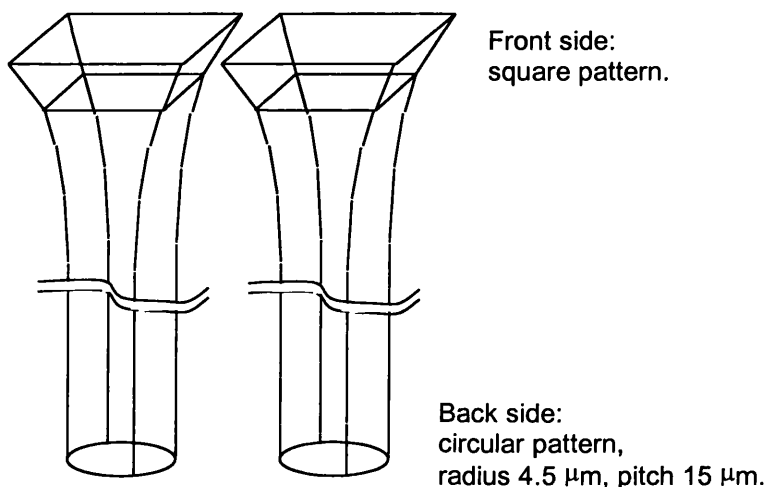


Figure 2-10. Approximate microchannel morphology of electrochemically etched silicon.

Note that the side that did not feature the pyramidal etching pattern, shown in Figure 2-9(c), was subsequently used as the “top” side for probe arraying (Chapter 5), as well as in epifluorescence imaging using an upright microscope (Chapter 3), following the observation that the side with the pyramidal holes produced higher levels of scattering and reflection of the epi-illumination light.

2. 3. 4. 3. Calculations of geometrical parameters of interest

The channel array morphology for the substrates used in this work, as determined from SEM pictures, as well as the expressions for several geometrical parameters of interest and their numerical values calculated from the data above, are given in Table 2-4.

Table 2-4 shows that the enlargement in effective surface area for a MCS chip is half that for a 10 μm channel diameter MCG chip with the same thickness and same lateral dimensions. This reflects the lower open fraction of the microchannel silicon material, as a consequence of the thicker walls.

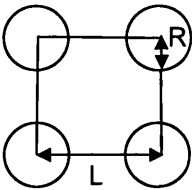
<div>Microchannel silicon chip</div> <div></div> <div>Square channel packing</div> <div>Channel radius: $R = 4.5 \mu\text{m}$</div> <div>Centre-to-centre spacing: $L = 15 \mu\text{m}$</div> <div>Chip thickness: $T = 0.5 \text{ mm}$</div> <div>Lateral dimensions: $A^2 = 1 \times 1 \text{ cm}^2$</div>	Parameter	Expression	Value
	Open fraction	$\varepsilon = \pi \left(\frac{R}{L} \right)^2$	0.28
	Single channel surface area	$s = 2 \pi R T$	$1.41 \times 10^{-2} \text{ mm}^2$
	Single channel volume	$v = \pi R^2 T$	31.8 pL
	Density of channels	$d = \frac{\varepsilon}{\pi R^2} = \frac{1}{L^2}$	$4.4 \times 10^3 \text{ mm}^{-2}$
	Chip internal surface area	$S = 2\pi \frac{R}{L^2} A^2 T$	63 cm^2
	Chip internal volume	$V = \pi \left(\frac{R}{L} \right)^2 A^2 T$	$14.0 \mu\text{L}$
	Surface-to-volume ratio	$S/V = 2/R$	$0.44 \mu\text{m}^{-1}$
	Surface enlargement	$S/A^2 = \frac{2\varepsilon T}{R}$	63

Table 2-4. Expressions and numerical values for several geometrical parameters of a macroporous silicon substrate (Infineon Technologies AG, München, Germany).

2. 4. Deep dry etching of silicon

2. 4. 1. The Advanced Silicon Etch (ASE) process

Investigations into the suitability of the ASE process for the fabrication of microchannel silicon biochip substrates were made possible after a suitable machine had become available within the Department of Electronics and Electrical Engineering, University of Glasgow. The main considerations and results are presented below.

2. 4. 1. 1. Principle

As mentioned in Section 1. 2. 6. 1. 2., the ASE process, developed from the original Bosch process,¹⁰⁸ relies on the alternating of etching periods and protective polymer deposition steps

to yield highly anisotropic etching profiles. The fluorine-based reagent used is a mixture of SF_6 and C_4F_8 .

The mechanism for the etching of silicon is based on dissociation, ionisation and attachment of SF_6 to generate fluorine free radicals which are directly involved in the reactive chemical etching of the silicon substrate, according to the following reaction:



Silicon is removed from the substrate as silicon tetrafluoride, SiF_4 . As the etching reactions proceed spontaneously, rather than being driven by ion bombardment of the substrate, as is the case with chlorine- and bromine-based processes, high etch rates are observed. However, the resulting etching mechanism is essentially isotropic.

As stated, etching anisotropy is brought about by the polymerisation of C_4F_8 into a circa 10 nm thick fluorocarbon polymer layer that prevents etching of the underlying silicon. The passivating polymeric layer forms essentially in regions where ion bombardment is limited, *i.e.* on the sidewalls of the etched structures, thereby inhibiting lateral etching. In the direction perpendicular to the ion bombardment flow, *i.e.* the bottom of the pits, the passivating layer is thinner than it is on the sidewalls, hence a significant axial etch rate.¹⁰⁸

2. 4. 1. 2. Relevance to the fabrication of flow-through silicon chips

In order to ensure sufficient structural rigidity and mechanical strength of the flow-through DNA chips, a minimal substrate thickness of 250-300 μm is required. The etching of microchannels with feature sizes of 10 μm or less thus translates into aspect ratios in excess of 25:1. In addition, for the chips to feature a high density of microchannels, open fractions of > 0.4 are required. Consequently, the etching process must be able to accommodate the removal of large amounts of silicon.

Also, the required large depth of etching is expected to entail long etching run times (several hours), over which significant variations in the etching conditions (changes in diffusion and consumption of reactants, as well as in the efficiency of ion bombardment into, and removal of the reaction products from, the small, deep trenches) are likely to take place.

Besides, the choice of a suitable sacrificial masking layer is crucial to the successful implementation of the process. In the $\text{SF}_6 / \text{C}_4\text{F}_8$ plasma etching process described above, erosion of the photoresist mask is believed to be necessary to promote the anisotropic nature of the etching process, as the associated release of carbon-rich products contributes to the formation of the sidewall passivating layer. This, along with the large etching depths, makes the use of thick photoresist sacrificial layers necessary.¹²²

2. 4. 2. Implementation of the process for the fabrication of microchannel silicon substrates

2. 4. 2. 1. Materials and methods

2. 4. 2. 1. 1. Apparatus

All the experiments described below were carried out on an STS machine (Surface Technology Systems Ltd., Newport, UK) running the ASE process. The machine is based on an inductively coupled plasma (ICP) system in which the radiofrequency (RF) coil generator is operated at an excitation frequency of 13.56 MHz, to produce uniformly distributed, high plasma densities at low pressure and room temperature. The resulting high fluorine radical concentrations reduce the loading effect of silicon on the fluorine radicals, resulting in improved uniformities at high exposed areas. A second RF generator produces a bias frequency of 4 MHz which controls the energy of the ions striking the wafer surface.

2. 4. 2. 1. 2. Sacrificial masking layers

Two types of thick photoresists were used as sacrificial masking layers: a positive, diazoquinone-based photoresist, AZ4562 (Hoechst AG, Germany) and a negative photoresist, SU8 SM-1060 (Sotec Microsystems, Renens, Switzerland). The latter contains 60% of EPON SU8 epoxy-based material and 1-6% of photoinitiator in γ -butyrolactone (GBL). AZ4562 could be processed to a maximum thickness of 15 μm , with a resolution of circa 2 μm . Much thicker layers of SU8-SM1060 could be obtained (up to 50 μm), however the resolution was not better than 5 μm for 20 μm -thick layers.

2. 4. 2. 1. 3. Contact photomasks

The layout of the photolithographic pattern was designed using WaveMaker software and transferred into CATSTM software on a Sun Sparc workstation. The pattern comprised four different arrays, each consisting of square cross-section openings arranged in a square packing configuration. The arrays varied in feature size and pitch as listed in Table 2-5. Each array covered a 12 x 12 mm² area.

Array	Feature size (μm)	Pitch (μm)
A	5	50
B	20	65
C	30	75
D	40	85

Table 2-5. Photolithographic pattern used in Advanced Silicon Etch experiments.

A Leica 5 electron beam writer was used to write two 2.5 inch x 2.5 inch ferric mask plates, a brightfield one for use with the negative photoresist and a darkfield one for use with the positive photoresist. The pattern featured each of the four arrays A, B, C and D in quadruplicate.

Although a square cross-section is not the most appropriate channel morphology for biochip applications (due to non-uniform diffusion distances in heterogeneous bioassays, and exacerbated non-specific adsorption of biomolecules at the edges), it was used at this early stage of the investigation because it made morphological analysis of the etched substrate (requiring cleaving prior to SEM analysis) easier.

2. 4. 2. 1. 4. Substrates

Two types of silicon wafers were used in this work: 1 inch diameter, $250 \pm 15 \mu\text{m}$ thick (Siltronic, Archamps, France) and 4 inch diameter, $525 \pm 15 \mu\text{m}$ thick (Shin-Etsu Corp., Tokyo, Japan). Both were {100} in crystallographic orientation and one-side polished.

The thinner, smaller wafers were used in combination with the thinner (AZ4562) photoresist. One single $12 \times 12 \text{ mm}^2$ pattern was transferred onto each 1 inch diameter wafer. The thicker wafers were coated with a $20 \mu\text{m}$ thick layer of SU8 and patterned with the whole six-array pattern; this allowed for the possible dependence of etching performance on aspect ratio to be investigated.

2. 4. 2. 2. Experimental

2. 4. 2. 2. 1. Photolithography of AZ4562

1 inch diameter wafers were cleaned as described in Section 2. 3. 2. 2. 3 and dried at 120°C for two hours. A layer of HMDS (1,1,1,3,3,3-hexamethyldisilazane) was spun on each wafer (1500 rpm for 15 s) in order to promote subsequent adhesion of the photoresist to the silicon surface. A few millilitres of AZ4562 photoresist were dispensed onto the whole surface of the wafer, using a 5 mL syringe. No filtering was used due to the high viscosity of the resist. The layer of photoresist was allowed to equilibrate and planarise over the wafer surface for 5 min, before being spun at 1500 rpm for 30 s. The coated wafer was let to sit for another 10 min, then soft-baked at 90°C for 30 min. Exposure through the darkfield photomask was carried out at an illumination power density of 0.52 mW cm^{-2} for 70 s, using an HTG mask aligner. The exposed photoresist was then developed in a 1:4 AZ400K: RO water solution, for 3.5 min, under mild agitation. A post-baking step (120°C , 20 min) was carried out. Finally, the wafer was rinsed with ample RO water and blow-dried.

2. 4. 2. 2. 2. Photolithography of SU8-1060

4 inch diameter wafers were cleaned and dried as above. SU8-1060 was dispensed onto each wafer so as to cover the whole surface. The coated wafer was let to sit for 10 minutes, before

being spun at 500 rpm for 5 seconds to eject some of the excess photoresist, and spun a second time for 25 seconds, with an initial ramping up of the spinning rate from 500 rpm to 1000 rpm over 5 s. The coated wafer was soft-baked on a levelled hot plate at 60°C for 10 min and at 90°C for 30 min. It is important that the hot plate be horizontal for SU8 layers of uniform thickness to be obtained, as resist flow readily takes place at this stage. After the soft bake step, the photoresist layer should have become moderately hard and should not be tacky. The above procedure consistently yielded a $20.0 \pm 0.5 \mu\text{m}$ thick SU8 layer, as determined from surface profiling measurements. Exposure was carried out for 30 s, at 0.52 mW cm^{-2} , through the brightfield photomask. A post-exposure bake was carried out on a hot plate, for 5 min at 60°C followed by 15 min at 90°C. This ramping up of the temperature was implemented as a way to reduce stress within the resist layer. As the T_g (glass temperature) of SU8 is about 55°C, some cross-linking takes place during the lower temperature baking step that stabilises the layer. Development was carried out using EC solvent, with mild agitation, for a total development time of about 3 min, broken into three 1 min steps between which the sample was immersed in fresh IPA to remove non cross-linked photoresist, coming off as white scum. The sample was then rinsed in IPA and blow-dried. No hardbake was performed as this was found to induce cracking of the SU8 layer.

2. 4. 2. 2. 3. Silicon etching

The STS machine was operated with the parameters set as described in Table 2-6. These parameters were used in all the etching runs.

Parameter	Value	Parameter	Value
Coil power	600 W	SF ₆ flow rate	130 sscm
Platen power	12 W	C ₄ F ₈ flow rate	85 sscm
Etching step duration	12 s	Lid temperature	45 °C
Passivation step duration	9 s	Platen temperature	20 °C

Table 2-6. Parameter settings used for the deep dry etching of silicon through the Advanced Silicon Etch process.

2. 4. 3. Results and discussion

Figure 2-11 is an SEM image of the cleaved edge of a 250 μm thick silicon wafer having been subjected to a 360 minute long etching run through a 15 μm thick AZ4562 photoresist sacrificial masking layer, patterned with an array of $5 \times 5 \mu\text{m}^2$ openings.

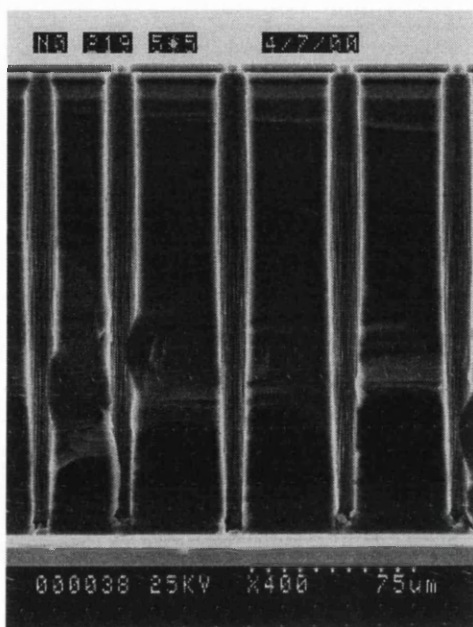


Figure 2-11. Scanning electron microscope image of the cleaved edge of a 250 μm thick silicon wafer, etched through a 15 μm thick AZ4562 photoresist sacrificial masking layer patterned with an array of $5 \times 5 \mu\text{m}^2$ openings, for 360 minutes.

Figure 2-11 shows that the wafer has been etched all the way through. However, a high extent of undercutting was observed, as clearly evidenced by a sharp increase in channel width in the upper part of the wafer, just below the photoresist layer. Over the upper third of the wafer thickness, the etched channels exhibited straight and near-vertical walls, but the cross-section was about 18 μm , which is circa 3.6-fold the feature size of the masking layer. The lower part of the channels exhibited significant tapering, resulting in a circa 8 μm channel feature size on the bottom side.

The etch rate was determined over the time course of the etching process by measuring the etch depth at regular intervals, in a cumulative etching procedure. The initial etch rate (for the first 30 minutes of etching) was $3.2 \mu\text{m min}^{-1}$, while between 5 hours and 5.5 hours of etching, the etch rate had dropped to $0.8 \mu\text{m min}^{-1}$. The thickness of the AZ4562 masking layer was measured to have decreased from 15 μm to about 5 μm over the 6 hour long etching run. This suggests that the suitability of such a photoresist layer to longer etch runs, and even more significantly, to larger etching depth, is limited. As AZ4562 could not be successfully processed to layer thicknesses larger than 15 μm , SU8 was used for the masking of thicker wafers.

Figure 2-12 shows SEM images of the cleaved edge of a 525 μm thick silicon wafer etched through a 20 μm thick SU8 photoresist sacrificial masking layer, patterned as described in Section 2. 4. 2. 1.

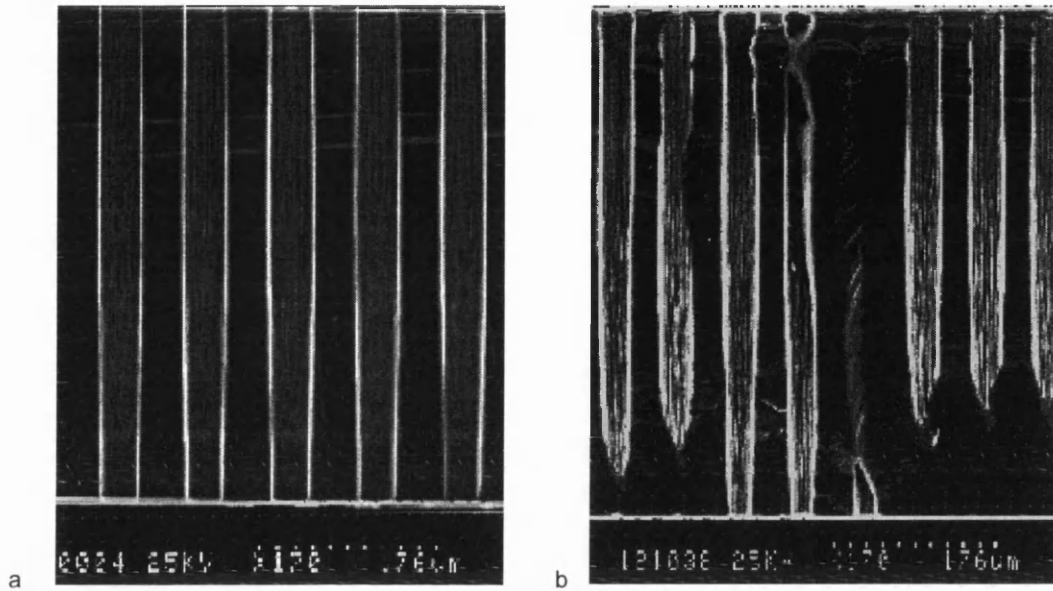


Figure 2-12. SEM images of the cleaved edge of a 525 μm thick silicon wafer etched through a 20 μm thick SU8 photoresist sacrificial masking layer. (a) 40 x 40 μm^2 openings (420 minutes etching time); (b) 20 x 20 μm^2 openings (615 minutes etching time).

Figure 2-12(a) shows 40 x 40 μm^2 cross-section channels etched over a depth of circa 470 μm . The etch time was 420 minutes, giving a 1.1 $\mu\text{m min}^{-1}$ average etch rate. The etching pattern was highly regular. The upper part of the channels featured straight, vertical walls, while the lower half exhibited some tapering. Figure 2-12(b) shows the etched channels obtained for a 20 x 20 μm^2 feature size photoresist array pattern. The etching time was extended to 615 min, which resulted in the wafer being etched all the way through. The channel cross-section over the upper quarter of the wafer thickness was about 35 μm , which evidenced a very significant (175%) undercutting effect, measured as the ratio of the cross-section of the widest part of the channel to the feature size of the masking pattern. The lower part of the channels was characterised by some bowing effect, and the feature size of the channel openings on the bottom side of the wafer was circa 25 μm .

Aspect ratio-dependent etching was evidenced by the difference in etching depth observed between the 20 x 20 μm^2 array and the 40 x 40 μm^2 array over a 420 minute-long etch run. Whereas the 40 x 40 μm^2 pattern had been etched over circa 470 μm (Image (a) in Figure 2-12), the 20 x 20 μm^2 array had been etched over 365 μm only, which represented a 22% lower average etching rate. Etching the 20 x 20 μm^2 array through the 525 μm -thick wafer, as shown in Image (b) of Figure 2-12, required an additional >120 min etching time, and gave a less uniform microstructure.

The smallest feature size pattern that could be transferred to the 20 μm thick SU8 layer was $10 \times 10 \mu\text{m}^2$. Attempts at etching this pattern all the way through the 525 μm thick wafer did not succeed within an 11 hour-long etching run. Longer etching times were deemed unreasonable.

The work presented above has confirmed the suitability of the ASE process for the fabrication of flow-through microchannel silicon structures by deep dry etching. The use of thick photoresists as sacrificial masking layers made it possible to etch wafers as thick as 525 μm all the way through. However, the dimensions and morphology of the etched channels were found to be highly dependent on the feature size of the mask pattern, and on the etching depth (*i.e.*, the wafer thickness). The level of aspect ratio that could be achieved was compromised by serious undercutting effects, while tapering of the lower part of the microchannels was observed in most of the etched structures. Further optimisation of the operating parameters may yield a reduction in the extent to which these undesirable effects take place.

The thick photoresists used here have been demonstrated to be compatible with the etching process. Whilst the use of the positive resist was limited by a maximum layer thickness of circa 15 μm , the negative resist, SU8, could be photolithographically processed as 50 μm thick layers, making it suitable to long (over 12 hours) etching runs. However, SU8 suffered from a lower resolution which limited the pattern to feature sizes larger than 5 μm . Another problem with SU8 was the difficulty encountered in the removal of the resist layer from the substrate after processing.

2. 5. Poly(dimethylsiloxane), PDMS

2. 5. 1. Fabrication of PDMS structures by imprinting against a master

PDMS readily lends itself to imprinting and molding into small feature size and / or high aspect ratio microstructures.⁶⁰ The versatility and ease of use of PDMS has been exploited in the fabrication of microanalytical devices for on-chip electrophoresis,¹⁹ centrifugal analysis¹⁰⁹ and microfluidics,¹²³ as well as microelectromechanical systems.⁶⁰

PDMS “kits” are commercially available, at a low cost, which comprise two components, a siloxane oligomer base and a platinum-containing curing agent. When these two components are combined in appropriate relative proportions, polymerisation of the siloxane oligomers is induced. From a chemical point of view, the curing of PDMS involves the addition of the silicon hydride bonds of cross-linking oligomers across the vinyl groups of siloxane oligomers, in the presence of the Pt-based catalyst. Multiple organometallic linkages (-Si-CH₂-CH₂-Si-) are created, forming a three-dimensional polymeric network. In practice, the cross-linking reaction is accelerated by heating the prepolymer mixture to 60-120°C for one to a few hours.^{19,60,124,125}

A procedure for the fabrication of flow-through PDMS microstructures is given below.

The procedure consists of four main steps: (i) microfabrication of a master with a suitable morphology; (ii) passivation (reduction of the surface energy) of the master, in order to facilitate subsequent release of the PDMS imprint; (iii) molding of liquid PDMS prepolymer against the master; and (iv) curing of the prepolymer and release of the PDMS imprint from the master.

2. 5. 2. Fabrication of masters for the production of PDMS microchannel substrates

2. 5. 2. 1. Requirements

The possibility of producing microchannel PDMS structures by using a master consisting of an array of small feature size, self-standing pillars was suggested in Section 1. 2. 6. 1. 2. For the fabrication of flow-through structures (*i.e.*, via channels as opposed to blind holes), the height of the pillars must be larger than the thickness of the PDMS imprint. Two techniques were considered for the fabrication of masters featuring accordingly high aspect ratio and high (> 200 μm) pillars: photolithographic microstructuring of a thick photoresist, SU8, and deep dry etching of silicon. Both techniques were closely related to those used in the dry etching of silicon described in Section 2. 4.

2. 5. 2. 2. Photolithographic microstructuring of thick photoresist

2. 5. 2. 2. 1. Principle

It has been shown in Section 2. 4. 2. 2. 2 that a SU8-type negative photoresist could be processed to a thickness of several tens of microns. Here, investigations into the possibility of processing a more viscous version of that photoresist to a thickness of several hundred microns is reported.

2. 5. 2. 2. 2. Experimental

Materials

SU8 SM-1070 (Sotec Microsystems) was chosen for its high viscosity (15 Pa s, versus 1.5 Pa s for SU8 SM-1060) resulting from a high content in SU8 material (70% versus 60% for SU8 SM-1060). A photomask was produced, as described in Section 2. 4. 2. 1. 3, which featured an array of clear 200 μm diameter circles over an opaque background, arranged in a square pattern, at a pitch of 500 μm , over a 7.5 x 8.0 mm² area. These relatively large feature sizes were used in the first instance, as the level of resolution of thick SU8 layers was not known *a priori*.

Photolithography of SU8-1070

A 3 inch diameter wafer was cleaned and dried as described in Section 2. 4. 2. 2. 1. A few millilitres of SU8-1070 were dispensed onto the wafer, so as to cover the whole surface. The resist layer was allowed to planarise for 1 hour. The wafer was spun at 500 rpm, first for 5 s to remove some of the excess photoresist, then a second time for 10 s. The coated wafer was again let to sit for about 2 hours, until disappearance of the edge bead, before being soft-baked on a levelled hot plate at 60°C for 1 hour and at 90°C for another 3 hours, until enough solvent had evaporated for the resist layer to have become moderately hard. The wafer was then submitted to an illumination dose of 280 mJ cm⁻², through the photomask, implemented as three sequential 3 min exposure steps at 0.52 mW cm⁻², separated by 1 min relaxation steps. This breakdown of the exposure time was necessary in order to avoid overheating of the photoresist, as submitting substrates to an uninterrupted 9 min exposure period was found to result in the formation of a hard, yellow “skin” on the surface. A post-exposure bake was carried out on a hot plate, for 5 min at 60°C followed by 30 min at 90°C. Development was carried out using EC solvent (Shipley, UK), under strong mechanical agitation, for a total time of about 15 min, broken into 3 min steps between which the sample was immersed in fresh IPA to remove non cross-linked photoresist. Finally, the sample was rinsed in IPA and blow-dried.

2. 5. 2. 2. 3. Results

Figure 2-13 shows SEM images of an array of SU8 self-standing micropillars. The images were acquired using a Hitachi S-800 scanning electron microscope operated at 10 kV.

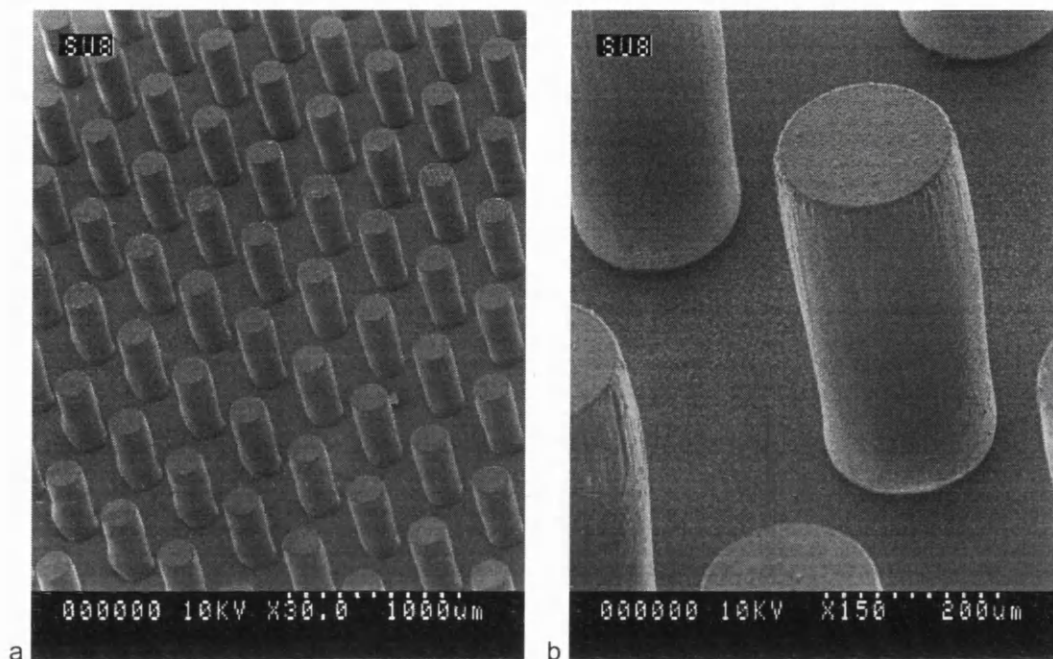


Figure 2-13. SEM images of an array of self-standing micropillars produced by photolithographic structuring of a 380 μm thick layer of SU8-1070 negative photoresist. The pillars feature a 200 μm diameter circular cross-section and are arranged in a square pattern with a pitch of 500 μm . (a) 30x magnification; (b) 150x magnification.

Figure 2-13(a) shows the regularity of the arrangement of the SU8 pillars. The height of the pillars was measured from SEM images as 380 μm . It is remarkable that a photoresist layer of this thickness could be obtained in one single spin-coating step, and subsequently patterned using standard UV lithography equipment. Successful removal of non-cured SU8 from the substrate during the photoresist development step was evidenced by the high standard of cleanliness of the surface of the underlying silicon wafer. Adhesion of the SU8 pillars to the silicon substrate was strong, despite the fact that no adhesion promoter was used, and although a few pillars were broken during the final blow-drying step (see Section 2. 5. 4. 3).

However, Figure 2-13(b) shows that the shape of individual pillars was not perfectly cylindrical (although smooth sidewalls were obtained, suggesting very limited scattering of UV light within the photoresist layer during exposure). The observed distortion of the pillars is likely to have taken place upon flowing of incompletely cured photoresist during the post-exposure baking step, as suggested by the shape of the lower part of the pillars in the bottom-left corner of the image in Figure 2-13(a). Incomplete curing of SU8 might also be the cause for the higher fragility of the few pillars that broke upon blow-drying. It is expected that more regularly shaped pillars can be produced by increasing the duration of the exposure step, and/or that of the pre-exposure soft-bake step.

Overall, the photolithographic microstructuring of SU8-1070 turned out to be time-consuming, although not particularly labour-intensive (except the long developing step). The fabrication of structures with higher aspect ratios than those shown in Figure 2-13 has not been attempted in the framework of this thesis, but it is foreseen that the most challenging aspects will consist in (i) the empirical determination of appropriate pre-exposure bake and exposure times, and (ii) the removal of uncured photoresist from the substrate during the development step, as the highly viscous resist is likely to become entangled within the dense array of pillars. Also, pillars with smaller cross-sections are expected to exhibit a lower adhesion to the silicon substrate. If required, the use of an epoxy-functionalised organosilane (e.g., glycidopropyltrimethoxysilane) might provide enhanced adhesion.

2. 5. 2. 3. Deep dry etching of silicon

2. 5. 2. 3. 1. Principle

The procedure used to fabricate silicon microchannel chips, described in section 2. 4, was adapted to the fabrication of self-standing silicon pillars, by patterning the sacrificial protective photoresist layer through a negative image of the contact photomask used previously.

2. 5. 2. 3. 2. Experimental

4 inch diameter, 525 μm thick silicon wafers were processed as described in Section 2. 4. 2. 2. 1, using AZ4562 photoresist as the sacrificial masking layer. The photomask used featured four patterns, all covering a 12 x 12 mm² area, consisting of opaque hexagons with 50, 75, 100 and 200 μm diameters respectively, arranged in a hexagonal packing.

2. 5. 2. 3. 3. Results

Figure 2-14 shows SEM images of self-standing silicon pillars afforded by ASE processing of silicon wafers. Figure 2-14(a) shows an early attempt at etching 50 μm diameter pillars. The resulting structure featured typical problems associated with deep dry etching techniques: etching “leg”, characterised by a recess around the base of the pillars, and small vertical spikes between pillars, caused by the presence of photoresist residues left on the wafer surface after photolithographic processing. Figure 2-14(b) and Figure 2-14(c) show that these problems could be corrected by careful optimisation of the experimental parameters, as described above, resulting in regular arrays of well-defined, 50 μm and 100 μm diameter, circa 250 μm high pillars. A thick layer of photoresist can be seen to remain on top of the pillars, suggesting the possibility to further increase the etch depth.

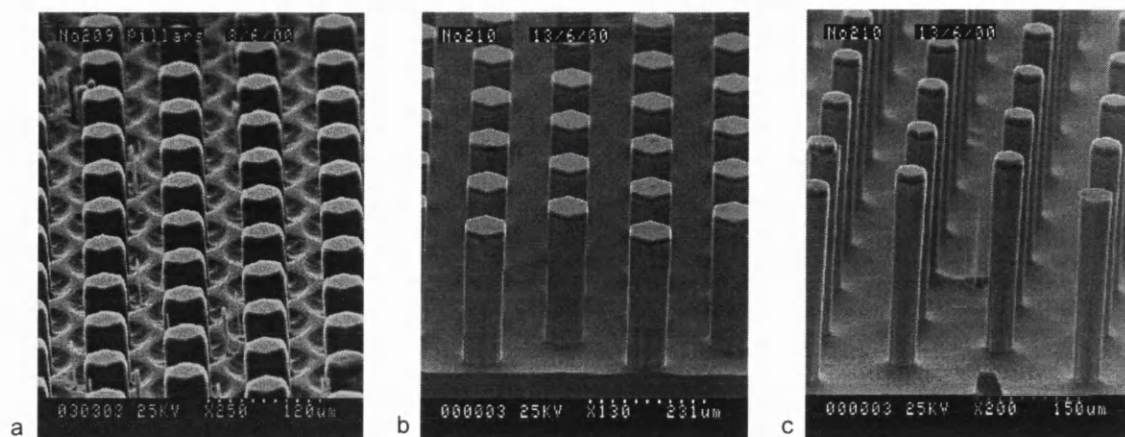


Figure 2-14. Arrays of self-standing silicon micropillars produced by Advanced Silicon Etch processing of silicon wafers patterned with AZ4562 photoresist. (a) 50 μm diameter, circa 200 μm high pillars; (b) 100 μm diameter, circa 250 μm high pillars; (c) 50 μm diameter, circa 250 μm high pillars.

The average etch rate for this run was estimated as circa $1.6 \mu\text{m min}^{-1}$. A slight undercutting of the pillars is observed in Figure 2-14(c), making this structure inappropriate as a master for PDMS imprinting, as the release of the cured PDMS structure would be impeded.

Nevertheless, it is likely that this problem can be solved through semi-empirical optimisation of the etching parameters.

2. 5. 3. Master passivation

2. 5. 3. 1. Aim

The high effective surface area of the masters described above (a direct consequence of their small feature size, high aspect ratio characteristics) results in exacerbated physical interactions between the master and the PDMS imprint. As these interactions are detrimental to the release of the imprint, it is important that surface passivation of the master be implemented, as a way to facilitate the release of the PDMS imprint from the master. This can be readily achieved by coating the master with a film of low energy compound, such as a fluorinated polymer.

2. 5. 3. 2. Experimental

One of the photolithographically microstructured SU8 masters, fabricated as described in Section 2. 5. 2. 2 above, was placed in a dessicator containing a few drops of 1H, 1H, 2H, 2H-perfluorooctyltrichlorosilane (Fluka #77279), also known as tridecafluoro-1,1,2,2-tetrahydrooctyl-1-trichlorosilane, $\text{C}_6\text{F}_{13}\text{C}_2\text{H}_4\text{SiCl}_3$. The dessicator was then evacuated to a moderate vacuum so as to favour vaporisation of the silane compound. The vacuum was applied for a period of an hour, over which the master progressively acquired a whitish colouration.

2. 5. 4. PDMS molding and release

2. 5. 4. 1. Principle

Casting of PDMS against a master can be achieved simply by pouring the liquid prepolymer mixture over the master, before proceeding to the curing of the PDMS. However, as stated above, the fabrication of flow-through microchannel structures implies that the top of the pillars remains clear from any prepolymer, lest blind channels are formed. This required the viscosity of the PDMS prepolymer to be reduced. As dimethylsiloxane oligomers are intrinsically non-polar compounds, the prepolymer mixture was diluted with hexane, a non-polar solvent, so as to produce a less viscous prepolymer solution.

2. 5. 4. 2. Experimental

PDMS base and curing agent (RS Components, UK; ref. 494-966) were combined in a 10:1 ratio and mixed thoroughly. The mixture was then diluted with an equal volume of hexane. 3 μ L of the thinned PDMS prepolymer were poured onto the passivated SU8 master. The cast prepolymer was allowed to stabilise at room temperature for 15 min. Observation under an optical microscope showed that the layer of prepolymer was slightly shallower than the SU8 posts, as desired. The cast prepolymer was baked at 65 °C for 4 hours. Finally, the cured PDMS was peeled off the master using two pairs of tweezers.

2. 5. 4. 3. Results and discussion

After curing, the PDMS structure could easily be peeled off the master that had been passivated. Figure 2-15 shows darkfield stereomicroscopy images of the PDMS microchannel chip released from the passivated master. All the pillars remained attached to the underlying silicon wafer upon release of the PDMS structure, confirming that adhesion of the SU8 pillars to silicon was strong. The yellow box in Figure 2-15 corresponds to an area of the master over which the pillars had been broken before PDMS casting (as mentioned in Section 2. 5. 2. 2. 3). The PDMS chip was circa 350 μ m thick.

The feasibility of using PDMS imprinting for the fabrication of flow-through microchannel structures with moderate feature size and aspect ratio characteristics has thus been demonstrated. However, the approach is limited in terms of feature size and aspect ratio characteristics by the need to release the PDMS imprint from the master after curing. Problems associated with the use of masters with small feature size, high aspect ratio characteristics include increased fragility and reduced adhesion of the thin and tall self-standing pillars, as well as increased physical interactions between the master and the imprint due to the large surface area of contact involved. This makes it necessary to use masters with high mechanical resiliency as well as suitable surface passivation procedures.

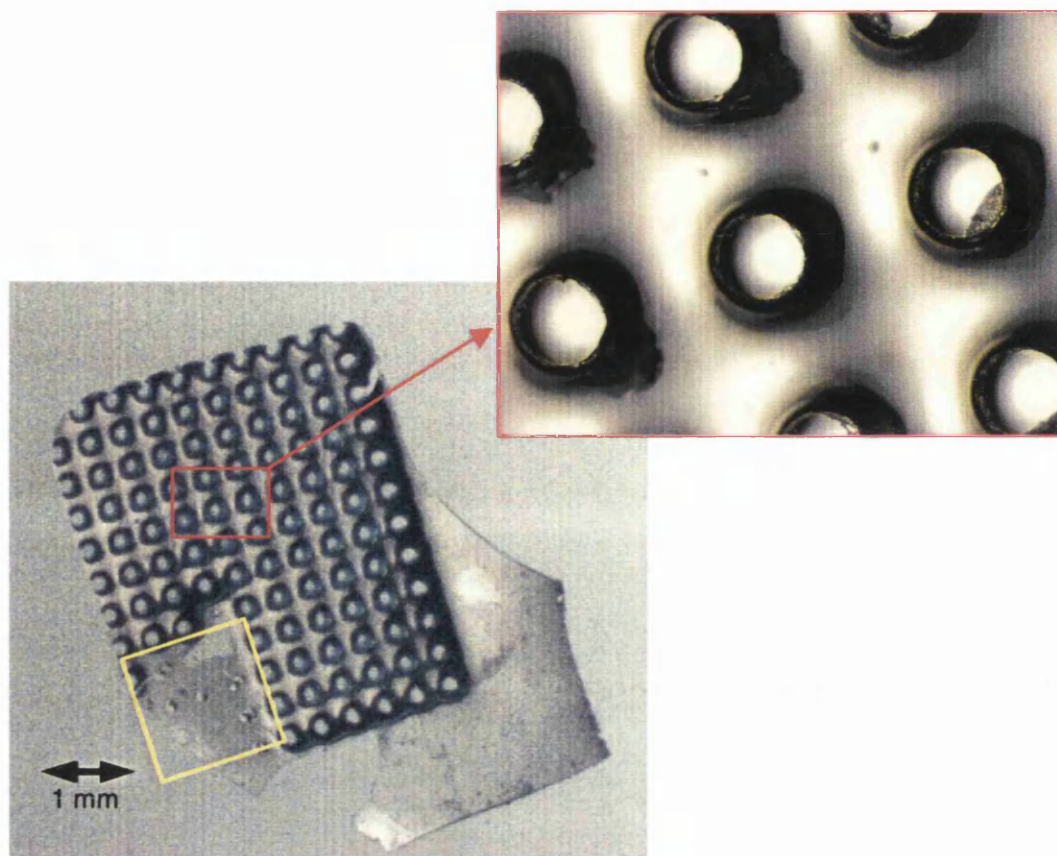


Figure 2-15. Stereomicroscopy images of a microchannel substrate produced by casting PDMS against an SU8 master (shown in Figure 2-13) passivated with perfluorooctyltrichlorosilane. The PDMS chip is circa $350\ \mu\text{m}$ thick and features $200\ \mu\text{m}$ diameter channels arranged in a square pattern at $500\ \mu\text{m}$ pitch. The yellow box corresponds to a damaged area of the master (see text for details).

Besides thick photoresist microstructuring and deep dry silicon etching, possible alternative techniques for the fabrication of self-standing pillar arrays include sequential thermal oxidation and silicon dioxide stripping of MCS substrates, as well as molding of UV-curable polyurethane against, for example, a MCS chip, which can then be dissolved in HF to release a self-standing polyurethane pillar array. An alternative master passivation technique is the plasma-induced polymerisation of a fluorocarbon layer in an RIE machine.¹²⁵ Surface passivation might also be complemented by the use of heating to facilitate release of the imprint from the master, by exploiting possible differences in the expansion coefficients of PDMS and the master material.

2. 6. Conclusions

As shown in this chapter, a number of techniques can be used for the fabrication of highly regular, well defined microchannel structures to be used as flow-through biochip substrates. The relative merits of glass and silicon materials as biochip substrates still have to be investigated in the context of chemical derivatisation and optical detection, which is the focus of the next two chapters.

CHAPTER 3. FLUORESCENCE DETECTION FROM MICROCHANNEL BIOCHIPS

3. 1. Introduction

As stated in Section 1. 2. 6. 5, the fact that fluorescence methodologies are at the core of a wide range of bioassays, including multiplexed heterogeneous nucleic acid hybridisation assays, prompted the development of an instrumental method for the fluorescence-based detection of heterogeneous hybridisation events taking place along the sidewalls of microchannel substrates. This chapter starts with a description of the basic physical principles of fluorescence and a brief account of the common implementations of epifluorescence microscopy for the imaging of biochips (Section 3. 2). A characterisation of the optical properties of microchannel substrates, based on a series of simulations (Section 3. 3. 2) and experiments (Section 3. 3. 3), is then described. Finally, the design and subsequent evaluation and optimisation of an epifluorescence imaging procedure appropriate for microchannel chip-based bioassays are reported in Section 3. 3. 4.

3. 2. Fluorescence as a detection scheme in bioanalytics

3. 2. 1. Physical principles of fluorescence

3. 2. 1. 1. Molecular photoactivation and deactivation processes

Molecular fluorescence is a radiative deactivation process, whereby a photo-excited molecule in a singlet state returns to its ground state by emission of a photon. Fluorescence can be seen as a three-stage photoluminescence process whose outcome is determined by (i) excitation of the fluorophore, (ii) conformational changes and environmental interactions taking place during the excited-state lifetime period, and (iii) fluorescence emission.

The various possible activation and deactivation processes of a molecule are best illustrated by a Jablonski-type diagram,^{126,127} as shown in Figure 3-1. The Jablonski diagram schematically represents the energy levels of a molecule, namely the ground state S_0 , the first and second excited electronic singlet states S_1 and S_2 , and the triplet state T_1 . Four vibrational states (v) are shown for each energy level; rotational levels are not shown.

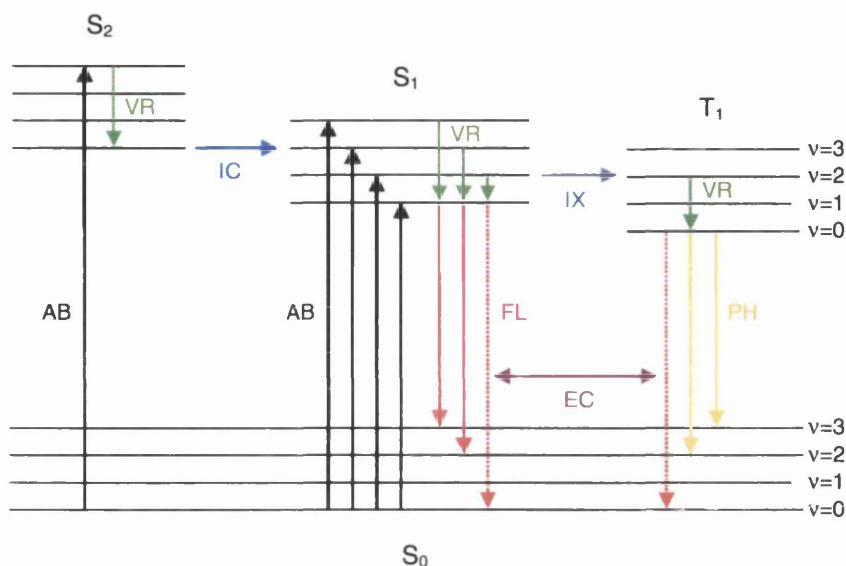


Figure 3-1. Energy-level Jablonski diagram, showing the various possible activation and deactivation processes for a hypothetical molecule. S_0 : ground state; S_1 , S_2 : excited electronic singlet states; T_1 : triplet state; v : vibrational state. AB: absorption; VR: vibrational relaxation; IC: internal conversion; IX: inter-system crossing; EC: external conversion; FL: fluorescence; PH: phosphorescence.

Excitation of a molecule to various vibrational levels in the first and second singlet states takes place, on a femtosecond time scale, through photon absorption (AB). Molecules in excited vibrational states rapidly dissipate their excess vibrational energy (over 10^{-10} - 10^{-11} s) by vibrational relaxation (VR), a non-radiative deactivation process through which energy goes into thermal or vibrational motion of the solvent molecules. Excess vibrational energy can also result from a non-radiative transition between two electronic states of the same multiplicity (S_1 and S_2), called internal conversion (IC). This process requires the lower vibrational levels of the higher electronic state, S_2 , to have similar energy levels as the higher vibrational states of the lower energy level, S_1 . IC takes place on a picosecond time scale. The excess vibrational energy resulting from internal conversion is dissipated through vibrational relaxation.

Fluorescence (FL) occurs as a radiational transition between electronic states of the same multiplicity ($S_1 \rightarrow S_0$ for most molecules). Fluorescence originating from direct excitation of the S_1 state or IC to the S_1 state is referred to as prompt fluorescence, and occurs on a nano- to millisecond time scale. Longer-lived fluorescence emission (delayed fluorescence) is observed when S_1 is populated by indirect mechanisms, *e. g.* thermally-assisted $T_1 \rightarrow S_1$ intersystem crossing.

External conversion (EC) refers to non-radiative processes in which the excess energy of excited states is transferred to other species (solvent, other solutes). Non-radiative transition between two electronic states of different multiplicities (S_1 and T_1) is called intersystem crossing (IX). Following IX, deactivation of the triplet state involves vibrational relaxation to the

ground vibrational level, followed by either EC or IX to the ground electronic state S_0 , or radiational deactivation through phosphorescence (PH).

3. 2. 1. 2. Spectral characteristics of fluorescence

Since the fluorescence process is slower than vibrational relaxation and internal conversion, fluorescence emission takes place exclusively from the ground vibrational state of S_1 , to various vibrational levels of S_0 . Thus, fluorescence emission is observed as a single, broad energy band at longer wavelengths than the $S_0 \rightarrow S_1$ absorption band; the difference in wavelength between the absorption and fluorescence emission bands is called the Stokes shift. The fluorescence excitation spectrum of a molecule, which reflects excitation of the molecule to singlet states through photon absorption, is in most cases identical to its absorption spectrum.

3. 2. 1. 3. Fluorescence quantum yield

The fluorescence intensity associated with a given molecule in given conditions of photoexcitation is determined by the relative competition between the various radiative and non-radiative deactivation routes discussed above. The fluorescence quantum efficiency (QE) or fluorescence quantum yield is defined as the ratio of the steady-state fluorescence radiant power to the absorbed radiant power. It is related to the rates of radiative and non-radiative deactivation of the first singlet excited state by the following equation:

$$\phi_F = \frac{k_F}{k_F + k_{NR}} \quad (\text{Equation 3-1})$$

where k_F and k_{NR} are the first-order rate constants for fluorescence and non-radiative deactivation, respectively. The rate constants depend on the structure and environment of the fluorophore.

3. 2. 1. 4. Fluorescence quenching and photobleaching

Fluorescence quenching refers to several bimolecular processes that reduce the quantum yield of a molecule without affecting the shape of its emission spectrum. Dynamic or collisional quenching is an external conversion process through which energy is non-radiationally transferred from an excited molecule to other molecules during collisions. In aqueous solutions at room temperature, dynamic quenching of fluorescence is usually negligible for sub-millimolar quencher concentrations. Dissolved oxygen and heavy atoms such as iodide can result in significant dynamic quenching of some fluorophores.

Static quenching is observed when the fluorophore (in its ground state) forms a stable complex with a quencher. Long-range or Förster quenching results from non-collisional energy transfer between molecules. Non-radiational deactivation takes place through dipole-dipole coupling, in which the excited fluorophore acts as an energy donor to the quencher. The latter becomes

excited and can either undergo non-radiational deactivation, or emit a type of luminescence called sensitised fluorescence. Long-range quenching is further discussed in the context of fluorescence resonance energy transfer (Section 7. 2. 1. 1).

Excited-state reactions involve the formation of excimers (excited-state dimers with altered emission spectra) between an excited-state molecule and a similar molecule in a ground-state. Excimer formation requires relatively high (> 1 mM) concentrations. Excimer luminescence is usually shifted to longer wavelengths with respect to the luminescence emission of the monomer.

Photobleaching refers to the irreversible destruction of an excited fluorophore under high-intensity illumination. Although multiple photochemical pathways are responsible for photobleaching, the latter essentially occurs from the triplet excited state and thus follows inter-system crossing.

3. 2. 2. Quantitative fluorescence measurements in heterogeneous bioassays

3. 2. 2. 1. Analyte fluorescence signal

Heterogeneous fluorescence bioassays imply the quantitative measurement of fluorescence from surface-bound fluorophores. In the case of nucleic acid hybridisation assays, the latter most usually refer to fluorescent labels attached to target molecules that are hybridised to surface-bound probes. Alternatively, the fluorescent label might be located on the probes themselves, e.g. in “molecular beacon” strategies (Section 7. 2. 1. 2).

The analyte fluorescence signal resulting from the excitation of a fluorophore can be expressed as follows:

$$E_L = \int_{\lambda'} B_{\lambda F} Y(\lambda') R(\lambda') d\lambda' \quad (\text{Equation 3-2})$$

where $B_{\lambda F}$ is the spectral radiance of fluorescence (in $\text{W cm}^{-2} \text{sr}^{-1} \text{nm}^{-1}$), $Y(\lambda')$ is the emission throughput factor (or optical collection efficiency), and $R(\lambda')$ is the detector responsivity.

Fluorescence is emitted anisotropically, i.e. E_L is uniformly distributed in space over a solid angle of 4π steradian. λ and λ' refer to the wavelengths of the excitation and fluorescence radiations, respectively, and, when used as a subscript, to quantities related to these wavelengths. The integral in Equation 3-2 extends over the range of wavelengths incident on the photodetector.

The spectral radiance of fluorescence, $B_{\lambda F}$, can be decomposed as follows:

$$B_{\lambda F} \propto Y_{\lambda} \int_{\lambda} \phi_{\lambda}^A d\lambda \quad (\text{Equation 3-3})$$

where Y_λ is the fluorescence spectral power yield (in nm^{-1}), and ϕ_λ^A is the radiant power absorbed by the analyte.

The integral in Equation 3-3 covers the range of wavelengths that impinge onto the fluorophore. Y_λ is characteristic of the emission spectrum of the fluorophore, and thus is directly related to its quantum efficiency. ϕ_λ^A can in turn be decomposed as follows:

$$\phi_\lambda^A \propto B_\lambda Y(\lambda) \alpha^A(\lambda) \quad (\text{Equation 3-4})$$

where B_λ is the spectral radiant power of illumination (in $\text{W cm}^{-2} \text{sr}^{-1} \text{nm}^{-1}$), $Y(\lambda)$ is the excitation throughput factor (or optical excitation efficiency), and $\alpha^A(\lambda)$ is the spectral absorbance of the fluorophore. $\alpha^A(\lambda)$ is characteristic of the excitation spectrum of the fluorophore.

3. 2. 2. 2. Background signals

In practice, the quantitative determination of the amount of fluorescence radiation emitted from a given fluorophore requires that the associated analytical signal be extracted from the total signal, to which background and other extraneous signals contribute.¹²⁴ Therefore, minimisation of the levels of background signals and associated noise is critical in quantitative fluorescence measurements. The principal sources of background signals encountered in heterogeneous fluorescence bioassays are elastic scattering and reflection of excitation radiations, Raman scattering, and background fluorescence, as discussed below.

Excitation radiations are prone to elastic scattering and reflection by the substrate as well as by the sample or other solution (if present during the measurement), and optical elements, e.g. spectral filters. As elastic scattering and reflection signals occur over the range of excitation wavelengths (*i.e.*, in practice, the range of wavelengths passed by the excitation wavelength selector; see Section 3. 2. 2. 3), elimination of most of these signals is possible through the use of excitation and emission filters with non-overlapping bandpasses. Rayleigh scattering of light by molecules has a fundamental nature and thus can not be eliminated; the intensity of Rayleigh scattering is proportional to the sixth power of the radius of a molecule and the inverse fourth power of the excitation wavelength.

The Raman effect is inherently weak (a typical Raman cross-section is 10^{-29}cm^2 , whereas a typical absorption cross-section is 10^{-16}cm^2); however, Raman bands of the solvents occasionally contribute to the background signal in fluorescence measurements. For a given molecular species, the maximum wavelength of the Stokes Raman band, λ_R , can be predicted from the Raman shift of the molecule, $\Delta\nu$, and the excitation wavelength, λ_{ex} , as follows:

$$\lambda_R = \frac{\lambda_{\text{ex}}}{1 - \lambda_{\text{ex}} \Delta\nu} \quad (\text{Equation 3-5})$$

The Stokes shift for fluorophores commonly used in bioassays is greater, on the energy scale, than the Raman shift for water ($0.339 \mu\text{m}^{-1}$), which permits efficient spectral rejection of Raman signals.

Background fluorescence is caused by fluorescent species other than the analyte fluorophores, such as concomitants (including other fluorophores in multicolor experiments) and contaminants, and by endogenous fluorescence from the substrate and the optics. Spectral discrimination is usually not sufficient to totally eliminate background fluorescence.

3. 2. 2. 3. Long-wavelength fluorescence measurements

The use of fluorophores that can be efficiently excited in the far-red part of the visible electromagnetic spectrum is potentially beneficial to fluorescence-based bioassays, due to reduced levels of background.¹²⁸

The autofluorescence of most materials, including biological materials as well as organic and inorganic materials (such as plastics and glass, respectively) is reduced at long visible wavelengths. Rayleigh scattering is also reduced, as the inverse fourth power of the excitation wavelength. Another advantage is the availability of low-cost, miniature solid-state laser diodes that emit in the red and far-red (635, 670 and 780 nm).¹²⁹ These light sources offer stable and relatively high outputs in addition to long operating lifetimes and low maintenance costs, which make them suitable alternatives to gas lasers, in particular in the context of integrated analytical devices. As a result, a number of long-wavelength fluorophores, including DBCy5, Cy7, NN382 and IRD-41, with excitation maxima at circa 670 nm, 748 nm, 780 nm and 787 nm respectively, have been developed for use in bioanalytical applications.^{27,129-133}

Limitations associated with far-red fluorescence measurements include a decreased optical resolution, higher optical transmission losses (the transmittance of mirrors and lenses decreases above 650 nm due to the presence of anti-reflection coatings), and higher levels of chromatic aberration from objective lenses. Axial chromatic aberrations do not significantly alter imaging in non-confocal systems, due to the high depth of field. These limitations are impeding in specific applications only.

3. 2. 2. 4. Epifluorescence microscopy imaging

As stated in Section 1. 2. 6. 5. 2, the morphology of microchannel substrates restricts the implementation of microchannel chip fluorescence imaging to epifluorescence microscopy. A schematic drawing of an imaging epifluorescence microscope is shown in Figure 3-2.

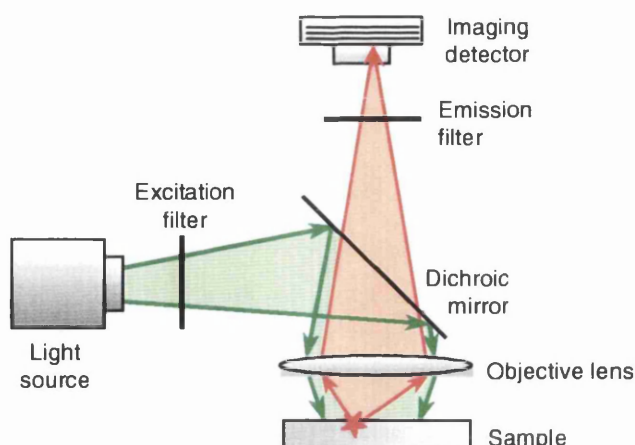


Figure 3-2. Schematic drawing of an imaging epifluorescence microscope configuration. Light from a conventional or laser source is spectrally filtered by an excitation filter and directed towards the objective lens by a dichroic mirror, which reflects the excitation light. Fluorescence emitted by the sample is collected by the same objective lens and focused onto the detector, after passing through the dichroic mirror and being spectrally filtered by the emission filter.

The design of an epifluorescence microscope is characterised by the use of a single objective lens, through which excitation light is focused onto the substrate and fluorescence light is collected (and transmitted to the detector). This is made possible by the use of a dichroic mirror, which reflects the shorter wavelength excitation light whilst transmitting the longer wavelength fluorescence light. The epifluorescence configuration allows fluorescence imaging of biochips to be carried out in optimised conditions. High levels of spatial resolution, as required in the case of high-density microarrays, are made possible by the use of high magnification, high NA objective lenses. Background minimisation is achieved through the use of filter sets (comprising an excitation filter, an emission filter and a dichroic mirror) whose spectral characteristics are optimised for the detection of the fluorophore of interest. Efficient excitation of the fluorophore within the excitation bandwidth is ensured by high power tungsten-halogen, mercury or laser sources (which provide a high spectral radiant power of illumination, B_λ in Equation 3-4) and high NA objective lenses (which provide a high excitation throughput factor, $Y(\lambda)$ in Equation 3-4). Efficient collection of the emitted fluorescence light is ensured by high NA objective lenses (which provide a high emission throughput factor, $Y(\lambda')$ in Equation 3-2). Finally, transduction of the fluorescence light emitted within the bandwidth of the emission filter into an electrical signal is ensured by the use of highly sensitive detectors, such as photomultiplier tubes (PMTs) and charge-coupled device (CCD) cameras (which provide a high detector responsivity, $R(\lambda')$ in Equation 3-2). Increased levels of axial resolution are achieved by the placement of confocal pinholes in the beam paths, so that only a very thin region is probed.^{39,134,135}

3. 2. 3. CCD-based fluorescence imaging

3. 2. 3. 1. CCD cameras

Charge-coupled devices (CCDs) were commercially introduced in 1973. CCD cameras combine a CCD photodetector chip with the associated read-out electronics. Over the last decade, the use of scientific-grade CCD cameras as high-sensitivity imaging detectors in luminescence methodologies (such as fluorescence microscopy and microplate-based chemiluminescence assays) has gained widespread acceptance.¹³⁶⁻¹³⁸ The use of digital cameras makes fluorescence imaging data directly accessible in digital form, which facilitates objective (statistical) quantitative data treatment as well as comparison and archiving. In addition, digital data lend themselves to direct image processing such as image arithmetic, filtering, contrast enhancement, and flat fielding.

3. 2. 3. 2. Principle of CCD photodetection

The functionality of a CCD can be compared to that of electronic film. A CCD chip is a MOS (metal-oxide-semiconductor) solid-state device composed of a two-dimensional array of pixels. Upon exposure to light, photons absorbed at an individual pixel create electron-hole pairs in the silicon junction of that pixel. Over the duration of exposure, photoelectrons generated at each pixel accumulate in an electric potential well, before being transferred from one well to another (through charge coupling) to an analog readout amplifier. An individual pixel can integrate signals until the single pixel full well capacity is reached; thus, the full well capacity, along with the readout noise characteristics, directly affects the dynamic range (*i.e.* number of “gray levels”) of a CCD. An analog-to-digital converter (ADC) provides digital output. The number of photoelectrons required to produce one digital count, *i.e.* the magnitude of amplification, is referred to as the gain of the system; in order to take full advantage of the dynamic range of the CCD chip, the digitisation rate of the ADC is usually chosen so as to match the dynamic range of the CCD at a gain of 1. Most scientific CCD cameras allow pixel binning, which consists in combining charges from adjacent pixels during readout, prior to digitisation, thereby permitting a reduction in the readout noise.¹³⁶

3. 2. 3. 3. Features and performance of CCD cameras

3. 2. 3. 3. 1. Spectral response and quantum efficiency

Unlike photocathodes, in which the conversion of photons into photoelectrons is ensured by a alkali metal photoemissive surface, solid-state detectors such as CCDs rely on the absorption of a single photon at the sensor to create an electron-hole pair in a suitable silicon junction. This endows CCDs with potential intrinsic single-photon detection capability, although various noise sources (in particular, dark current and readout noise, as discussed below) affect the sensitivity of detection. Also, since the number of electron-hole pairs generated is in direct proportion to the number of incident photons, CCDs exhibit highly linear responses.

The spectral response of CCD chips is particularly well suited to visible, including far-red, light detection. Figure 3-3 shows the quantum efficiency, as a function of the wavelength of incident light, for a SITe SIA003AB back-thinned illuminated CCD, at room temperature. The quantum efficiency of this chip is seen to be in excess of 80% between 450 and 750 nm. As a comparison, bialkali photocathodes have a peak response around 350-450 nm, with a maximum quantum efficiency of 20-30%.

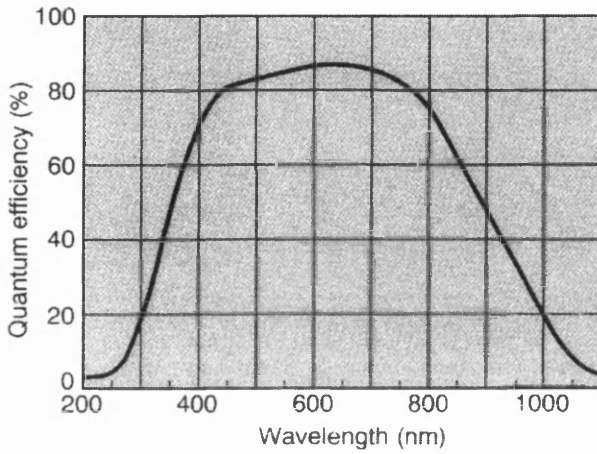


Figure 3-3. Spectral responsivity curve (at room temperature) for a SITe SIA003AB back-thinned illuminated CCD (from ref. 139).

3. 2. 3. 3. 2. Signal-to-noise ratio considerations

The performance and precision of a photodetector operated under given conditions is determined by the magnitude of the signal relative to the uncertainty in the measurement of that signal, characterised by the signal-to-noise ratio (S/N). In the case of a CCD camera, a S/N value can be associated to each individual pixel, for each frame acquired over a given integration time. The total noise, expressed in $\bar{\epsilon}$ rms (root mean square) per pixel, includes contributions from photon noise, readout noise and dark current noise.

Photon noise is a fundamental noise associated with the particle nature of light. The fluctuation of a photon flux follows a Poisson statistical distribution, so that photon noise increases as the square root of the signal. Readout noise is associated with electronic treatment of the signal on the CCD chip, and is proportional to the square root of the readout rate. Dark current is generated at high levels by silicon at room temperature. However, the dark current decreases with decreasing temperature, according to the following equation which relates the number of dark current electrons generated per unit time, N_{dc} , to the temperature, T :

$$N_{dc} = CT^{2/3} e^{-E_{bg}/2kT} \quad (\text{Equation 3-6})$$

where C is a constant, k is Boltzmann's constant, and E_{bg} is the band gap energy of silicon, which is itself a function of temperature:

$$E_{bg} = 1.1557 - 7.021 \times 10^{-4} \times T^2 / (1108 + T) \quad (\text{Equation 3-7})$$

As a rule of thumb, the dark current of a CCD decreases by half when the temperature is decreased by 7-8°C. Noise associated with the variation of the dark current over time follows a Poisson statistics. Thus, the rms dark current noise, expressed in \bar{e} / pixel, is equal to the square root of the dark current. Overall, the S/N for a pixel is given by:

$$S/N = \frac{\Phi Q \Delta t}{\sqrt{\Phi Q \Delta t + N_{dc} \Delta t + N_{ro}^2}} \quad (\text{Equation 3-8})$$

with Φ : photon flux (photons pixel⁻¹ s⁻¹),
 Q : CCD quantum efficiency,
 Δt : integration time (s),
 N_{dc} : dark current (\bar{e} pixel⁻¹ s⁻¹), and
 N_{ro} : readout noise (\bar{e} rms pixel⁻¹).

3. 3. Fluorescence detection from microchannel structures

3. 3. 1. Introduction

The influence of the geometrical optical configuration on the levels of fluorescence and background signals obtained in epifluorescence microscopy measurements is clearly apparent from Equations 3-2 to 3-4, in which the optical excitation and emission efficiency factors, $Y(\lambda)$ and $Y(\lambda')$, are involved. In the case of a 3D substrate, the overall optical configuration includes the substrate morphology, in such a way that the detection of fluorescence signals associated with fluorophores located inside the structure is determined by both the optical properties of the structure itself and the imaging properties of the optics. In the conventional (*i.e.*, non confocal) epifluorescence imaging scheme, the total amount of fluorescence collected and transmitted to the detector includes contributions from above and below the focal plane. Fluorescence generated outside the focal plane will contribute to the overall signal, provided that the associated radiations are guided to the focal plane (waveguiding of the chip), and/ or that the imaging optics actually probe the volume of the chip where the fluorescence is generated (depth-of-field of the imaging optics). In addition, the structure itself directly affects the imaging properties of the optics by distorting the path of light within the field of view of the optics. As a result, the system {substrate + optics} has to be considered as a whole in terms of optical properties. This approach was used, by means of simulations and experimental measurements, to investigate the process of fluorescence detection from microchannel structures, as presented below.

3. 3. 2. Simulation of the process of fluorescence detection from microchannel structures

3. 3. 2. 1. Introduction

The simulation work presented in this section was part of an effort to gain insight into the mechanism of light propagation inherent to microchannel chips. To that end, the morphology and optical properties of MCG and MCS substrates were correlated to the extents to which a microchannel sidewall-bound fluorophore could be excited and to which the emitted fluorescence radiation could be collected and transmitted to the photodetector.

3. 3. 2. 2. Methods

3. 3. 2. 2. 1. Geometrical optics and ray-tracing procedures

The concept of geometrical optics is based on the intuitive idea of a ray of light, representing the path along which light energy travels, together with the concept of surfaces that reflect and / or transmit light. Ray-tracing procedures thus consist in following the paths of rays through a system of reflecting and refracting surfaces.¹⁴⁰

Figure 3-4 illustrates the mechanism of light propagation at a smooth interface between two media with different refractive indices (RIs). The symbol n henceforth represents the refractive index.

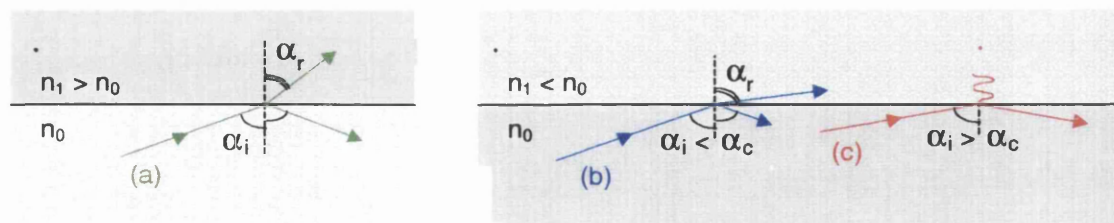


Figure 3-4. Propagation of electromagnetic radiations at the interface between two media with different refractive indices, n_0 and n_1 . α_i is the incidence angle, α_r the refraction angle and α_c the critical angle. (a), (b) Partial reflection; (c) total internal reflection. See text for details.

A ray of light impinging on the interface between a medium of low RI and a medium of higher RI (ray (a) in Figure 3-4) undergoes partial reflection at the interface, whereby the ray is partly reflected within the medium of origin and partly refracted into the other medium. Both the reflected and refracted rays are coplanar with the incident ray and the normal to the surface. The reflected ray makes an angle equal to the incidence angle, whilst the direction of the refracted ray is given by Snell's law:

$$n_0 \sin \alpha_i = n_1 \sin \alpha_r \quad (\text{Equation 3-9})$$

where n_0 and n_1 are the refractive indices of the origin and destination media, respectively, and α_i and α_r are the incidence and refraction angles, respectively, measured from the normal to the surface. The relative extents to which a ray undergoes reflection and refraction depend on the optical properties of the interface as well as on the angle of incidence of the ray. The fraction of energy that is reflected is characterised by the reflectivity, which is predicted by Fresnel's law:

$$\rho = 1/2 (\sin^2 (\alpha_i - \alpha_r) / \sin^2 (\alpha_i + \alpha_r) + \tan^2 (\alpha_i - \alpha_r) / \tan^2 (\alpha_i + \alpha_r)) \quad (\text{Equation 3-10})$$

where ρ is the reflectivity and α_i and α_r are the incidence and refraction angles, as defined above.

A ray passing from a medium of high RI to a medium of lower RI undergoes partial reflection only if the incidence angle is lower than the so-called critical angle α_c , given by

$$\alpha_c = \arcsin (n_1 / n_0) \quad (\text{Equation 3-11})$$

In this case (ray (b) in Figure 3-4), Fresnel's law applies, as above, and the refracted ray is bent away from the normal. If the incidence angle is higher than the critical angle (ray (c) in Figure 3-4), total internal reflection (TIR) occurs at the interface, accompanied by the generation of an evanescent electromagnetic field, perpendicular to the interface, which tails out into the medium of lower RI.

3. 3. 2. 2. 2. Algorithmic formulation and numerical computations of the ray-tracing procedure

Simple though the laws of geometrical optics are, implementation of the ray-tracing approach to the analysis of complex optical systems can be extremely labour-intensive, as the number of rays to be traced must be large enough to ensure that a thorough exploration of all possible ray paths within the optical system is made. In certain particular applications, the symmetry of the optical system of interest and the simplicity of shape of the surfaces involved can be taken advantage of, so as to reduce the ray-tracing procedure to relatively simple algorithms in which, for example, only meridional rays (*i.e.*, rays that propagate within a diametral plane in a cylindrically symmetrical system) are taken into account.^{141,142} In more general cases, however, such as the present case of the epifluorescence imaging of a microchannel chip, where the presence of non-meridional ("helical") rays can not be neglected, it is necessary to formulate ray tracing in a generic vector form, as described by Welford and Winston,¹⁴³ so that the ray-tracing procedure can be efficiently handled through numerical computations.

A number of software packages are commercially available that allow the analysis, based on algorithms derived from geometrical optics, of three-dimensional imaging and non-imaging optical systems. OptiCAD 5.0 software (OptiCAD Corp., Santa Fe, NM) was used in the framework of this thesis. OptiCAD allows complex optical systems to be defined, in a computer-aided design (CAD) format, as sets of surfaces and volumes to which a number of optical properties, such as index of refraction, surface reflectance and bulk absorptance, can be

assigned. A powerful feature of OptiCAD is its unconstrained (*i.e.* nonsequential) approach to ray tracing; rays are not constrained as to the order in which components are intersected, nor to the number of times the same component may be intersected. The computation of the propagation of a ray is not discontinued until one of three termination conditions (which can all be adjusted by the user) is fulfilled: (i) the number of surfaces hit has exceeded a given number, (ii) the energy of a sub-ray has fallen below a given fraction of that of the original ray, and (iii) the level of ghosting (*i.e.*, the number of rays derived from the original ray) has become larger than a specified number.

3. 3. 2. 2. 3. Use of OptiCAD software for the simulation of the process of fluorescence detection in microchannel biochips

The simulations were based on the subdivision of the fluorescence detection process into two independent processes: (i) excitation of the fluorophores by illumination of the microchannel chip, and (ii) collection of the emitted fluorescence and transmission thereof to the photodetector. Fluorescence emission was simulated by defining individual fluorophores as self-luminous, incoherent point sources to which an isotropic emission distribution was associated. Fluorescence excitation was simulated by imparting to each fluorophore of interest a radiant energy that reflects the extent of excitation of that fluorophore, in accordance to Equation 3-3. Although the simulations drew upon the physical principles exposed in Section 3. 2. 2, the fluorescence excitation and emission spectra of the model fluorophores used in the simulations were not explicitly taken into account, as the intrinsic properties of the fluorophores were assumed not to vary within the excitation and emission spectral bandpasses. Thus, a single excitation wavelength and a single emission wavelength were considered in the simulation; these wavelengths only came into account through the values assigned to the refractive indices of the structure and the immersion medium. The wavelengths were assumed to be in the range 620-680 nm, so as to simulate fluorescence measurements with red fluorophores such as Cy5 (which exhibits an excitation maximum at circa 630 nm and an emission maximum at circa 670 nm).

3. 3. 2. 2. 4. Models for different types of microchannel chips

MCG chips

Cutout sections of MCG chips were modelled according to the morphology and dimensions reported in Table 2-1, *i.e.* regular array of 10 μm diameter cylindrical channels, arranged in an hexagonal packing pattern, with a centre-to-centre spacing of 12 μm . Each model channel was defined as a polygonally faceted object featuring a 72-side polygonal cross-section, approximating a circular cross-section. Figure 3-5 shows a 19-channel model structure, as used throughout the simulation work. Increasing the number of channels resulted in prohibitively long computation times.

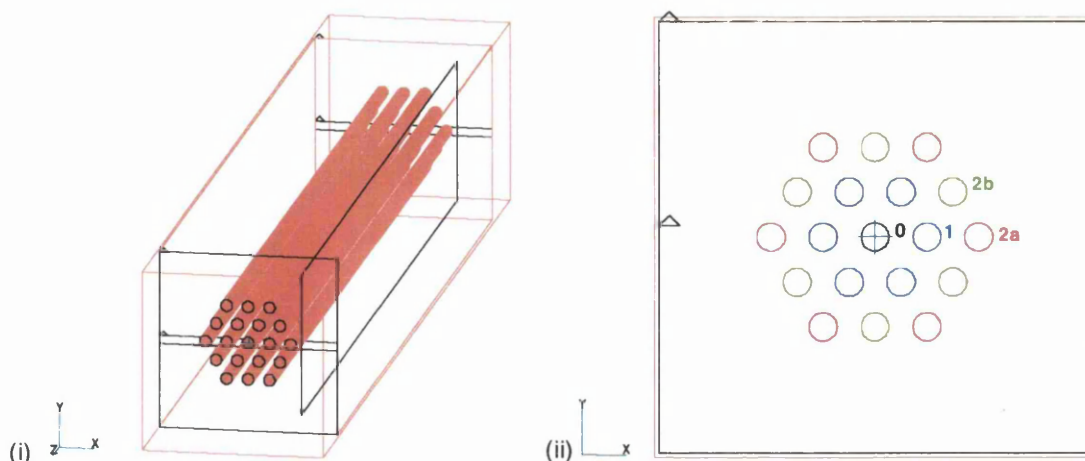


Figure 3-5. 19-channel model cutout structure used in light propagation simulations with OptiCAD software. (i) 3D view; (ii) front face. The labelling of the four different types of channels (according to their relative position from the centre) is indicated.

Due to the symmetry of the hexagonal pattern, the 19-channel cutout featured 4 different types of channels, differing by their relative position from the centre. These channels were labelled as follows: 0 (central channel), 1 (direct neighbours of the central channel), 2a (aligned with channel 0 and one type 1 channel) and 2b.

The RI of the dielectric material was set equal to 1.70, which is the value (at 620-680 nm) for the heavy flint, 55% lead oxide-containing glass used for the fabrication of the MCG material. The RI of the medium in which the chip was immersed (corresponding to the inside of the channels plus thin layers of fluid at the front and the back of the chip) was set equal to either 1.0 (air) or 1.33 (aqueous solution); the latter case corresponds to experimental conditions in which fluorescence imaging is carried out while buffer is filling the channels. Bulk absorbance and autofluorescence of the material were not considered. Although lead-rich glasses are known to exhibit fluorescence emission over a wide portion of the electromagnetic spectrum, from purple to green, upon ultraviolet (UV) illumination,¹⁴⁴ the effect could be neglected in the present case of long-wavelength fluorescence imaging. No volumetric or surface scattering was considered either.

MCS chips

In order to gain direct insight into the effect of the substrate material upon the waveguiding properties of microchannel chips, a morphology identical to that of MCG chips described above was used to model MCS chips. The RI of the silicon microstructure was set equal to 3.85.¹⁴⁵ Unlike glass, silicon exhibits a significant volumetric absorbance in the visible region of the electromagnetic spectrum, due to its bandgap of 1.12 eV at 293 K. The absorption coefficient,

k , was taken equal to 0.017 (between 620 nm and 680 nm),¹⁴⁵ which gave a value for the extinction coefficient of $4\pi k/\lambda = 0.33 \mu\text{m}^{-1}$ at a wavelength, λ , of 650 nm.

3. 3. 2. 2. 5. Parameter input and data output

A set of Visual Basic (Microsoft Corp., Seattle, WA) and OptiCAD macro commands was written to provide a maximum level of automation to the simulation procedure. The parameters related to the morphology and optical properties of the model microchannel chip under study were input into the OptiCAD computation engine via an ASCII text file, generated by a Visual Basic macro from an Excel file. Conversely, the raw data resulting from each computation were retrieved from OptiCAD into ASCII text files before being formatted and displayed in Excel.

3. 3. 2. 2. 6. Quantitative simulation of the fluorescence detection process

Collection of the fluorescence radiations

In order to study the extent to which the axial position of a fluorophore within a microchannel affected the amount of signal collected by the imaging optics, simulations were carried out in which a single fluorophore (simulated by an incoherent point source featuring an anisotropic distribution of light emission, as stated above) was placed inside the central channel of a 19 channel cutout (as shown in Figure 3-5), at a fixed distance of 10 nm from the sidewall, but at increasing distances from the front face of the chip. For each axial position, radiant energy propagating within the 3D system was mapped by positioning virtual "films" at suitable locations. These films were used to record both the spatial distribution of energy within the system (radiometric mapping), and the angles made by rays at their point of intersection with the film. Typically, a minimum of 10,000 rays were traced. Each computation required between 0.5 and 5 hours on a Pentium II PC.

Recordings of the angular distribution of the radiant energy were used to simulate the effect of the NA of the objective lens, as fluorescence radiating from the front side of the microchannel structure can only be collected (before being transmitted to the detector) if the radiations fall within the acceptance angle of the objective lens. The acceptance semi-angle of a lens, α_{max} , is related to the NA of the lens by:

$$NA = n_0 \sin \alpha_{max} \quad (\text{Equation 3-12})$$

Note that the focal plane of the objective lens was set on the front face of the chip.

Cross-talk of fluorescence radiations

A particular issue that the simulations sought to address consisted in assessing the extent to which inter-channel optical cross-talk of the emitted fluorescence radiations took place within a microchannel structure. The phenomenon of optical cross-talk is illustrated in Figure 3-6.

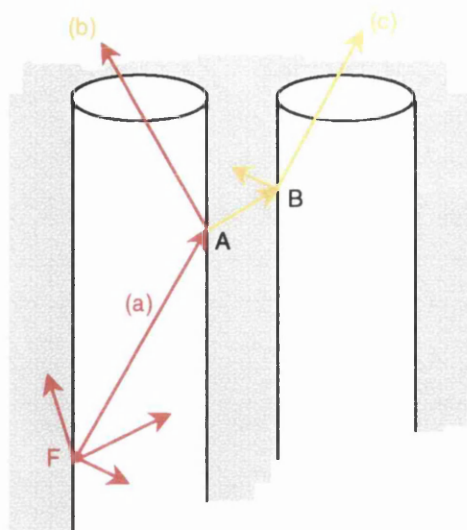


Figure 3-6. Schematic depiction of the phenomenon of inter-channel optical cross-talk in microchannel structures. Ray (a), which is part of the fluorescence radiations emitted isotropically by a sidewall-bound fluorophore, F , undergoes partial reflection on the microchannel sidewall at point A ; the reflected ray, (b), exits the front plane of the chip from within the channel in which F is located, whereas the refracted ray is refracted once more at point B and exits the front plane of the chip from another channel than that in which F is located.

As fluorescence is emitted isotropically, *i.e.*, over a full solid angle of 4π sr, most rays (such as ray (a) in Figure 3-6) interact with the sidewall of the microchannel from which they are emitted. As shown in Figure 3-4(a), the interaction is characterised by partial reflection of the ray, whereby the refracted light propagates through the sidewall, before undergoing another partial reflection at the sidewall of the neighbouring channel. This process results in rays (such as ray (c) in Figure 3-6) to exit the front surface of the chip from a channel different from that in which they were originally emitted. Note that cross-talking of a ray can extend over a larger number of microchannels.

Cross-talk is an important issue in the context of microchannel chip-based fluorescence bioassays, as the multiplexing nature of the approach (which is essentially based on spatial discrimination of biosensing elements by the imaging system) can be impaired by the occurrence of cross-talk, if the latter extends over distances commensurate with the feature size of the biorecognition elements.

In order to investigate cross-talk by means of simulations, radiometer films were placed in one peripheral channel of each type (1, 2a and 2b), in addition to the central channel (type 0), in the 19 channel model cutout structure of Figure 3-5(b).

Fluorescence excitation

As shown in Equation 3-4, the extent of excitation of a fluorophore is proportional to the amount of excitation light that reaches the fluorophore. As stated in Section 3. 2. 2. 4, the epifluorescence detection scheme entails illumination of the substrate with excitation light through the same objective lens as that used for the collection of the emitted fluorescence. As a consequence, excitation radiation was focused on the front surface of the chip. Knowledge of how these radiations propagated within the microchannel structure was required in order to assess the extent to which sidewall-bound fluorophores located at various axial distances from the front face of the chip were excited.

The process of fluorescence excitation was simulated by illuminating the chip, from the front, with an energy distribution corresponding to that obtained at the output of a microscope objective lens. Two different distributions were used, corresponding to low (0.13) and high (0.75) NA objective lenses, respectively; these NA values correspond to those of actual objective lenses used in experimental studies (see Section 3. 3. 3). In the case of an achromatic lens, the illumination semi-angle is identical to the acceptance angle defined above. Values for the illumination semi-angle (given by Equation 3-12) for the 0.13 and 0.75 NA lenses were 5.6° and 34.3° , respectively, in water ($n=1.33$).

In the simulations, the illuminated area was defined so as to comprise the opening of the central channel, plus the interstitial area around it extending to the edge of the first ring of neighbouring channels, as shown in Figure 3-7. The excitation intensity in the central channel was then taken as the sum of the excitation intensities in all the 19 channels of the chip cut-out. This procedure simulated a uniform illumination of the front face of the chip through an objective lens of given NA, while taking inter-channel cross-talk of the illumination radiations into account.

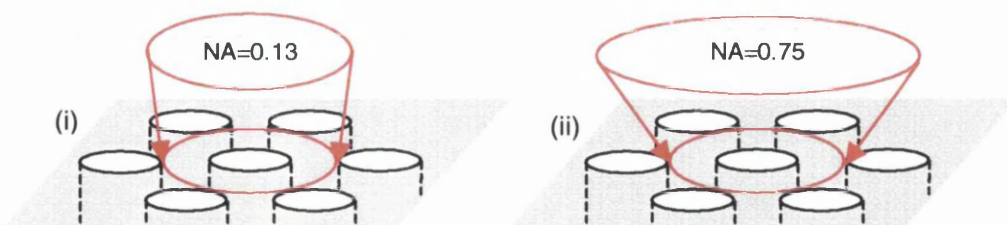


Figure 3-7. Schematic representation of the epi-illumination of the front face of a microchannel chip through objective lenses of various NA, as used in simulations of the excitation of microchannel sidewall-bound fluorophores. (i) NA=0.13 (illumination semi-angle $\alpha_{\max} = 7.5^\circ$, in water); (ii) NA=0.75 ($\alpha_{\max} = 48.6^\circ$).

As in the case of fluorescence emission, the radiation wavelength only came into account through the values assigned to the RIs. Radiometer film planes located at several axial distances from the front surface of the chip were used to record the radiant energy, as above.

Fluorescence detection

As stated above, the efficiencies of excitation and collection of a given microchannel sidewall-bound fluorophore are dependent upon its axial position (distance from the front face of the chip). The actual fluorescence signal detected by imaging the front face of the chip with an epifluorescence microscope is a convolution of the two processes mentioned above (Equations 3-2 to 3-4). As the processes of fluorescence excitation and fluorescence collection were treated independently in the simulations, a numerical convolution was implemented to determine the fluorescence detection efficiency associated with microchannel sidewall-bound fluorophores located at various axial positions.

3. 3. 2. 3. Results and discussion

3. 3. 2. 3. 1. Reflectivity of the microchannel sidewalls

Figure 3-8 shows a plot of the reflectivity, calculated from Fresnel's law, of a monochromatic, unpolarised radiation impinging onto a glass ($n=1.70$) / water ($n=1.33$) interface and a silicon ($n=3.85$) / water interface, as a function of the planar incidence angle.

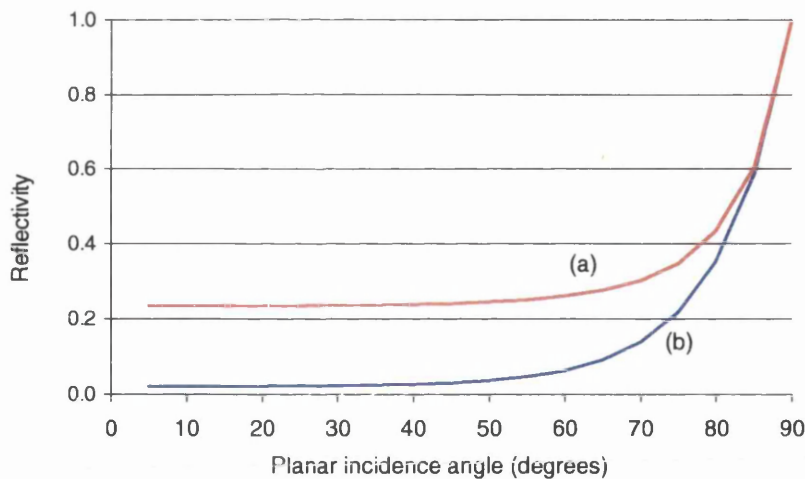


Figure 3-8. Reflectivity of a monochromatic, unpolarised radiation at the interface between water ($n=1.33$) and (a) silicon ($n=3.85$) and (b) heavy flint glass ($n=1.70$), as predicted from Fresnel's law.

Figure 3-8 shows that the silicon surface exhibits a higher level of reflectivity than the glass surface, especially at steeper incidence angles. This suggests a higher waveguiding efficiency of meridional rays inside the microchannels of a MCS chip, as compared to a MCG chip. However, the relative extents to which refraction and absorbance take place in the two different types of microchannel chips have to be considered; these will depend on the optical properties of the interface, as well as on the angle of incidence of the rays, as predicted by Fresnel's law. Since microchannel sidewall-bound fluorophores are located within the medium of lower RI, the emitted fluorescence will undergo a series of partial reflections on the sidewalls of the

microchannels, as shown in Figure 3-4(a); as a consequence, one can expect a significant portion of the radiations to be travelling inside the wall separating adjacent microchannels. This holds true for excitation radiations as well as for fluorescence radiations.

3. 3. 2. 3. 2. Waveguiding of the fluorescence radiations

Inter-channel optical cross-talk in glass and silicon microchannel chips

Figure 3-9(i) shows the simulated intensity profile of the fraction of radiant fluorescence energy that was guided to the front surface of a 19 channel model MCG chip immersed in air ($n=1.0$), where fluorescence was emitted by a single model fluorophore located at a distance of 10 nm from the sidewall of the central channel, and at an axial distance of 10 μm from the front plane of the chip.

Figure 3-9(i) gives a quantitative account of the phenomenon of inter-channel optical cross-talk in MCG. From the simulation, it is apparent that most of the emitted fluorescence energy radiated from the opening of the central channel, in which the emitting fluorophore was located, whilst only a small fraction of the emitted fluorescence radiation was seen to emerge from the opening of neighbouring channels. Fluorescence intensity profiles obtained in simulations where the fluorophore was placed at increasing axial distances (50 μm to 450 μm) from the front plane showed an even less significant level of cross-talk than that shown in Figure 3-9 (i). Likewise, lower levels of cross-talk were obtained in simulations in which the chips were immersed in aqueous solution ($n=1.33$).

Figure 3-9(i) also shows that, in the absence of light scattering off the front surface of the chip, no significant amount of fluorescence energy radiated from the interstitial area of the front plane. A close analysis of the ray propagation pattern in OptiCAD confirmed that, although a number of rays propagated inside the solid glass wall separating adjacent microchannels, these rays underwent total internal reflection on the front surface of the substrate, and thus were not refracted out of the glass material. This suggests the possibility of minimising the amount of surface scattering, hence the level of background signals, by polishing the front surface of MCG chips to an optical standard of flatness.

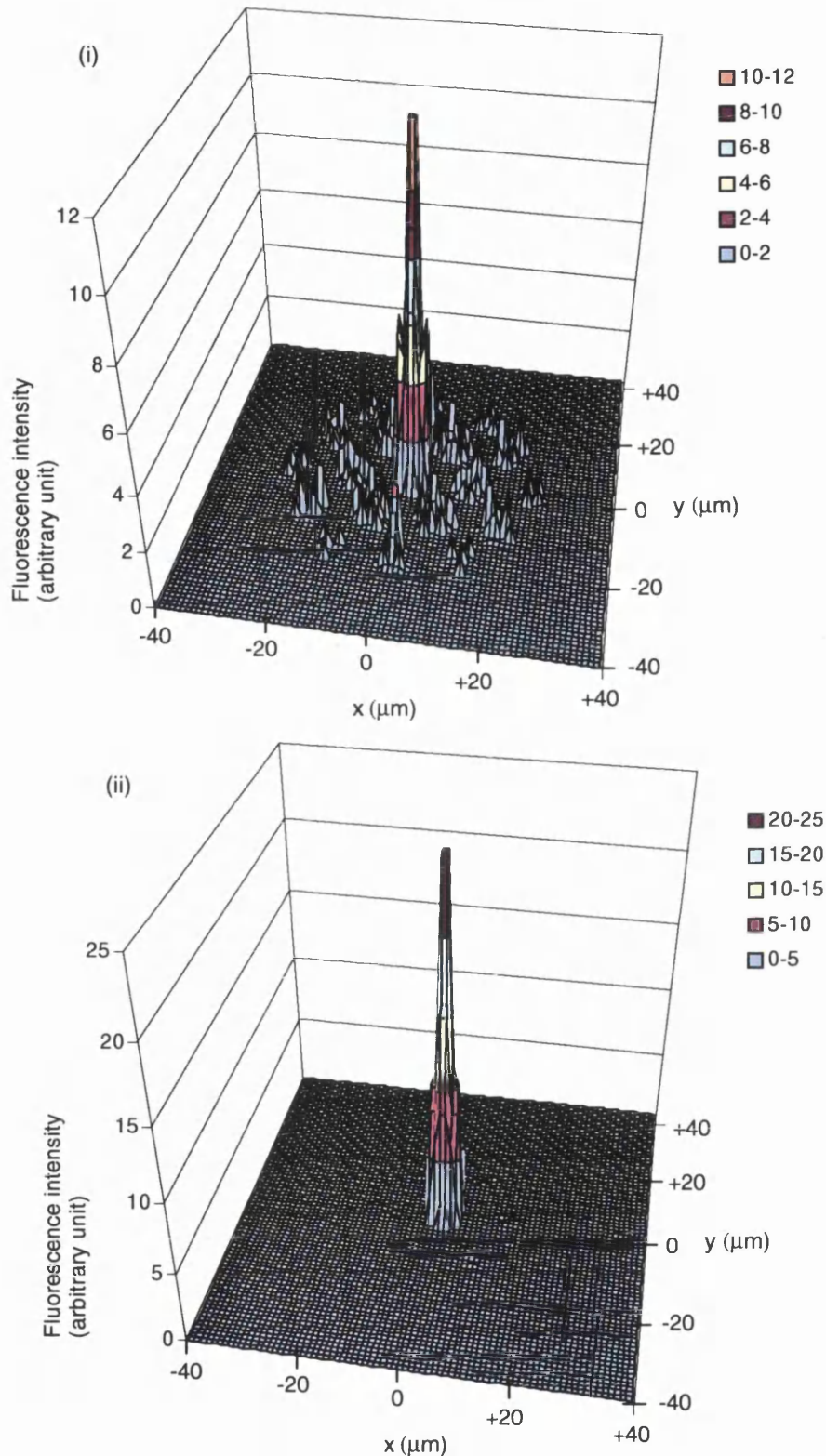


Figure 3-9. Simulated three-dimensional intensity profiles of the fraction of radiant fluorescence energy transmitted to the front surface of a 19 channel model microchannel glass chip immersed in air ($n=1.0$), illustrating the inter-channel cross-talk of fluorescence emitted by a single model fluorophore located close to the sidewall of the central channel and at an axial distance of $10\text{ }\mu\text{m}$ from the front face of the chip. The x and y axes correspond to two orthogonal directions on the front face of the model structure, as defined in Figure 3-5. (i) model MCG chip; (ii) model MCS chip.

Figure 3-9(ii) shows the intensity profile obtained for a model MCS chip, in the same conditions as above. In this case, all of the fluorescence radiations were seen to be confined within the central channel, indicating that inter-channel optical cross-talk did not take place to any significant extent. This was due to the fact that silicon has a high bulk absorptivity, which resulted in attenuation of the fluorescence energy refracted inside the solid silicon wall. Nevertheless, the amount of fluorescence radiation that propagated within the central channel and reached the front face of the model MCS chip was larger than in the case of a MCG chip [note the difference in the scales of the energy axis between Figure 3-9(i) and Figure 3-9(ii)], as expected from the higher level of reflectivity of silicon as compared to glass, shown in Figure 3-8 above.

Waveguiding properties of different types of microchannel chips

Figure 3-10 shows the fraction of fluorescence, emitted by a single fluorophore, that was guided to the front surface of model glass and silicon microchannel chips, as a function of the axial position of the fluorophore with respect to the front surface of the chip. Radiant fluorescence energy was measured over the 19 channels of the model structure. The plots for model microchannel chips of identical morphology, but with 100% absorbing and 100% reflective sidewalls, are also shown for comparison.

Figure 3-10 shows that, for all the types of microchannel chips except the one with totally reflective sidewalls, the fraction of emitted fluorescence guided all the way to the front face decreased sharply as the emitting fluorophore was located at increasing axial distances from the front face.

In the case of the chip with totally reflective sidewalls (curve (a) in Figure 3-10), half of the emitted fluorescence was expected to reach the front plane, as a result of fluorescence being emitted isotropically and confined within the microchannel, leading to 50% of the radiation propagating towards the front face of the chip and 50% towards the back face. This was observed in the results of the simulation, except for a small decrease as the emitting fluorophore was located at increasing distances from the front plane. This decrease was ascribed to termination of rays that were emitted in directions close to perpendicular to the microchannel axis and thus were involved in a large number of interactions with the sidewall before reaching the front surface. The termination criterion based on the number of surfaces hit was set at 10,000 in this simulation. The effect of ray termination was small enough to be neglected in the computations.

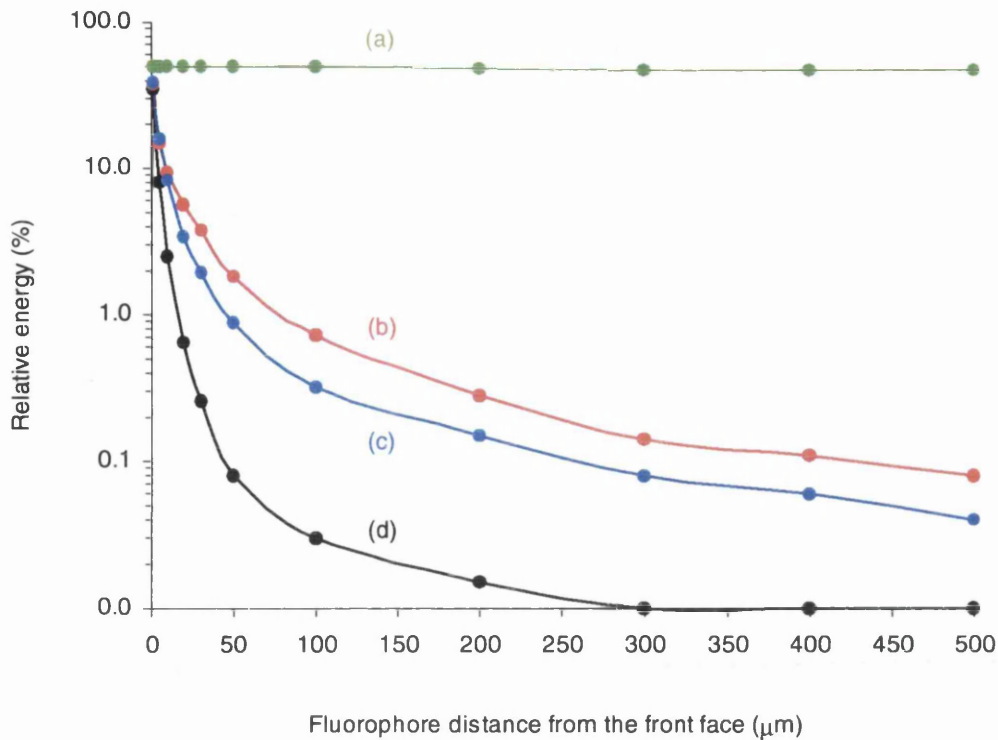


Figure 3-10. Relative amount of fluorescence radiation, emitted by a single fluorophore, that is guided to the front face of different types of microchannel chips immersed in water ($n=1.33$), as a function of the axial position of the fluorophore with respect to the front face of the chip. (a) 100% reflective material; (b) glass ($n=1.70$, $k=0$); (c) silicon ($n=3.85$, $k=0.017$); (d) 100% absorptive material.

In the case of the model MCG chip, in the absence of bulk absorption from the glass material and from the fluid filling the channels, the decrease observed in Figure 3-10 was essentially due to the fact that radiation emitted in non-axial directions did not reach the front plane of the chip within the $100 \times 100 \mu\text{m}^2$ radiometer film over which the radiant energy of fluorescence was measured. This effect, referred to as long range cross-talk, is evidenced in Figure 3-11 below. Long-range cross-talk was studied by recording the radiant energy of fluorescence impinging onto a radiometer film plane positioned perpendicular to the front face of the chip, and separated from the central channel by two peripheral channels. Figure 3-11 shows the intensity profile in the film plane, when the fluorophore was located at an axial distance of $100 \mu\text{m}$ from the front surface.

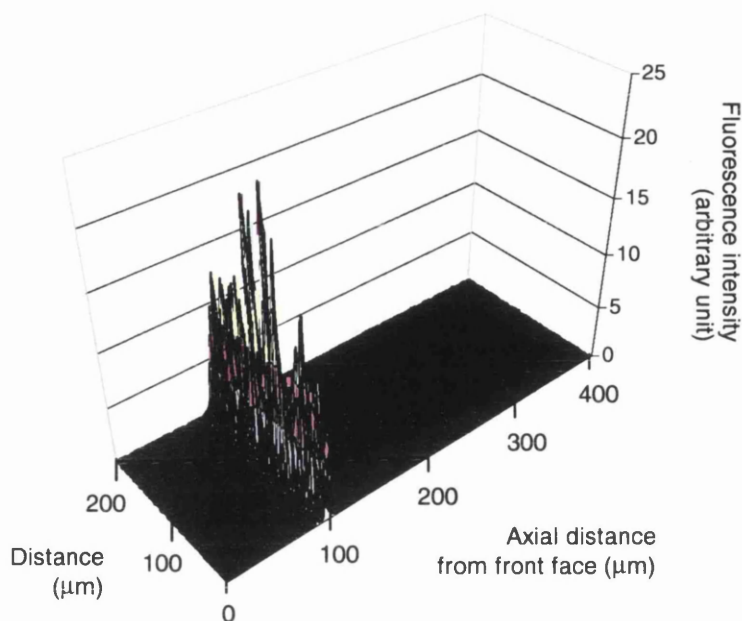


Figure 3-11. Radiant energy in a plane (shown in Figure 3-5i) perpendicular to the axis of the central channel, showing long range cross-talk across two rows of channels, in the case of a single fluorophore located at an axial distance of 100 μm from the front surface of a MCG chip immersed in water.

The intensity scale of Figure 3-11 is identical to that of Figure 3-9. Clearly, a large fraction of fluorescence emitted by the fluorophore radiated transversally across the MCG structure, over a transversal distance of at least two channel diameters, and did not reach the front surface. However, it is also apparent from Figure 3-11 that long-range cross-talk was restricted to a narrow range of directions, close to the normal.

In the case of silicon chips (curve (c) in Figure 3-10), rays that were diffracted into the silicon wall underwent partial absorption ($k=0.017$). This counteracted the higher reflectivity exhibited by the silicon/air interface as compared to the glass/air interface (see Figure 3-8) and resulted in MCS chips exhibiting a lower level of waveguiding than MCG chips. Nevertheless, both glass and silicon microchannel chips exhibited a significantly enhanced waveguiding effect as compared to the non-reflective, totally absorptive chip (curve (d) in Figure 3-10).

The effect of the RI of the immersion medium on the waveguiding properties of MCG chips is illustrated by Figure 3-12 which shows that the model MCG chip exhibited a slightly higher level of waveguiding when the channels were filled with air ($n=1.0$) than when they were filled with an aqueous solution ($n=1.33$), as expected from Fresnel's law. In practice, however, the effect of the immersion medium on other experimental factors, such as the imaging properties of the lens (in particular the NA) and the quantum yield of the fluorophore, would have to be taken into account.

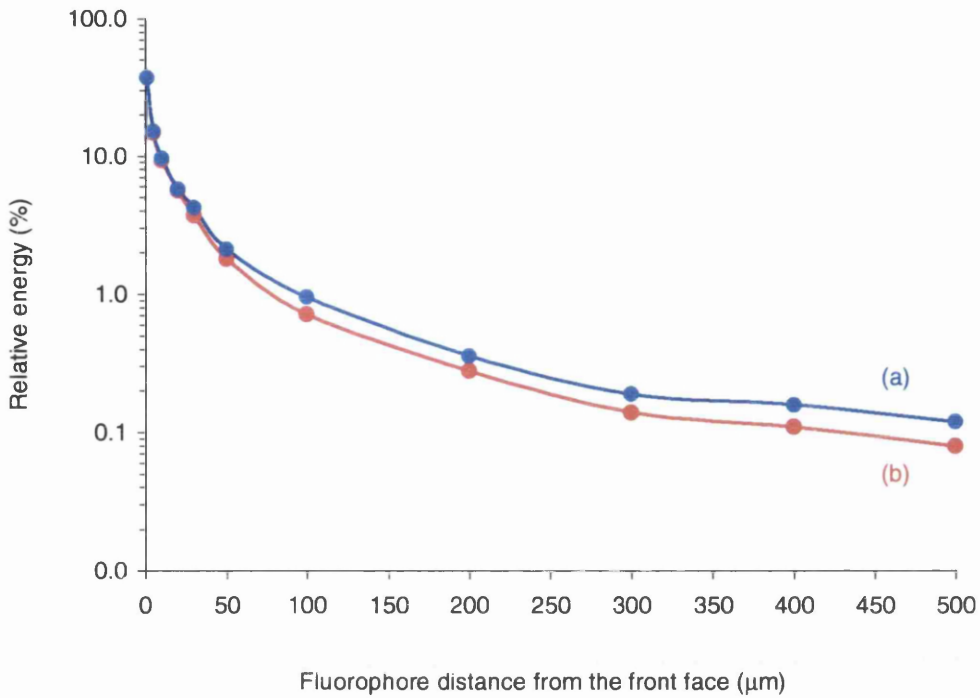


Figure 3-12. Relative amount of fluorescence, emitted by a single fluorophore, that is guided to the front surface of a microchannel glass chip immersed in (a) air ($n=1.0$) and (b) water ($n=1.33$), as a function of the position of the fluorophore with respect to the front face of the chip.

Angular distribution of the waveguided fluorescence

The angular distribution of the waveguided fluorescence radiation is shown in Figure 3-13, where the fraction of fluorescence energy (relative to the total energy that reaches the front face of the chip) that falls within a given NA was plotted as a function of the axial position of the fluorophore with respect to the front surface. Figure 3-13 corresponds to the case of a MCG chip in which only fluorescence radiations that did not undergo cross-talk were considered.

Figure 3-13 shows that, as the emitting fluorophore was located farther away from the front face of the chip, a larger fraction of the fluorescence radiation exited the microchannel within a restricted range of angles. Accordingly, the NA of the objective lens used to image the chip determined the relative contribution to the collected fluorescence signal of fluorophores located at different axial distances, such that the use of a lower NA objective lens resulted in an increased contribution from fluorescence originating from deeper inside the chip. According to Figure 3-13, all the fluorescence energy emitted by fluorophores located at distances larger than 200 μm was confined within a NA of 0.25 as it exited the front face of the chip from the opening of the microchannel in which the fluorophore was located. This suggests that the use of a low NA lens would not be detrimental to the collection of most of the fluorescence radiation.

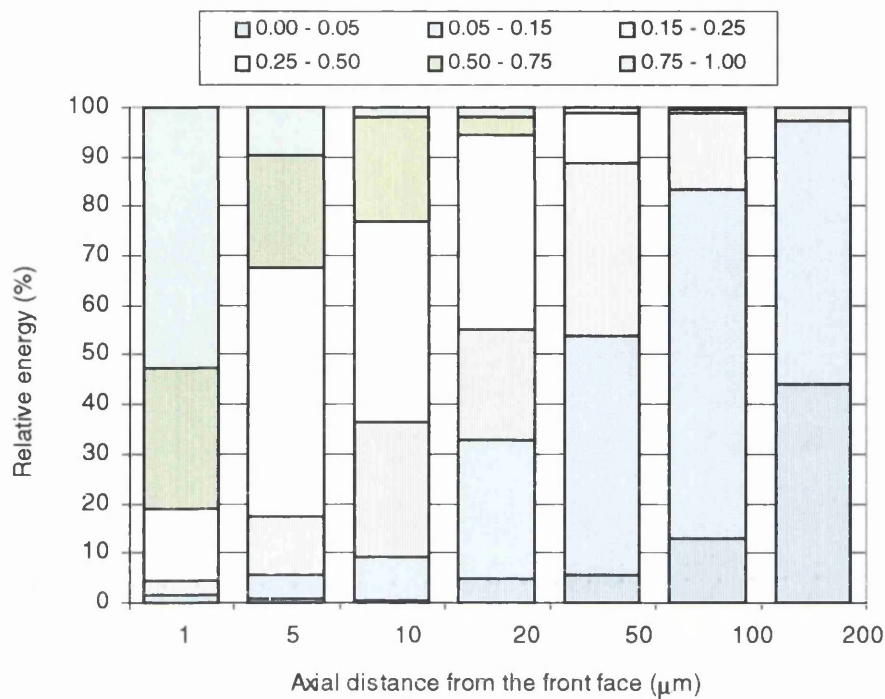


Figure 3-13. Fraction of fluorescence energy (emitted by a single fluorophore) that falls within a given numerical aperture, relative to the total fluorescence energy that reaches the front face of a microchannel glass chip immersed in water, as a function of the axial position of the fluorophore with respect to the front face of the chip. The legend corresponds to ranges of NA values.

The angular distribution of the fluorescence emitted from each peripheral channels (1, 2a and 2b) was also simulated. It was found that rays participating in cross-talk emerged from neighbouring channels at angles corresponding to NA values greater than 0.5. This suggests that the use of a low NA objective lens to image the chip would actually result in a lower level of apparent cross-talk.

3.3.2.3.3. Waveguiding of the excitation radiation

The excitation of fluorophores located near the sidewall of a microchannel involves two types of rays, as schematically depicted in Figure 3-14: rays, such as ray (a) in Figure 3-14, that enter the microchannels directly, and propagate according to the mechanism described above, including inter-channel cross-talk; and rays, such as ray (b) in Figure 3-14, that impinge onto the interstitial area of the front face of the chip and are refracted into the solid wall.

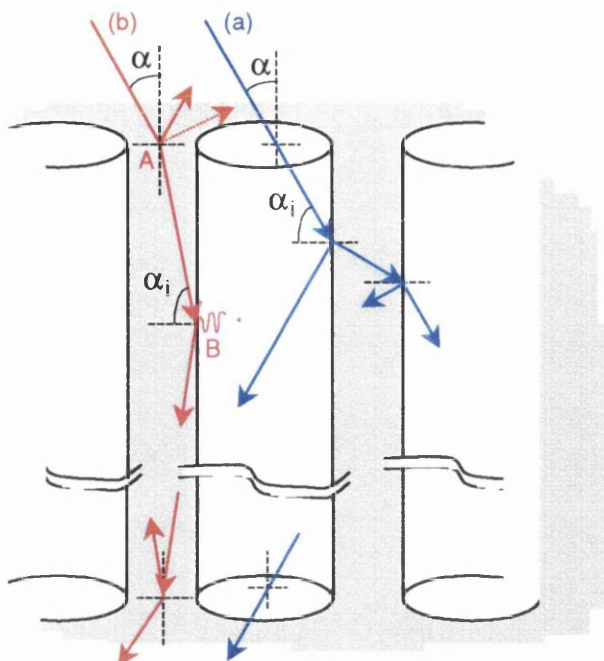


Figure 3-14. Schematic illustration of the propagation of excitation radiation inside a microchannel chip, upon epi-illumination of the chip through an objective lens with the focus set on the front face of the chip. Ray (a) enters a microchannel directly through its opening, while ray (b) is refracted inside the solid wall after impinging onto the interstitial area of the front face of the chip, at point A, resulting in the generation of an evanescent field at point B along the microchannel sidewall. See text for details.

Reflectivity on the front surface of the chip is low, as shown in Figure 3-8, especially at steep incidence ($\rho < 5\%$ for $\alpha < 45^\circ$), such that, upon epi-illumination of the front face of the chip, a large fraction of the incident energy will be coupled into the glass matrix and subsequently impinge onto the microchannel sidewall at grazing incidence, thereby undergoing TIR at the sidewall. As stated above, TIR is accompanied by the generation of an evanescent electromagnetic field along the channel wall.

The intensity of the evanescent field $I(z)$ decays exponentially with the distance z from the interface, according to:

$$I(z) = I_0 \exp(-z/d_p) \quad (\text{Equation 3-13})$$

where I_0 is the intensity at the interface, at which $z = 0$, and d_p is the penetration depth. The latter is typically of the order of a wavelength, which is larger than the distance over which heterogeneous biorecognition events are localised (the length of a nucleic acid duplex arranged in a double helix configuration is circa 3.4 \AA per base pair). This implies that fluorescence bioassays taking place along the microchannel sidewall will benefit from the excitation radiation provided by the evanescent field. The effect is however difficult to quantify, both through simulation and experimentally. In practice, the generation of the evanescent field is affected by

the significant levels of light scattering and diffuse reflection taking place on the front face of the chip, as well as on the channel sidewalls, and by bulk absorptivity of the microchannel matrix.

Figure 3-15 shows the axial distribution of the excitation intensity within MCG and MCS chips, as a result of the epi-illumination of the chips through an objective lens of given NA (simulated as shown in Figure 3-7), with the focus adjusted on the front face of the chip. Two values for the NA were considered, 0.13 and 0.75.

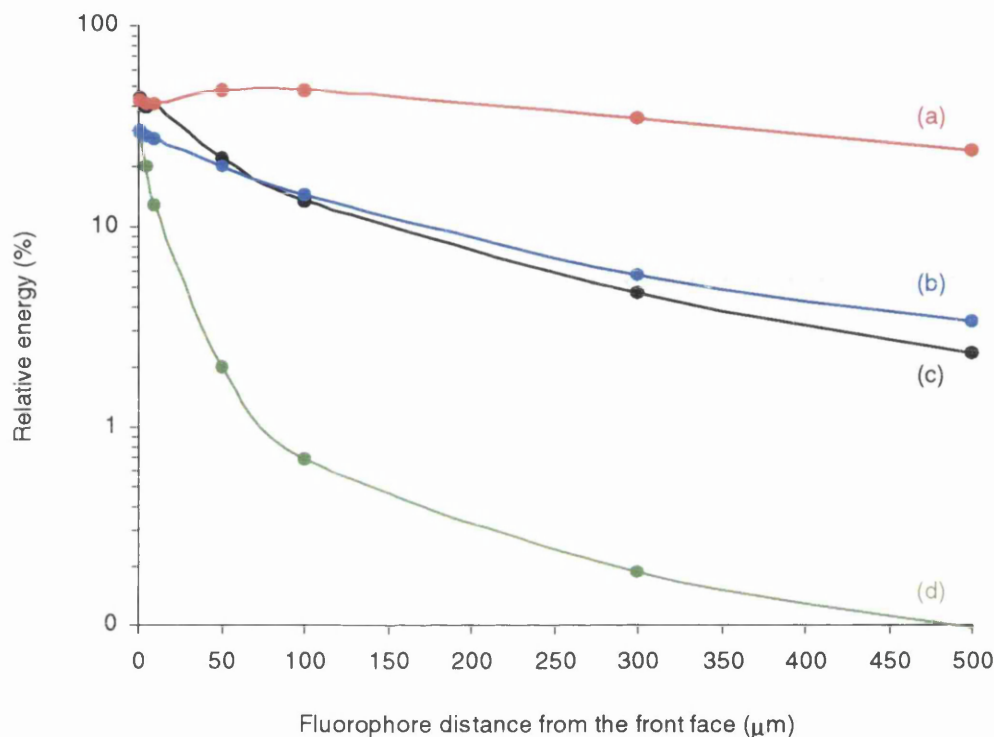


Figure 3-15. Axial distribution of the excitation intensity within two types of microchannel chips immersed in water, as results from the waveguiding of excitation light focused on the front surface of the chip through an objective lens of given NA. (a) MCG, NA 0.13; (b) MCS, NA 0.13; (c) MCG, NA 0.75; (d) MCS, NA 0.75. The energy is expressed as a percentage of the energy impinging onto the front face.

Figure 3-15 shows that, as expected, the use of a lower NA lens resulted in a higher axial uniformity of illumination intensity over the thickness of the chip, whether MCG or MCS, due to enhanced reflection and reduced refraction along the microchannel sidewalls. Figure 3-15 also shows a significant difference in the axial distribution of excitation intensity between MCG chips and MCS chips. At short axial distances, the excitation intensity was higher in the case of the MCG chip, due to the fact that a lower fraction of the excitation radiation was reflected upon impinging onto the interstitial surface, because of the lower reflectivity of the glass surface as compared to that of the silicon surface. At larger distances from the front surface, the difference in excitation intensity observed between MCG chips and MCS chips could be explained by the difference in light propagation mechanisms specific to each type of chips, as stated in the discussion of the waveguiding of the fluorescence emission. In the case of the MCG chip

illuminated through a NA of 0.13, the feature at 50-100 μm was due to indirect illumination through cross-talk from neighbouring channels.

3. 3. 2. 3. 4. Efficiency of fluorescence detection

The results of the convolution of the fluorescence excitation process with the fluorescence collection process is shown in Figure 3-16.

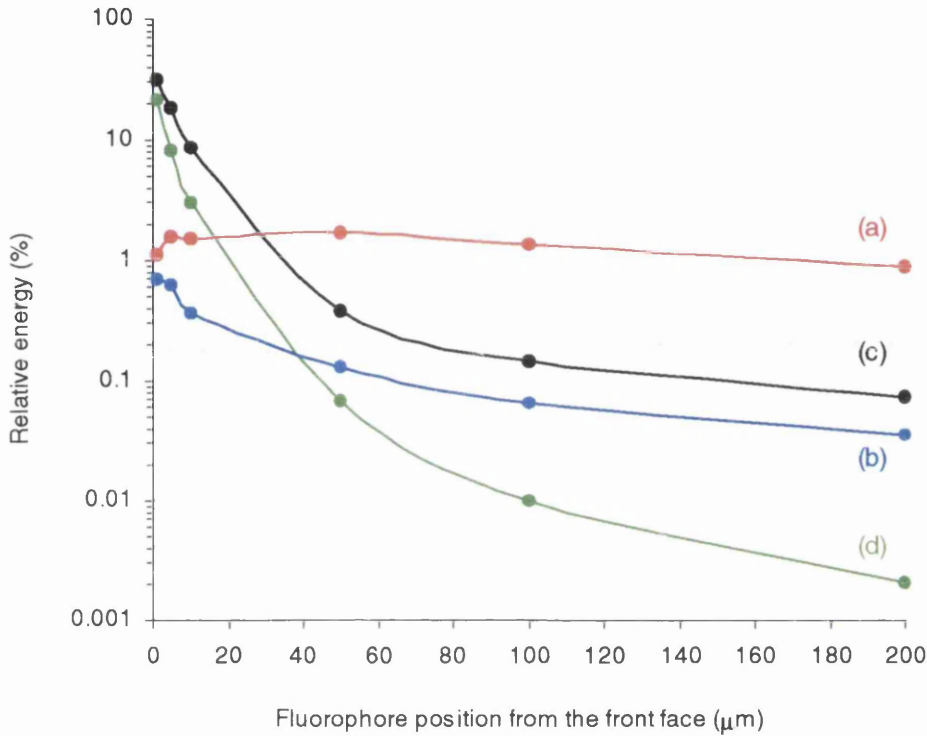


Figure 3-16. Efficiency of detection of a sidewall-bound fluorophore through epifluorescence imaging of the front face of a microchannel chip with an objective lens of given numerical aperture, as a function of the axial position of the fluorophore with respect to the front face of the chip. (a) MCG, NA 0.13; (b) MCS, NA 0.13; (c) MCG, NA 0.75; (d) MCS, NA 0.75. The detection efficiency is expressed as the fraction of emitted fluorescence energy that is collected by the lens and transmitted to the photodetector.

Figure 3-16 illustrates the axial dependence of the efficiency of detection of a sidewall-bound fluorophore. In the case of a MCG chip imaged with an objective lens of NA 0.13, the simulation indicated that the detection efficiency was remarkably uniform over a chip thickness of 200 μm , with between 1% and 2% of the emitted energy being collected by the objective lens and transmitted to the photodetector. In the case of a MCS chip, imaged with the same lens, the detection efficiency was found to be lower and to decrease more sharply with increasing axial distance. For both types of chips, the use of a higher NA objective lens provided a higher detection efficiency for fluorophores located at short axial distances; however, the detection efficiency dropped by more than two orders of magnitude over 200 μm .

3. 3. 2. 3. 5. Conclusions

The simulations reported above have provided useful insight into the optical properties of microchannel structures. MCG appears to be well suited to microchannel chip-based fluorescence bioassays, as the transparency of the glass matrix permits efficient excitation of fluorophores located along the channel sidewalls, and each microchannel acts as a light guide that focuses fluorescence radiation along the axial direction, with limited inter-channel cross-talk. As far as MCS is concerned, the suitability of this material to fluorescence bioassays is limited, in terms of optical properties, by the opacity of silicon in the visible part of the electromagnetic spectrum, which limits the extent to which fluorophores can be excited. The simulations have also pointed at the benefits provided by the use of low NA optics. A number of factors, including scattering of light by the microchannel matrix, could not be simulated accurately; therefore, the simulations were complemented by experimental investigations, which are presented below.

3. 3. 3. Experimental characterisation of the optical properties of microchannel biochip substrates

3. 3. 3. 1. Introduction

The work reported here aimed at corroborating and complementing the simulations described above, and at further evaluating the suitability of an epifluorescence approach to the detection of fluorophores from microchannel chips. Note that the experiments were designed so that derivatisation of the microchannel substrates under investigation (as a first step towards immobilisation of fluorophores onto the microchannel sidewalls) was not required.

From a bioanalytical point of view, the use of microchannel substrates of increased thickness provides a way of increasing the number of probe molecules immobilised within each spot without increasing the lateral dimensions of the spots, thereby potentially improving the analytical performance of the chip in the context of fluorescence-based bioassays. However, the simulations reported above have clearly indicated the limitations of the approach, by pointing at the technical difficulty of detecting fluorophores from increasingly thick microchannel chips. Therefore, a range of chip thicknesses were considered in the experiments reported here, as a first step in the optimisation of the substrate morphology.

3. 3. 3. 2. Experimental

3. 3. 3. 2. 1. Materials

Cylindrical boules of MCG from Galileo Electro-Optics Corp. and Collimated Holes Inc., with channel diameters of 10 μm , 25 μm and 50 μm , were wafered, as described in Section 2. 2. 1. 2, to produce 0.5 mm, 1 mm and 2 mm thick chips. Care was taken to ensure that the

chips were diced so that the front and back planes were perpendicular to the sidewalls of the microchannels. The surfaces of the chips were not polished after dicing. MCS chips, with 750 μm , 320 μm , 150 μm , 70 μm and 25 μm diameter channels, were produced by ASE dry etching of a 380 μm thick silicon wafer (Compart Tech Corp.), as described in Section 2. 4. 2. A PDMS chip with 200 μm diameter channels, similar to that shown in Figure 2-15, was also used.

2D fluorescent spots were produced by covalently immobilising a fluorescent dye, tetramethylrhodamine-5-maleimide (mal-TAMRA; Molecular Probes, Eugene, OR), on the surface of planar glass substrates. This was achieved by depositing aliquots of 10 μM mal-TAMRA solution onto standard float glass microscope slides (BDH, Poole, UK) that were previously silanised with mercaptopropyltrimethoxysilane, MPTS (Sigma). The dye spots were allowed to dry, during which process the maleimide moieties reacted with the surface thiol groups to form covalent thioether bonds. The spots were then washed with ample RO water and blow-dried with N_2 . 2 nL and 1 μL aliquots of mal-TAMRA solution were dispensed, using a piezoelectric arrayer (see Chapter 5) and a manual micropipette, to form circa 260 μm and 1.5 mm diameter spots, respectively. Silanisation of the glass slides was carried out as follows. The slides were first cleaned by sequential treatment with isopropanol, acetone, methanol, and RO water, rinsed with RO water, and further treated by immersion in 1 M nitric acid, water, and ethanol, 10 min each. The chips were then blow dried and baked at 80°C for 4 hours. Silanisation was performed by incubation of the substrates in a 2.5% solution of MPTS in toluene (Sigma, HPLC grade), at room temperature, for one hour. The slides were then washed by sequential ultrasonication in toluene, 1:1 toluene: absolute ethanol, and ethanol, 2 min each. Finally, the chips were baked at 80°C for 4 hours to promote condensation of the silane film.

3. 3. 3. 2. 2. Instrumentation

Fluorescence imaging was carried out using a Microphot microscope (Nikon, Tokyo, Japan) fitted with an epifluorescence attachment and a 100 W mercury lamp, coupled to a water-cooled, monochrome, 16-bit CCD camera (SpectraVideo SV10K, PixelVision, Tigard, OR, USA). A picture of the setup is shown in Figure 3-17.

The fluorescence filter set used was DM580-G2A (Nikon), comprising a 510-560 nm bandpass excitation filter, a 580 nm dichroic mirror and a 590 nm long pass emission filter. The SV10K camera is built around a SITe SIA003AB back-thinned illuminated CCD, whose spectral responsivity curve, shown in Figure 3-3, indicated the suitability of this camera to long-wavelength fluorescence imaging. A KG5 IR blocking filter (Omega Optical, Brattleboro, VT, USA) was placed in front of the CCD to reduce background in the infrared, to which the CCD is sensitive (Figure 3-3). The objective lens used was a 4x Plan DL (Nikon), with a NA of 0.13.

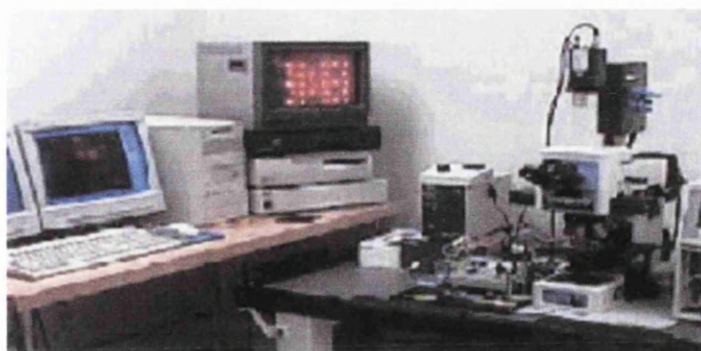


Figure 3-17. Photograph of the combination of a Nikon Microphot epifluorescence microscope and a PixelVision SV10K cooled CCD camera used for the imaging of microchannel biochips.

3. 3. 3. 2. 3. Procedure

The optical properties of microchannel chips relevant to the fluorescence imaging process, namely transparency, waveguiding and inter-channel cross-talk, were investigated by means of the epifluorescence imaging procedure schematically presented in Figure 3-18.

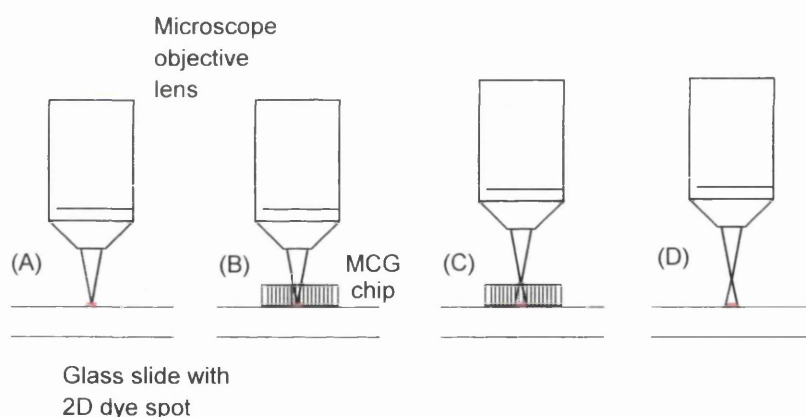


Figure 3-18. Epifluorescence imaging procedure for the investigation of the optical properties of microchannel glass chips, with a two-dimensional, circa $260\ \mu\text{m}$ diameter fluorescent TAMRA spot immobilised on the surface of a silanised planar glass substrate. (A) In-focus imaging of the 2D spot; (B) imaging of the 2D spot through the chip; (C) imaging of the front surface of the chip, with the 2D spot underneath; (D) imaging of the 2D spot with a level of defocusing equal to the chip thickness. The dimensions of the 2D spot and the microchannels have been exaggerated for clarity.

In this procedure, the microchannel chips of various characteristics were used in combination with a 2D fluorescent spot of mal-TAMRA. The MCG and PDMS chips were used with the smaller (circa $260\ \mu\text{m}$) spot, which covered an area that would encompass 370 individual $10\ \mu\text{m}$ diameter microchannels on a 0.6 open fraction MCG chip. The larger ($1.5\ \text{mm}$ diameter) 2D spot was used in combination with the MCS chips.

The CCD camera was operated at 256K (by allowing iced water to flow through the built-in thermoelectric cooling element), 2x2 pixel binning, and 2 s integration time. These settings were determined from preliminary measurements so as to take full advantage of the inherent sensitivity and dynamic range of the CCD camera. All the fluorescence images were acquired in a 2-point correction mode, which ensured flattening of the optical field while providing a dark offset for each pixel. The images were saved as 16-bit TIFF files and processed using IPLab software (Scanalytics, Inc., Fairfax, VA).

The procedure depicted in Figure 3-18 was carried out manually, for each chip, during the data acquisition process, as follows. First, a focused image of the reference spot was acquired (Image A). The chip of interest was subsequently placed on top of the reference spot, in the optical path of the lens, and an image of the reference spot was acquired (Image B). The sample was then moved away from the lens by a distance equal to the chip thickness, so that the front surface of the chip was now in the focal plane, and Image C was acquired. Finally, the chip was removed and an image of the reference spot was acquired (Image D), with a negative amount of defocusing equal to the chip thickness. Quantitative data were obtained by determining the signal, S , as the area under the peak in the radial intensity profile, after 2-point baselining of the curve.

3. 3. 3. 3. Results and discussion

3. 3. 3. 3. 1. Imaging properties of microscope objective lenses in three dimensions

By design, the ability of a microscope objective lens to produce a sufficiently sharp image is restricted to a short distance on each side of the focal plane, in the object space, referred to as the depth-of-field (DOF) of the lens. In a non-confocal epifluorescence imaging scheme, images formed on the detector include contributions from fluorophores and scattering sites located within a whole range of optical planes. The weight of the contribution from each optical plane is determined by the imaging properties of the lens in that plane. If the object is thicker than, or lies out of, the depth-of-field of the lens, significant blurring of the image occurs. Figure 3-19 illustrates how the imaging properties of a microscope objective lens are affected by the position of the object (in this case, a 2D fluorescent spot) relative to the focal plane.

As seen in Figure 3-19, out-of-focus images of the spot were characterised by a spatial spreading which made the spot appear wider than its actual physical dimension. As the level of defocusing increased, the edges of the spot became blurred, resulting in the overall diameter of the spot image to increase. The overall intensity of the spot image also decreased. The increase in the dimensions of the spot image with increasing amounts of defocus is shown in Figure 3-20.

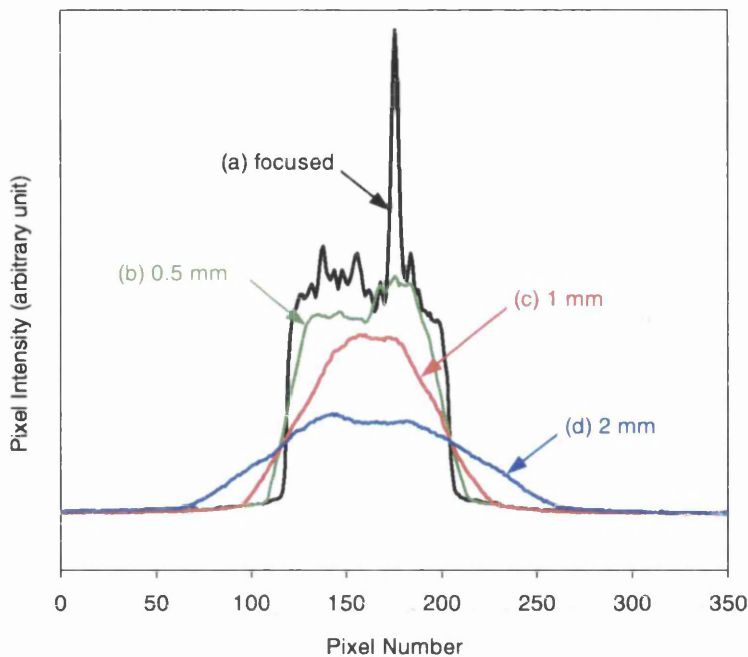


Figure 3-19. Radial intensity profiles associated with the epifluorescence images of a two-dimensional fluorescent spot imaged with a 4x, 0.13 NA microscope objective lens at different levels of defocusing: (a) focused image; (b) 0.5 mm defocusing; (c) 1 mm defocusing; (d) 2 mm defocusing. Each curve was obtained by averaging 4 adjacent pixel rows.

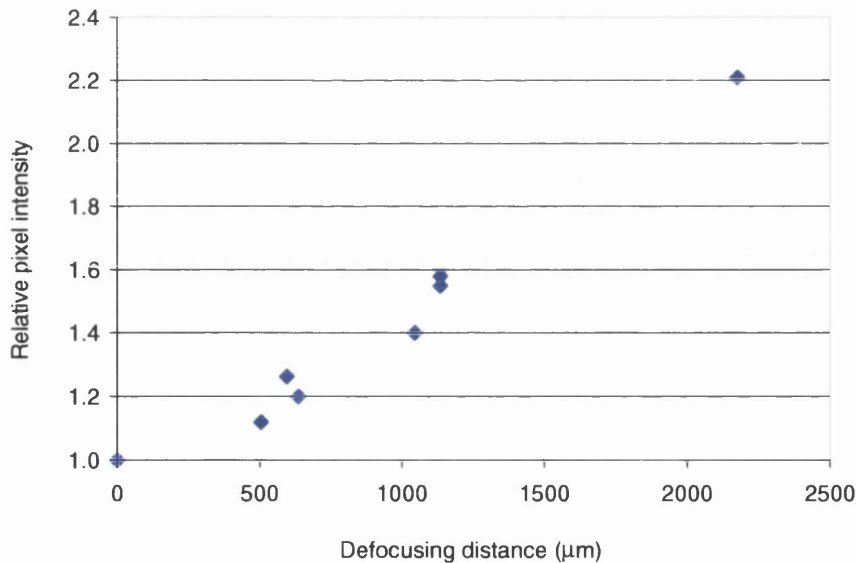


Figure 3-20. Width of the out-of-focus image of a two-dimensional reference fluorescent TAMRA spot on planar glass, relative to that of the in-focus image, as a function of the level of defocusing. A 4x, 0.13 NA microscope objective lens was used.

Out-of-focus images of a reference spot were also characterised by a lower intensity than the in-focus image, as illustrated by Figure 3-21 which shows a plot of the out-of-focus to focused intensity ratios of the spot image as a function of the amount of defocusing.

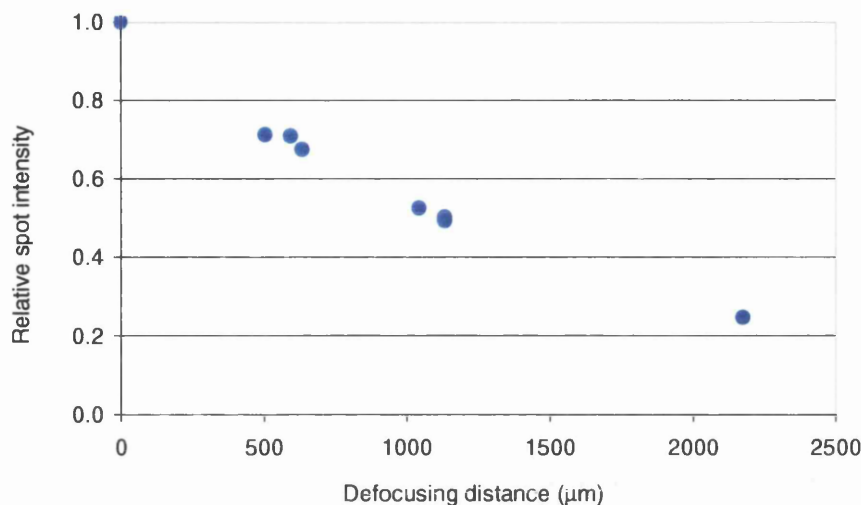


Figure 3-21. Fluorescence intensity of the out-of-focus image of a two-dimensional reference fluorescent TAMRA spot, relative to that of the in-focus image, as a function of the level of defocusing. A 4x, 0.13 NA microscope objective lens was used.

In the case of the 4x, 0.13 NA lens used in the experiment of Figure 3-18, both the increase in diameter and the decrease in intensity were seen to be roughly linear with the level of defocusing. At a defocusing distance of 0.5 mm, the diameter and brightness of the spot image were determined as 1.15 and 0.75 times that of the focused image, respectively.

Figures 3-12 to 3-14 illustrate the concept of depth-of-field (DOF). In an imaging system, the DOF refers to the distance in the object space over which the system delivers an “acceptably sharp image”. An expression for the DOF of an epifluorescence microscope was given by Piller:¹⁴⁶

$$DOF(\mu m) = \frac{1000}{7 \times NA \times M} + \frac{\lambda(nm)}{2000NA^2} \quad (\text{Equation 3-14})$$

where NA is the numerical aperture of the objective lens,
 M is the total magnification of the system,
and λ is the wavelength of illumination, in nm.

Equation 3-14 indicates that the depth-of-field of an epifluorescence imaging system increases with decreasing NA , decreasing magnification, and increasing wavelength. As the criterion for what constitutes an “acceptably sharp image” is somewhat subjective, and might vary widely depending on the application (the criterion used in the derivation of Equation 3-14 is not specified in Piller’s publication), Equation 3-14 was not used to infer absolute DOF values.

3.3.3.3.2. Optical properties of MCG and MCS chips

MCG chips

Multiple information could be inferred from the procedure represented in Figure 3-18.

Comparison of images A and B indicated how the imaging properties of the lens were altered by the presence of the chip in the optical path; this characterised the level of transparency of the chip. Comparison of images A and C reflected the waveguiding efficiency of the chip, combined with the imaging properties of the lens for a defocusing distance equal to the chip thickness, whilst comparison of images C and D gave direct insight into the waveguiding properties of the chip. Figure 3-22, (a) to (d) show images A to D, as described in Figure 3-18, for a 0.5 mm thick, 10 μm channel diameter Galileo MCG chip.

In all the images of Figure 3-22, the 2D spot was clearly seen, with various levels of sharpness. Variations in the levels of signal and background with chip thickness were also evidenced. The fact that the 2D spot was not uniform, as seen in Figure 3-22(a) and discussed later, provided a means to check that the extent of radiation “scrambling” through the MCG chip was limited. In particular, the bright dot present within the spot, seen in Figure 3-22(a), was visible in Figure 3-22, (b)-(d).

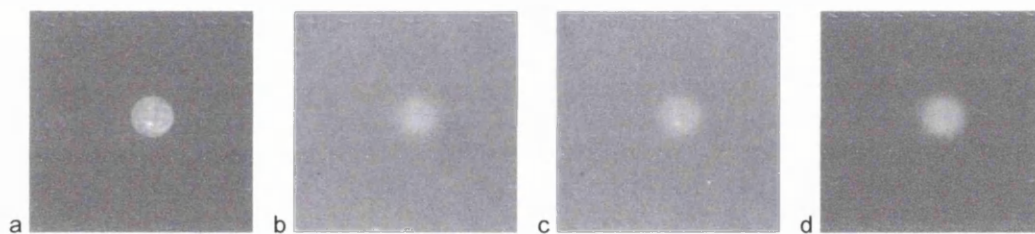


Figure 3-22. (a)-(d) Epifluorescence images A to D associated with the procedure described in Figure 3-18, for a 0.5 mm-thick microchannel glass chip. The 2D fluorescent spot was circa 260 μm in diameter.

Figure 3-23(a) shows an image equivalent to that of Figure 3-22(c), but for a MCG chip of larger channel diameter.

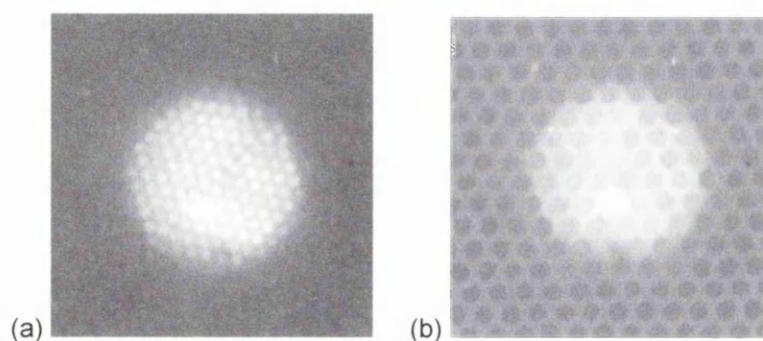


Figure 3-23. Image C, as defined in Figure 3-18, for MCG chips from different manufacturers:

(a) Galileo, 1 mm thick, 25 μm channel diameter and (b) Collimated Holes, 1 mm thick, 50 μm diameter.

In Figure 3-23, individual microchannels could be distinguished. In Figure 3-23(a), the microchannel openings appeared brighter than the interstitial surface, in agreement with the simulation results of Figure 3-9(a). However, Figure 3-23(b) showed the opposite pattern, with the channel openings being darker than the glass matrix. This confirmed the differences in waveguiding properties between the MGC materials from the two manufacturers, as was suggested in Figure 2. 2.

Figure 3-24 shows the radial intensity profiles of the images shown in Figure 3-22. Each curve was obtained by averaging the four median columns of pixels in each spot image.

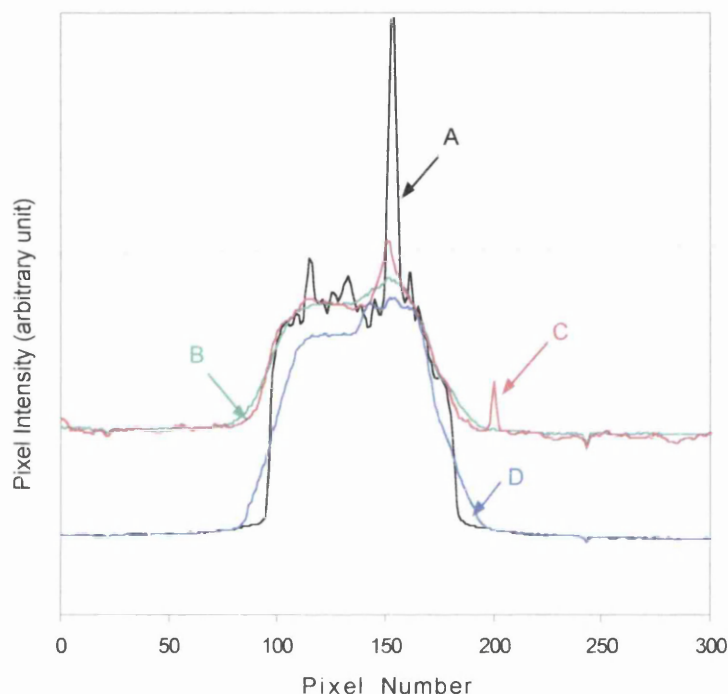


Figure 3-24. Radial intensity profiles associated with the images of Figure 3-22. Each curve was obtained by averaging 4 adjacent pixel rows.

Figure 3-24 illustrates the relative levels of signal and background associated with images A-D. Curve A is representative of the focused image of the 2D spot, and shows the non-uniformity of the latter. Curve D is associated with the image of the 2D spot at an amount of negative defocusing equal to the chip thickness, and shows the associated blurring of the spot, as discussed above. Curve B is representative of the image of the 2D spot as seen through the chip, and shows an attenuation in the net fluorescence signal and an increase in the level of background, both caused by the MGC structure. Finally, curve C is associated with the image of the 2D spot with the focus adjusted on the front surface of the chip. As compared to curve B, curve C was characterised by similar levels of signal and background, which demonstrated the compatibility between the chip thickness and the imaging properties of the lens.

Figure 3-25 shows the effect of the chip thickness on the characteristic ratios $S(C)/S(A)$, $S(C)/S(D)$ and $S(B)/S(A)$, where S is the net fluorescence signal and A-D were as defined in Figure 3-18, for 10 μm channel diameter MCG chips.

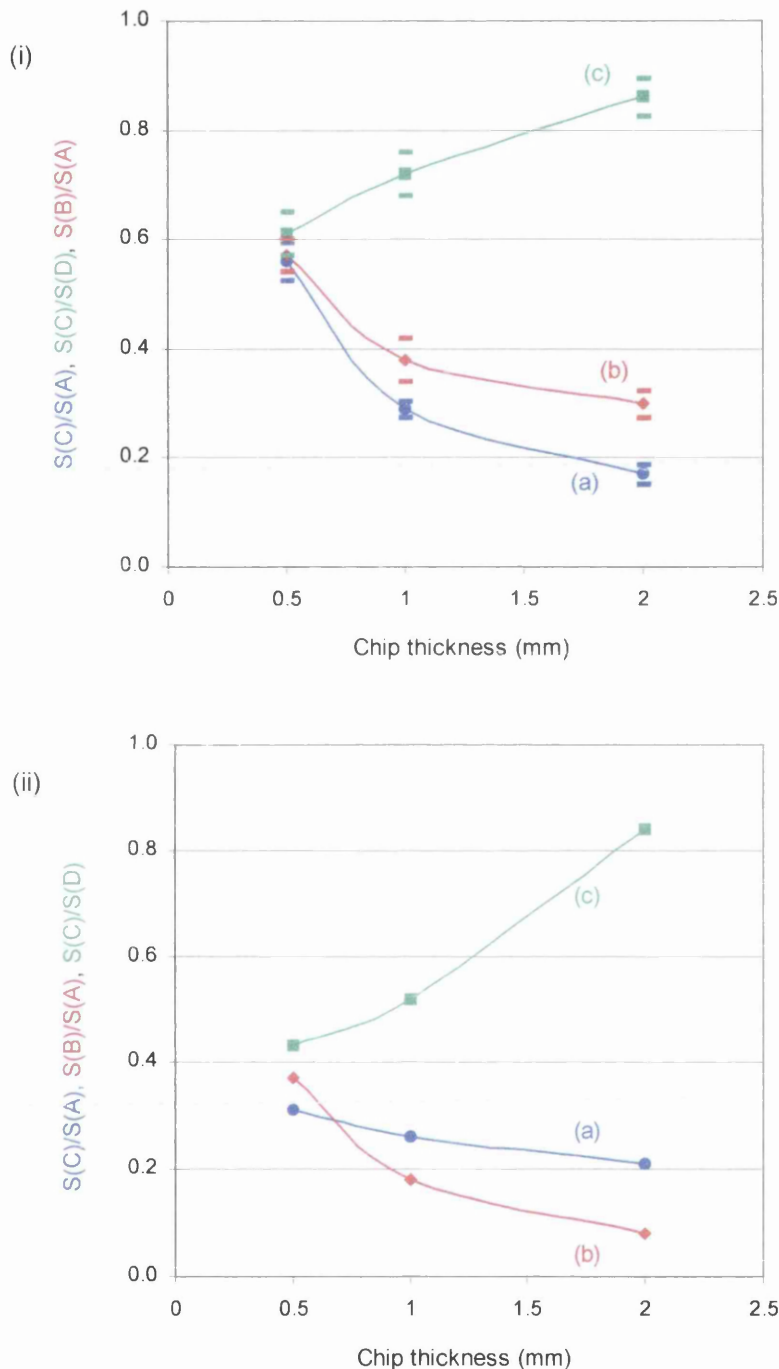


Figure 3-25. Characteristic ratios $S(C)/S(A)$ (a), $S(B)/S(A)$ (b), and $S(C)/S(D)$ (c) for 10 μm channel diameter MCG chips from (i) Galileo Corp. and (ii) Collimated Holes Inc, as a function of the chip thickness. The bars represent averages and 95% confidence intervals for 3 independent measurements. See text for details.

As expected, the fraction of net fluorescence signal collected by adjusting the focus on the front surface of the chip, characterised by the ratio $S(C)/S(A)$, decreased as the chip thickness increases. This resulted from a combination of two factors: attenuation of the fluorescence signal caused by the presence of the substrate in the optical path, and loss in the excitation and collection efficiencies of the lens induced by the defocusing. The contribution from the latter factor was evidenced by comparison with $S(B)/S(A)$, in which no defocusing was involved. Importantly, $S(C)/S(A)$ and $S(B)/S(A)$ were not statistically different in the case of a 0.5 mm thick MCG chip, suggesting that no significant attenuation of the signal resulted from defocusing itself. Signal attenuation by the substrate was due, for the major part, to reflection (both specular and diffuse) and scattering of light on the front surface of the chip, and thus was not proportional to the chip thickness. The ratio $S(C)/S(D)$ characterised the waveguiding efficiency of the chip, since it represents the relative intensity of fluorescence that is detected through the chip with the focus on the front surface of the chip, as compared to that detected directly. For the range of chip thicknesses studied here, $S(C)/S(D)$ was less than unity, which indicated that the signal originating from the 2D spot was actually attenuated by the presence of the chip in the optical path. However, as the chip thickness increased, the waveguiding ability of the chip progressively compensated for the defocusing-induced loss of detection efficiency of the objective lens.

MCS and PDMS chips

The procedure schematically described in Figure 3-18 was carried out with the dry etched MCS chips, using the 4x, 0.13 NA objective lens as above. Figure 3-26 shows a plot of the ratio $S(C)/S(D)$ as a function of the diameter of the microchannels, where $S(C)$ was determined as the total pixel intensity over an area covering a single channel opening and $S(D)$ was determined over the same area of the 2D spot.

In the case of the MCS chips, Figure 3-26(a) shows a decrease in $S(C)/S(D)$ with decreasing channel diameter, indicating that the efficiency of fluorescence detection within the MCS chip decreased with increasing aspect ratio of the microchannels. The rate of decrease was higher for small ($< 200 \mu\text{m}$ diameter) channels, illustrating the fact that these small channels with opaque walls act as aperture stops with respect to the excitation light delivered by the objective lens, resulting in a reduced illumination of the fluorescence spot. In the case of a 0.5 mm thick MCG chip, $S(C)/S(D)$ was determined as circa 0.6 for $10 \mu\text{m}$ diameter microchannels, as seen in Figure 3-25(a). Figure 3-26 suggests a one order of magnitude lower value for an equivalent MCS chip. This is in satisfactory agreement with the simulation results shown in Figure 3-16.

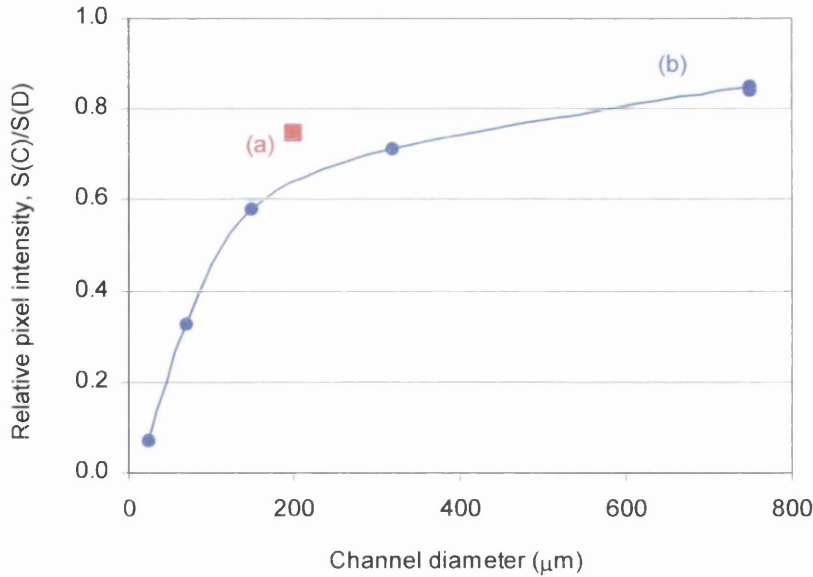


Figure 3-26. Relative intensity $S(C)/S(D)$ (as defined in Figure 3-18), for (a) a 200 μm channel diameter, 350 μm thick PDMS chip, and (b) 0.5 mm thick MCS chips, as a function of the channel diameter. $S(C)$ was determined as the total pixel intensity over an area covering a single channel opening and $S(D)$ was determined over the same area of the two-dimensional spot.

$S(C)/S(D)$ was determined as circa 0.75 in the case of the 200 μm channel diameter, 350 μm thick PDMS chip, as shown in Figure 3-26(b). This value is higher than that for a MCS chip with the same channel diameter, as expected from the high transparency of the PDMS matrix.

3. 3. 3. 3. Conclusions

The experiments reported above have corroborated the main results obtained from the simulation work, namely the remarkable waveguiding properties of MCG (including the low levels of apparent cross-talk) and the large attenuation of fluorescence signals that characterise the use of MCS.

In addition, the experiments have pointed at two important effects: the generation of significant background signals upon illumination of MCG substrates, ascribed to autofluorescence of, and scattering of light by, the glass matrix; and the importance of the depth-of-field of objective lenses on their behaviour in three-dimensional imaging. The extent to which these factors affect the performance of epifluorescence imaging schemes in the context of microchannel chip-based fluorescence bioassays is reported in the next section.

3. 3. 4. Quantitative detection of fluorophores from microchannel biochip substrates

3. 3. 4. 1. Introduction

The experiments reported in this section were concerned with the assessment of the detectability of fluorophores present on the sidewalls of MCG and MCS substrates. As stated in Section 1. 1. 2. 4. 2, the ability to detect low amounts of fluorophores, in a quantitative fashion, is a prerequisite to the use of microchannel structures as biochip substrates in gene expression measurements. An epifluorescence imaging procedure, designed according to the knowledge gained from the results of Sections 3. 3. 2 and 3. 3. 3, was tested and optimised using microchannel chips spotted with low amounts of a fluorescent dye. The fluorophore molecules were merely adsorbed on the sidewalls of the microchannels, as a model for fluorescently-labelled target nucleic acid hybridised to sidewall-bound probes.

3. 3. 4. 2. Experimental

3. 3. 4. 2. 1. Materials

0.5 mm thick, 10 μm channel diameter MCG chips (Galileo Electro-Optics Corp.) and MCS chips (Siemens) were spotted with 10 nL aliquots of solutions of the fluorescent dye Cy5 (Amersham Pharmacia Biotech), dissolved to various concentrations (from 50 nM to 1 pM) in RO water. Spotting was carried out with a piezoelectric arrayer, as later described in Chapter 5. Each Cy5 concentration was spotted as 16 replicates, in the form of a 4x4 array, with a center-to-center spot spacing (*pitch*) of 400 μm . 16 different Cy5 concentrations were spotted on each microchannel chip (resulting in a total of 256 spots being present on each 12 x 12 mm² chip). In addition, 0.2 μL aliquots of a 10 μM mal-TAMRA solution were dispensed in three corners of each chip, to produce “reference” spots. Spotted chips were allowed to dry in a dessicator.

3. 3. 4. 2. 2. Instrumentation

The epifluorescence microscopy instrumentation was as described in Section 3. 3. 3. 2. 2, with a Cy5 filter set (HQ-Cy5, Chroma Technology Corp., catalogue # 41008) being used in addition to the Nikon DM580-G2A set. The HQ-Cy5 filter set comprised a 590-650 nm bandpass excitation filter, a 660 nm dichroic mirror and a 660-740 nm bandpass emission filter.

A bespoke epifluorescence microscope platform, schematically represented in Figure 3-27, was also used.

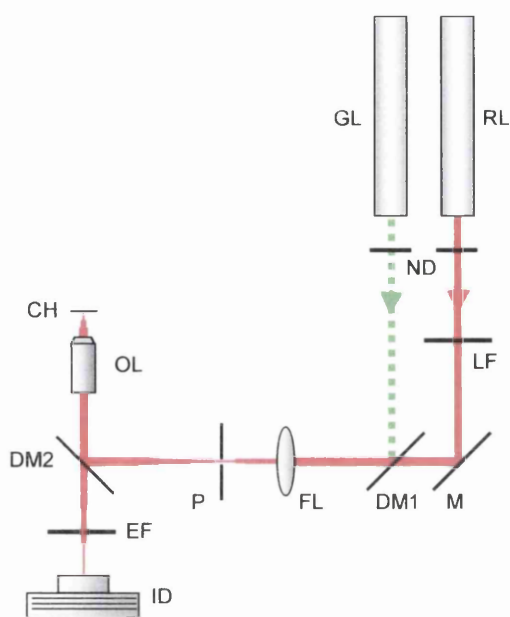


Figure 3-27. Schematic representation of the bespoke epifluorescence microscope platform used for the imaging of microchannel biochips. RL: red He-Ne laser; GL: green He-Ne laser; ND: neutral density filters; LF: laser line filter; M: mirror; DM1 and DM2: dichroic mirrors; FL: focusing lens; P: pinhole; OL: objective lens; CH: chip; EF: emission filter; ID: imaging detector. See text for details.

The microscope platform was set up on high resolution mechanical stages for precise positioning of the optical elements and the microchannel chip to be imaged. The latter was held in a custom-designed metallic holder set up on a 3 translation, 1 rotation micropositioner (Elliot Scientific Ltd, Herts, UK). Dual-wavelength excitation was provided by a green (543 nm) and a red (633 nm) He-Ne lasers (Coherent, Santa Clara, CA, USA). LF was a 633 ± 3 nm filter (Omega Optical XF46). FL was a Newport PAC086 achromat lens, with a f-number of 3.0 and a focal length of 15 cm. DM1 was a DM580 (Nikon) dichroic mirror. DM2 was a Cy3/Cy5 dual dichroic mirror (Omega Optical XF2053). EF was either an Omega Optical XF3019 (580-630 nm bandpass) filter (EF1), or the emission filter from the Chroma HQ-Cy5 filter set (EF2). The 4x objective lens and CCD camera mentioned above were used with the bespoke platform, after being dismantled from the Nikon microscope.

3. 3. 4. 3. Procedures

3. 3. 4. 3. 1. Image acquisition

The microchannel chip to be imaged was secured in the custom holder placed on the micropositioner. The TAMRA spots were used for lateral and axial (focus) alignment of the chip within the field of view of the objective lens. To that end, imaging of the TAMRA spots was achieved by illuminating the chip with the green laser (the red laser was shut off) whilst the emission filter EF1 was placed in front of the CCD. As the TAMRA spots were produced from a solution of relatively high concentration, these spots were very bright and thus could be imaged

by the CCD camera using short integration times (< 100 ms), which facilitated the positioning of the chip within the field of view of the objective lens, including adjustment of the focus.

Once the chip was correctly aligned, the 4x4 arrays of identical Cy5 spots were sequentially positioned within the field of view (by translating the chip of a distance equal to the separation between adjacent 4x4 arrays, *i.e.* 1 mm), and imaged with the CCD camera. For Cy5 fluorescence imaging, the red He-Ne laser was used while the green laser was shut off, and EF2 was substituted for EF1 as the emission filter. Illumination was blocked between measurements in order to reduce photobleaching and sample heating. The illumination power in the focal plane of the objective lens was adjusted to 1.2, 3.1 or 7.8 mW cm⁻² by placing neutral density filters in the laser beam path. A silicon photodetector (Anritsu ML910B) was used to measure the illumination power. The CCD camera was operated at 256 K. Integration time and level of pixel binning were varied (from 1 s to 10 s and from 1x1 to 3x3, respectively) as described below. The field of view of the imaging system (objective lens and CCD camera) was wide enough to allow the imaging of entire 4x4 arrays of Cy5 spots.

3. 3. 4. 3. 2. Experimental determination of Cy5 photobleaching

The extent to which photobleaching of the Cy5 molecules took place at a level of illumination power equal to 1.2 mW cm⁻² was determined by acquiring a sequence of images of a 4x4 array of fluorescent spots containing 300 amol Cy5 each, with an integration time of 2 s for each image. 15 images were acquired sequentially, so that the final image showed Cy5 spots that had been submitted to a cumulative illumination time of 30 s. The same experiment was repeated, with a new set of spots, using sequential integration times of 10 s.

3. 3. 4. 3. 3. Image processing and data analysis

Data analysis was carried out from the raw images, saved as TIFF files, using IPLab software. The determination of a S/N value for each spot involved the definition of a disc, covering the entire surface of the spot, and a ring, surrounding the disc, outside the spot area. The net fluorescence signal for each spot, S , was determined by subtracting the average pixel intensity of the ring from that of the disc. The background noise associated with each spot, N , was determined as the standard deviation of the intensity of the set of pixels enclosed within the ring. The limit of detectability (LOD) of a spot was defined as the lowest amount of fluorophore contained in the spot for which $S/N \geq 3$.

3. 3. 4. 4. Results and discussion

3. 3. 4. 4. 1. Use of the fluorescent dye, Cy5

Upon allowing spotted microchannel chips to dry, evaporation of the solvent took place, leading to adsorption of the dye molecules on the sidewall of the microchannels. The number of adsorbed dye molecules in each spot was thus directly proportional to the concentration of the

solution used for spotting, so that spots were produced which contained between 0.5 fmol and 10 zmol of dye.

The fluorescent dye used in this investigation was Cy5, an arylsulfonate pentamethyne derivative which is excited to circa 90% of its absorption maximum by the 633 nm line of a red HeNe laser. As a “red” fluorophore, Cy5 provides the advantages associated with long-wavelength fluorescence measurements, as mentioned in Section 3.2.2.3. Cy5 is a fluorophore of choice in bioassays, including nucleic acid hybridisation assays, due to its high photostability (resistance to photobleaching) and the availability of close structural partners within the family of cyanine derivatives (Cy3, Cy5.5).

3.3.4.4.2. Microchannel biochip imaging platform

Epifluorescence microscope

As shown in Sections 3.3.2 and 3.3.3, the imaging of microchannel biochips, in which analyte fluorophores are distributed axially as well as laterally, requires the use of imaging optics of sufficiently large depth-of-field. This precluded the use of both high NA objective lenses and confocal configurations. Accordingly, the epifluorescence microscope platform used here was based on a 4x, 0.13 NA lens whose suitability to the fluorescence imaging of microchannel chips has been shown in Sections 3.3.2.3.4 and 3.3.3.3.1. By the same token, the wide field of view of this lens (circa 4 mm²) provided an opportunity to implement CCD-based detection, as discussed below.

Note that the Nikon Microphot microscope used in Section 3.3.3 could not be used in the detectability experiments reported here due to the absence of a calibrated translation stage. In addition, in the measurements described here, the use of two distinct, non-overlapping optical channels for the reference (TAMRA) spots and the analyte (Cy5) spots greatly reduced the extent of photobleaching undergone by the Cy5 spots in the course of the experiment, as alignment of the chip within the field of view could be carried out under green light illumination.

CCD camera

The main requirements concerning the CCD camera were a high sensitivity and a high dynamic range. These requirements are best fulfilled in the case of cooled, back-illuminated, high quantum efficiency CCD chips. As a high level of resolution is not required in the imaging of microarrays, a CCD with large pixels was preferable, since the full well capacity, and by extension the dynamic range, of a CCD increase with pixel size. With these considerations in mind, the PixelVision SpectraVideo SV10K camera was selected. This camera featured a CCD chip comprising 1024 x 1024 pixels of area 24 x 24 μm², a 16-bit level of digitisation, and a built-in Peltier cooling system, giving a dark current level of 2 ē pixel⁻¹ s⁻¹ at -35°C and a readout noise level of 15-25 ē rms at 500 kHz readout rate (manufacturer's specifications). As the dark current of a CCD decreases by half when the temperature is decreased by 7-8°C, dark current

levels as low as $10 \text{ e}^- \text{ pixel}^{-1} \text{ s}^{-1}$ were obtained by operating the CCD at 256 K, the minimum achievable using the Peltier system. This translated into dark current noise levels of $< 4 \text{ e}^- \text{ rms}$ for an integration time of 1 s.

3.3.4.4.3. Optimisation of the imaging system for the detection of low fluorophore amounts from MCG substrates

Figure 3-28 shows the fluorescence image of a 4x4 array of spots containing 100 amol of Cy5 each. Knowing that the chips were spotted at a pitch of $400 \mu\text{m}$, the diameter of the spots could be estimated as about $200 \mu\text{m}$.

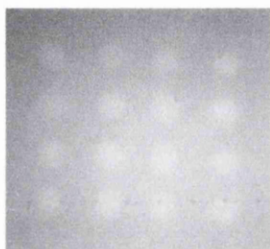


Figure 3-28. Fluorescence microscopy image of a 4x4 array of spots, each spot resulting from the adsorption of 100 attomoles of Cy5 fluorophore at the surface of a 0.5 mm thick, $10 \mu\text{m}$ channel diameter MCG substrate. The image was acquired over an integration time of 10 s, with the CCD camera operated at 256 K and 1x1 pixel binning. The illumination power in the focal plane of the objective lens was 1.2 mW cm^{-2} .

The image shown in Figure 3-28 was not subjected to any digital processing after acquisition. The optical field can be seen to be non perfectly uniform, even though the 4x4 array was placed in the central part of the field of view of the lens (of which it covered about half the area) for imaging. This prompted the use of the "disc and ring" image processing method for the calculation of S/N values, so that N was measured individually for each spot, thereby reducing variability in S/N measurements associated with non-uniform illumination within the field of view.

The detectability of a fluorescent spot is directly related to the S/N of its image. In addition to the optical configuration of the imager (including the illumination power), the conditions in which the CCD is operated significantly affect the detectability, as shown by Equation 3-8. Two regimes can be distinguished, depending on which source of noise (fundamental or non-fundamental) is limiting. In the low light regime (small photon flux, Φ , in Equation 3-8), the photon noise is small, such that the S/N is limited by the readout noise and the dark current noise.

Identification of the limiting sources of background noise

The effect of the integration time upon the S/N provided a way to identify the limiting sources of background noise. The readout noise was expected to be the limiting source of noise at low

light levels. Equation 3-8 suggests that, as long as the readout noise remains the chief contribution to the total noise, increasing the integration time results in a proportional increase in S/N. However, as photon noise increases with integration time, photon noise is expected to become the dominant source of noise beyond a certain integration time, in which case the S/N increases only with the square root of the integration time.

Figure 3-29 shows the effect of the CCD integration time on the measured S/N values associated with fluorescent spots containing 30, 100 and 300 amol Cy5.

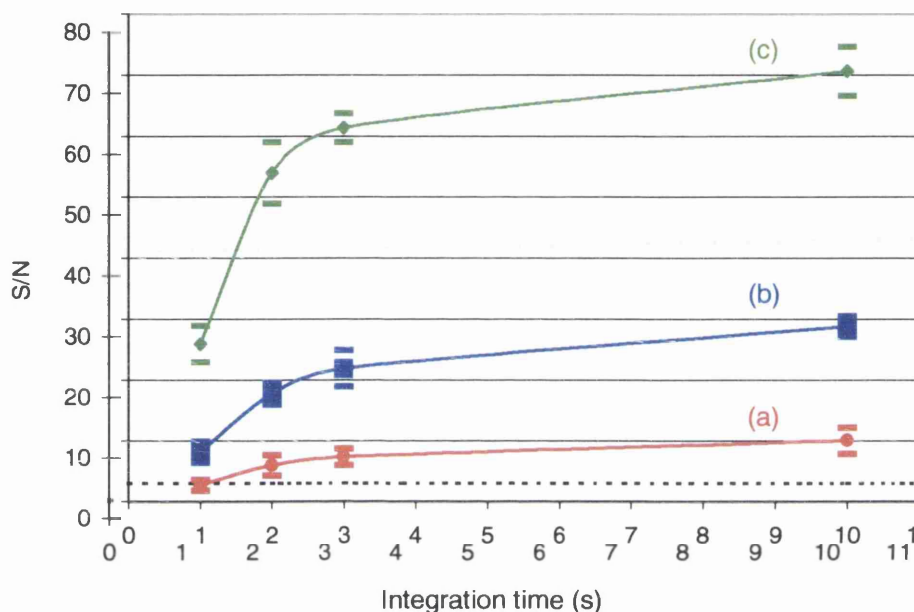


Figure 3-29. S/N values for fluorescent spots (produced by the dispensing of 10 nL aliquots of Cy5 solution onto 0.5 mm thick, 10 μ m channel diameter MCG substrates), as a function of the CCD integration time. The illumination power in the focal plane of the objective lens was 1.2 mW cm⁻². The CCD camera was operated at 256 K and 1x1 pixel binning. Number of Cy5 molecules per spot: (a) 30 amol (10 nL of a 3 nM solution); (b) 100 amol (10 nL of a 10 nM solution); (c) 300 amol (10 nL of a 30 nM solution). The bars represent the 95% confidence intervals determined from the simultaneous imaging of 16 identical spots.

A comparison between the three curves shown in Figure 3-29 shows that, over the range of integration times investigated, higher S/N values were obtained for higher amounts of fluorophore, indicating that the epifluorescence imaging approach provided an at least semi-quantitative determination of the amount of fluorophores present within spots. The detection limit for Cy5 was less than 30 amol (for integration times of at least 2 s).

As the integration time was increased from 1 s to 2 s, a circa 2-fold increase in S/N was observed for each spot, as expected from a readout noise-limited regime. However, as the integration time was further increased to 10 s, the rate of increase of S/N diminished, suggesting an increased contribution of the photon noise (in addition to that of the dark current

noise) to the total background noise. This behaviour indicates that, when integration times longer than 2 s were used, the measurements were carried out in a photon noise-limited regime, in which the detectability of fluorophores was limited by the MCG chip, rather than by the CCD photodetector. This is in agreement with the generation of significant levels of background by the MCG substrate itself, through light scattering, as already suggested in Section 3.3.3.2.

The increase in S/N observed with increased integration times suggests that the limit of detection (LOD) can be improved by using longer integration times, although obvious limitations of this approach are longer assay readout times and increased photobleaching and sample heating, which can be deleterious to the sample and affect the validity of the assay. In addition, the increase in background signal associated with increased integration time would contribute to reducing the dynamic range of the measurements.

Photobleaching

As the validity of the previous discussion, based on the data shown in Figure 3-29, could be affected if significant photobleaching of the fluorescent dye occurred over the course of the experiment (by contributing to the lower rate of increase in S/N between 3 s and 10 s integration time, as compared to that observed between 1 s and 2s), the extent to which photobleaching of the Cy5 molecules took place at the levels of illumination power used (1.2 mW cm^{-2}) was determined, in an independent experiment, as described in Section 3.3.4.3.2. The results are shown in Figure 3-30.

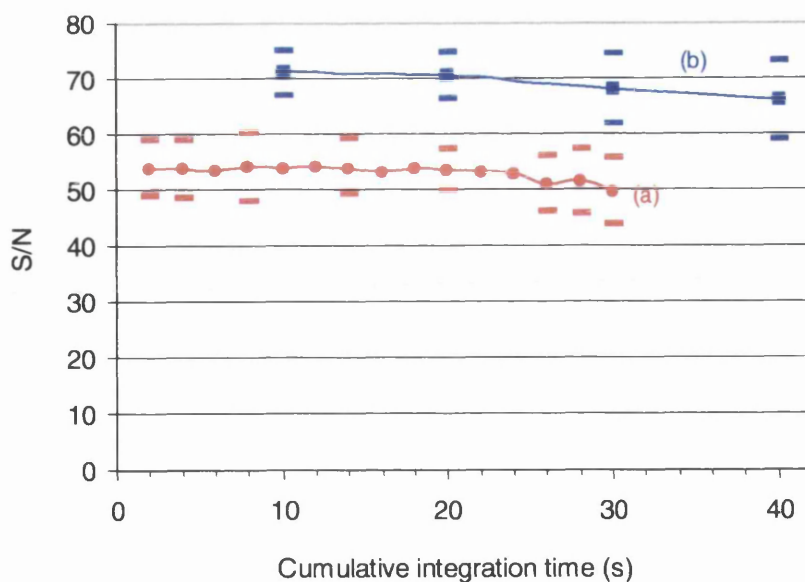


Figure 3-30. Dependence of the S/N values for fluorescent spots (300 amol Cy5 deposited onto 0.5 mm thick, 10 μm channel diameter MCG substrates) on the number of consecutive measurements, under an illumination power of 1.2 mW cm^{-2} . CCD integration time: (a) 2 s; (b) 10 s. The bars represent the 95% confidence intervals determined from the simultaneous imaging of 16 identical spots.

Figure 3-30 shows that no significant photobleaching took place over 20 s, indicating that photobleaching did not affect the validity of the measurements above, in which the maximum cumulative illumination time each spot was submitted to was 16 s.

Calibration curves

Figure 3-31(a) shows the experimentally determined calibration curve for spots comprising between 30 amol and 5 fmol of Cy5, imaged using a 1 s integration time. The dependence of the S/N on the amount of dye was found to be approximately linear over that range, with an associated correlation coefficient greater than 0.990. This remarkable standard of linearity is in agreement with curve (a) of Figure 3-16. The LOD was determined as about 50 amol.

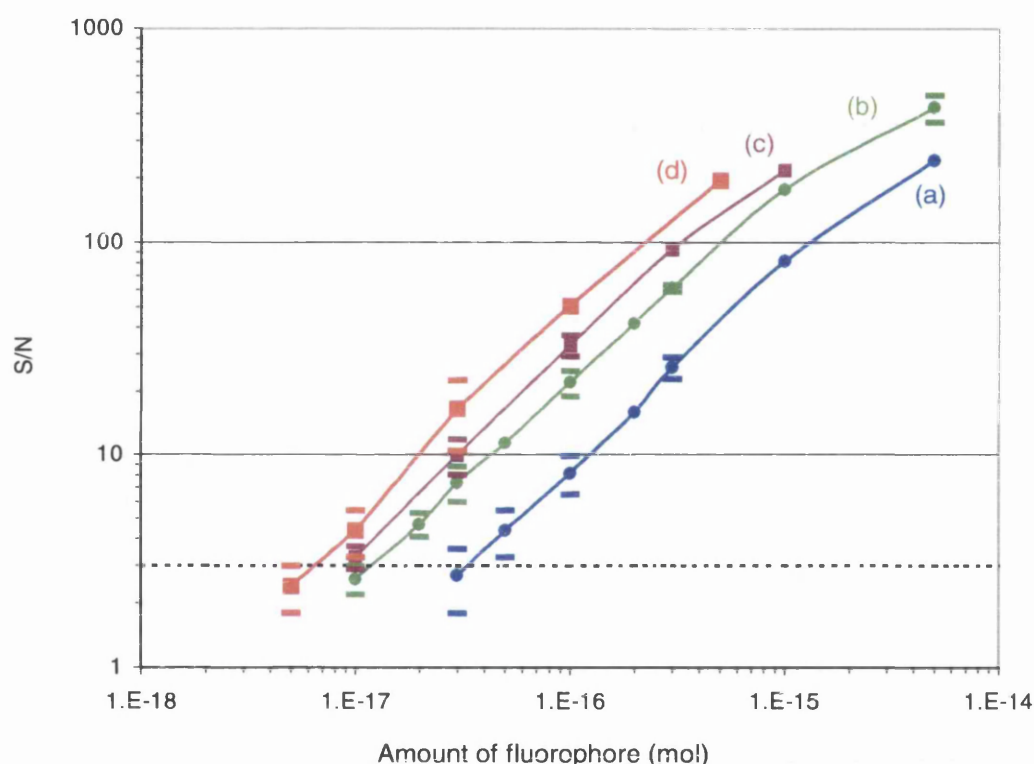


Figure 3-31. S/N values for fluorescent spots (produced by the dispensing of 10 nL aliquots of Cy5 solution onto 0.5 mm thick, 10 μ m channel diameter MCG substrates), as a function of the amount of fluorophore present in each spot. The CCD camera was operated at 256 K, and at integration time and pixel binning of (a) 1 s, 1x1; (b) 3 s, 1x1; (c) 1 s, 3x3; (d) 3 s, 3x3. The illumination power in the focal plane of the objective lens was 1.2 mW cm⁻². The bars represent the 95% confidence intervals determined from the simultaneous imaging of 16 identical spots.

Figure 3-31(b) shows the experimentally determined calibration curve, using a 3 s integration time. The curve was again approximately linear (correlation coefficient 0.998) over a range of Cy5 amounts extending from 10 amol to 1 fmol of Cy5. The increase in S/N provided by the

increase in integration time as compared to Figure 3-31(a) resulted in an improved LOD of about 15 amol.

Increasing the detectability by pixel binning

Figure 3-31(c) shows the experimentally determined calibration curve, using a 1 s integration time and a 3x3 level of pixel binning. The readout noise-limited nature of the measurements is confirmed by the fact that the use of a 3x3 binning level resulted in a circa 9-fold increase in S/N, as expected from the discussion of Section 3.2.3.1. At 3 s integration time, the readout noise was not the dominant source of noise, as shown by the fact that pixel binning only resulted in a moderate increase in signal to noise (curve (d) in Figure 3-31).

Increasing the detectability by increasing the illumination power

As indicated by Equation 3-3, increasing the radiant power of illumination (B_λ in Equation 3-4) is expected to result in an increase in the spectral radiance of fluorescence, $B_{\lambda F}$, and thus in the analyte fluorescence signal, E_L (Equation 3-2). However, background signals stemming from scattering and autofluorescence from the MCG substrate are also expected to increase under increased illumination. Figure 3-32 shows the effect of an increase in illumination power on the S/N of 10 amol Cy5 spots imaged at 1 s integration time and 3x3 pixel binning.

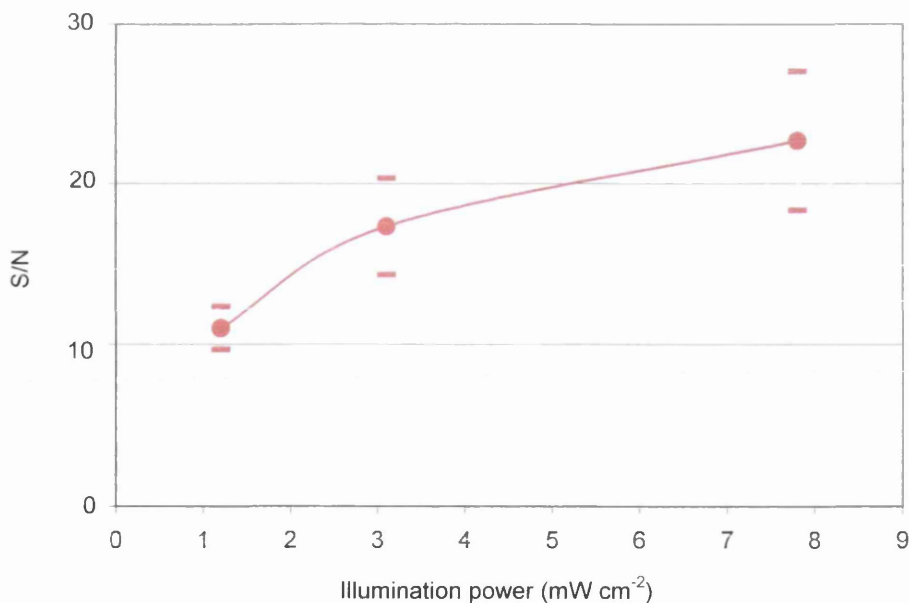


Figure 3-32. S/N values for fluorescent spots (produced by the dispensing of 10 nL aliquots of Cy5 solution onto 0.5 mm thick, 10 μ m channel diameter MCG substrates) containing 30 amol Cy5, as a function of the illumination power. The CCD camera was operated at 256 K, 3x3 pixel binning and 1 s integration time. The bars represent the 95% confidence intervals determined from the simultaneous imaging of 16 identical spots.

Figure 3-32 shows an increase in the S/N of the spots under increased illumination. This increase is moderate, however, as S/N was multiplied by 2 upon increasing the illumination power by a factor 8. The use of increased levels of illumination power exhibits the same practical limitations associated with photobleaching and sample heating as the use of longer integration times, indicating the existence of a trade-off in the conditions of imaging between enhanced detectability and possible degradation of the biochip and / or the sample during imaging.

The “commercial” instrumentation consisting of the Nikon Microphot microscope fitted with a 100 W Hg lamp provided a maximum illumination power in the object plane of 1.2 mW cm^{-2} , with the excitation filter in place, as determined using the Anritsu silicon photodetector. Coupling the SV10K CCD camera to that instrument provided similar performance to that obtained using the laser-based microscope platform at the same level of illumination power, with a LOD of 12 amol achieved by operating the CCD camera under the optimal conditions of 3 s integration time and 3x3 pixel binning.

3. 3. 4. 4. 4. Conclusions

The detectability of a fluorescent dye, Cy5, adsorbed on the sidewall of MCG has been shown to be in the low attomole range, using commercially available instrumentation, after optimisation of the experimental parameters involved in the epifluorescence imaging scheme.

The LOD is limited by background signals produced by the microchannel substrate, suggesting that the polishing of the front face of MCG chips might enhance the detectability by reducing light scattering. The LOD has been shown to increase upon using longer integration times and higher levels of illumination power; however, there are practical limitations associated with this approach, namely increased photobleaching of the dye and higher instrumental budget.

3. 4. Conclusions

The investigations of the optical properties of MCG and MCS reported in this chapter have evidenced a significant difference between the two materials. MCG was shown to exhibit remarkable optical characteristics that make it particularly appropriate to heterogeneous fluorescence assays. Excitation of microchannel sidewall-bound fluorophores is enhanced by the transparency of the matrix as well as by the generation of an evanescent field along the channel sidewalls, while collection of the emitted fluorescence is facilitated by the confinement and focusing of radiations within the microchannels. This results in the possibility of detecting very low amounts of fluorescent molecules immobilised on the microchannel sidewalls. MCS is less suitable to photoluminescence detection, as the opacity and absorptivity of the matrix are detrimental to photoexcitation of fluorophores. However, MCS substrates might be applicable to chemiluminescence assays, which do not rely on photoexcitation of the reporter molecules (as

further discussed in Chapter 7). A method for the attachment of probe molecules on the sidewalls of MCG and MCS substrates is presented in the next two chapters.

CHAPTER 4. FUNCTIONAL ATTACHMENT OF OLIGONUCLEOTIDE CAPTURE PROBES ONTO SOLID SUBSTRATES

4. 1. Introduction

As stated in Section 1. 1. 2. 2. 3, the derivatisation of solid substrates for DNA chip applications requires a surface chemistry that provides a robust and functional immobilisation of the probe molecules. For short oligonucleotide probes, these requirements are most readily met by covalent end-attachment strategies. A procedure for the functionalisation of glass, silicon and PDMS materials, based on organosilane chemistry, is presented here. The approach relies on the fact that all the microchannel substrates described in Chapter 2 can be treated so as to exhibit a silica-rich surface. In this chapter, the validity of the attachment strategy for heterogenous nucleic acid hybridisation assays is demonstrated; planar substrates were used in the first instance as they lent themselves more readily to processing and surface analysis than microchannel substrates. Functionalisation of the latter is presented in the next chapter.

4. 2. Strategies for the covalent attachment of oligonucleotide capture probes onto silica-rich surfaces using organosilane chemistry

4. 2. 1. Organosilane surface chemistry

Organosilane compounds are widely used for the surface modification of silica-like surfaces. The availability of many derivatives (encompassing a wide range of chemical functionalities), combined with the remarkable self-assembly characteristics of this class of molecules, have made silane compounds the basis of versatile chemical strategies for the tailoring of surface properties such as hydrophilicity and chemical reactivity. Organosilane chemistry has had a significant impact on a number of applications ranging from synthetic chemistry (phase transfer catalysts) and analytical chemistry (gas and liquid chromatography) to biotechnology (biomolecule immobilisation for biosensing applications).

4. 2. 1. 1. Principle

A silane molecule comprises a central Si atom which is bound to between one and three moieties that can readily be substituted by a suitably reactive surface hydroxyl group. Most commonly encountered hydroxyl-substitutable groups are -Cl (chlorosilanes) and -OMe and -OEt (alkoxysilanes). Functional groups available in the organosilane class of compounds include amine, thiol (or mercapto-), epoxy (or glycido-), carboxyl, and olefin moieties. The coupling between the silane molecule and the biomolecule to be immobilised can be direct or indirect, in the latter case a cross-linker is used.

4. 2. 1. 2. Chemical mechanisms for reactions between organosilane compounds and surface hydroxyl groups

Silanisation can be carried out in the liquid phase. Vapour-phase silanisation is also possible, due to the relatively high volatility (high vapour pressure) of organosilane compounds.

4. 2. 1. 2. 1. Liquid-phase silanisation

The halogen and alkoxy groups of silane compounds are extremely reactive towards water. Therefore, the mechanism of bond formation between organosilane compounds and surface hydroxyl groups differs whether the silanisation process is carried out in aqueous solution or in a completely dry organic solvent.

The mechanism of silane deposition in aqueous solution, where significant cross-linking of the silane molecule occurs, is shown in Figure 4-1 (the case of a trimethoxysilane is considered in the illustration).

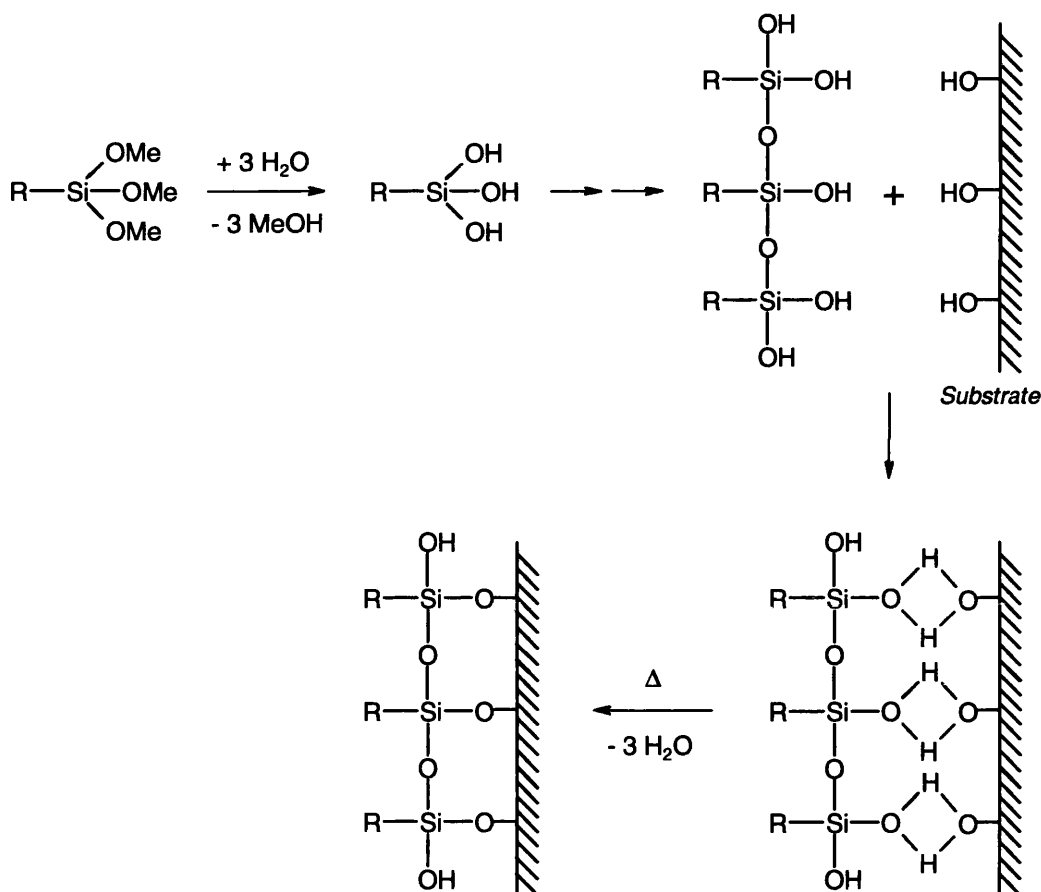


Figure 4-1. Mechanism for the reaction between an organosilane compound (here, a trimethoxysilane is considered) and a silica-like surface, in the presence of water (adapted from Ref. 147). H-bonds are shown in red.

In the presence of water, the silane molecules undergo hydrolysis and condensation before deposition on the surface, resulting in the formation of silanol groups. These silanol groups form physical H-bonds (shown in red in Figure 4-1) with surface silanols as well as with neighbouring hydrolysed silane molecules. The subsequent condensation into siloxane (chemical) bonds leads to the formation of a three-dimensional polymeric network on the surface, whose thickness and uniformity are difficult to control.

On the contrary, if the surface to be silanised is dehydrated before silanisation and a water-free organic solvent is used, direct condensation of the chloro- or alkoxy groups with the surface silanols is the only possible mechanism for the formation of chemical bonds. Some studies suggest that direct condensation of alkoxysilanes with a silica surface does not take place in a water-free medium, unless amine catalysis is brought about by the presence of ammonia or by the use of an aminosilane compound.¹⁴⁷

Self-assembled monolayers (SAMs) of trichloro- or trialkoxy-silanes can be formed on silica surfaces by controlling the amount of interfacial water present on the surface. In practice, the substrate is first dehydrated, then rehydrated by exposure to controlled humidity, so as to form a monolayer of surface water. In these conditions, the oxidation of the silane molecules is limited to surface anchoring sites, and highly ordered and densely packed silane films can be obtained.¹⁴⁷ This effect of interfacial water on the formation of silane films points at the different behaviour of different silica-rich materials when subjected to silanisation in the same conditions. For example, glass and silica differ in that glass has been shown to adsorb more water than silica, hence a greater surface hydration.¹⁴⁸

4. 2. 1. 2. 2. Vapour-phase silanisation

Whereas gas-phase silanisation reactions are similar to those involved in dry organic solvents, reaction conditions within the vapour are more easily controlled. Thus, the formation of silane layers is more reproducible than from the liquid phase. In addition, since the vapour is enriched in more volatile monomer, monolayer coverages can be achieved.

4. 2. 1. 3. Pre-silanisation treatment of silica-rich surfaces

A substrate is amenable to silanisation only if exposed silanol moieties are present at its surface. Surface silanols can be in one of three configurations, geminal, isolated or vicinal. Silica-rich surfaces can also feature strained siloxane bridges, in which two surface Si atoms are linked to a single oxygen atoms. For a hydroxyl group to be reactive, it has to be in an isolated or geminal configuration, as opposed to vicinal silanols which are bridged in pairs through H-bonding.¹⁴⁷ Thus, cleaning and activation of silica-rich surfaces prior to silanisation is a prerequisite, in order not only to remove organic and non-organic (heavy metals) surface contaminants, but also to generate suitably reactive surface silanol groups. Pre-silanisation substrate preparation procedures typically involve degreasing with organic solvents, followed by a treatment with a strong oxidant and a final activation step in acidic conditions.

A number of liquid-phase chemical methods can be found in the literature for the cleaning and activation of glass and silica surfaces prior to silanisation. All are based on various combinations of organic solvents, bases and acids, and oxidising agents, at various temperatures, such as the RCA Standard Clean 1 procedure which consists in the immersion of the substrate in 1: 1: 5 NH_4OH : H_2O_2 (30%): H_2O at 80 °C for 5 minutes. A comparative assessment of eight of these methods applied to soda lime glass slides has been reported recently by Cras *et al.*¹⁴⁸ The investigation was based on goniometric analysis, *i.e.* the measurement of equilibrium contact angles of sessile drops, to assess the cleanliness of the surface. The rationale of the approach was that removal of contaminants from a glass surface leaves a highly hydrophilic surface, characterised by low water contact angles. Cras *et al.* showed that cleaning methods based on strongly acidic conditions (HCl , H_2SO_4) resulted in the most hydrophilic surfaces, whereas basic solutions (KOH , NaOH) were found to lead to surface heterogeneities, due to a leaching and/or etching effect. A treatment in 1: 1 MeOH : HCl , followed by immersion in concentrated H_2SO_4 , was found to provide the most efficient surface cleaning. However, the value of the results presented by Cras *et al.* is somewhat diminished by the fact that the investigation was based solely on contact angle measurements, a method which is known to be sensitive to surface heterogeneity.

Plasma etching processes can be used instead of, or in complement to, liquid phase processes, for the cleaning of silica surfaces. Treatment of a substrate with a low-power O_2 plasma for a few minutes is known to be efficient in the removal of organic contamination.

4. 2. 2. Derivatisation of oligonucleotides to be used as covalently-bound capture probes

4. 2. 2. 1. Reactive nucleophile terminal groups

Amine and thiol moieties are nucleophile groups that exhibit reactivity towards suitably derivatised surfaces, through direct or cross linker-mediated binding. Incorporation of a nucleophile moiety at the 3' or 5' end of a synthetic oligonucleotide molecule is readily achieved during synthesis,¹⁴⁹ and this approach was used in this thesis. In the case of amino-terminated oligonucleotides, the 5' primary amine is a stronger nucleophile than the exocyclic amines on the bases,⁹³ which yields selectivity to the fixation process (levels of end-attachment of the order of 90% have been reported), hence a better biorecognition activity of the immobilised probe.

4. 2. 2. 2. Spacer arms

As stated above (Section 1. 1. 2. 2. 3), a spacer arm is required between the support and the surface-bound probe in order to avoid detrimental steric and/or electrostatic effects resulting from crowding of the surface.

An investigation into the effect of spacer arms onto the hybridisation of surface-bound, synthetic oligonucleotide probes to PCR products has been presented by Zhang *et al.*⁹⁰ In this study, 5'-aminohexyl-terminated oligonucleotides were covalently attached to nylon membranes through carbodiimide-mediated condensation of the terminal amines with the carboxyl groups present on the membranes. Spacer arms consisted of hexaethylene glycol units (incorporated into the probes during synthesis, as phosphoramidite adducts), whose number was varied between 0 and 3. The combined lengths of the aminohexyl linker and one hexaethylene glycol unit is 28 Å, when fully extended. The results of the investigation show that the presence of at least one linker unit provides a 4-fold increase in hybridisation efficiency as compared to the case when no linker is used. Conversely, Southern and Mir suggested the existence of an optimum length, beyond which steric crowding occurs due to "dissolution" of the probe inside the volume of the matrix formed by the spacer.⁴⁹

As an alternative to ethylene glycol units,^{9,90} polydeoxythymidylate (poly dT) groups can be used as spacer arms.^{37,114} The link between the poly dT unit and the terminal nucleophile moiety usually involves a carbonyl chain, typically C₆.⁴⁵ The length of a fully extended hexyl linker plus the phosphate group of the first thymine residue is circa 12.8 Å. This distance is believed to be the minimal distance below which detrimental steric effects take place. One triethylene glycol unit is approximately equivalent in length to two dT residues.

4. 2. 3. Examples of oligonucleotide probe attachment to silanised surfaces

A number of procedures have been reported for the attachment of appropriately derivatised oligonucleotides to various organosilane-modified surfaces, for use in heterogeneous DNA hybridisation applications.

Amino-terminated oligonucleotides can be attached directly to glycidoxypropylsilane-modified surfaces through a reaction resulting in the formation of a secondary amine upon opening of the oxirane ring. Using this strategy, Cloarec *et al.*⁵⁷ reported surface densities of 10^{12} 20-mer oligonucleotide probes per cm² on oxidised silicon wafers (100 Å silicon dioxide). Beattie and coworkers¹⁵⁰ achieved surface densities of 10^{10} - 10^{11} probe molecules (9-mer oligonucleotides with triethylene glycol phosphoryl spacers) per mm² of planar glass surface. This equates to a 30 - 100 Å spacing between adjacent probes, considering that the effective surface area of glass is about twice that of an atomically smooth surface. Stimpson *et al.*¹⁰⁹ reported similar densities of surface coverages of 3×10^9 - 3×10^{10} probe molecules per mm² on planar glass slides.

Maskos and Southern have used glycidoxypropylsilane-treated glass slides as substrates for the *in situ* synthesis of oligonucleotides, achieving surface densities of 110 fmol mm⁻², equivalent to adjacent probes being 39 Å apart.⁹ The attachment of amino-terminated oligonucleotide to glycidoxypropylsilane-treated Ta₂O₅ substrates has also been reported.²⁸

Amino-terminated oligonucleotides and PCR products have also been immobilised onto aminosilanised glass slides,³⁷ using a phenylisocyanate cross-linker. The attachment was shown to be specific to the terminal amino groups, with respect to the internal amines of the nucleobases. Oligonucleotides bearing a terminal thiol moiety have been attached to oxidised silicon wafers.⁵⁸ The latter were first silanised with an aminosilane and then derivatised so as to exhibit iodoacetamide groups, that are reactive towards the thiols. 21-mer ODNs were immobilised at a density of 250 fmol mm⁻².

4. 2. 4. Optimisation of the probe coverage density

Whilst the functionality of oligonucleotide probe layers for DNA hybridisation sensors is increased by the use of end-attachment strategies combined with the use of appropriate linkers, another important parameter that significantly affects heterogeneous hybridisation efficiencies is the coverage density of probes. From the previous section, covalent attachment of nucleic acid probes onto solid surfaces usually results in coverage densities in the range 10¹⁰ - 10¹¹ molecules per mm², equivalent to 16 - 165 fmol mm⁻². The coverage density can be optimised between these two values: increasing the surface density of probes will result in an increase in hybridisation kinetics until the trend is reversed due to steric crowding.

A short oligonucleotide strand, assumed to have the shape of a rigid rod and to stand normal to the support, would cover an approximately 5 x 5 Å² area.¹⁵¹ However, the diameter of a double helix of double-stranded DNA (e.g., probe-target hybrid), likewise assumed to be rod-shaped, is 20 Å. If standing perpendicular to the surface, this hybrid would have a footprint of 314 Å², while a hybrid of two 25-mers laying flat on the surface would have a footprint of 1700 Å², considering that each base pair in the duplex is 3.4 Å in length.

Steel *et al.*⁸³ have conducted a thorough experimental investigation of the effect of probe surface density upon hybridisation efficiency. A model system was used in which thiol-derivatised, single-stranded oligonucleotides were immobilised as sub-monolayers on a Au surface. The coverage density of oligonucleotides could be controlled by forming mixed monolayers with 6-mercapto-1-hexanol. A chronocoulometric method was used that provided quantitative analysis of both single- and double-stranded DNA at the Au electrodes. The hybridisation efficiency, characterised by the ratio of the number of targets having hybridised at equilibrium to the number of probes present, was monitored for probe coverage densities in the range 10¹² - 10¹³ molecules per cm². The hybridisation efficiency for a 25-mer target to a 25-mer probe was found to exhibit a maximum for a value of the probe coverage of 4 x 10¹² molecules per cm² (or 66 fmol mm⁻²), equivalent to 2500 Å² per probe molecule. This coverage density is circa 50% less than that for a closely packed layer of duplexed laying flat on the surface.

Other experimental determinations of hybridisation efficiency for various probe coverage densities have been reported. Beattie *et al.*¹⁵⁰ found that hybridisation of 21-mer targets to 9-mer probes having a triethylene glycol phosphoryl spacer was maximum for a 100 fmol mm⁻²

probe coverage density. O'Donnell and coworkers⁵⁸ showed that circa 40% of 21-mer probes attached at a 250 fmol mm⁻² coverage density were available for hybridisation. This translates into a density of hybridised target of 100 fmol mm⁻², in excellent agreement with the results of Beattie *et al.* A similar investigation involving allele-specific oligonucleotide (ASO) probes and 157 base long PCR amplicons as targets was conducted by Guo *et al.*³⁷ The optimum surface density for hybridisation to the 157 base long target was found to be 500 Å² per probe molecule, equivalent to 330 fmol mm⁻². At this coverage density, the hybridised fraction was 20%.

4. 2. 5. Blocking of non-specific adsorption

The performance of most heterogeneous bioassays is significantly affected, in terms of reliability, accuracy and sensitivity, by the occurrence of electrostatic and/or hydrophobic interactions between the analyte and the substrate. Reducing the extent of non-specific binding to an acceptable level requires the “blocking” of the biosensing surface. A number of different types of chemical or biological blocking agents can be used in heterogeneous hybridisation assays.¹⁵² These usually consist of large molecules, such as proteins, and organic oligomers or polymers, e.g. poly(acrylic acid).²⁸ The blocking agent can either be used as a pre-hybridisation treatment of the chip or as a component of the hybridisation buffer.

4. 3. Strategy for the functional immobilisation of oligonucleotide capture probes onto glass and oxidised silicon and PDMS substrates

4. 3. 1. Organosilane

The use of functional organosilane compounds for the covalent tethering of biomolecules onto silica-rich surfaces was suggested by Eigler *et al.*¹⁵³ The authors carried out a comparative assessment of several commercially available silanes, using contact angle measurements as a semi-quantitative guide to determine film quality and reproducibility. Glass coverslips and fused silica fibres were treated in the liquid phase with mercapto-, amino- and epoxy-functionalised silanes. The substrates were first activated by immersion in 1: 1 HCl: MeOH, then water rinsed, immersed in concentrated H₂SO₄, water rinsed, boiled in water, and air dried. Silanisation of the substrates was carried out by immersion in a 2% solution of silane in dry toluene, for 2 hours, followed by rinsing with dry toluene and air drying. The results of the contact angle measurements are given in Table 4-1.

Organosilane reactive group	Equilibrium water drop contact angle (mean value and standard deviation, °)
mercaptomethyldimethylethoxy-	54.0 ± 0.2
mercaptopropyltrimethoxy-	58.0 ± 0.3
4-aminobutyldimethylethoxy-	68.0 ± 0.4
4-aminobutyltriethoxy-	60.0 ± 0.3
glycidopropyltrimethoxy-	52.0 ± 0.9

Table 4-1. Equilibrium water drop contact angles for silica-rich surfaces silanised with different types of organosilane compounds (from ref. 153)

The results presented in Table 4-1 show that the thiol-functionalised silane films exhibit contact angles with the lowest levels of standard deviation, indicating a higher coverage uniformity than those obtained with amino- and epoxy-silanes. The glycidopropyltrimethoxysilane, in particular, shows a high level of non-uniformity, with an associated relative standard deviation in excess of 1.5%. Besides, as compared to the aminosilanes, the mercaptosilanes present lower contact angles, hence a lower hydrophobicity. This characteristic is important in terms of wetting properties of the microchannel substrates, as the generation of 3D spots of oligonucleotide probes on flow-through substrates relies on capillary action, as discussed in the next chapter. A higher level of hydrophilicity of the microchannel wall will enhance permeation of aqueous solutions into the pores. Consequently, mercaptosilane was selected as a starting point in the derivatisation of microchannel substrates. A trialkoxy derivative was chosen due to its self-assembly capability, as shown in Figure 4-1.

4. 3. 2. Reactive nucleophile and linker on the probe

Nucleophile-terminated oligonucleotide probes can not be tethered directly to surface-bound nucleophile thiol groups; a cross-linker is required to establish a chemical bond between the thiol moieties on the substrate and the nucleophile group on the probe. Although the use of thiol-terminated probes along with a homofunctional cross-linker is possible, this approach suffers from possible probe-probe and surface-surface cross-linking. A more reliable alternative is offered by the use of amino-terminated probes along with a thiol-to-amine heterobifunctional cross-linker. The stronger nucleophilicity of a 3'- or 5'-end primary amine as compared to the exocyclic amines on the bases allows for selective end-attachment. All the oligonucleotide probes used in this thesis were 16- to 25-mers which featured a 3'-aminohexyldeoxy-thymidylate modifier (amino C₆ dT), incorporated during synthesis. The 6-carbon aliphatic chain served as a linker and spacer. The use of 3'-aminohexyldeoxythymidylate-modified

oligonucleotide probes has been shown to be superior to propanolamine (amino C₃) and heptylamine (amino C₇) modifiers in terms of hybridisation efficiency.¹⁵³

4. 3. 3. Cross-linking

A number of heterobifunctional cross-linkers are available for the coupling of an amine to a thiol moiety. Functional groups reactive to amines include aldehydes, isothiocyanates, succinimidyl esters and sulfonyl chlorides, which react to form alkylamine (via a Schiff base), thiourea, carboxamide and sulfonamide linkages, respectively. Thiols readily react with alkylating agents such as iodoacetamide and maleimide derivatives to form thioethers. Succinimidyl esters are generally preferred over isothiocyanate derivatives because the former are more reactive with amines and yield more stable adducts (a strong amide bond is formed). Iodoacetamide derivatives are intrinsically light-sensitive, making maleimides a more reliable alternative. Thus, the preferred amine-to-thiol cross-linkers are heterobifunctional compounds, which combine a succinimidyl ester with a maleimide group. Several such compounds are commercially available, with a variety of aromatic and aliphatic cross-bridges between the two terminal functional groups. s-GMBS (N-[γ -maleimidobutyryloxy]sulfo succinimide ester) was used in this work. The presence of a sulfonate group on the N-hydroxysuccinimide (NHS) ring of s-GMBS imparts solubility in aqueous solution to the molecule, which would otherwise exhibit a low solubility in water due to the presence of the succinimidyl ester group. By using s-GMBS rather than GMBS, no organic solvent such as DMSO was required, thereby alleviating the problems associated with the reduced levels of hybridisation efficiencies observed for DMSO-treated capture probes.¹⁵³

Cross-linking is a two-step reaction process. In order to allow for each reaction to take place in optimised conditions (in terms of solvent, pH, and relative amount of reagents), it is preferable that the two steps be conducted separately. In addition, the order in which the two steps are carried out is to be taken into consideration. Reacting the cross-linker with the probe first is a homogeneous reaction (to be subsequently followed by a heterogeneous reaction), whereas if the cross-linker is reacted with the silanised surface first, two heterogeneous reactions are involved. The second option is less preferable due to the fact that surface thiols react to some extent with succinimidyl esters, leading to cross-linker molecules being attached to the substrate by the “wrong” end. Although the product is unstable, the final probe coverage will be reduced.

The derivatisation of amino-terminated probes with s-GMBS requires a large excess of cross-linker, in order to compensate for the relatively high rate of hydrolysis of the NHS group of the cross-linker. The rate of hydrolysis of the NHS ester increases with increasing pH. Likewise, hydrolysis of maleimides to maleimic acid can take place to a significant extent above pH 8. Besides, although maleimides can react with amines (a primary, aliphatic amine at the 3' end of an oligonucleotide has a pK_a close to 7.0), the reaction requires a higher pH than the reaction of maleimides with thiols. Thus, by keeping the pH close to 7.0, the amine moiety on the probe is

made to react selectively with the NHS group of s-GMBS, leaving the maleimide group unreacted, hence readily reactive to the surface-bound thiols in the second step. However, removal of the excess cross-linker is necessary so that the latter does not compete with the derivatised probe in the reaction with the surface thiols.

In the second step, selectivity of maleimide towards thiols is an issue as some non-reacted, amine-terminated probe might still be present and these amine-terminated probe could react with the maleimide of the cross-linker to yield inter-probe cross-linking. However, at pH 7, the reactivity of maleimide towards thiols is selective by a factor of three orders of magnitude with respect to the reactivity of maleimide towards amines.

4. 3. 4. Overall surface modification and capture probe attachment process

Throughout this thesis, the strategy used for the covalent attachment of ODN probes onto silica-rich surfaces, including the sidewalls of MCG and MCS chips, is depicted in Figure 4-2.

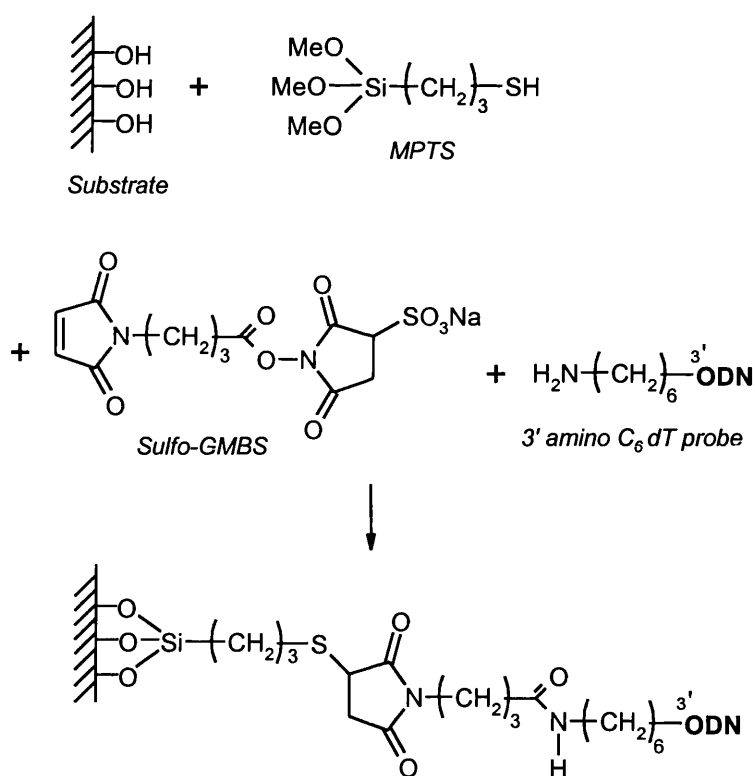


Figure 4-2. Strategy used for the covalent attachment of amino-terminated oligonucleotide probes onto the silica-like surface of solid substrates.

Note that the cross-linker contributes to the overall spacer length between the surface and the probe. The length of the s-GMBS residue is 10.2 Å. This adds to the 12.8 Å of the C_6 linker to give a total spacer arm of 23 Å.

4. 4. Generation of reactive silanol moieties on planar substrates in preparation for silanisation

The need to generate suitably reactive surface silanol groups on silica-rich substrates in order to ensure successful silanisation has been stated in Section 4. 2. 1. 3. In this section, the issue is addressed in the case of planar glass, silicon and PDMS substrates.

4. 4. 1. Surface oxidation of silicon substrates

4. 4. 1. 1. Issues

Due to the high affinity of Si for oxygen, untreated silicon wafers kept in air at room temperature are normally covered with a thin layer of native oxide (circa 3 nm thick). However, it is not certain that the latter be stable and uniform enough to ensure a satisfying level of silane coverage after silanisation. In addition, silicon is a highly hydrophobic material, therefore aqueous solutions do not readily permeate the microchannels of MCS substrates, making liquid-phase treatment of the latter unreliable.

The chemical reactivity of a silicon surface can be favorably modified, in preparation for silanisation, by resorting to oxidation, whereby a surface layer (a *superstrate*) of silicon dioxide is formed on the silicon substrate. Surface oxidation of silicon can be achieved through a number of processes including thermal, chemical, and anodic oxidation (the latter being carried out either in a liquid electrolyte or in a gaseous plasma). Anodic oxidation is anisotropic in nature and thus not applicable to high aspect ratio microchannel substrates such as macroporous silicon. The same holds true for deposition methods, in particular chemical vapour deposition (CVD). As discussed below, chemical and thermal oxidation are isotropic processes, which makes them applicable to high aspect ratio structures.

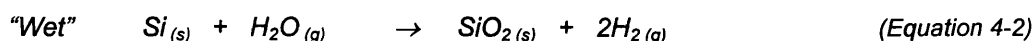
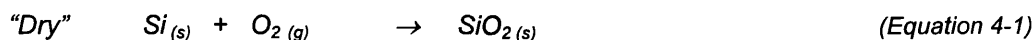
In this section, aspects of thermal and chemical oxidation of silicon relevant to the subsequent silane chemistry-based surface derivatisation of silicon substrates are discussed. The main issue regarding the grown oxide layer concerns its density and porosity, as this will affect subsequent silanisations in which the behaviour towards hydration and the effective surface area of the silicon dioxide surface play a role. Another issue is the thickness of the oxide layer, and its uniformity. Control of the oxide layer thickness requires that the kinetics of the thermal oxidation process be understood. Finally, the possible generation of structural stress during oxidation has to be considered.

4. 4. 1. 2. Thermal oxidation of silicon

The thermal growth of a thin layer of silicon dioxide on silicon substrates is a basic feature of planar microfabrication technology.^{59,154} Silicon dioxide layers are used for impurity masking during diffusion, for surface protection and passivation, and as elements in active devices, e.g. as a dielectric in CMOS (complementary metal-oxide-semiconductor) transistors.

4. 4. 1. 2. 1. Principle

Thermal oxidation of silicon takes place in the presence of oxygen or water vapour, at elevated temperatures. Overall chemical reactions for the oxidation of silicon in “dry” (O₂) and “wet” (H₂O) atmospheres are as follows:



Thermal oxidation of silicon is typically carried out in an oxidising atmosphere of oxygen or water vapor, or both, in resistance-heated cylindrical quartz tubes. Such furnaces, used in silicon microelectronics, allow for precise temperature control ($\pm 1^\circ\text{C}$) over a significant length of the tube called the *flat zone*. In open-tube oxidations, oxidising agents are introduced at one end of the furnace and allowed to be freely exhausted at the other end.

The experimental conditions used during thermal oxidation of silicon should ensure that an excess of oxidising reactants is maintained inside the tube, and in particular at the surface to be oxidised, which might be an issue in the case of high aspect ratio structures. Under these conditions, the temperature remains the controlling factor in open-tube oxidations, so that a uniform oxide layer can be grown within the flat zone of the furnace.

4. 4. 1. 2. 2. Kinetics of thermal oxidation

Experimental investigations into the kinetics of thermal oxidation of silicon, based on radiotracer measurements, have shown that oxidation proceeds by inward diffusion of oxidising species through the oxide layer, rather than by the outward motion of Si to the outer oxide layer surface, as is the case in anodic oxidation. Consequently, the mechanism of thermal oxidation of silicon involves three processes: (i) dissolution of the oxidising species (O₂ and/or H₂O) into the oxide layer, at the gas-oxide interface; (ii) diffusion of the oxidising species through the growing oxide layer; and (iii) reaction of the oxidising species with the silicon substrate, at the oxide-silicon interface.

A mathematical model for the oxidation of silicon has been derived by Deal and Grove.¹⁵⁵

Two distinct regimes of oxidation kinetics can be distinguished over the course of the oxidation process: at first, the oxide growth rate is essentially linear, as the reaction at the oxide-silicon interface is limiting; after oxidation has been allowed to proceed for a sufficiently long period of time (corresponding to about 100 nm of grown oxide), a parabolic growth rate, controlled by diffusion through the oxide layer, is observed. The Deal and Grove model was later refined by Wolters, by accounting for the solubility and transport behaviour of water in silica.¹⁵⁶ The time-dependence of the oxide layer thickness, x , is expressed by the following equation:

$$x = \frac{A}{2} \left[\left(1 + \frac{t + \tau}{A^2 / 4B} \right)^{1/2} - 1 \right] \quad (\text{Equation 4-3})$$

where $A = 2D (1 / k_s - 1 / h)$ and $B = 2 D C^* / N$, with

D : diffusion coefficient of the oxidising species through the oxide,

k_s : rate constant of the oxide formation reaction,

h : gas-oxide mass transfer coefficient,

C^* : equilibrium bulk concentration of oxidising species inside the oxide,

N : number of molecules of oxidising species per unit volume of oxide, and

τ : time constant accounting for the initial presence of a native oxide layer.

The validity of the model has been demonstrated over a wide range of experimental conditions. Predicted effects of temperature and partial pressure of the oxidising species on the rate constants have been confirmed experimentally. The reaction-limited (linear) growth presents an Arrhenius-type exponential dependence on temperature, as well as a dependence on the crystallographic orientation of the silicon substrate. The magnitude of the diffusion-limited (parabolic) growth rate also shows an exponential dependence on temperature. The parabolic rate constant is directly proportional to the partial pressure of the oxidising species.

The model also accounts for the experimentally observed fact that wet oxidation is faster than dry oxidation, in the same conditions of temperature and partial pressures of oxidising species. This is a result of the three order of magnitude higher equilibrium solubility of H_2O , as compared to O_2 , in SiO_2 . Typical open-tube oxidation rates in dry oxygen (in which the oxidising species is O_2 at a partial pressure of 1 atm) are 60 nm h^{-1} at 1000°C . Passing the oxygen through a water bath prior to its introduction into the furnace results in an increase in the moisture content of the gas stream (wet O_2 oxidation), thereby increasing the oxidation rate. The moisture content of the gas stream is determined by the temperature of the water bath and the flow rate of the gas stream. A neutral carrier gas (N_2 , Ar) can be substituted for oxygen with a minimal decrease in the rate of oxidation. Faster oxidation rates are obtained in *steam oxidation* conditions, when the amount of water present is such that it does not limit the oxidation rate (*i.e.* a partial pressure of water of 1 atm is maintained in the oxidation tube). Empirical values of the linear and parabolic rate constants have been tabulated for a range of oxidising atmospheres, temperatures and partial pressures of the oxidising species.

A number of intrinsic properties of the silicon substrate itself have an effect on the oxide growth rate. The crystallographic orientation of the substrate (*i.e.* type of crystallographic plane exposed) influences the kinetics of the linear growth phase, as an effect of the surface concentration of Si bonds acting as oxidation sites; for example, oxidation of $\{111\}$ Si is faster than that of $\{100\}$ Si. The presence of dopants in the Si substrate has an effect on the oxidation rate as well.

4. 4. 1. 2. 3. Physical properties of thermal oxide layers grown in various conditions

The thermal oxidation process gives a material whose density decreases with increasing water content of the oxidative atmosphere. The following values have been reported: 2.24 - 2.27 g cm⁻³ for dry oxygen oxidation; 2.18 - 2.21 g cm⁻³ for wet oxygen oxidation; 2.00 - 2.20 g cm⁻³ for steam oxidation. By comparison, silicon and fused silica have a density of 2.33 and 2.21 g cm⁻³, respectively.

Upon growing a thermal oxide, the thickness of the substrate decreases, since silicon is being consumed. In addition, the relatively open network structure of amorphous silicon dioxide causes a significant volume change in the overall structure. For a final oxide layer thickness of t , the substrate thickness is reduced by $0.45t$ whereas the overall thickness of the substrate and superstrate is increased by $0.55t$. The volume increase is localised at the Si/SiO₂ interface, which can result in significant interfacial stress, leading to dopant redistribution as well as creation of point defects and dislocations inside the silicon. Whereas dopant redistribution is not an issue for silicon used as a passive biochip substrate, defects can be deleterious to the structural rigidity and optical properties of the material. If oxidation is conducted at temperatures above 950°C, very low levels of stress are observed, due to a viscous flow of the oxide layer.¹⁵⁴

4. 4. 1. 3. Thermal oxidation of planar silicon substrates

As stated above, optimisation of the thermal oxidation process for planar silicon chips was focused on obtaining a uniform (in thickness and in physical properties) oxide layer. Flat silicon pieces were used to assess the oxidation rates that could be achieved with the limited facilities at hand.

4. 4. 1. 3. 1. Experimental

Materials and apparatus

4 inch-diameter, 525 ± 15 μm thick, n-doped, 32.2 - 37.8 Ω cm, {111} silicon wafers (Shin-Etsu Corp.) were diced into 15 x 15 mm² pieces. The chips were cleaned in IPA, Pirhana solution and buffered HF for 1 minute to remove any contaminated native oxide layer.

A 4 inch diameter quartz furnace, normally used for layer diffusion in microelectronics device fabrication, was used. The set-up is shown in Figure 4-3. A quartz holder, designed to hold 1-2 cm² substrates in an upright position, was used.

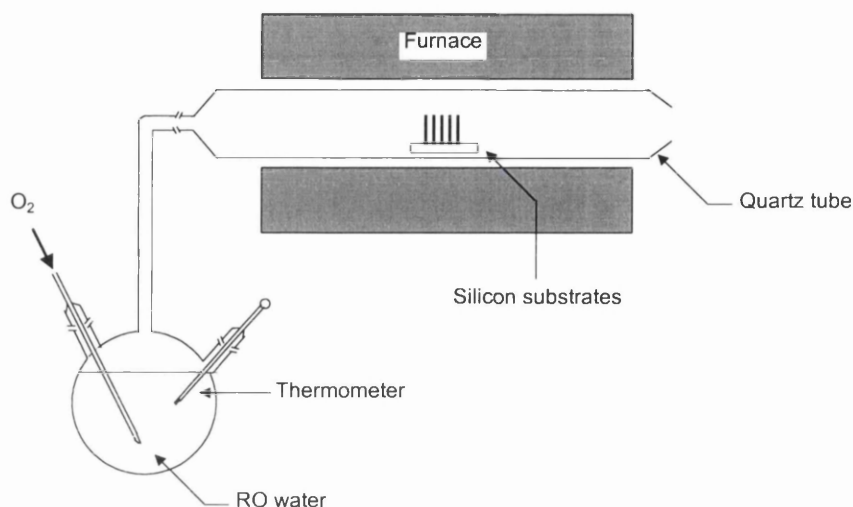


Figure 4-3. Set-up used for the thermal oxidation of macroporous silicon chips.

Procedures

The bath of ultrapure water was kept at room temperature, in the absence of any temperature regulation capability and of heating mantels for the gas lines between the water bath and the tube. The silicon chips were held upright, perpendicular to the gas flow, in the flat zone of the furnace. The chips were cleaned in IPA, Pirhana solution and 40% HF for 1 min to remove any contaminated native oxide layer. Two batches of four flat silicon chips were oxidised at circa 1050°C and $1.5\text{ cm}^3\text{ min}^{-1}$ O_2 flow rate, for 4.5 hours and 8 hours, respectively.

4. 4. 1. 3. 2. Results and discussion

In order to obtain a high quality layer, oxidation was carried out at temperatures above 950°C , to reduce stress. An open-tube, wet O_2 oxidation procedure was chosen for the flexibility it offers in terms of growth rate, since the latter can be altered by simply changing the flow rate of O_2 gas. Varying the water content of the oxidative atmosphere also allows for the density, hydroxylation and wettability of the material to be adjusted. In addition, the equipment used was limited in terms of oxygen flow rate, making dry oxygen oxidations impedingly slow.

As the $\text{SiO}_2\text{-on-Si}$ material system consists of a transparent superstrate on a reflective substrate, measurements of the superstrate thickness is possible by ellipsometry, to a lower limit of circa 50 nm. This method is faster than the measurement of a step height, after localised etching of a portion of the silicon oxide layer, by surface profiling (*i.e.*, tracking of the position of a mechanical stylus as it is traversed across the step). In addition, ellipsometry requires less sample manipulation, in addition to being non-destructive. Direct thickness measurement of the oxide layer grown in the microchannels of the macroporous silicon chips is not possible by ellipsometry. Alternatives include microgravimetric measurements of the weight gain and SEM imaging of a localised etch, but no attempt at using these methods was made.

The oxide thickness grown was measured, by ellipsometry, to be 237.0 ± 4.3 nm for 4.5 hours of oxidation and 378.7 ± 2.8 nm for 8 hours of oxidation. Further characterisation of the oxide thickness versus oxidation time curve was not deemed necessary.

4. 4. 1. 4. Chemical oxidation of silicon

The suitability of chemical oxidation as a pre-silanisation treatment of MPS substrates was investigated, as a possible less labour-intensive alternative to thermal oxidation.

Although cleaning solutions commonly used in the pre-processing treatment of silicon wafers consist of mixtures of hydrogen peroxide and mineral acids, the actual surface oxidising effect, as opposed to just cleaning, is not clear. Immersion of silicon substrates in a 1: 1: 5 HCl (30%): H₂O₂ (30%): H₂O solution has been reported to result in the formation of a 1 nm thick SiO₂ layer. This treatment renders silicon substrates hydrophilic, however the surface can quickly become hydrophobic again by adsorption of hydrocarbon impurities from the ambient air or from plastic containers.

4. 4. 2. Surface oxidation of PDMS substrates

4. 4. 2. 1. Introduction

The amenability of PDMS to surface oxidation by O₂ plasma discharge has been reported by Morra *et al.*,¹⁵⁷ and by Chaudhury and Whitesides.¹⁵⁸ Extensive surface characterisation studies carried out by these authors, based on static secondary ion mass spectrometry (SSIMS), X-ray photoelectron spectroscopy (XPS) and infra-red spectroscopy, have evidenced the formation of surface hydroxyl groups upon plasma treatment, indicating that -OSi(CH₃)₂O- moieties are converted to -O_nSi(OH)_{4-n} groups. In this thesis, the notation PDMS^{ox}, as coined by Whitesides *et al.*, is used henceforth to refer to the thin (< 50 Å) silica-like layer present on the surface of oxidised PDMS.

A lack of durability of the thin silica-like layer on the surface of PDMS^{ox} has been evidenced by contact angle measurements, which showed the advancing contact angle of water to increase from 30° immediately after plasma oxidation, to 79° after 15 minutes in air and to 93° (close to the value for native PDMS) after 45 minutes in air.^{123,157} However, PDMS^{ox} was shown to be stable when immersed in solvents, suggesting that the alteration of the surface properties observed in air only resulted from rapid adsorption of contaminants. Chemisorption of organosilane compounds onto PDMS^{ox} has been demonstrated in fundamental studies of surface interactions¹⁵⁸ and in hemocompatibility studies for bioengineering applications.¹⁵⁹ This property was used as a starting point for surface derivatisation of PDMS substrates, in prevision of subsequent attachment of oligonucleotide probes.

4. 4. 2. 2. Experimental

4. 4. 2. 2. 1. Materials and apparatus

A two-component PDMS kit containing base and curing agent was obtained from RS Components. Mercaptopropyltrimethoxysilane (MPTS), toluene (99.8%, HPLC grade) and absolute ethanol were from Sigma (St Louis, MO). O₂ plasma was generated using a Plasma Technology BP80 machine.

4. 4. 2. 2. 2. Procedure

PDMS slabs, circa 1 mm thick, were made by pouring a suitable volume of well-mixed PDMS prepolymer (10:1 ratio of base to curing agent) into a glass Petri dish, letting the prepolymer equilibrate and degas at room temperature for 30 min, and curing at 65 °C for 4 hours. Finally, the PDMS was cut out into 12 x 12 mm² pieces. In order to facilitate peeling of the PDMS slabs, the dish was previously silanised by reaction with dichlorodimethylsilane (Sigma), diluted to 2% in chlorobenzene, for 10 min, then rinsed with chlorobenzene and RO water, and blow-dried.

The PDMS substrates were washed in ethanol and blow-dried with N₂. Oxidation was achieved by exposure to a 20 sccm, 13 mT O₂ plasma for 1 minute, in the BP80 machine operated at 100 W. The oxidised substrates were immediately immersed in toluene. Then, silane was slowly added to the toluene, to a final concentration of 2.5%, under strong agitation provided by a rotating table.

The activated PDMS substrates were subsequently derivatised with oligonucleotide probes as described in Section 4. 5. 1.

4. 5. Validation of the strategy for the attachment of oligonucleotide capture probes onto planar substrates

The validity of the strategy was checked using planar substrates, due to the fact that surface analysis is difficult to implement with microchannel substrates, whilst a range of techniques are readily available for planar surfaces, including fluorescence microscopy, XPS and FT-IR.

4. 5. 1. Analysis of immobilised probe layers by fluorescence microscopy

4. 5. 1. 1. Introduction

The choice of fluorescence microscopy for the analysis of immobilised oligonucleotide probe layers was justified by the suitability of the technique for the imaging of planar substrates. In addition, the technique allowed for direct investigation of possible surface effects associated with fluorescent labels, in prevision of studies concerned with the microarraying of microchannel substrates (Chapter 5). Accordingly, two complementary series of experiments were

conducted: (i) immobilisation of fluorescently labelled probes, followed by characterisation by fluorescence microscopy imaging, and (ii) immobilisation of non-labelled probes, followed by indirect fluorescence labelling (staining) and imaging.

4. 5. 1. 2. Experimental

4. 5. 1. 2. 1. Materials

Substrates and reagents

Standard float glass microscope slides were obtained from BDH (Poole, UK). 4 inch-diameter, $525 \pm 15 \mu\text{m}$ thick, n-doped, $32.2 - 37.8 \Omega \text{ cm}$, {111} silicon wafers were purchased from Shin-Etsu Corp. PDMS base and curing agent were from RS Components, UK.

Mercaptopropyltrimethoxysilane (MPTS), toluene (99.8%, HPLC grade), absolute ethanol, 20x sodium saline citrate (SSC) buffer (0.3 M sodium citrate and 3 M NaCl) and 20x SSPE (saline sodium phosphate EDTA) buffer (0.2 M phosphate buffer, 2.98 M NaCl and 0.02 M EDTA) were from Sigma. The heterobifunctional cross-linker s-GMBS was purchased from Pierce (Rockford, IL). Sodium dodecyl sulfate (SDS) was obtained from Sigma.

A synthetic 18-mer ODN probe, P1-c, of sequence "C"ACCATTTTAGAGCCCCTA"T", where "T" denotes a 3'-aminohexyldeoxythymidylate modifier and "C" a 5' Cy5 phosphoramidite label, was obtained as a lyophilised powder from Cruachem Corp. (Glasgow, UK). 200 μM stock solutions were prepared from the lyophilised powder by dilution in 0.1x TRIS-EDTA (TE) buffer (1 mM TRIS HCl, pH 8 and 0.1 mM EDTA, sodium salt) and kept at 4°C. An 18-mer ODN probe, P2-b, of sequence "B"CCCAGGGAGACCAAAAGC"T", where "T" is as above and "B" is a 5' biotin label, obtained from Operon Technologies (Alameda, CA), was dissolved to 30.8 μM in RO water and kept at 4°C.

A 1 mg mL⁻¹ streptavidin-Cy5 stock solution was prepared by diluting 1 mg of FluoroLink™ Cy5 labelled streptavidin (PA 45001, Amersham Pharmacia Biotech) in 1 mL RO water. The staining solution used for the fluorescence detection of biotinylated probes was made by diluting the stock solution 200-fold in 1x SSC.

Instrumentation

The deposition of ODN spots on MCG and flat glass chips was performed manually, using a micropipette (Gilson, Viliers le Bel, France).

Fluorescence imaging involved the use of the instrumentation described in Section 3. 3. 3. 2. 2, except that an HQ-Cy5 (Chroma Technology Corp., ref. 41008) fluorescence filter set was used instead of the 580-G2A set.

4. 5. 1. 2. 2. Methods

Sample preparation

Preparation of activated PDMS substrates. PDMS slabs were made, plasma oxidised and silanised as described in Section 4. 4. 2. 2.

Preparation of glass and silicon substrates. The glass slides were diced into 12 x 12 mm² pieces, which could fit into 10 mL beakers in prevision of subsequent liquid-phase treatments. The silicon wafers were diced likewise. The glass and silicon substrates were then cleaned according to a procedure commonly used in microelectronics. The chips were placed in a beaker (individually, to prevent overlapping) and treated sequentially with IPA, acetone, methanol, and RO water. The substrates were subjected to 5 minute ultrasonication periods in each solvent. Care was taken, upon substituting one solvent for the next, to avoid the formation of drying marks. Finally, the substrates were rinsed with ample water and blow-dried with N₂.

Oxidation of silicon substrates. One of the silicon chips was thermally oxidised as above, for 4.5 hours, resulting in the formation of a circa 250 nm silicon dioxide superstrate. A second silicon chip was chemically oxidised by immersion in a 1: 1: 5 HCl (30%): H₂O₂ (30%): H₂O solution, for 15 minutes, followed by rinsing with ample water and blow drying. A third silicon chip was used without any further treatment.

Surface activation and silanisation of glass and silicon substrates. Activation of the surface hydroxyl moieties was achieved by immersion in 1 M nitric acid, water, and ethanol, 10 minutes each. The chips were then blow dried and baked at 80°C for 4 hours before silanisation. No further dehydration was carried out prior to silanisation. MPTS was stored dry, at 4°C, in order to reduce alteration through hydrolysis and oligomerisation. Prior to use, the bottle of MPTS was allowed to equilibrate to room temperature before opening so as to avoid condensation of ambient moisture inside the stock solution. MPTS was diluted to 2.5% v/v in toluene (Sigma, HPLC grade) that had previously been dried on 3 Å molecular sieves. Silanisation was performed by incubation of the substrates in the silane solution at room temperature, for one hour. The chips were placed in separate beakers to avoid overlapping. The chips were then washed by sequential ultrasonication in toluene, 1:1 toluene: absolute ethanol, and ethanol, 2 minutes each. Finally, the chips were baked at 80°C for 4 hours to promote condensation of the silane film.

Probe activation. The stock solutions of Cy5-labelled probe, P1-c, and biotinylated probe, P2-b, were allowed to reach room temperature, and their concentrations were determined by optical density measurements at 260 nm. The following formula was used:

$$C_{probe} = A_{260} (V_{cuv} / V_{probe}) (33,000 / MW) \quad (\text{Equation 4-4})$$

where C_{probe} is the concentration of the probe solution, in μM ,

A_{260} is the absorbance of the probe solution at 260 nm,

V_{cuv} is the volume of diluted probe solution used in the measurement,

V_{probe} is the volume of original probe solution used in the measurement,

MW is the molecular weight of the probe.

A 5 μL aliquot of probe solution was diluted in 500 μL RO water for the measurements. As TRIS (tris(hydroxymethyl)aminomethane) contains a primary amine that can compete with the terminal amine of the probes in the reaction with the NHS ester of s-GMBS, the 30 μM solution of Cy5-labelled ODN was desalted prior to reaction with the cross-linker. This was achieved by gel filtration on MicroSpin G-25 microcentrifugation columns (Amersham Pharmacia Biotech). The Sephadex resin in the column was first re-suspended by spinning at 735 g for 1 min. 50 μL of ODN solution were then applied to the column and centrifugated at 735 g for 2 min. Half of the desalted solution of Cy5 labelled probe and the 30.8 μM solution of biotinylated probe were then diluted to 12.5 μM in 1x SSC buffer (15 mM sodium citrate and 150 mM NaCl; from 20x concentrate, Sigma) in the presence of a 10-fold excess of s-GMBS, and incubated at room temperature for one hour. Excess s-GMBS was eliminated by gel filtration, using MicroSpin columns as above. The other half of the desalted solution of Cy5 labelled probe was diluted to 12.5 μM in 1x SSC buffer; no cross-linker was added.

Reaction of the probe with the silanised surface. Microchannel and planar DNA chips were initially produced by manual dispensing of activated probe solution onto silanised substrates, using a manual micropipet. This approach is obviously limited in terms of reproducibility and array density, because of the large dispensed volumes resulting in accordingly large spots. Nevertheless, the manual dispensing of microlitre spots onto planar substrates was used to investigate the attachment chemistry, whilst an investigation into the automated sub-microlitre spotting of microchannel DNA chips, using a robotic microarrayer, is presented in the next Chapter. 8 spot replicates were produced on the five types of substrates (glass, thermally oxidised silicon, silicon with native oxide, plasma-oxidised PDMS, and non-oxidised PDMS). The same procedure was repeated with the Cy5 labelled probe that had not been reacted with the cross-linker. The cross-linker-reacted biotinylated probe was spotted onto glass and thermally oxidised silicon substrates. Each spot was produced by the dispensing of a 1 μL aliquot. After spotting, the chips were incubated for circa 36 hours in a low-light, low-humidity atmosphere.

Washing non-covalently bound probes. Non-covalently bound probes were washed off the chips by immersion in 5 mL of a solution of 1x SSC and 0.1% SDS for 15 minutes, followed by exhaustive rinsing with first fresh 1x SSC, then RO water, and blow-drying with N_2 .

Staining. Substrates that had been spotted with the biotinylated probes were incubated for 15 min with the staining solution, then washed with ample 1x SSC and RO water and blow-dried with N_2 .

Sample analysis

Images of the replicated fluorescent spots were acquired with the CCD camera operated at 256 K, with a 2x2 level of binning and 1 s integration time. The net fluorescence signal for each spot, S , was determined by subtracting the average pixel intensity over the spot area from that of a non-spotted area.

4. 5. 1. 3. Results and discussion

4. 5. 1. 3. 1. Fluorescence imaging of immobilised Cy5-labelled ODN probes

Figure 4-4 shows fluorescence microscopy images of Cy5-labelled ODN probes, immobilised on four types of substrates, namely glass, silicon (covered with native oxide only), thermally oxidised silicon and PDMS^{ox}. The substrates were imaged after non-covalently bound probe molecules had been washed off the substrate by a detergent solution.

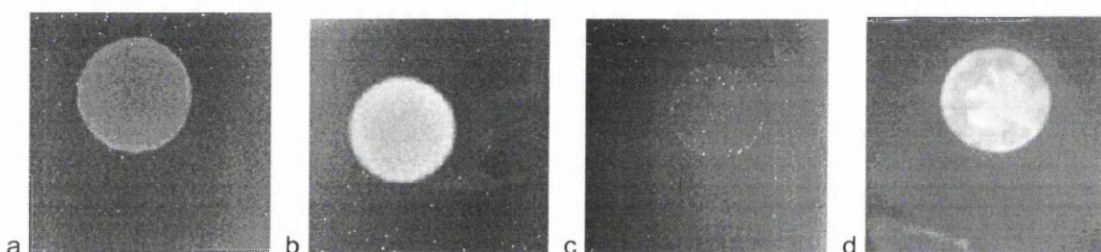


Figure 4-4. Fluorescence microscopy images of fluorescently-labelled ODN probes immobilised on planar substrates: (a) glass; (b) thermally oxidised silicon (1 μm thick oxide layer); (c) silicon (with native oxide only); (d) O_2 plasma-oxidised PDMS. Each spot was formed by the dispensing of a circa 0.5 μL aliquot of a 12.5 μM Cy5-labelled probe, activated with sulfo-GMBS, onto the silanised substrate, followed by washing of non-covalently bound probe molecules. The images were acquired with a Nikon Microphot epifluorescence microscope, using a 4x microscope objective lens, and coupled to a PixelVision CCD camera operated at 256 K, 2x2 pixel binning and 1 s acquisition time.

All four images shown in Figure 4-4 were obtained under the same experimental conditions of fluorescence imaging. All the spots of ODN probe were well-defined and could be clearly distinguished from the background. The spots formed on silicon covered with native oxide only exhibited a smaller diameter, supposedly reflecting the higher level of hydrophobicity of this material as compared to the silanised silica-like surface of the other substrates. The smearing marks seen in some of the images were formed during washing of non-covalently attached probe molecules, which reacted with the silanised surface outside of the spot area.

The net fluorescence intensities, with the associated 95% confidence interval inferred from 6 to 8 spot replicates, are given in Table 4-2. Spots which differed significantly in dimensions from other spots formed on the same substrates (due to the lack of reproducibility of the manual spotting procedure) were not used in the calculation.

Substrate	Cross-linker	No cross-linker
Glass	108.8 ± 68.1 (n=6)	19.3 ± 11.2 (n=6)
Thermally oxidised silicon	253.5 ± 192.1 (n=8)	18.5 ± 9.1 (n=8)
Chemically oxidised silicon	23.7 ± 18.0 (n=7)	21.4 ± 15.8 (n=7)
Silicon with native oxide	14.0 ± 11.1 (n=8)	16.2 ± 12.9 (n=8)
PDMS ^{ox}	174.3 ± 79.2 (n=6)	22.6 ± 14.0 (n=6)
PDMS	23.1 ± 12.4 (n=7)	19.7 ± 12.5 (n=6)

Table 4-2. Net fluorescence intensities for spots of Cy5-labelled oligonucleotide probe deposited on various planar substrates. The intensities are given as 95% confidence intervals, calculated from n spot replicates.

Due to the different nature of the substrates, and despite the fact that imaging was carried out under identical conditions, the values for the net fluorescence intensities were not necessarily directly proportional to the number of probe molecules present within the spots. For example, the fact that the spots formed on thermally oxidised silicon appeared brighter than those on glass might be due to the higher reflectivity of both the excitation and fluorescence emission radiations at the surface of the silicon wafer.

In the case where cross-linker was used, the observed fluorescence intensities from glass, thermally oxidised silicon and oxidised PDMS samples were not statistically different from one another. However, the fluorescence intensities from the non-oxidised silicon substrate and from the chemically oxidised silicon substrate were found to be much lower than that from the thermally oxidised silicon substrate. Likewise, much lower signals were observed from PDMS than from PDMS^{ox}. This confirmed the relevance and suitability of the silicon thermal oxidation and PDMS plasma oxidation procedures to the subsequent silanisation of these substrates.

The much higher fluorescence intensities obtained in the presence of cross-linker confirmed the covalent nature of the bonds formed between the probe molecules and the silanised surfaces. The fact that the net fluorescence intensities obtained in the absence of cross-linker were statistically different from zero indicated that some extent of non-covalent binding, that was not removed by the 1x SSC/0.1% SDS washing step, took place on the silanised surface. A fraction of these non-covalent interactions might have been caused by the fluorescent label present on the probe molecules.

4. 5. 1. 3. 2. Fluorescence imaging of stained probe spots

This experiment was implemented as a way to check the extent to which the fluorescent label affected the attachment of the probe to the surface. Table 4-3 shows the net fluorescence intensities for spots of biotinylated probe (with and without cross-linker) deposited on glass, thermally oxidised silicon and PDMS^{ox}, after staining with Cy5-labelled streptavidin.

Substrate	Cross-linker	No cross-linker
Glass	69.2 ± 27.9 (n=9)	13.7 ± 16.1 (n=8)
Thermally oxidised silicon	184.0 ± 62.3 (n=8)	9.2 ± 11.4 (n=9)
PDMS ^{ox}	145.1 ± 72.3 (n=8)	8.6 ± 15.3 (n=7)

Table 4-3. Net fluorescence intensities for spots of biotinylated oligonucleotide probe deposited on various planar substrates and stained with Cy5-labelled streptavidin. The intensities are given as 95% confidence intervals, calculated from n spot replicates.

As in the case of the fluorescently-labelled probe, signals statistically different than zero (at a 95% confidence level) were obtained when cross-linker was used. In the absence of cross-linker, however, signals not statistically different from zero were obtained, indicating that non-covalently bound probe molecules had been washed off the surface before staining. Thus, the small level of probe adsorption previously observed with Cy5-labelled probes can be assigned to the presence of the fluorophore label.

In addition, the relative signal intensities between the three substrates, when cross-linker is present, are in the same order as in Table 4-2. The lower absolute values of net fluorescence intensity obtained here, as compared to Section 4. 5. 2. 3. 1, reflected higher levels of background signals (surface adsorption of staining molecules) as well as difference in the extent of labelling of each probe molecule (including the fact that each avidin molecule could bind to four biotin molecules).

4. 5. 1. 3. 3. Conclusions

Beside confirming the validity of the immobilisation approach, these experiments have shown that fluorescent labels present on ODN probes contribute to enhanced adsorption of the probes to the surface. This result can be extended to the case of heterogeneous fluorescence hybridisation assays, in which the target molecules, rather the probes, are labelled. However, the extent to which the use of indirect labelling (staining) might reduce non-specific binding of the targets to the surface remains to be investigated in the case where blocking of non-specific adsorption is implemented; also, it is likely that the effect of the fluorescent label might be reduced in real samples where the size of the targets (prepared from mRNA) is larger than that of the ODN probes used here.

4. 5. 2. Further characterisation and validation of the attachment strategy

Complementary work aiming at characterising and assessing the validity of the attachment strategy described above was conducted outside the framework of this thesis, in a collaborative effort with the laboratory of Bioanalytical Chemistry, Imperial College of Science, Technology and Medicine, London, UK.

The determination of coverage densities of thiol groups obtained through the silanisation procedure described above was carried out using quantitative X-ray Photoelectron Spectroscopy (XPS) and radiolabelling experiments. The latter involved the derivatisation of silanised glass and thermally oxidised silicon surfaces with dithiobispyridine, followed by reaction with 1,2-¹⁴C cysteamine hydrochloride (American Radiolabeled Chemicals, Inc.). The radioligand was then cleaved from the surface and mixed with scintillation cocktail. A scintillation counter was used to measure the radioactivity of the solution. Knowledge of the specific activity of the radioisotope permitted the surface density of thiol groups to be calculated. The coverage density of free thiols was determined as circa 2×10^{11} per mm^2 , equivalent to 330 fmol mm^{-2} , on planar lead-rich glass slides and thermally oxidised silicon wafers.¹⁶⁰

The robustness of the surface modification and attachment chemistry was assessed, for flat glass slides and thermally oxidised silicon wafers, through a series of experiments using radiolabelled probes, as a complement to the fluorescence imaging experiments described in Section 4. 5. 1. Control experiments using non-amino modified probes (to confirm the selectivity of end attachment over side attachment), and / or omission of the cross-linker (as above), have confirmed the covalent nature of the bonds formed between the probe molecules and the various silica-rich surfaces. In these experiments, radiolabelling of the ODN probes was achieved by incubation with ³³P dATP in the presence of polynucleotide kinase. Phosphorimaging was used to measure the radioactivity of the surfaces.¹⁶⁰

The yield of the reaction between the NHS group of s-GMBS and the terminal amine moiety of ODN probes (reaction through which a maleimide moiety is attached at the 3' end of the probe), was experimentally determined as circa 60% when implemented as described in Section 4. 5. 1. 2. 2 above.¹⁶¹

4. 5. 3. Heterogeneous hybridisation on flat glass and oxidised silicon and PDMS substrates

4. 5. 3. 1. Introduction

The experiments reported in this section aimed at confirming the activity of ODN probes immobilised to silica-rich substrates through the procedure described above in terms of heterogeneous nucleic acid hybridisation.

4. 5. 3. 2. Experimental

4. 5. 3. 2. 1. Materials

The hybridisation experiments involved the use of unlabeled probes and fluorescently labeled ODN targets. The sequences for the probes P3 and P4 and the targets T3 and T4 (purchased from Glen Research, Sterling, VA) were "T"CCGCTGCCGCTGTCA, "T"CCCTGGTATGAGCCCATCTATC, "F"TGACAGCGGCAGCGG, and "F"AAGATAGATGGGCTCATACCA, respectively, where "F" represents a 5'-carboxyfluorescein phosphoramidite (6-FAM) label and "T" is as above. The complementary pairs P3-T3 and P4-T4 are representative of the genes C-myc and TNF- α , respectively.

The Cy5-labelled probe P1-c described above was used to provide a reference spot for alignment and focusing during the imaging process. The ODNs were obtained as a lyophilised powder and subsequently dissolved to appropriate concentrations in 1x SSC (probes) or 1x SSPE (targets). The blocking agent was an aqueous solution of 0.02% polyvinylpyrrolidone (PVP) and 0.02% ficoll. Fluorescence imaging involved the use of the instrumentation described in Section 3. 3. 2. 2, with the addition of a DM510-B2A (Nikon) fluorescence filter set that was used for FAM imaging.

4. 5. 3. 2. 2. Methods

The pre-treatment and silanisation of glass, oxidised silicon and oxidised PDMS substrates (one of each type) was carried out as described in Section 4. 5. 2. 2. 2. The preparation of activated probe solutions and the spotting onto the activated substrates were also achieved as in Section 4. 5. 2. 2. 2; no desalting of the probe was required since TE was not used. A total of 5 spots were deposited on each chip: one spot of P1-c in the centre, and duplicate spots of P3 and P4. The blocking agent was also used to wash non-covalently bound probes. Spotted chips were immersed in 0.2 mL of blocking solution for 15 minutes, then blow-dried and dried at 80°C for one hour.

Hybridisation with each chip was carried out by enclosing 100 μ L of sample within a cell consisting of a PDMS wall in conformal contact with the chip, and a glass coverslip acting as a lid to prevent evaporation, as shown in Figure 4-5. The hybridisation sample consisted of 100 nM of target T3 and 50 nM of target T4 in 1x SSPE. Each chip was subjected to sequential

hybridisation periods of 20, 40, 60, 150, 90 and 390 minutes, resulting in cumulative hybridisation times of 20, 60, 120, 270, 360, 750 min. After each sequential hybridisation period, the chip was washed for several minutes with a solution of 1x SSPE and 0.1% SDS, blow-dried and imaged. A fresh 100 μ L of target solution was used in each successive hybridisation.

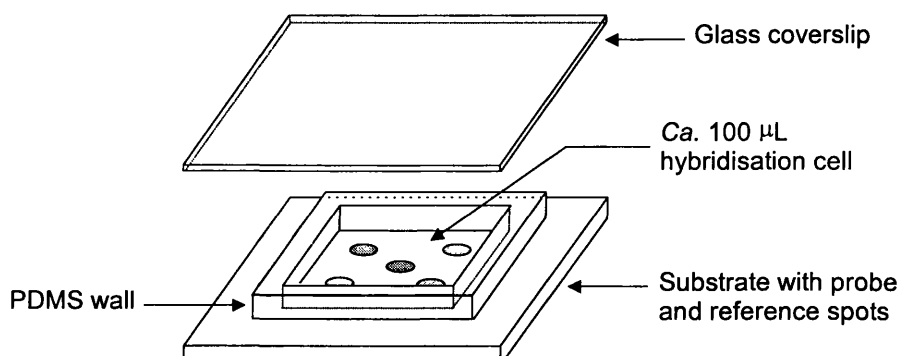


Figure 4-5. Setup used to carry out heterogeneous hybridisation assays with planar DNA chips.

The reference spot present on each substrate was imaged through the FAM optical channel, at each step of the sequential hybridisation, thereby providing a check for the formation of any possible mismatched probe-target duplexes. Image analysis (determination of a S/N value for each spot) was implemented as the disc and ring method previously used in Section 3. 3. 4.

4. 5. 3. 3. Results and discussion

The reference spot present on each substrate was used to position the chip within the field of view of the lens and to adjust the focus. This approach was necessary, especially for short hybridisation periods for which the number of hybridised targets was small, resulting in very low signals in the FAM optical channel. As in the experiments of Section 3. 3. 4, the use of dyes with different spectral characteristics for the reference and the target label contributed in reducing the extent of photobleaching of the latter.

The cumulative hybridisation approach gave insight into the kinetics of hybridisation, in the absence of any real-time monitoring scheme. Figure 4-6 shows the evolution of the S/N of each spot after each sequential hybridisation step, for the three different types of chips.

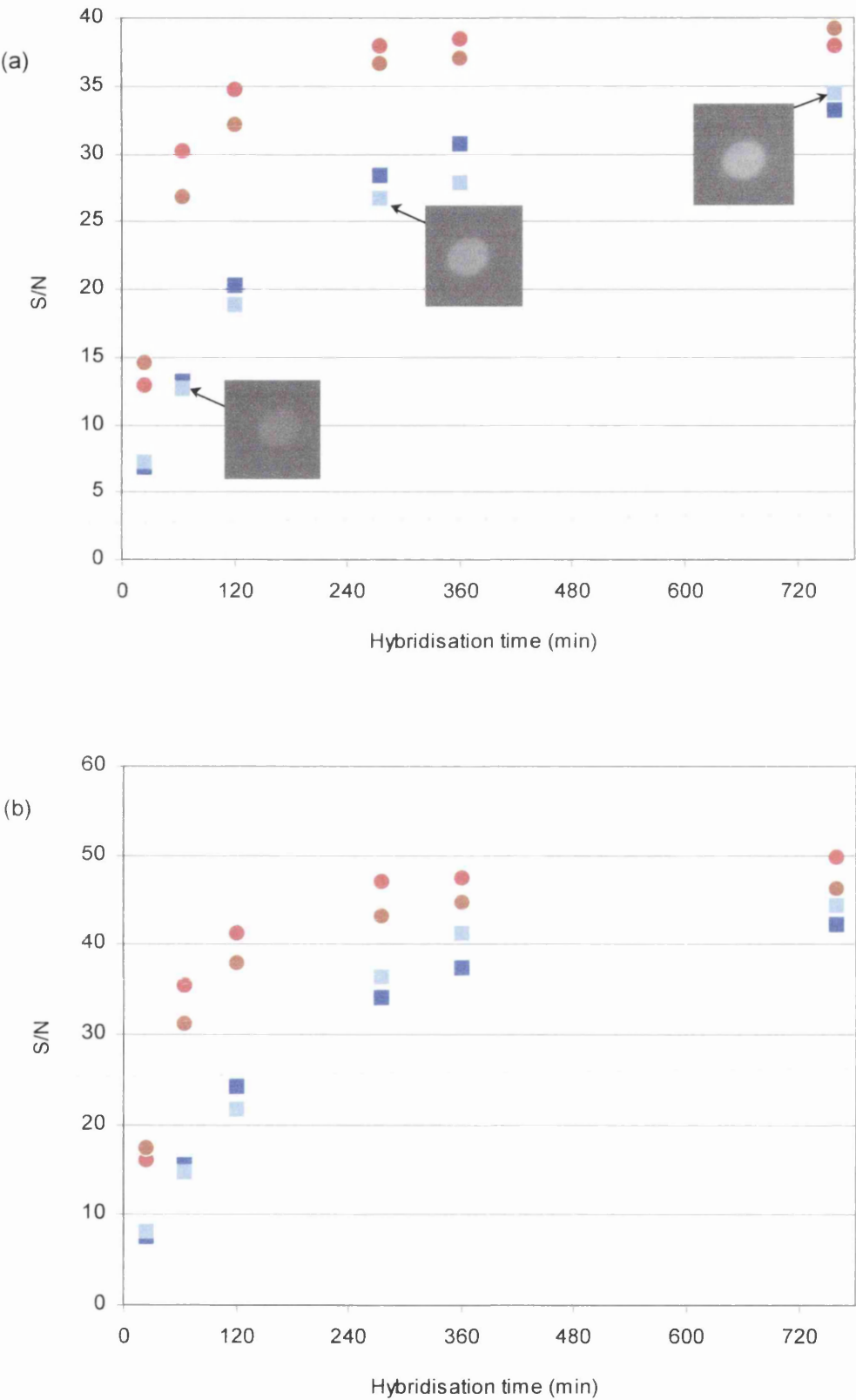


(Figure 4-6, continued on next page)

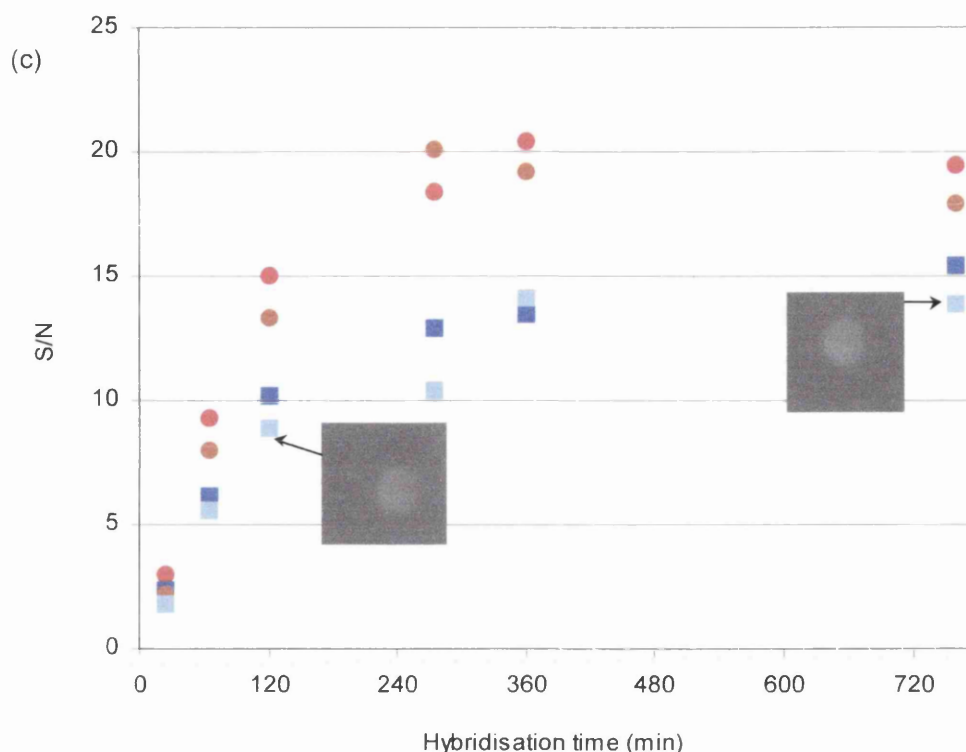


Figure 4-6. Evolution of the S/N of ODN spots during sequential hybridisation of planar chips. a) glass; b) thermally oxidised silicon; c) O_2 plasma-oxidised PDMS. Circles: target T3 (100 nM); squares: target T4 (50 nM).

In the case of the glass and thermally oxidised silicon chips, all the plots of S/N versus hybridisation time exhibited a similar shape, characterised by an initial quasi-linear increase followed by a progressive lowering of the increase rate. A plateau was reached after circa 4 hours of hybridisation in the case of the more concentrated target, T3, with S/N values of 37-39 and 44-50 on the glass and silicon chips, respectively. Similar (slightly lower) levels of S/N were reached in the case of T4 after about 12 hours. The initial rate of increase of S/N, measured as the tangent to the curve at an hybridisation time of zero, was about twice higher for T3 (present in the hybridisation cell at 100 nM) than for T4 (50 nM).

The shapes of the curves are characteristic of pseudo-first order binding kinetics, as expected in the case of a heterogeneous hybridisation assay in which the solution-borne target is in excess over the probe. The spots formed on the flat substrates were about 0.8 mm in diameter; assuming that silanisation resulted in a coverage density of free thiol groups of 330 fmol mm^{-2} (Section 4.5.3), a maximum of circa 160 fmol probe molecules could be covalently immobilised within each spot. Thus, the hybridisations were in effect carried out in conditions of a vast excess (1-2 orders of magnitude) of targets with respect to the probes. Consequently, the concentration of the targets in the hybridisation cell could be considered to remain equal to its initial value, i.e. 100 nM for T3 and 50 nM for T4, over the course of the experiment.

The formation of a nucleic acid duplex by hybridisation of a target to a probe can be described by the following equation:



where k_1 is the binding rate constant and k_{-1} is the dissociation rate constant. The present situation in which targets are present in a vast excess with respect to the probes corresponds to a saturation hybridisation behaviour, in which the evolution over time of the amount of duplex formed is given by:

$$[\text{Duplex}]_t = [\text{Duplex}]_\infty (1 - \exp(-t / \tau)) \quad (\text{Equation 4-6})$$

$$\text{with } [\text{Duplex}]_\infty = [\text{Probe}]_0 \quad (\text{Equation 4-7})$$

$$\text{and } \tau = (k_1 [\text{Target}]_0 + k_{-1})^{-1}, \quad (\text{Equation 4-8})$$

where $[\text{Duplex}]_\infty$ is the surface density of probe-target duplex at saturation,
 $[\text{Probe}]_0$ is the surface density of probe within each spot,
 $[\text{Target}]_0$ is the initial concentration of target in the sample,
 and τ is the relaxation time.

The difference observed experimentally between T3 and T4 in the initial rates of increase of S/N, characterised by the tangent to the curves at $t = 0$, reflects the difference in the concentrations at which the two targets are present in the sample. No curve fitting was attempted, as this would have required additional experimental data (for a series of $[\text{Target}]_0$ values).

Considering that each spot was formed by the deposition of 0.5 μL of a 12.5 μM probe solution, and taking into account the fact that circa 60% of the probe molecules were activated upon incubation with s-GMBS,¹⁶¹ an estimated 7500 fmol of activated probe molecules were present within each spot, before washing off non-covalently bound probes, representing a > 20-fold excess with respect to the number of thiol anchoring sites present over the surface covered by each 0.8 mm diameter spot. This probably resulted in a high density of immobilised probes, up to 330 fmol mm^{-2} (the coverage density of thiol anchoring groups) and higher than the optimal 66 fmol mm^{-2} , causing possible steric crowding effects. Nevertheless, the bioactivity of the probes towards heterogeneous hybridisation was demonstrated.

The difference in S/N observed between the two spots of same probe sequence deposited on each substrate, seen in Figure 4-6, probably reflects a difference in the number of immobilised probe molecules within each spot, as accounted for by Equation 4-7.

The S/N of the reference spot imaged through the FAM optical channel remained below 3 throughout the hybridisation sequence, indicating that no significant formation of mismatched probe-target duplexes took place.

In the case of the PDMS chip, the experimental data showed some deviation from a pure pseudo-first order kinetics. In particular, the S/N for T4 exhibited a decrease over the last hybridisation period (between 6 and 12 hours). The background signal did not increase significantly over that period; however, the fluorescence intensity of the reference spot, imaged through the Cy5 optical channel, was found to decrease by circa 16% over the whole course of the experiment (12 hours), whereas this decrease was lower than 3% in the case of the glass and silicon chips. This phenomenon was ascribed to a loss of probe from the surface over the course of the experiment, suggesting a degradation of some of the covalent bonds between the probes and the silanised PDMS^{ox} layer or, more likely, a degradation of the silanised PDMS^{ox} surface. A loss of probe would also account for the lower levels of S/N obtained in the case of the PDMS chip with respect to the glass and silicon chips.

4. 6. Conclusions

A strategy has been developed for the covalent immobilisation of ODN probes onto glass and thermally oxidised silicon substrates that is suitable to the production of DNA chips. The bioactivity of the surface-bound probes in multiplexed heterogeneous hybridisation assays with ODN targets has been demonstrated through the monitoring of hybridisation kinetics.

Heterogeneous hybridisation was observed even though the coverage density of probes was not optimised. Although the possible occurrence of steric crowding in the experiments reported above was not studied, the use of a less concentrated probe solution would probably have been beneficial to the uniformity and functionality of the spots. The issue of optimising the probe coverage density for enhanced functionality is addressed in the next chapter, where the probe immobilisation strategy presented above is applied to microchannel substrates.

CHAPTER 5. ARRAYING OF MICROCHANNEL SUBSTRATES WITH OLIGONUCLEOTIDE PROBES

5. 1. Introduction

The generation of multiple sensing elements on a solid substrate is the major step in the fabrication of a DNA chip. The levels of accuracy, precision and repeatability that can be achieved in the probe attachment process determine the suitability of the chip to quantitative nucleic acid hybridisation analysis. In this chapter, the arraying of microchannel substrates with ODN probes, in order to produce medium-density flow-through microchannel oligoarrays, is reported.

Since the use of MCG chips of increased thickness provides a way of increasing the number of probe molecules immobilised within each spot without increasing the lateral dimensions of the spots, a range of chip thicknesses were considered, in terms of the effectiveness of the process of probe immobilisation on the microchannel sidewalls. In this respect, the physical-chemical processes that control the formation of spots on microchannel substrates were investigated. The specific morphology and wetting properties of the microchannel substrates were taken into account in the arraying process, leading to optimisation of the aliquot volume and concentration of the probe solutions to be dispensed.

5. 2. Constraints associated with the use of microchannel substrates

The morphology of microchannel substrates introduces specific constraints in terms of surface modification of the channel sidewalls.

5. 2. 1. Liquid-phase treatment of microchannel glass and microchannel silicon

Although the microchannels readily fill by capillary action, their non-interconnected nature results in each channel behaving as a quasi-independent microreservoir, whose interface with the outer medium is restricted to the channel opening, on both sides of the chip. This limits both fluid exchange between the inside of the microchannels and the medium in which the chip is immersed, and reagent access to the surface of the channel walls. Likewise, for a solute to be rinsed out of the inner volume of a microchannel, large diffusion distances are involved due to the high aspect ratio of the microchannels. Furthermore, the rate of evaporation from the inside of the microchannels is low, due to the limited surface area of the liquid / air interface.

These characteristics lower the efficiency of convective mixing procedures commonly employed with planar substrates, such as the use of a shaking and / or rotating table, and the flushing of solvents or solutions over the surface. As a way to enhance fluid and solute exchange within the microchannels, ultrasonication was used during liquid-phase chemical treatment. The large

effective surface area of the microchannels promotes bubble nucleation at the channel walls, thereby further increasing convective mixing.

The small feature size of the microchannels makes the use of viscous solutions, such as concentrated sulfuric acid used in cleaning / activation procedures, labour-intensive in that extremely long rinsing times are required. Strongly basic solutions are known to have an etching action on silica surfaces, resulting in an increased roughness of the surface, hence an increased effective surface area. Although this is not necessarily detrimental in terms of subsequent derivatisation and biofunctionalisation of a substrate, the optical properties of the surface are significantly affected, as surface roughness greatly increases light scattering at interfaces between media of different refractive indices. In the case of microchannel materials to be used as biochip substrates, the need to ensure compatibility with optical detection schemes such as fluorescence implies that the waveguiding properties of the substrate be maintained, as evidenced in the previous chapter. It is therefore important that the level of smoothness of the microchannel walls be not compromised by any etching action of the cleaning solutions. Therefore, concentrated sulfuric acid and strongly basic solutions were not used in the surface treatment of microchannel substrates.

5. 2. 2. Thermal oxidation of microchannel silicon

As shown earlier, surface oxidation of silicon substrates is required so as to allow for the functional attachment of probes through organosilane chemistry. In the case of MCS substrates, controlling the thickness of the oxide layer is important for morphological reasons, since the layer thickness will directly affect the diameter of the microchannels. The thermally grown oxide layer must be uniform in thickness from one microchannel to the next.

Other considerations than chemical reactivity pertain to the surface oxidation of the sidewalls of MCS substrates. As a dielectric material, silicon dioxide can protect fluorescent labels from possible fluorescence quenching by the silicon substrate. In terms of optical detection, the growing of an oxide layer along the microchannel sidewalls could be used to beneficially alter the waveguiding properties of the chip, for example through the fabrication of "hybrid" Si / SiO₂ microchannel chips where thin silicon walls would prevent inter-channel cross-talk while the presence of a silicon dioxide layer would allow for the generation of an evanescent electromagnetic field along the sidewalls. Finally, the controlled growing, and subsequent removal, of a layer of silicon dioxide along the sidewalls of the microchannels provides a means to alter the dimensions of the channels; this could be used in developmental and characterisation studies.

5. 3. Piezoelectric ink-jet arraying of microchannel substrates

5. 3. 1. Experimental

5. 3. 1. 1. Materials and reagents

MCG chips of various thicknesses (0.5 mm, 1 mm and 2 mm) were wafered from a 10 μm pore diameter boule of MCG, obtained from Galileo Electro-Optics Corp. (Sturbridge, MA, USA). The surfaces of the chips were not polished after dicing. Macroporous silicon chips, obtained from Infineon Technologies AG (München, Germany), were 0.5 mm thick and featured a square array of circa 10 μm feature size channels, as shown in Figures 3-7 and 3-8. Standard float glass microscope slides (BDH, Poole, UK) were used as planar substrates, for comparative purposes.

The probe used, P2-f, was a fluorescently labelled, amino-terminated 18-mer oligonucleotide of sequence "F"CCCAGGGAGACCAAAGC"T", where "T" denotes a 3'-aminohexyldeoxy-thymidylate modifier and "F" a 5'-carboxyfluorescein phosphoramidite (6-FAM) label.

A non-labelled probe, P2, with sequence and 3' modifier as above, was also used. The probes were purchased as a lyophilised powder from Glen Research (Sterling, VA) and subsequently dissolved to appropriate concentrations in 1x SSC.

5. 3. 1. 2. Apparatus

Oxidation furnace

Thermal oxidation of MCS chips was carried out using the instrumentation described in Section 4. 4. 1. 3. 1.

Microarrayer

As stated above, structured immobilisation of multiple biorecognition sites on microchannel substrates has to rely on spotting techniques. In the work presented in this thesis, piezoelectric technology was chosen over syringe-solenoid technology due to its inherently lower dispensing volume capability, permitting the production of higher density biochips. Microchannel DNA chips were produced using a Packard BioArrayer piezoelectric spotter (Packard Instrument Co., Meriden, CT), a photograph of which is shown in Figure 5-1. This instrument features a multiple printing head with four 75 μm internal diameter capillary tips, capable of dispensing as little as 0.35 nL per piezo actuation. Upon spotting, the tips remain some 100 μm above the surface. The resolution of the positioning stage is 10 μm laterally and 50 μm vertically.

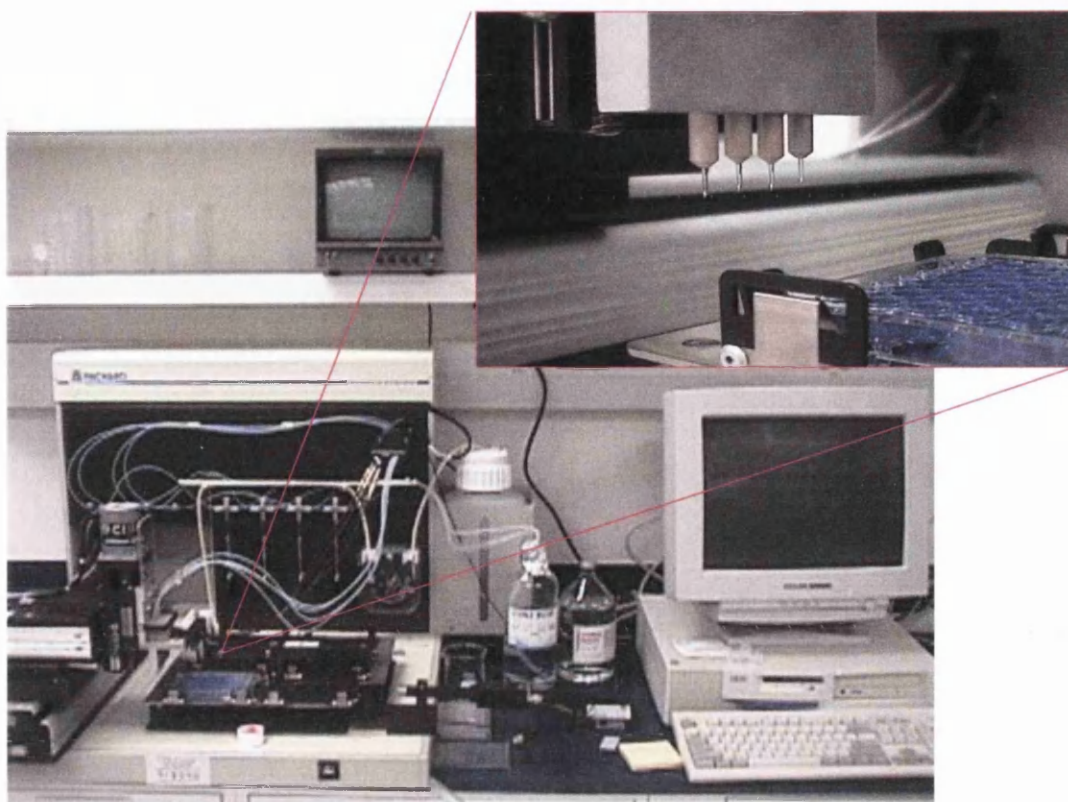


Figure 5-1. Photograph of the piezoelectric ink-jet spotter (Packard Biochip Arrayer 1) used to produce microchannel DNA chips. The insert shows the printing head with its 4 dispensing tips.

Brightfield and fluorescence microscopy

Spotted chips were imaged by white light brightfield microscopy and epifluorescence microscopy using an Eclipse E800 epifluorescence microscope (Nikon, Tokyo, Japan) fitted with an Orca C4742-95 color, 12-bit CCD camera (Hamamatsu, Hamamatsu City, Japan). Objective lenses, also from Nikon, were a 4x Plan Apo and a 20x Fluor, with NA values of 0.45 and 0.20, respectively. The fluorescence filter set used was DM510-B2A (Nikon). The use of “yellow” FAM labels (excitation maximum circa 495 nm, emission maximum circa 520 nm) rather than longer wavelength dyes was justified by the low spectral responsivity of the Orca camera above 550 nm, as shown in Figure 5-2.

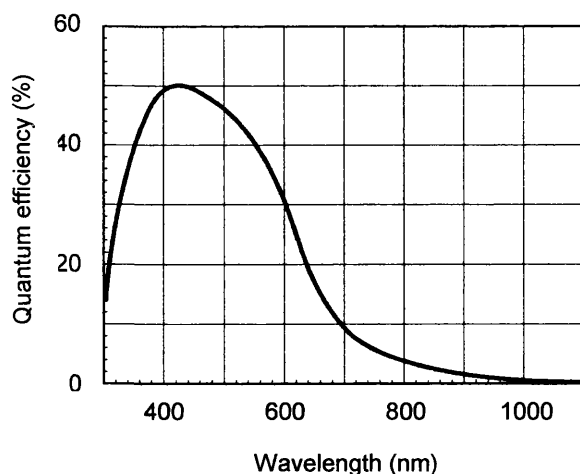


Figure 5-2. Spectral responsivity curve of the Hamamatsu Orca CCD camera (manufacturer's data).

5. 3. 1. 3. Procedures

5. 3. 1. 3. 1. Preparation of activated MCG and MCS substrates

Thermal oxidation of MCS substrates

As stated above, optimisation of the thermal oxidation process for MCS chips was directed towards the obtention of a uniform (in thickness and in physical properties) oxide layer over the whole array of microchannels. Care was thus taken to ensure that the batch of chips to be oxidised were placed within the flat zone of the furnace. As the number of MCS chips available was limited to a small number, and layer thickness measurements on microchannel substrates are difficult to implement, planar silicon reference pieces were used first to assess oxidation rates. Planar silicon pieces were also used to determine the flat zone of the furnace.

A batch of three MCS chips, plus one planar reference piece, were oxidised at circa 1050°C and 1.5 cm³ min⁻¹ O₂ flow rate, for 8 hours. Prior to oxidation, the chips were cleaned in IPA, Pirhana solution and buffered HF for 1 minute to remove any contaminated native oxide layer. After oxidation, the MCS chips as well as the planar chip exhibited a purplish hue, indicating the presence of an oxide layer. Ellipsometric measurements indicated the presence of a 353.7 ± 2.1 nm oxide thickness on the reference piece.

Surface activation of MCG and oxidised MCS substrates

The MCS chips were thermally oxidised as described in Section 5. 3. The procedure used for the cleaning of MCG and thermally oxidised MCS chips was similar to that used with planar substrates. Ultrasonication was used, as justified above. The chips were individually placed in a beaker and subjected to sequential 10 minute ultrasonication periods in IPA, acetone, methanol, and RO water. As with planar substrates, care was taken to avoid the formation of

drying marks. Finally, the substrates were rinsed with ample water, blow-dried with N₂ and further dried at 120°C for at least 1 hour.

Activation of the surface hydroxyl moieties was achieved by sequential sonication in 1 M nitric acid, water, and ethanol, 10 minutes each. The chips were then blow-dried and baked at 80°C for 12 hours before silanisation. The same protocol was used for the planar glass chips. As justified above, the use of strong bases and concentrated sulfuric acid was avoided.

Silanisation

Microchannel chips were incubated in 2.5% v/v MPTS in dry toluene, at room temperature, for one hour. The number of silane molecules contained within the volume of solution enclosed within each single channel is in a 3 order of magnitude excess as compared to the amount needed for a monolayer coverage. Therefore, thorough washing is required at the end of the incubation period, in order to remove the excess silane. This was achieved by washing the chips by sequential 10 minute ultrasonication steps in toluene, 1:1 toluene: absolute ethanol, and absolute ethanol. Between each sonication step, the chips were drained by blotting on low-lint absorbent tissue. Finally, the chips were baked at 80°C for 4 hours.

5. 3. 1. 3. 2. Preparation of activated probe solutions

A 30 µM solution of FAM-labelled probe, P2-f, and 30 µM and 60 µM solutions of non-labelled probe, P2, were prepared as described in Section 4. 5. 2. 2. 2.

5. 3. 1. 3. 3. Microarrayer operation

The Packard Biochip arrayer comprised a holder for a 384-well microtitre plate, into which the probe solutions to be dispensed were introduced by pipetting. The microchannel chips were placed in a specially designed tray whose external dimensions were identical to those of a microtitre plate. The tray held 24 (6 x 4) microchannel chips of standard 12 mm x 12 mm dimensions. The desired array pattern for each chip to be spotted was entered into the computer memory, as was the location of each probe solution in the microplate. Although the arrayer is a highly automated apparatus, the appropriate setting of a number of operating parameters was incumbent to the user, as discussed below.

Loading of the printing tips

Operation of the piezoelectric mechanism requires the entire printing capillary to be filled with an incompressible fluid. As a consequence, air is not suitable for that purpose. Loading of the tips is achieved by aspiration from a syringe pump. As the total volume that is required to fill the capillary is, in most instances, much larger than the volume of probe solution to be dispensed, a plug of water is first aspirated, followed by a sufficient volume of the probe solution. In this approach, diffusion of probe molecules into the water plug over time can not be avoided, which leads to mixing, and dilution of the probe solution, at the water-probe solution interface.

Therefore, the volume of probe solution that is aspirated into the capillary must be sufficient to ensure that the time-expanding mixing zone does not reach the lower part of the printing tip over the time frame of the arraying job. In practice, the volume of probe solution that was aspirated into the capillary before each arraying job was 10 times the volume of probe solution to be spotted. Given the relatively low value for the diffusion coefficient of probe molecules in aqueous solutions (circa $10^{-7} \text{ cm}^2 \text{ s}^{-1}$ for < 20 base long ODNs), this ensured that the probe solutions were dispensed at their original concentration.

Washing of the tips

Since the experiments described in this chapter involved a single probe sequence to be arrayed on each chip, print tips were not cleaned between the loading of different concentration solutions. However, the arrayer was programmed to proceed in order of increasing concentrations. Two different tips were used for the FAM-labelled and non-labelled probes, respectively.

Chips prepared for experiments described in subsequent chapters required the spotting of several different probe sequences, and/or different concentrations of the same probe, onto a single chip, such that the four tips available on the printing head did not suffice for the whole arraying job to be carried out without the need to clean at least one of the tips. In that case, thorough cleaning of the tips was necessary in order to alleviate contamination by carry-over. The cleaning of a tip involves the flushing out of the remainder of solution, followed by the loading of ultrapure water and the in-line sonication of the tip. The efficiency of the cleaning process could benefit from the use of organic solvents instead of water. However, the purity of organic solvents is known to be compromised by the presence of bacteria that grow inside the tubings when these are filled with water, and are subsequently dislodged from the tubing wall by the organic solvent. The presence of these adventitious bacterial particles is not compatible with the small dimensions of the printing tips (75 μm internal diameter), which are extremely prone to clogging.

Arraying of the activated substrates with the activated probe

Microarraying was carried out in ambient conditions, with no particular control over environmental humidity and dust. Neither the sample containers nor the chips were cooled during operation.

2 nL, 5 nL and 20 nL aliquots from the 30 μM solution of fluorescently-labelled probe were deposited onto each glass chip (0.5 mm, 1 mm and 2 mm thick MCG, and planar glass), in quadruplicate. MCG and thermally oxidised MCS chips were arrayed with 1 nL, 2 nL, 3 nL and 5 nL spots of a 30 μM solution of the non-labelled probe. The silicon chips were spotted with the flat side (*i.e.* the side, shown in Figure 2-9(c), that does not feature the KOH pyramidal etching pits) facing up. A 0.5 mm thick MCG chip was also spotted with 5 nL and 20 nL aliquots from 30 μM and 60 μM solutions of the non-labelled probe, in quadruplicate.

5. 3. 2. Results and discussion

5. 3. 2. 1. Differences in wetting properties between microchannel glass and planar glass

5. 3. 2. 1. 1. Compared dimensions and standard of uniformity of spots

Brightfield optical microscopy images of the spotted chips were acquired, after evaporation of the spotting buffer (*i.e.*, in a "dry" state) but prior to any subsequent washing. All of the images of spotted MCG and planar glass chips were acquired with the focus set on the front (top) surface. These brightfield images provide a convenient way to determine the physical size of the spots, due to aggregation of the spotting solution and formation of buffer crystals inside the microchannels.

Figure 5-3(b) shows the radial intensity profiles of the brightfield (Figure 5-3(a)) and epifluorescence (Figure 5-3(c)) images of equivalent spots of fluorescently labelled ODN probes deposited on planar glass and MCG, using the piezoelectric arrayer.

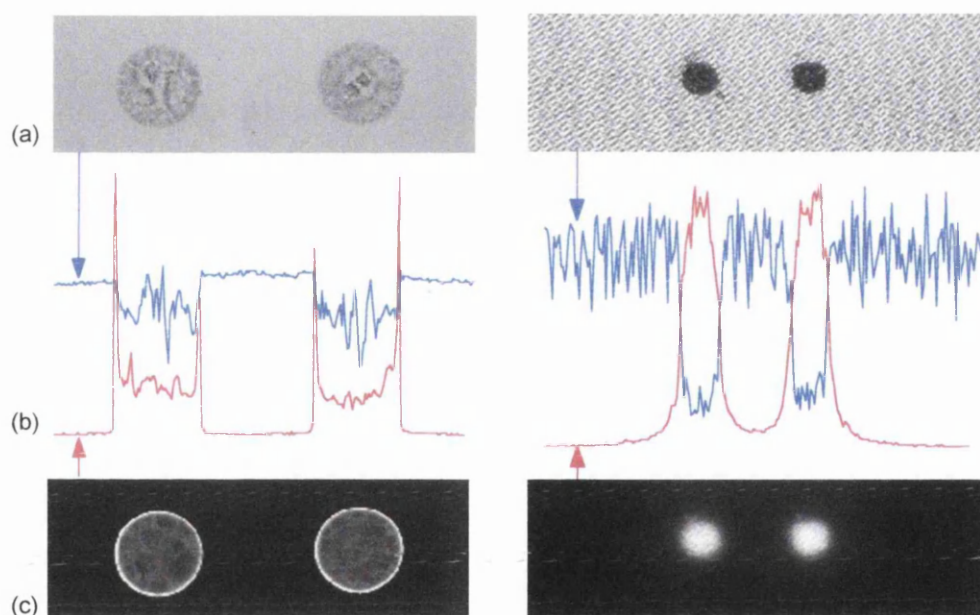


Figure 5-3. Brightfield (a) and epifluorescence (c) microscopy images, and associated radial intensity profiles (b), of spots formed by the dispensing of 5 nL aliquots from a 30 μ M solution of fluorescently-labelled probe in 1x SSC, onto a planar glass slide (left) and a microchannel glass chip (right). The images were acquired using a 4x, 0.2 NA lens. Each profile curve was obtained by averaging 4 adjacent pixel rows.

In the case of the planar glass substrates, both the brightfield image and the fluorescence image show a poor level of uniformity of the spots, including the presence of buffer crystals having formed during evaporation of the spotting solution. The bright outer rings seen in the fluorescence image are due to scattering of the excitation light at the edge of the spots.

A number of publications concerned with the arraying of DNA probes on planar solid substrates have reported such inhomogeneities within spots,^{71,72,111} and ascribed the effect to the transport of material from the center to the edges of the deposited droplets upon evaporation. By comparison, the spots on the MCG substrate appear to be much more uniform. In particular, no outer rings can be seen in the fluorescence image. In addition, the spots formed on MCG exhibit a smaller footprint, with a diameter of circa 40% that measured on planar glass.

An observation not directly relevant to the present study, but closely related to the work presented in Chapter 3 of this thesis, is the significant difference in the shapes of the intensity profiles of the MCG spots between the fluorescence image and the brightfield image. The intensity profiles show some extent of spatial spreading of the fluorescence signal on the MCG chips, a phenomenon that is not observed with planar glass chips for which the dimensions of the spots are not significantly different between the brightfield image and the fluorescence image. This effect is related to inter-channel optical cross-talk in microchannel glass and to imaging properties of microscope objective lenses in three dimensions.

5.3.2.1.2. Processes governing spot generation on microchannel substrates

The smaller footprint and higher uniformity of MCG spots, as compared to planar glass spots, reflect the differences in wetting properties between the two types of substrates. When a droplet of liquid is released from the capillary tip of the piezoelectric spotter, and impinges onto the surface of a MCG chip, the liquid undergoes lateral and axial redistribution, through both spreading over a certain area of the front surface of the substrate and drawing into the microchannels by capillary action. Since the latter takes place on a short time scale with respect to evaporation, probe and buffer molecules present in the dispensed liquid can be assumed to be uniformly distributed between all of the microchannels encompassed by the dispensed volume. Any redistribution of probe molecules occurring upon subsequent evaporation of the solvent is confined within the volume of each microchannel, rather than taking place over the whole spot area as in the case of planar substrates.

The wetting properties of MCG substrates are a combination of the surface tension properties of both the interstitial area and the channel walls, and the capillary action induced by the microchannels. Consequently, it can be expected that only part of the total dispensed volume will be drawn into the microchannels, the remaining fraction of the dispensed volume forming a convex meniscus on the surface of the chip. The extent of this fraction is expected to depend on the dispensed volume, as well as on the morphology (channel diameter, open fraction, and chip thickness) and surface properties (hydrophobicity) of the microchannel substrate. The effect of these parameters, including chip thickness, upon the spot dimensions, was investigated and the results are presented below.

5.3.2.2. Parameters affecting the dimensions of oligonucleotide spots on microchannel glass

5.3.2.2.1. Effect of chip thickness and dispensed volume upon the spot dimensions

The rationale for investigating the effect of chip thickness lies in the possibility of modulating the effective surface area of microchannel substrates of given morphology, *i.e.* same channel diameter and same open fraction, in direct proportion to the chip thickness.

Figure 5-4 shows brightfield images of spots resulting from the deposition of various volumes of the same probe solution onto MCG chips of various thicknesses.

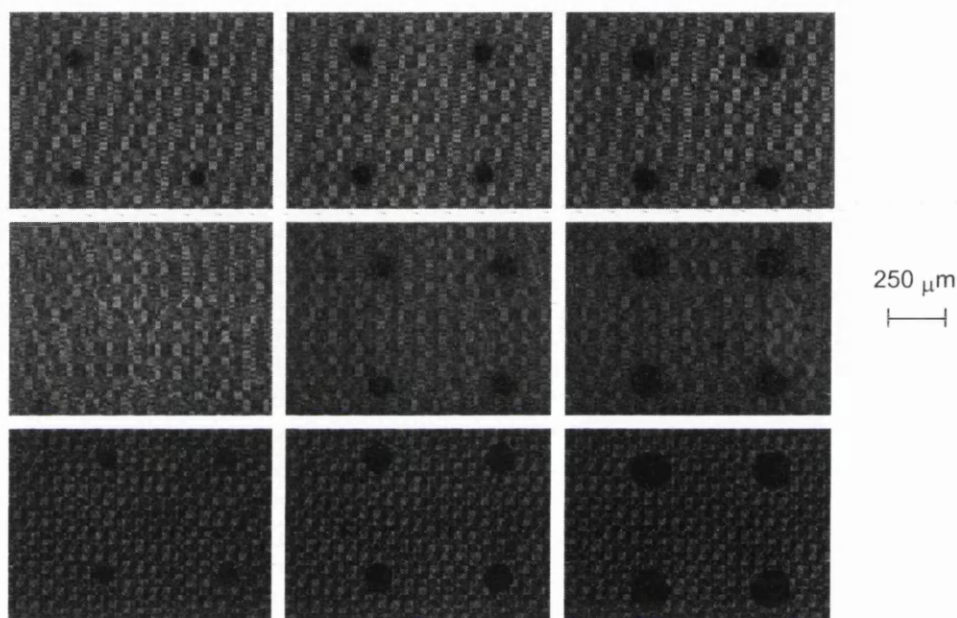


Figure 5-4. Brightfield images, acquired with a 4x, 0.20 NA objective lens, of 30 μ M ODN spots (in quadruplicate) on microchannel glass, prior to washing. Left to right: 5, 10 and 20 nL; bottom to top: 0.5 mm, 1 mm and 2 mm thick chips. The generation of 5 nL spots on the 1 mm thick chip was impeded by a spotter disfunction.

As expected, Figure 5-4 shows that the spot dimensions are affected not only by the spotted volume, but also by the thickness of the chip. At identical spotted volumes, smaller spots are formed on thicker chips. Although the degree of porosity of the chip (determined by both the channel diameter and the open fraction) is also expected to affect the spot dimensions, the effect of this parameter was not studied. The diameters of the spots are plotted as a function of the dispensed volume in Figure 5-5.

The spot diameters obtained on planar glass are also shown, for comparative purposes.

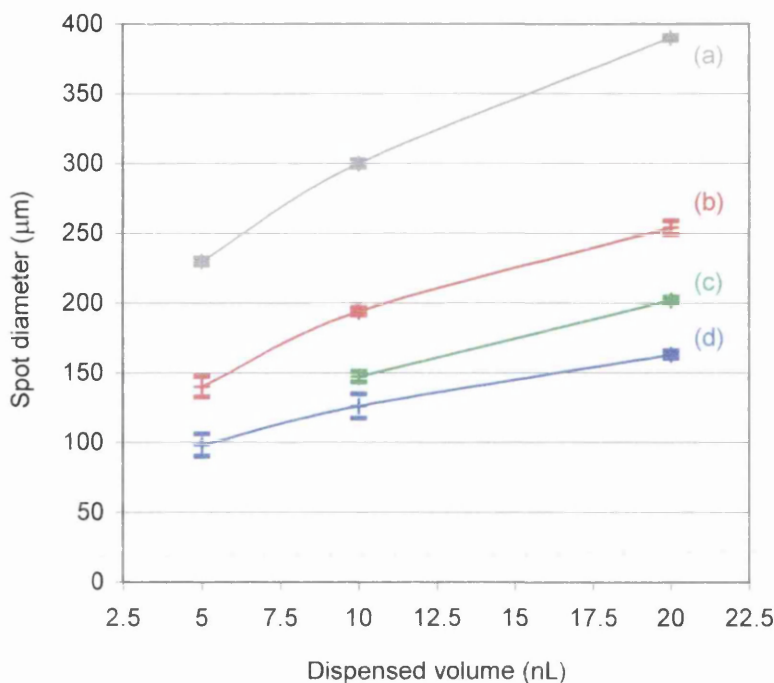


Figure 5-5. Spot diameters for different glass chips, as a function of the dispensed volume, measured from the brightfield images of Figure 5-4. (a) Planar glass; (b) 0.5 mm thick MCG; (c) 1 mm thick MCG; (d) 2 mm thick MCG. The bars represent the 95% confidence intervals for 4 spots.

As intuitively expected, the rate of increase in spot dimensions with increasing dispensed volume is larger for thinner chips.

From the knowledge of the dimensions of a spot generated by the delivery of a given volume of solution on MCG, the fractions of the dispensed volume that either fill the microchannels, or form a meniscus at the surface of the chip, can be estimated. The values for the morphological parameters of MCG reported in Table 3-1 were used in the calculation. The spot dimensions used are those determined from the brightfield images of Figure 5-4 for dispensed volumes larger than 5 nL, and from Image (a) of Figure 5-7 (see below) for volumes lower than 5 nL. The results of the calculation of the ratios V_{dr} / V_{ch} , where V_{dr} is the volume of the aliquot of probe solution dispensed onto the microchannel substrate, and V_{ch} the internal microchannel volume encompassed by the resulting spot, are shown in Table 5-1.

The calculated ratios V_{dr} / V_{ch} are seen to encompass a wide range of values below and above unity. The numbers smaller than 1 point at the possibility of the dispensed volume being less than the combined volumes of the microchannels over the spot area. For all the chips, the trend shown in Table 5-1 is clear, with the values for V_{dr} / V_{ch} increasing as the dispensed volume increases.

Chip thickness (mm)	Dispensed volume (nL)					
	1	2	3	5	10	20
0.5	0.54	0.70	0.84	1.03	1.08	1.26
1	NA	NA	NA	0.75	0.94	0.99
2	NA	NA	NA	0.53	0.64	0.82

Table 5-1. Calculated ratios V_{dr} / V_{ch} , where V_{dr} is the volume of an aliquot of a 30 μM solution of oligonucleotide probe in 1x SSC buffer dispensed onto the microchannel substrate using the ink-jet spotter, and V_{ch} is the internal microchannel volume encompassed by the resulting spot. The internal microchannel volume encompassed by a spot was estimated from the footprint of the spot, determined by brightfield imaging, and the morphology of the microchannel substrate.

In the case of the 1 mm and 2 mm thick chips, the dispensed volume does not suffice to fill the entire volume of the microchannels, suggesting that probe attachment in the top part of the channels will be compromised. In the case of the 0.5 mm thick chip, there is an excess liquid for dispensed volumes larger than 5 nL. These conditions are favorable, in terms of probe attachment, for coating the whole microchannel wall. A dispensed volume of 5 nL closely matches the internal volume of the microchannels, while the dispensing of lower volumes results in partially filled microchannels.

5. 3. 2. 2. 2. Optimisation of the concentration of the spotting solution

For a MCG chip of given thickness, channel diameter and open fraction, a given number of anchoring sites is available on the wall of each microchannel. The total number of sites available within a given spot area can be calculated from the silane coverage density and the spot footprint area. As stated in the previous chapter, the former was determined as 2×10^{11} molecules per mm^2 , whilst the latter can be assessed from the brightfield image of the spot of interest. Here, the case of a 0.5 mm thick chip is considered. As the spot dimensions used are those determined from the brightfield images of Figure 5-4, in which the probes were spotted at 30 μM , the calculation is valid within a range of probe concentrations in which the latter does not significantly affect the dimensions of the spots.

As stated earlier, the optimum probe coverage density is 66 fmol mm^{-2} . For a given spotted volume, the number of probe molecules dispensed is proportional to the spotting concentration; however, the limited binding efficiency of the s-GMBS activation step (60%) has to be taken into account in the determination of the number of covalently attached probes. Table 5-2 shows the calculated optimal concentration of spotting solution for this level of concentration to be reached (assuming uniform distribution of probe inside the channels).

Dispensed volume (nL)	Number of thiol groups within 3D spot area (10^{10})	Spotting concentration (in μM) for a probe coverage density of 66 fmol mm^{-2}
5	38.8	42.7
10	74.5	41.0
20	127.7	35.1

Table 5-2. Calculated numbers of binding sites and optimal spotting concentration for oligonucleotide probe spots on 0.5 mm thick, 10 μm channel diameter microchannel glass chips. A silane coverage density value of 2×10^{11} molecules per mm^2 was used in the calculations.

As seen from Table 5-2, the optimal concentration varies between 35 μM and 43 μM for dispensed volumes between 5 nL and 20 nL. These values are close enough to the 30 μM value used in the experimental determination of the spot dimensions to validate the underlying assumption that the spot size is not affected by the probe concentration within this range, as confirmed by Figure 5-6.

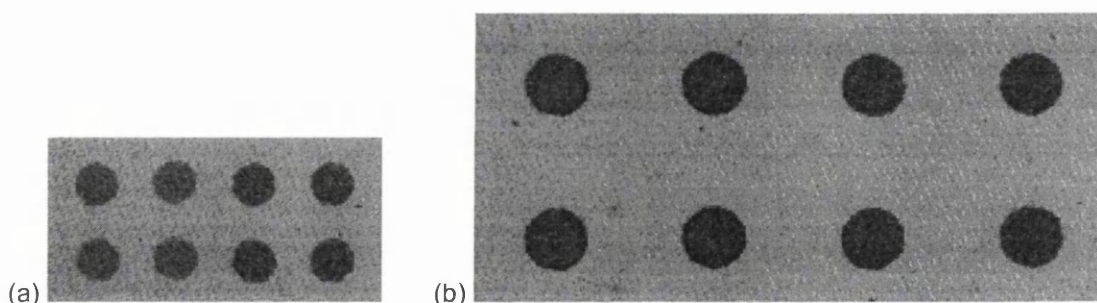


Figure 5-6. Brightfield images of oligonucleotide probe spots formed on microchannel glass from solutions of variable concentration in 1x SSC. (a) 5 nL, 30 μM (left) and 60 μM (right); (b) 20 nL, 30 μM (left) and 60 μM (right).

The fact that an increase in probe concentration from 30 μM to 60 μM does not significantly affect the dimensions of 5 nL to 20 nL spots is easily understood by the predominance, in the spotting solution, of the buffer molecules, which are present at 2-3 orders of magnitude higher concentrations than the probe molecules (1x SSC contains 15 mM sodium citrate and 150 mM NaCl). In addition, the ODN probes are of relatively short length (18-mers), and thus do not impart any marked polymeric behaviour to the solution, as would be the case for cDNA fragments with secondary structure conformations. Also, even though the probes used here were labelled with a fluorescent dye, comparison with similar spots (same volume, same concentration) of non-labelled probes, as for example in Figure 5-7(a) below, show that the fluorescent label does not significantly affect the spot dimensions.

5. 3. 2. 3. Comparison of oligonucleotide spots formed on microchannel glass and on microchannel silicon

The wetting properties of MCS were expected to differ from those of MCG, due to differences in morphology and surface tension properties, the latter resulting from different silane coverage densities. In order to assess to what extent this affected spot formation, a MCG chip and a MPS chip, both 0.5 mm thick, were arrayed with identical volumes (from 1 nL to 5 nL) of the non-labelled probe solution. The silicon chips were spotted with the flat side upwards.

Figure 5-7 shows brightfield microscopy images of the spots formed on both substrates.

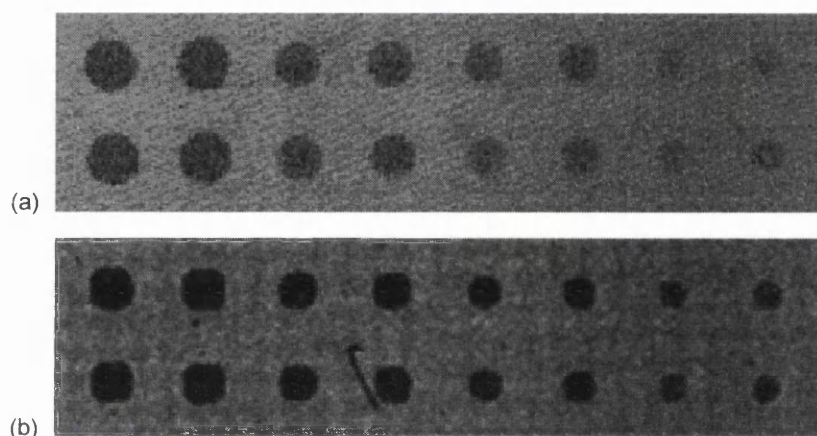


Figure 5-7. Brightfield images of oligonucleotide spots on microchannel substrates. (a) Microchannel glass; (b) thermally oxidised macroporous silicon. The probes were deposited from a 30 μ M solution in 1x SSC with dispensed volumes of 5 nL, 3 nL, 2 nL and 1 nL, in quadruplicate from left to right.

Figure 5-7 shows that the spots formed on macroporous silicon have a 5-10% smaller footprint than the spots formed on MCG. The shape of the spots differs slightly between the two substrates, and seems to reflect the arrangement of the microchannels (hexagonal packing on MCG, square packing on macroporous silicon).

5. 4. Flow-through washing of microchannel chips

As the probe activation step (reaction through which a maleimide moiety is attached to the 3' end of the probe) that is part of the immobilisation strategy described in Chapter 4 has a limited (circa 60%) binding efficiency, a fraction of the activated probe molecules delivered to the surface of a microchannel chip do not bind covalently to the thiol anchoring sites. These probes have to be removed from the sidewalls of the microchannels before the latter can be used in heterogeneous hybridisation assays. As these non-covalently bound probes are involved in physical interactions with the substrate, simple immersion of the chip in a washing solution is not sufficient; some mechanical force is required to overcome the physical interactions and flush the molecules out of the microchannels. This section reports the implementation of forced convection of washing solution through microchannel chips, using

flow cells specially designed and fabricated for use with MCG chips. An attempt at assessing the uniformity of flow over the array of microachannels is also presented.

5.4.1. Experimental

5.4.1.1. Materials

A 0.5 mm thick microchannel glass chip was silanised and spotted with a 16x16 array of 5 nL aliquots from the 30 μ M solution of activated fluorescently-labelled probe P2-f, as in Section 5.3.1.3. A planar glass slide was processed likewise.

5.4.1.2. Instrumentation

5.4.1.2.1. Glass / PDMS flow cell

The simple design of this type of cell was based on disposable PDMS parts that were fabricated without any specific tooling. Figure 5-8 shows a schematic drawing of the cell.

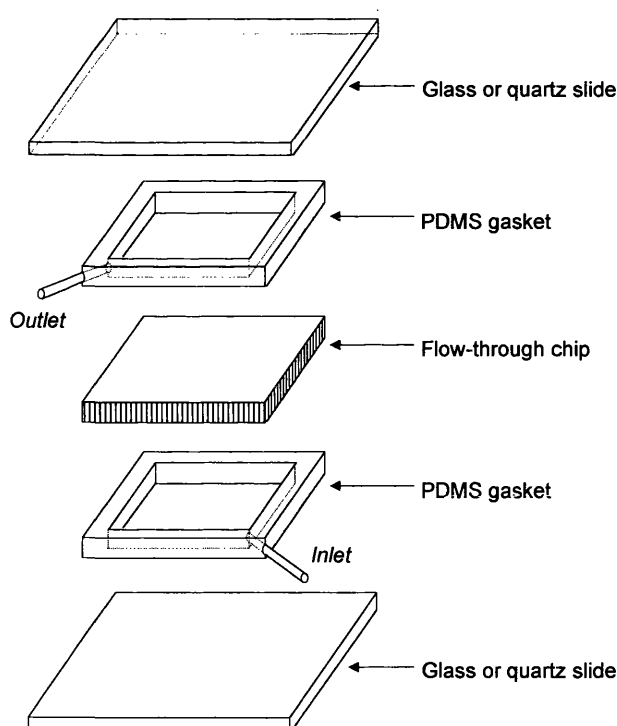


Figure 5-8. Schematic drawing (exploded view) of the glass / PDMS flow cell used in microchannel chip-based bioassays. The design is based on a five-layer configuration (see text). The light blue area represents the active area of the microchannel biochip.

The cell design is based on a five-layer sandwich configuration, of which the microchannel chip is the central layer. On both sides, PDMS serves both as gaskets and as the boundary walls of microchambers. The outer layers consist of glass or quartz slabs. The enclosed volume, henceforth referred to as the cell, comprises the open volume of the chip in addition to the top and bottom chambers. A 2-3 mm wide strip along the edge of the chip is used as a contact area for the PDMS gaskets. The active area of the microchannel chip is represented by the light blue area in Figure 5-8. The elastomeric properties of PDMS allows for a tight, leakproof seal with the surface of the chip to be achieved, by maintaining conformal contact through clamping. The glass or quartz slabs allowed visual inspection of the chip as well as *in situ* fluorescence detection.

The PDMS parts were fabricated so as to comprise a piece of small bore tubing, which serves as fluid inlet / outlet. Micropipet tips (BioRad) were used to that end. Teflon tubing (1/16" o.d.) with standard 1/4-28 flanged end fittings (Supelco, Poole, UK) were coupled to the micropipet tips by insertion and mere conformal fitting. The PDMS parts were made by first pouring a mixture of PDMS base and curing agent (RS Components, UK; ref. 494-966), in a 10: 1 ratio, over a micropipet tip positioned in a Petri dish, before curing the PDMS at 65 °C for 4 hours. A 12 mm x 12 mm square area was then cut out from the cured PDMS slab with the pipet tip protruding at 45° from one corner, and a square 8 mm x 8 mm window was open in the center of the slab, the very tip of the pipet being cut off in the process, creating the inlet / outlet channel. Finally, the PDMS part is peeled off the Petri dish.

Note that this cell configuration did accommodate chips with varying dimensions, including varying thickness. The thickness of the PDMS parts could easily be adjusted over a range of values. The lower limit was determined by the outer diameter of the micropipet tip, *i.e.* 350 µm, to which 100-150 µm must be added for elasticity. In the case of 500 µm thick gaskets and a 500 µm thick MCG chip, the volume of the cell amounted to 2 x 25 µL (chambers) plus circa 10 µL (MCG chip; see Section 2. 2. 2. 3), or circa 60 µL. Smaller volumes could be achieved by replacing the micropipet tip by a microchannel directly molded in the PDMS, which would make PDMS gaskets as thin as 50 µm, and cell volumes as small as 12 µL, possible.

5. 4. 1. 2. 2. Stainless steel flow cell

A more robust alternative to the disposable glass / PDMS cell type described above was fabricated according to the design shown in Figure 5-9. This flow cell was comprised of two machined stainless steel body parts. The bottom part featured a recess which accommodated microchannel chips of standard dimensions (12 x 12 x 0.5 mm³) and through which fluid was circulated via the inlet and outlet ports (fitted with standard Valco connectors). Leakproof sealing with the top part was ensured by a Viton gasket. The top part also comprised a quartz optical window through which the chip can be optically interrogated.

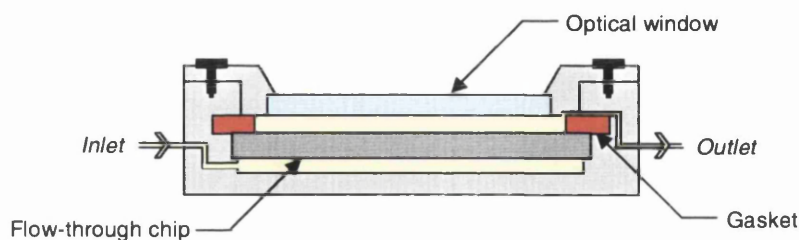


Figure 5-9. Schematic cross-sectional view of the stainless steel flow-through cell used in microchannel chip-based bioassays.

In this design, the top and bottom chambers were 79 μL and 90 μL in volume, respectively. In a subsequent design, the bottom part of the cell was modified so as to feature a concave bottom, in an effort to improve the filling process of the chip as well as the flow uniformity across the array of microchannels.

5. 4. 1. 2. 3. Pump

Either cell could be connected to a reservoir and a waste container with 1/16" o.d. Teflon tubing (Supelco) via Valco fittings. An Ismatec ISM-1014 peristaltic pump (Ismatec SA, Zürich, CH) was used.

5. 4. 1. 3. Procedures

The spotted chip was loaded "dry" into the stainless steel flow cell (the stainless steel flow cell with concave bottom was used). The latter was connected to the tubings and placed within the field of view of a Logitech QuickCam digital camera connected to a laptop computer.

1x SSC buffer was pumped from the reservoir through the flow cell at a continuous flow rate of 0.5 mL min^{-1} . The cell filling process was monitored by acquiring white light images of the MCG chip, through the optical window of the flow cell, at regular intervals.

In order to prevent air bubbles from being trapped inside the hybridisation cell over the course of the filling process, the flow cell was held at an angle so as to keep the outlet port in uppermost position. Gravity then ensured that the top chamber filled completely before liquid reached the outlet port.

The effectiveness of the convective washing process was assessed by fluorescence imaging of the MCG chip, inside the flow cell. An image of the dry chip was acquired, before washing. A second image was acquired after washing solution had been pumped through the chip for 10 min, at 0.5 mL min^{-1} ; buffer was not flushed from the cell prior to imaging. Fluorescence imaging of the MCG chip through the optical window of the flow cell was carried out as described in Section 5. 3. 1.

5. 4. 2. Results and discussion

Filling of the cell and establishment of the flow

Figure 5-10 illustrates the first stage of the convective pumping process through a microchannel glass chip. The 256 spot array patterned on the MCG chip is clearly visible in Images (a)-(i).

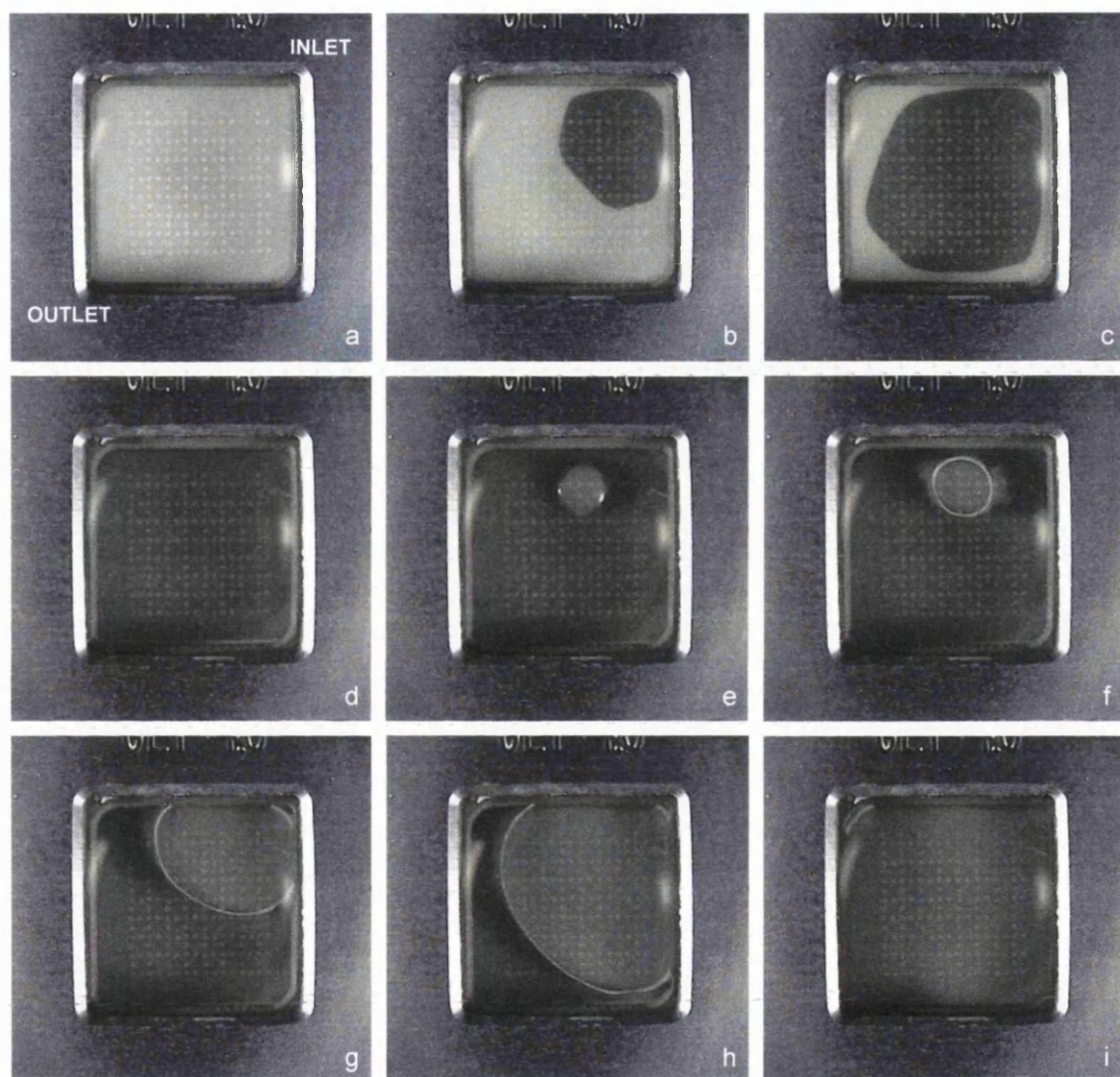


Figure 5-10. Establishment of a flow of working solutions through a microchannel glass chip, monitored by white light imaging. The microchannel glass chip shown here featured an array of 256 probe spots. The flow cell used was of the stainless steel type with concave bottom, as described in section 5. 4. 1. 2. 2. The locations of the inlet and outlet ports are indicated on Image (a). Hybridisation buffer (1x SSPE) was pumped at 0.5 mL min^{-1} through the cell. See text for details.

Image (a) of Figure 5-10 shows the dry MCG chip positioned inside the stainless steel flow cell. The locations of the inlet and outlet ports are indicated on the image. As previously stated, the inlet port was located below the microchannel chip while the outlet port was located above.

Images (b)-(i) were recorded at various time intervals during the pumping of buffer through the cell.

Images (b)-(d) show buffer entering the cell through the inlet port, below the chip. The liquid is seen to spread under the chip, without permeating it, due to the resistance to flow imposed by the small diameter of the channels. Image (d) shows the bottom chamber of the cell having been filled entirely. As the flow of liquid into the cell was sustained, pressure built up inside the bottom chamber, until liquid permeated some of the microchannels and burst into the top chamber, as seen in image (e). Images (f)-(h) show the permeation area spreading over the surface of the chip, from the inlet corner to the outlet corner. In Image (i), the whole cell (*i.e.*, bottom chamber, microchannels and top chamber) had been filled, and the flow of liquid through the outlet port was established.

5. 4. 2. 1. Uniformity of flow through the MCG chip

The use of fluorescent tracers for the investigation of fluid dynamics in planar microfluidic devices has previously been reported.¹⁶²⁻¹⁶⁴ In its simplest implementation, the approach relies on the use of a fluorescent compound in solution, whose time-dependent distribution within the fluidics circuitry is monitored by fluorescence imaging.^{162,163} Seeding the flow with latex microspheres is a possible alternative which offers higher sensitivity, due to the large number of fluorophores that can be attached to each bead. However, the approach is valid only if there is no substantial velocity gradient, *i.e.* no significant relative shear, across the particles, which requires the use of sub-micron particles.

A more elaborate variation of the same technique is based on photoactivation of fluorescence, through the use of “caged” photoactivable fluorescent dyes. Flash photolysis of UV-photo-activable fluorescent dyes (such as o-nitrobenzyl derivatives) provides a means to spatially and temporally control the release of tracer molecules within a flow pattern.¹⁶³ Although this technique is a powerful tool, it requires highly specific instrumentation.

In the former method, an epifluorescence microscope was used, providing imaging with lateral resolution in the plane of the device. With microchannel substrates, since the flow pattern is truly three-dimensional, imaging with both lateral and axial resolutions is required. This is in principle achievable through the use of a confocal microscope. In practice, however, the approach is limited by the impossibility to obtain a confocal image of a plane located more than a few microns below the surface of a microchannel chip (due to the large discrepancy of refractive index between the lead glass structure and the liquid filling the microchannels). In addition, the presence of fluorescent dye in the upper chamber is detrimental to the sensitivity of the confocal approach. Finally, the temporal resolution of fluid dynamic monitoring is limited by the rate of image acquisition of the confocal scanning process.

For these reasons, experimental investigations of fluid dynamics within flow-through microchannel substrates could not be successfully implemented. Rather than uniformity of flow,

uniformity of hybridisation over the array of spots of a MCG oligoarray was assessed experimentally, as described in Section 6. 2.

5. 4. 2. 2. Effectiveness of the washing procedure and uniformity of probe immobilisation

Figure 5-11 shows the fluorescence images of spots of fluorescently-labelled probe P2-f on MCG and planar glass, before and after washing.

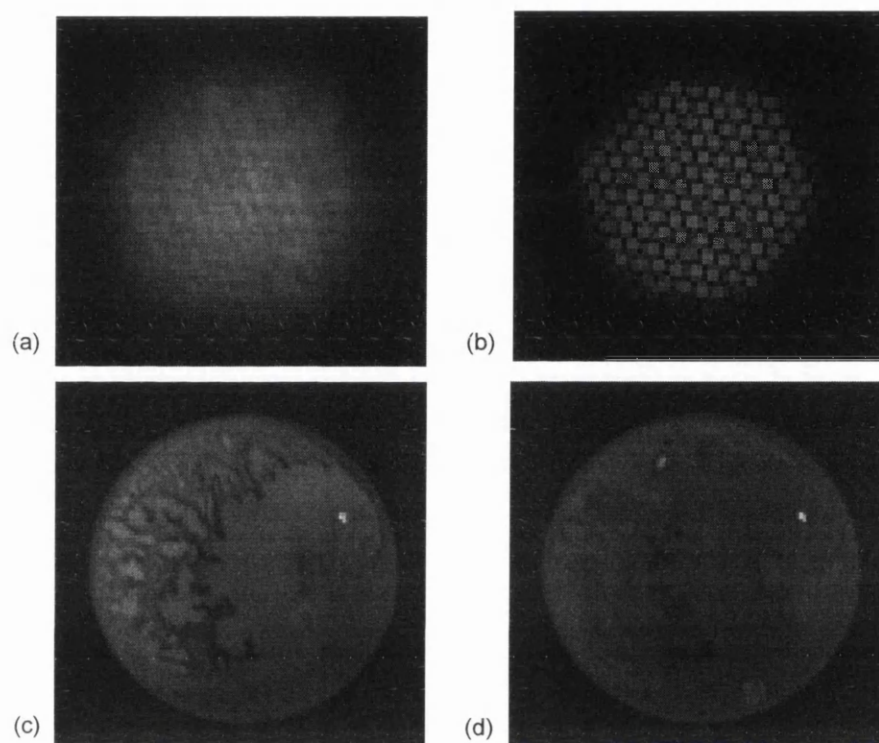


Figure 5-11. Fluorescence images of oligonucleotide probe spots on (a), (b) MCG and (c), (d) planar glass, before (left) and after (right) washing. The microchannel glass chip was washed by convective pumping of 1x SSC through the microchannels at 0.5 mL min^{-1} for 10 min, while the planar glass chip was washed with a washbottle. The images were acquired with a 20x, 0.75 NA objective lens. Different CCD camera settings were used between images (a)-(d).

The MCG chip was washed and imaged inside the stainless steel flow cell. Washing consisted in the convective pumping of 1x SSC through the microchannels at 0.5 mL min^{-1} for 10 min, as described above. The planar glass chip was washed with a washbottle and imaged inside the PDMS cell filled with washing buffer, so that both chips were covered with a layer of fluid and a glass slide (optical windows). Figure 5-11(c)-(d) show that, in the case of the planar substrate, the probe became immobilised in the pattern in which it dried, resulting in a poor uniformity of probe immobilisation.

Figure 5-11(a) shows that, before washing, probe molecules are present over the interstitial area, on the front surface of the chip; the apparent brightness of these probe molecules is enhanced, with respect to that of the probe molecules located inside the microchannels, by the fact that a low DOF (high NA) objective lens was used to image the chip. The distribution of

probes within the spot area is not uniform, though less so than in the case of the planar chip. Figure 5-11(b) shows a fluorescence image of the same MCG chip, after washing. Individual microchannels can now be clearly distinguished from one another, and the level of uniformity in fluorescence intensity from one channel to the next is high. The overall shape of the spot appears to reflect the hexagonal arrangement of the microchannels. The outer ring of reduced brightness is attributed to a combination of inter-channel cross-talk and three-dimensional imaging behaviour of the objective lens.

5. 5. Conclusions

The investigation presented in this chapter has shown that microchannel substrates exhibit favorable wetting properties permitting the generation of ODN probe spots with higher uniformity and smaller lateral dimensions than those achievable on planar substrates, provided that the spotting parameters are adjusted with respect to the morphological properties of the substrate, the characteristics of the dispensing mechanism and the rheological properties of the sample.

The validity of the procedures developed for the production of microchannel oligoarrays (immobilisation chemistry and microarraying) in the context of flow-through hybridisation assays is assessed in the next chapter.

CHAPTER 6. MICROCHANNEL OLIGOARRAY-BASED FLUORESCENCE HYBRIDISATION ASSAYS

6. 1. Introduction

The aim of the experiments presented in this chapter was to validate the applicability of the flow-through microchannel DNA chip platform described above to multiplexed, heterogeneous fluorescence nucleic acid hybridisation assays, and to demonstrate the advantages of the flow-through microchannel configuration over the conventional planar configuration. Convective pumping was used as the primary mechanism of sample delivery, although the feasibility of using electrokinetic sample pumping was investigated.

6. 2. Microchannel oligoarray-based fluorescence hybridisation assays with convective sample pumping

6. 2. 1. Introduction

Microchannel oligoarrays, produced in a configuration optimised from the knowledge gained through the investigations reported in Chapters 2 to 5, were used in hybridisation assays in which the sample was flown through the chip in a convective pumping mode. Synthetic ODN targets were used as a model for “real” samples of biological relevance prepared from mRNA. ODNs are cheaper, easier to obtain and to handle, and are nevertheless appropriate to characterisations of flow-through microchannel DNA chips from a bioanalytical and biotechnological point of view.

6. 2. 2. Experimental

6. 2. 2. 1. Materials

MCG chips were from Galileo Electro-Optics Corp. (Sturbridge, MA), with a thickness of 0.5 mm, a channel diameter of 10 μm and an open fraction of 0.6, as previously described.

Hybridisation experiments involved the use of unlabelled probes and fluorescently labeled ODN targets. The probe-target pairs P3-T3 and P4-T4, described in Section 4. 5. 4. 2, were used in addition to probe P5 and target T5 (Glen Research), of respective sequences "T"CAACAGGATGCTCACATTTAAGT and "F"AAACTTAAATGTGAGCATCCTGGTG, with "T" and "F" as previously defined. The complementary pair P5-T5 is representative of the IL-2 gene. Spots of the fluorescently labelled probe P2-f (defined in Section 5. 5. 1) were used as internal references. All the ODN lyophilised powders were dissolved to appropriate concentrations in 1x SSC (probes) or 5x SSPE (targets). The blocking agent was as described

in Section 4. 5. 4. 2, *i.e.* an aqueous solution of 0.02% polyvinylpyrrolidone (PVP) and 0.02% ficoll.

6. 2. 2. 2. Instrumentation

6. 2. 2. 2. 1. Convective fluidics for hybridisation

Pumping of working solutions through microchannel chips was achieved through forced convection, using the flow cell presented in Section 5. 4. 2. 2. 2. This flow cell was made part of a fluidic set-up, shown in Figure 6-1, that permitted all the steps of an assay (chip prewashing, sample injection, hybridisation by sample recirculation, and post-hybridisation washing) to be carried out sequentially, in a semi-automated mode, under continuous flow conditions (*i.e.*, the pump was not stopped over the course of an assay).

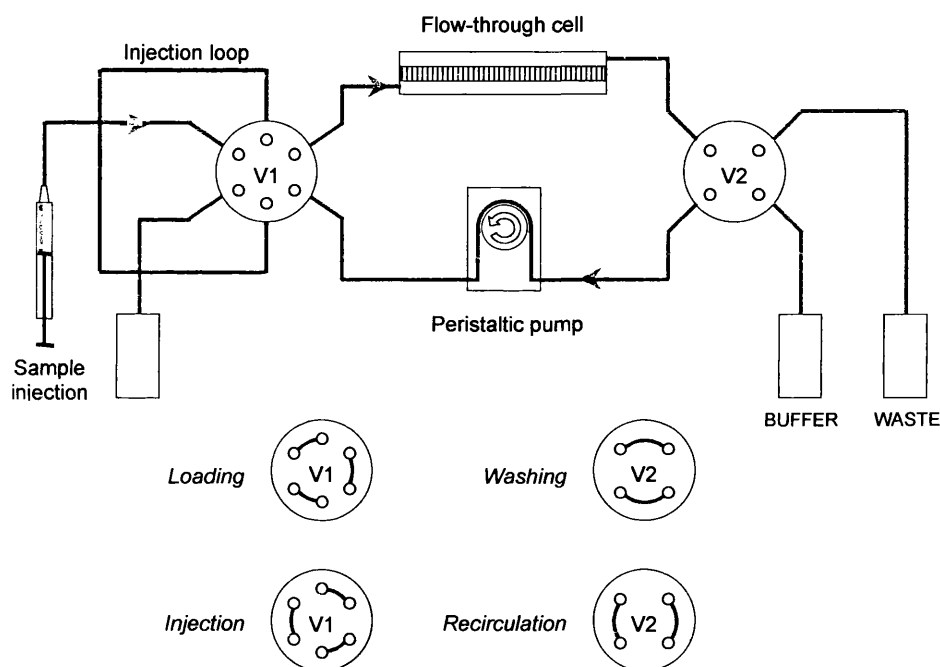


Figure 6-1. Schematic representation of the setup used for convective pumping (with recirculation) of working solutions in flow-through chip-based bioassays. V1: 6-port, 4-way rotary valve (2-position); V2: 4-port, 2-way rotary valve. Also shown are the positions of the valves corresponding to the various configurations of the fluidic system.

This set-up was based on an Ismatec ISM-1014 peristaltic pump and two rotary 2-position valves (Supelco, Poole, UK), denoted V1 and V2 in Figure 6-1. V1 was a 6-port, 4-way valve while V2 was a 4-port, 2-way valve. The fluid lines were 1/16" o.d. teflon tubing with 1/4-28 flanged tube end fittings (Supelco). The fluidics system could take various configurations, depending on the positions of the two valves. V1 controlled sample injection into the system, while V2 determined whether the flow-through chip is part of an open or closed loop. Manual actions required from the user during the course of an assay were limited to valve switching and buffer reservoir swapping.

With this set-up, liquid flowed through the chip in one direction only. This feature allowed one to take full advantage of the concave-bottomed cell (Section 5. 4. 2. 2. 2) to optimise the flow uniformity across the array of microchannels.

6. 2. 2. 2. 2. Epifluorescence microscopy imaging

Fluorescence imaging of microchannel oligoarrays was carried out using the combination of a Nikon Eclipse E800 microscope and a Hamamatsu Orca CCD camera described in Section 5. 3. 1. 2. The 4x Plan Apo objective lens, with a NA of 0.20, was used. The microscope was fitted with a translation stage that permitted precise lateral actuation of the flow cell within the field of view of the objective lens.

6. 2. 2. 3. Procedures

6. 2. 2. 3. 1. Preparation of MCG oligoarrays

The covalent attachment of the amino-terminated ODN probes to the MCG substrates involved in the production of flow-through MCG oligoarrays was achieved as described previously. Each chip was spotted, as described in Section 5. 3. 1. 3. 3, so as to feature 16 replicates of a 4 x 4 array, the latter comprising spots of the four probes P3, P4, P5 and P2-f, each in quadruplicate, as shown in Figure 6-2. Each spot was produced by the dispensing of a 5 nL aliquot of a 30 μ M probe solution onto the substrate. The spacing between adjacent spots was 400 μ m.

P5	P5	P3	P3
P5	P5	P3	P3
P4	P4	P2-f	P2-f
P4	P4	P2-f	P2-f

Figure 6-2. Layout of one of 16 replicates of a 4x4 array of oligonucleotide capture probe spots (each spot produced by the dispensing of a 5 nL aliquot of a 30 μ M solution of activated probe) forming the pattern of a microchannel glass oligoarray. P3, P4, and P5 were non-labelled probes while P2-f was a FAM-labelled probe, used as a reference for focusing and positioning.

Prior to use in flow-through hybridisation experiments, the chips were immersed in 0.2 mL of blocking agent for 10 minutes, then blow-dried and baked at 80°C for one hour.

6. 2. 2. 3. 2. Flow-through hybridisation

The hybridisation sample consisted of 50 μ L of a mixture of the targets T3, T4 and T5 at 2 nM, 20 nM and 10 nM concentrations, respectively, in 5x SSPE buffer. The hybridisation procedure, with associated fluidic system configurations, is presented in Table 6-1. A microchannel chip,

prepared as described above, was placed in the flow-through cell and the injection syringe was filled with sample solution before the procedure was started.

Step #	Assay step description	V1 valve position	V2 valve position	Buffer in reservoir	Duration
1	Chip pre-washing	Load	Wash	5x SSPE	15 min
2	Recirculation loop closing	Load	Recirc.	5x SSPE	5 s
3	Sample injection	Inject	Recirc.	5x SSPE	Immediate
4	Hybridisation	Inject	Recirc.	5x SSPE	3 h
5	Post-hybridisation (stringent) washing	Inject	Wash	1x SSPE	15 min

Table 6-1. Sequence of steps involved in the conduction of a flow-through chip-based hybridisation assay in recirculation pumping mode, related to the configurations of the fluidics system (determined by the positions of valves V1 and V2). A microchannel chip was placed inside the flow-through cell and the injection syringe was filled with sample solution prior to starting the procedure. Flow-through hybridisations were conducted at room temperature, at a 0.5 mL min^{-1} flow rate.

The volume of sample injected into the system was determined by the size of the injection loop (in blue in Figure 6-1). However, the total volume of the closed circuit (during recirculation) included the main loop (in purple in Figure 6-1) in addition to the injection loop, so that sample dilution was taking place in the system, over the course of the assay, by diffusion at the sample plug boundaries. In the set-up used, the volume of the main loop was circa $800 \mu\text{L}$ while that of the injection loop was $50 \mu\text{L}$. As seen from Table 6-1, pre- and post-hybridisation washing steps consisted in flowing 5x SSPE through the chip at 0.5 mL min^{-1} for 15 min.

6.2.2.3.3. Assay readout

After completion of the five steps of the flow-through hybridisation procedure described in Table 6-1, the chip was imaged in the flow cell filled with washing buffer, through the optical window. Each 4x4 array of spots was imaged sequentially with the 4x, 0.20 NA lens, by translating the flow cell within the field of view of the lens. The 16 images were acquired with the same CCD camera settings (same level of binning, and 10 s integration time) and subsequently assembled into a single image of the 256-spot oligoarray. S/N values associated with the spots were calculated as described in Section 3.3.4.3.3.

6. 2. 3. Results and discussion

The results of the investigation carried out in Chapter 5 suggested that the highest levels of axial uniformity of probe attachment over the whole effective surface area of MCG substrates are realised through the dispensing of ≥ 5 nL volumes on 0.5 mm thick, 10 μm channel diameter, 0.6 open fraction MCG substrates. The dispensing of smaller volumes was found to result in incomplete filling of the microchannels with the probe solution. Likewise, thicker chips spotted with ≤ 20 nL volumes exhibited incompletely filled microchannels. As a result, an optimised flow-through MCG configuration for quantitative heterogeneous nucleic acid hybridisation measurements is obtained by using 0.5 mm-thick chips arrayed with 5 nL spots of 43 μM probe concentration. In these experiments, chips were arrayed with 30 μM probe solutions, yielding a probe coverage density of 46 fmol mm^{-2} . This was lower than the alleged optimum but ensured that no steric hindrance occurred.

Each spot was 140 μm in diameter and comprised 90 fmol of probe molecules. As each of the four probe sequences was present within 64 spots over the chip, a total of 5.8 pmol of each of the probe sequences was available for hybridisation over the whole array, which represented a circa 6-fold excess with respect to the most concentrated target present in the sample. These conditions of an excess of each immobilised probe with respect to the cognate target sequence present in the sample were similar to those encountered in gene expression measurements where low amounts of targets are available, as stated in Section 1. 1. 2. 4. 2. The fluidics setup with convective pumping allowed for recirculation of the sample through the chip, the importance of which has been stated in Section 1. 2. 6. 4.

Figure 6-3 shows an epifluorescence image of the 256-spot microchannel oligoarray, after 3 hours of hybridisation with the target mixture followed by stringent washing in the flow cell. The arrangement of the spots in the image of Figure 6-3 corresponds to a mirror image of the spotting pattern shown in Figure 6-2, as the array was spotted and imaged with the same side facing upwards. The superstructure of the MCG material can be seen on the image.

Figure 6-3 shows some variability in the fluorescence intensity of the spots corresponding to each sequence. In particular, the spots located in the top left corner (red box in Figure 6-3) exhibited a reduced brightness. Two factors could have contributed to this lower fluorescence intensity: the fact that this part of the chip was used to adjust the initial position of the translation stage (lateral positioning in the center of the field of view, as well as axial focusing) and the camera settings (integration time), resulting in photobleaching of the spots; and a lower extent of duplex formation, resulting from, for example, a different flow rate in that part of the cell. The former is in fact the major contribution, as evidenced from the reduced brightness exhibited by the reference spot (probe P2-f).

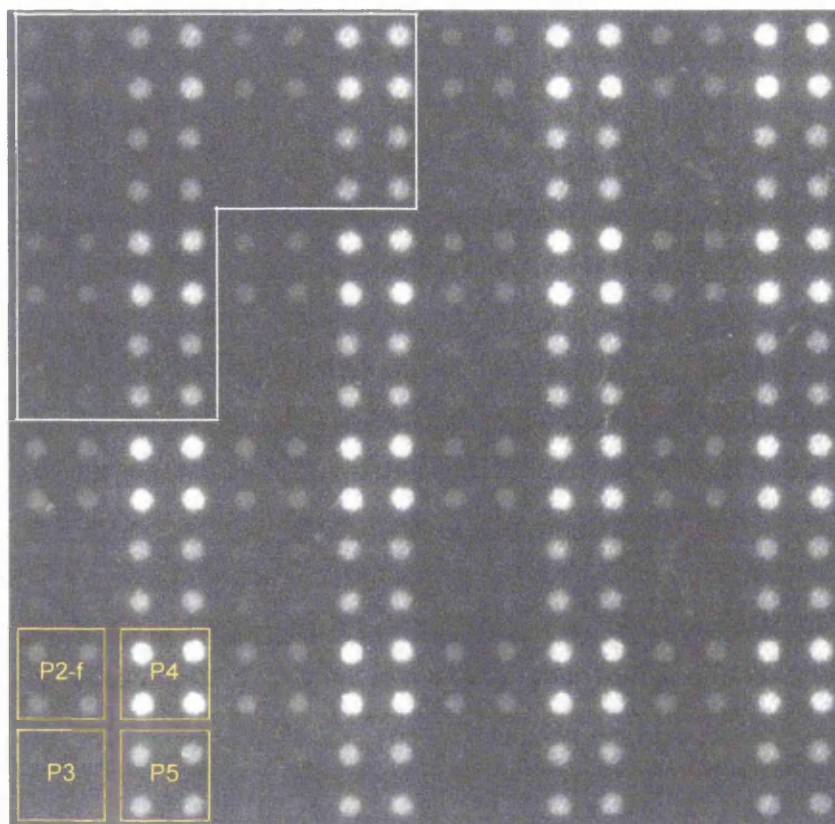


Figure 6-3. Epifluorescence image of a three-dimensional microchannel glass oligoarray, showing a pattern of FAM-labelled oligonucleotide targets hybridised to spots of complementary oligonucleotide probes. The image shows 16 replicates of a 4x4 array, the latter comprising four different probe sequences P3, P4, P5 and P2-f, each spotted in quadruplicate as indicated in the bottom left corner of the image. The spots of FAM-labelled probe, P2-f, were used as a reference for focusing and positioning. Each spot of the oligoarray comprised an estimated 90 fmol of probe molecules. The sample consisted of 50 μL of a mixture of the targets T3, T4 and T5 at 2 nM, 20 nM and 10 nM concentrations, respectively, in 5x SSPE buffer. Hybridisation was carried out by circulating the sample iteratively through the MCG oligoarray, under a constant flow rate of 0.5 mL min^{-1} , at room temperature, for 3 hours. Pre- and post-hybridisation washing steps consisted in flowing 5x SSPE through the chip at 0.5 mL min^{-1} for 15 min. The image was assembled from 16 images, acquired with 4x, 0.20 NA microscope objective lens and an integration time of 15 s.

Table 6-2 summarises the data obtained through quantitative analysis of the image of Figure 6-3. The S/N values determined for each sequence showed a relatively high coefficient of variation (CV) over the whole array (third row of Table 6-2). By judicious removal of data points where photobleaching had obviously occurred, the CV values were reduced by a factor of circa 2 or more. Variations in S/N between spots of the same sequence are believed to reflect mainly non-uniformities in the flow pattern within the flow cell (and, indirectly, target distribution within the hybridisation cell). The scanning approach used to image the chip ensured that non-uniformity of imaging conditions from one 4x4 array to the next were reduced to a minimum,

even if the objective lens did not provide a perfectly uniform optical field, with a higher illumination power in the center than on the edges.

Probe (90 fmol per spot)	Target, concentration (nM) in the 50 μ L sample volume	S/N		
		CV (%) over 64 spots	CV (%) over 52 spots	Average over 52 spots
P3	T3, 2	49.3	12.6	6.3
P4	T4, 20	19.5	10.3	216.5
P5	T5, 10	16.6	8.4	103.4

Table 6-2. Quantitative analysis data of a multiplexed fluorescence microchannel oligoarray assay. The oligoarray featured 16 replicates of a 4x4 array, the latter comprising four different probe sequences P3, P4, P5 and P2-f, each spotted in quadruplicate. The spots of FAM-labelled probe, P2-f, were used as a reference for focusing and positioning. The array was hybridised with 50 μ L of a mixture of the FAM-labelled ODN targets T3, T4 and T5 at 2 nM, 20 nM and 10 nM concentrations, respectively, in 5x SSPE buffer, at room temperature and under continuous recirculation of the sample through the MCG chip at a constant flow rate of 0.5 mL min⁻¹, for 3 hours. S/N: signal-to-noise ratio; CV: coefficient of variation.

The S/N values for P4 and P5 were in a 2.1: 1 ratio, in close agreement with the 2: 1 concentration ratio between T4 and T5. However, the S/N for T3 was circa 3 times lower than expected. This was attributed to a lower degree of labelling of T3 as compared to T4 and T5, as evidenced from the results of a similar but independent experiment in which all three targets were present at equimolar levels. Clearly, QC/QA (quality control / quality assurance) processing of the sample is a prerequisite for quantitative fluorescence assays.

An average S/N of 6.3 was obtained for P3, with a maximum of 1.5 fmol of target T3 being hybridised within each spot (100 fmol T3 present in the sample, hybridised to 64 spots). This indicates that, in the experimental conditions used to obtain the image of Figure 6-3, a LOD of < 1.5 fmol ODN target per spot was achieved. The absolute LOD is probably as low as a few hundred attomoles, given the reduced level of labelling of T3. This level of detectability was obviously significantly affected by the nature of the fluorescent labels used, as well as by the spectral characteristics of both the fluorescence filters and the CCD detector. As stated, a FAM label was chosen here because its spectral characteristics matched the spectral detection efficiency of the CCD camera used. The use of longer wavelength dyes such as TAMRA or Cy5, along with a CCD camera with enhanced detection efficiency in the red, are expected to provide lower levels of background noise, hence an improved detectability.

A dynamic range of 1.7 orders of magnitude of S/N was demonstrated (in Table 6-2) for a single image. The dynamic range is limited by two main parameters: the level of digitisation of the CCD camera (12 bit in the present case), and the level of background signal (pixel intensity in a

non-spotted area of the chip). The background signal was composed of contributions from the MCG matrix itself (light scattering and autofluorescence), from targets non-specifically adsorbed over the surface of the chip, and from scattering of light by the buffer molecules and the optical window of the flow cell. Non-specific adsorption is exacerbated in flow-through chip-based hybridisation assays by the high effective surface area and the high surface-to-volume ratio that characterise microchannel substrates.

6. 3. Relative performance of microchannel glass and planar glass oligoarrays

6. 3. 1. Introduction

This section describes the use of “pseudo” real-time fluorescence monitoring of hybridisation assays to demonstrate the realisation of the theoretical advantages of the flow-through microchannel configuration (Section 1. 2. 4) over the conventional planar configuration.

6. 3. 2. Experimental

6. 3. 2. 1. Materials

MCG chips were from Galileo Electro-Optics Corp. (Sturbridge, MA), with a thickness of 0.5 mm, a channel diameter of 10 μm and an open fraction of 0.6. Float glass slides were machined in order to produce planar glass chips with lateral dimensions and thickness ($12 \times 12 \times 0.5 \text{ mm}^3$) that ensured compatibility with the flow cell. A corner of these planar glass chips was cut off so as to allow liquid to flow from one side of the chip to the other.

As above, hybridisation experiments were carried out using non-labeled probes and fluorescently labeled ODN targets. The probe-target pair P5-T5 was used, in addition to the probes P6 and P7 and targets T6 and T7, of respective sequences

"T"CCTCTGACTTCAACAGCGACACT, "T"TCCTCCTGAGCGCAAGTACTC,

"F"AAGTGGGTGGCGCTGTTGAAGTCAGAGG, and

"F"AACACGAGTACTTGCGCTCAGGAGGA, respectively, with "T" and "F" as above. The complementary pairs P6-T6 and P7-T7 are representative of the genes GAPDH and β -actin, respectively. Spots of the fluorescently labelled probe P2-f (defined in Section 6. 2. 2) were used as internal references. All the ODNs (obtained as a lyophilised powder from Glen Research) were dissolved to appropriate concentrations in 1x SSC (probes) or 5x SSPE (targets). The blocking agent was an aqueous solution of 0.02% polyvinylpyrrolidone (PVP) and 0.02% ficoll.

The instrumentation used was as described in Section 6. 2. 2. 2, except that a 600 μL injection loop was used. A 10x, 0.45 NA Plan Apo objective lens (Nikon) was used in complement to the 4x lens.

6. 3. 2. 2. Methods

6. 3. 2. 2. 1. Preparation of MCG and planar glass oligoarrays

Covalent attachment of the activated ODN probes to silanised MCG and planar glass substrates was achieved as described previously. Each chip was spotted so as to feature 4 replicates of a 2 x 2 array, the latter comprising one spot of each of the four probes P5, P2-f, P6 and P7, as shown in Figure 6-4.

P2-f	P5	P2-f	P5
P7	P6	P7	P6
P2-f	P5	P2-f	P5
P7	P6	P7	P6

Figure 6-4. Layout of a 4x4 array of oligonucleotide probe spots (each spot produced by the dispensing of a 5 nL aliquot of a 30 μ M solution of activated probe) forming the pattern of microchannel glass and planar glass oligoarrays. P5, P6, and P7 were non-labelled probes while P2-f was a FAM-labelled probe.

Each spot was produced by the dispensing of a 5 nL aliquot of a 30 μ M probe solution onto the substrate. The spacing between adjacent spots was 400 μ m, so that the whole 16 spot array could be imaged with the 4x lens while one 2x2 array fitted within the field of view of the 10x lens.

6. 3. 2. 2. 2. Flow hybridisation with pseudo real-time monitoring by epifluorescence imaging

The hybridisation sample consisted of 600 μ L of a mixture of the targets T6, T5 and T7 at 2 nM, 1 nM and 0.4 nM concentrations, respectively, in 5x SSPE buffer. Hybridisations were carried out with continuous convective sample pumping, according to the procedure of Table 6-1, but for extended periods of time (6 hours). The sample solution flowed through the MCG chip, as in Section 6. 2, and over the planar glass chip.

After the chip (MCG or planar glass) had been loaded into the flow cell, the latter was fastened on the translation stage of the microscope. Focus and lateral positioning of the planar glass chips within the field of view of the objective lens were made difficult by the reduced brightness of the reference spot once the flow cell was filled with buffer and the non-covalently bound probes had been washed off; in practice, long integration times (several seconds), *i.e.* low frame rates, had to be used to produce images with sufficient S/N, which made the focusing procedure extremely time-consuming, and resulted in significant photobleaching of the reference spot. Focus adjustment was easier when the chip was “dry”; however, the position of the focal plane was altered after the cell had been filled with buffer. Therefore, a procedure had to be used

which involved adjusting the focus on the dry reference spot, then starting the pumping of buffer at a low flow rate, and re-adjusting the focus in real time, as the spot was being washed off by the flow of liquid.

Pseudo real-time monitoring of the hybridisation assay consisted in acquiring fluorescence images of the oligoarray (a quarter of the array was imaged with the 10x lens) for increasing hybridisation periods, during step 4 (hybridisation) of the procedure described in Table 6-1. Integration times were 3 s for the planar glass and 1.5 s for the MCG chips, respectively. Each image was processed as in Section 3.3.4.3 in order to determine the S/N value associated with each spot.

6.3.3. Results and discussion

The aforementioned procedure permitted the course of the hybridisation assay to be monitored in a fashion best described as “pseudo” real-time in that the S/N values inferred from the fluorescence images were affected by the presence of sample solution in the hybridisation cell during imaging. Increased background signals (hence reduced S/N) were caused by fluorescence from targets in solution and scattering of light by target and buffer molecules. In order to limit these contributions from the flowing sample, a 10x objective lens with a lower DOF than the 4x lens was used.

Figure 6-5(i) shows the evolution of the S/N of each probe sequence over time for the planar glass oligoarray. Curves (a) and (b) of Figure 6-5(i) are characteristic of an heterogeneous hybridisation assay, as previously discussed in Section 4.5.3. The S/N for T7 remained below the LOD ($S/N < 3$) over the whole duration of the assay (6 hours), as shown by curve (c) of Figure 6-5(i). The amounts of T7, T5 and T6 targets present in the sample plug were 240, 600 and 1200 fmol respectively, while the planar glass array featured a maximum of circa 14 fmol probe per spot (assuming complete covalent coupling of all the thiol anchoring sites to activated probes), equivalent to circa 55 fmol of each probe sequence, over 4 identical spots. These conditions correspond to an expected saturation behaviour of all the spots at sufficiently long assay times. Clearly, the P5 spot had not reached saturation after 6 hours of hybridisation, since its associated S/N was still much lower than that associated with T6.

The MCG oligoarray featured circa 360 fmol of each of the probes P5, P6 and P7. Therefore, only P5 and P6 were in conditions of probe saturation, while P7 was in conditions of target exhaustion. As seen in Figure 6-5(ii), both the P5 and P6 spots had reached near-saturation after 6 hours, indicating an enhanced assay kinetics as compared to the planar glass oligoarray. Saturation of the P6 spot (curve (a)) was reached after about 60 min, versus more than 240 min in the case of the planar glass array. The decrease in S/N observed after saturation was ascribed to photobleaching of the labels of the hybridised targets. The latter were more prone to photobleaching than those of the free targets in solution because they were submitted to direct illumination once hybridised.

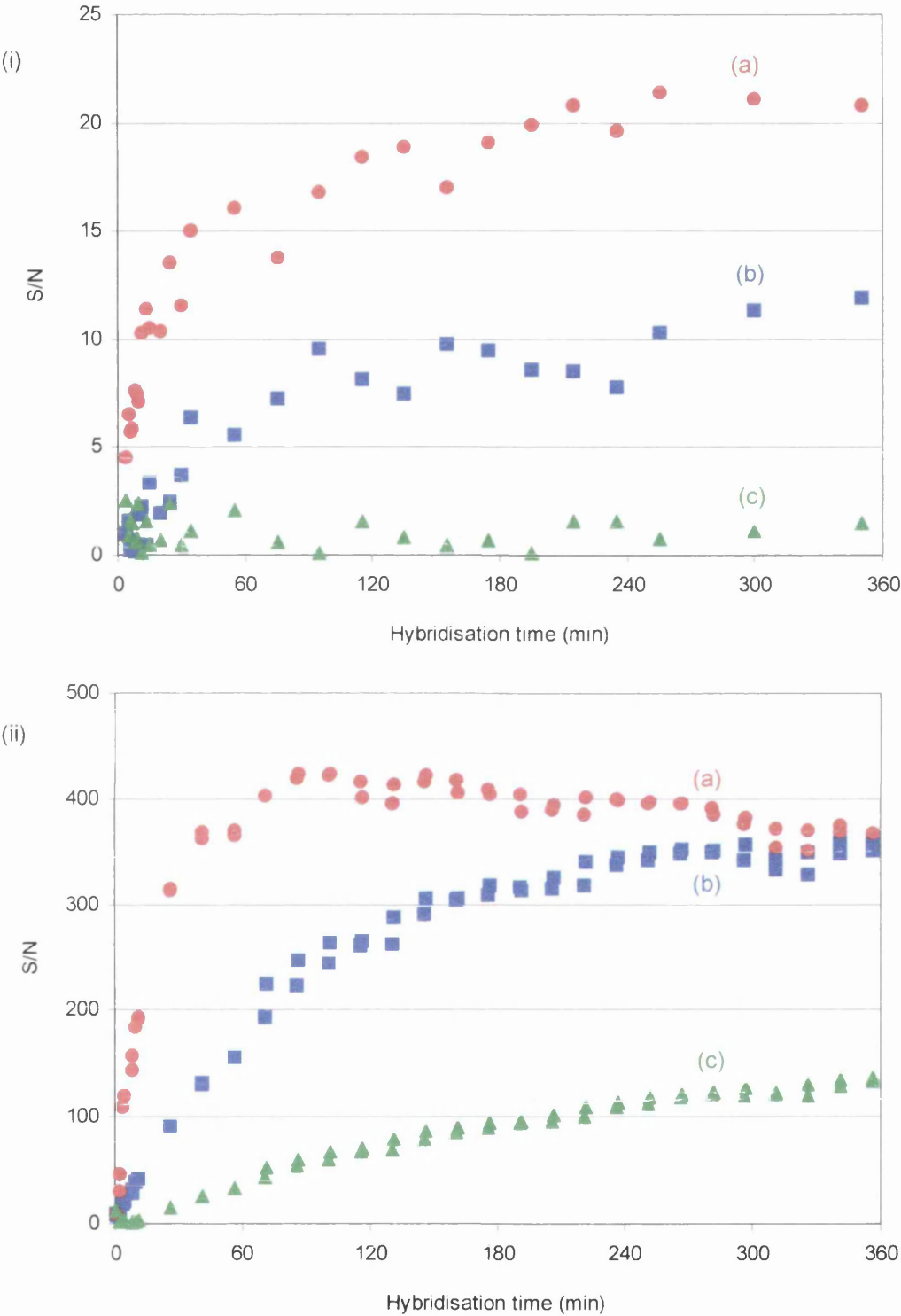


Figure 6-5. Pseudo real-time kinetics curves of multiplexed heterogeneous hybridisation of oligonucleotide targets to (i) a planar glass oligoarray and (ii) a microchannel glass oligoarray, at room temperature, upon continuous convective pumping of the sample at 0.5 mL min^{-1} through (resp. over) the microchannel (resp. planar) chip. Each array featured 16 spots comprising three non-labelled ODN probes and one FAM-labelled probe, all in quadruplicate. The sample consisted of $600 \text{ }\mu\text{L}$ of a mixture of three targets complementary to the probes at (a) 2 nM, (b) 1 nM and (c) 0.4 nM concentrations, respectively, in 5x SSPE buffer.

The P7 spot exhibited a smooth increase in S/N over time, the LOD being reached after about 10 minutes. Overall, the S/N values for the MCG array were higher by one to two orders of magnitude than those for the planar glass array.

Figure 6-6 shows fluorescence images of the planar glass and MCG oligoarrays after 230 min of hybridisation.

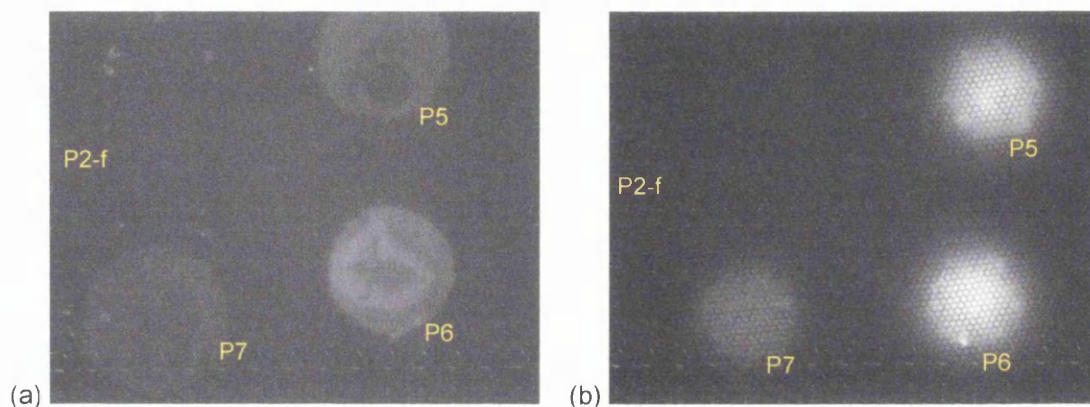


Figure 6-6. Fluorescence images of (a) a planar glass oligoarray and (b) a microchannel glass oligoarray, after 230 min of hybridisation with 600 μL of a mixture of oligonucleotide targets T6, T5 and T7 at 2 nM, 1 nM and 0.4 nM concentrations, respectively, in 5x SSPE buffer, under 0.5 mL min⁻¹ continuous flow and at room temperature. The images show one of four arrays of ODN probe spots of sequences P5, P6 and P7, as labelled on the image. The spot of FAM-labelled probe, P2-f, was used as a reference for focusing and positioning. The images were acquired with a 10x, 0.45 objective lens with integration times of (a) 1 s and (b) 0.3 s.

Figure 6-6 clearly shows that the MCG oligoarray provided higher S/N levels than the planar glass oligoarray. Incidentally, the fact that the reference spots had undergone significant photobleaching during the initial focusing step and over the duration of the assay is evidenced by the low level of brightness of P2-f in Figure 6-6(a) and Figure 6-6 (b).

6. 3. 4. Conclusions

The MCG oligoarray platform whose development is described in Chapters 2 to 5 has been shown to be suitable to multiplexed, heterogeneous nucleic acid hybridisation assays. In addition, the enhanced performance provided by the microchannel configuration as compared to the planar glass configuration has been evidenced by enhanced hybridisation kinetics (assay times shortened by a factor of circa 5) and higher S/N levels (by one to two orders of magnitude).

6. 4. Electrokinetic sample transport in microchannel oligoarray hybridisation assays

6. 4. 1. Introduction

In this section, the feasibility of substituting convective pumping of target molecules with electrophoretic pumping, as suggested in Section 1. 2. 6. 4. 2, is discussed.

6. 4. 1. 1. Electrophoretic transport of nucleic acids

Nucleic acids are highly charged molecules featuring relatively high electrophoretic mobilities. A typical value for the free-flow electrophoretic mobility of 40- to 60-base ODNs in TBE buffer (89 mM boric acid + 5 mM EDTA + 70 mM NaCl, pH 8.5) is $4 \times 10^{-4} \text{ cm}^2 (\text{V s})^{-1}$. This corresponds to a velocity of $4 \mu\text{m s}^{-1}$ at 1 V cm^{-1} electric field strength.¹⁶⁵

As efficient electrophoretic transport requires the application of high voltages, electrophoresis is usually accompanied by associated electrochemical effects resulting from the generation of faradaic reactions at the electrodes, in particular electrolysis of water:



Equation 6-1 represents the anodic oxidation of water, characterised by a redox potential, E_0 , of +1.23 V (versus NHE, at 25 °C and 1 atm) while Equation 6-2 represents the cathodic reduction of water ($E_0 = -0.83 \text{ V}$). As indicated by Equations 6-1 and 6-2, water electrolysis is accompanied by the release of molecular, possibly gaseous species (O_2 , H_2) as well as ionic, pH-altering species (H^+ , OH^-).

Another side effect encountered in electrophoretic systems is resistive heating of the medium (Joule effect). Upon establishing a bias voltage within an aqueous medium, resistive heating is induced according to Joule's law which states that the amount of heat generated per unit time and unit volume in an electrolyte of electrical conductivity σ subjected to an electric field strength E is equal to the density of power deposited in the liquid, $P = \sigma E^2$.

6. 4. 1. 2. Microchannel oligoarray-based hybridisation with electrophoretic pumping

Need to minimise the electrochemical and thermal side effects

Electrochemical and thermal side effects taking place in electrophoretic systems may hinder nucleic acid hybridisation. The production of pH-altering hydronium and hydroxide ions at the electrodes is likely to lead to local pH changes, unless the aqueous medium provides sufficient buffering capacity. In addition, any increase in the temperature of the medium would have an effect upon the stringency conditions of the nucleic acid hybridisation mechanism. Even if heat

is generated uniformly in the electrolyte volume, dissipation can only take place at the boundaries of the compartment, leading to the formation of temperature gradients which, in turn, are likely to result in convection effects. Electrochemical and thermal side effects will be all the more significant that the electric field strength and the current intensity across the medium are high, and will depend on the physical properties of both the microchannel chip material and the buffer used.

Choice of a suitable electrode configuration

Uniform axial transport of nucleic acid target molecules through a microchannel chip requires the establishment of a uniform axial electric field, which is best achieved by using paired electrodes positioned perpendicularly to the axis of the microchannels. In addition, the generation of an axial electric field of high intensity (to induce migration of the target molecules over the whole thickness of the chip, *i.e.* a few hundred microns, at a reasonable velocity) from a moderate bias voltage (to minimise deleterious electrochemical and thermal effects) is best achieved by minimising the distance between the paired electrodes.

Although a single pair of electrodes is *a priori* sufficient to generate an axial electric field across a microchannel chip, the use of an array of paired electrodes, in which each electrode pair is associated to one individual probe spot, appears to offer several advantages, including the possibility to perform sample loading and sample preconcentration at each spot as well as reduction of the amount of target present over the non-active area of the microchannel chip. Importantly, back-and-forth pumping of the target molecules through the chip (equivalent to recirculation in the case of convective pumping) implies frequent polarity reversal of the electrodes, which entails that each electrode in a pair has to be switched from an anodic to a cathodic state.

Choice of a suitable buffer

In a static or convective nucleic acid hybridisation process, the main role of the buffer is to provide shielding of the phosphodiester backbone so as to reduce electrostatic repulsions between complementary nucleic acid strands. Ideally, the hybridisation conditions, including the ionic strength of the buffer, should be optimised so as to provide adequate stringency. In the envisaged electrokinetically-assisted hybridisation mode, the buffer must also be compatible with migration of the nucleic acid target molecules. This requires a low conductivity buffer, as for a given current density, the lower the buffer conductivity, the higher the fraction of the current carried by the ODN molecules, hence the higher the migration rate of the latter. In addition, as mentioned above, the buffering strength should be sufficient to keep the pH of the medium within a restricted range.

6. 4. 1. 3. Integrated device design

Figure 6-7 shows a schematic representation of the device intended to be used for electrokinetically-assisted flow-through hybridisation. An array of electrodes is located on each side of the chip, with the electrodes parallel to the chip surface. Three distinct volumes can be distinguished: the internal volume of the chip (made up of all the channels) and two chambers, one on each side of the chip, between the front and back faces of the chip and the electrodes.

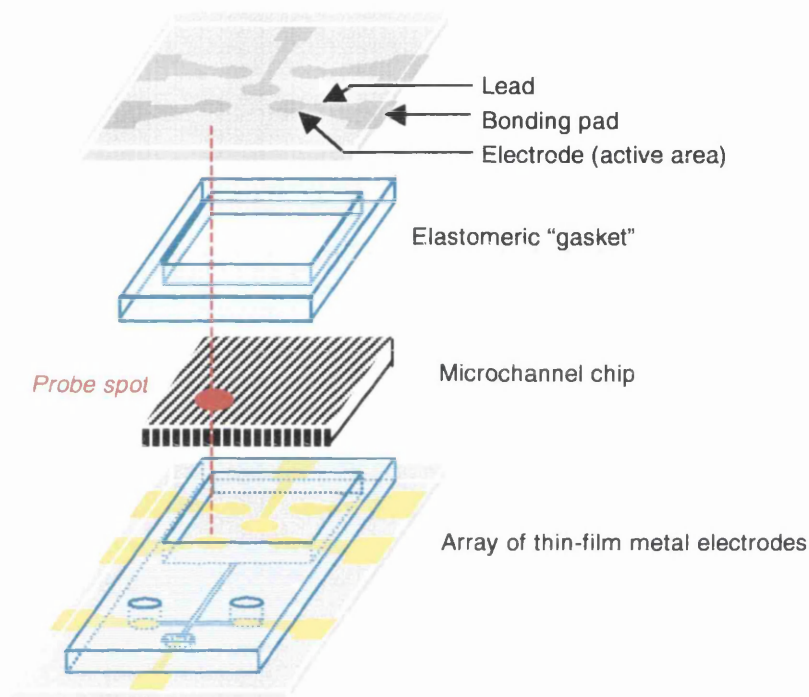


Figure 6-7. Schematic representation of the proposed integrated device for the implementation of electrokinetic target pumping in flow-through microchannel chip-based hybridisation assays. The microchannel DNA chip is sandwiched between two thin-film electrode arrays, with two thin elastomeric gaskets defining the upper and lower chambers of the hybridisation cell. The dashed red line illustrates the association of each sensing element (probe spot, schematically shown in red) with a pair of electrodes. Also shown in the bottom-left part of the drawing is a fluidic circuitry with associated electrodes for electrokinetic sample injection into the hybridisation cell.

Leads and bonding pads associated with each electrode are also patterned on the glass slides. The bonding pads are located outside of the PDMS gasket to allow for external connection to a power supply. A microchannel DNA chip can be reversibly integrated into the device by clamping, the flexibility of the PMDS gasket enabling a tight seal to be formed through mere conformal contact with a minimal amount of pressure applied. The glass slabs can be irreversibly bound to the PDMS gaskets through the bonding technique based on oxidising the PDMS in an oxygen plasma and immediately bringing both pieces into intimate contact,¹²³ but

this is not necessary if the whole device is enclosed inside a housing which permits the various elements to be maintained in place. The use of a thermostated housing, for example with a built-in Peltier cooler, can be considered.

6. 4. 1. 4. Adjustment of the experimental parameters

The geometry shown above, in particular the proximity of the electrodes from the hybridisation area, requires careful control over the electrochemical effects taking place at the electrodes (pH changes, gassing and electrode corrosion) and within the liquid medium (heating effects).

In conventional capillary electrophoresis (CE) or on-chip electrophoresis of biomolecules, separation of the molecules present in the sample according to differences in their electrophoretic mobilities takes place in a capillary whose two ends are plunged inside buffer-containing reservoirs where the electrodes are located. Gas evolution and production of hydronium and hydroxide ions that accompany water electrolysis taking place at the electrodes is not damaging to the experiment because the part of the capillary where the separation takes place is sufficiently remote from the electrodes so as to avoid perturbation of the separation medium by gas bubbles, and the amount of buffer available in the vicinity of the electrodes ensures neutralisation of pH-altering species over the (short) time frame of the separation run.¹⁶⁷ In addition, in CE, efficient heat dissipation is possible through the capillary wall. In the present case, the electrodes are positioned close to the microchannel chip, *i.e.* close to the hybridisation sites, so that the development of pH and temperature gradients in the vicinity of the electrodes is to be reduced as much as possible.

6. 4. 2. Device fabrication

6. 4. 2. 1. Introduction

A procedure was developed for the fabrication of devices of the type shown in Figure 6-7. Three types of electrodes were considered: Au and indium tin oxide (ITO) thin films, and Pt black porous thick films. Each has respective advantages and limitations, as described below.

Thin-film Au electrodes of microscopic dimensions can readily be fabricated by photolithographic thin film patterning; however, such electrodes are prone to corrosion in chloride ion-containing media,¹⁶⁶ such as SSC and SSPE buffers commonly used in nucleic acid hybridisation assays, through the formation of soluble AuCl_x complexes which can lead to delamination of the electrodes. The reaction involved is



which has an associated standard electrochemical potential of +1.005 V.

ITO is a transparent semiconductor commonly used in the manufacture of LCD (liquid crystal display) panels. A 200 nm thick layer of ITO has a typical optical transmittance of 80-85% in the

450-1000 nm wavelength range.¹⁶⁸ Unlike other transparent semiconducting materials such as aluminum- and gallium-doped zinc oxide, ITO thin film-coated glass and quartz substrates are commercially available from a number of vendors. The use of ITO electrodes would permit direct visual observation and optical addressing of the inside of the hybridisation cell, e.g. to check the absence of gas bubbles and to monitor the distribution (transport, hybridisation) of fluorescently-labelled target molecules by epifluorescence microscopy. However, as an oxide, ITO is readily reduced under cathodic biasing.

A limitation of thin-film planar electrodes in the context of the present application is their low surface area. Electrodes with a much higher effective surface area for the same lateral dimensions can be made from porous materials. Pt black is particularly appropriate in that respect. Thin film electrodes can be coated with Pt black films of controlled thickness and porosity through an electroplating process.¹⁶⁹ Pt has the additional advantage that it is less prone to corrosion by chloride ions than Au.¹⁷⁰

The leads that link the active area of an electrode to its associated bonding pad (see Figure 6-7) have to be passivated so as to electrically insulate them from the liquid medium filling the cell. It is crucial that the passivation layer present a sufficiently high and uniform electric field breakdown strength; for instance, the presence of a pinhole in the passivation layer would result in a local electrical current shorting and high electric field strength leading to exacerbated and deleterious electrochemical effects. Patternable dielectrics commonly used as passivating layers in microelectronics include silicon dioxide (SiO_2) and silicon nitride (Si_3N_4). These are usually deposited over a device by plasma-enhanced chemical vapour deposition (PE-CVD) and subsequently patterned by dry etching techniques.¹⁵⁴ SiO_2 presents a limitation in bioelectronics application, where devices are used in an aqueous environment, in that it can adsorb water to a significant extent, which reduces its electric field breakdown strength. Recently, photoresists such as SU8 have been shown to be appropriate as passivating layers in bioelectronics applications.¹⁷¹ However, as organic materials, photoresists are highly fluorescent over a wide range of wavelengths of the visible electromagnetic spectrum, which precludes their use in combination with *in situ* fluorescence detection.

The design shown in Figure 6-7 features a fluidics circuitry consisting of open reservoirs and closed channels permitting the injection of working solutions into the the lower chamber of the hybridisation cell. This circuitry can easily be defined within the PDMS gasket itself, by molding the latter against a master fabricated by direct photolithographic microstructuring of SU8 or by dry etching of Si, as described in Section 2. 5. 2.

6. 4. 2. 2. Experimental

6. 4. 2. 2. 1. Plastic contact photomasks for photolithography

It was decided to fabricate electrodes with relatively large feature sizes ($> 200 \mu\text{m}$ diameter) which would match the dimensions of probe spots produced by manual pipetting. Therefore,

electron-beam writer resolution was not required, and this provided an opportunity to assess the validity of a "rapid prototyping" approach based on the use of cheap plastic photomasks made through an offset lithography process from a retail reprography unit. This process offers limited resolution (450 dots per inch) but produces uniformly dark surfaces, which totally block UV-visible light, on acetates whose transparency in the UV is compatible with photolithographic patterning of S1818 and SU8 photoresists. All the required photomask patterns (Figure 6-8) were designed in CorelDraw 9.0 and exported into Adobe Photoshop 4.0 before being printed onto A4 acetate sheets.

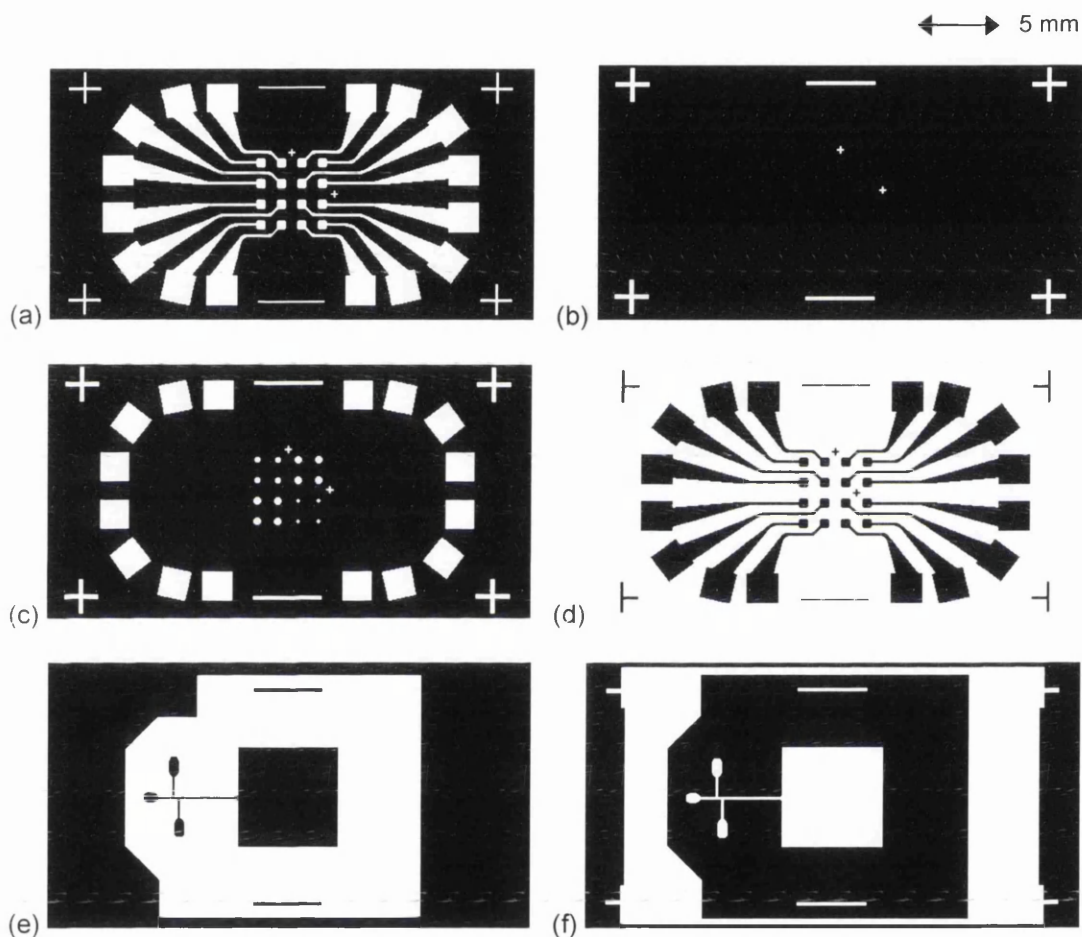


Figure 6-8. Layout of the contact photomasks used in the photolithographic steps of the device fabrication. (a), (b) Darkfield masks for the lift-off of Au with positive photoresist: (a) was used for the fabrication of Au electrodes and (b) for the fabrication of Au alignment marks on ITO-coated glass slides; (c) darkfield mask for the dry etching of silicon nitride through a positive photoresist sacrificial layer; (d) darkfield mask for the wet etching of ITO through a positive photoresist sacrificial layer; (e), (f) masks for producing masters used to mold PDMS gaskets with integrated fluidics circuitry: (e) was used to pattern a positive photoresist sacrificial layer onto the surface of a Si wafer that was subsequently dry etched, while (f) was used to directly produce a SU8 master. Each of the pattern has overall dimensions of $12.5 \times 25 \text{ mm}^2$.

Individual patterns were cut off from the A4 sheet and taped onto 2.5" x 2.5" quartz plate so that they could be used with a mask aligner (HTG, Oxford, UK) in the same way as ferric and chromium photomasks. Each photomask layout consisted of five adjacent repetitions of a given

pattern, so that five devices could be processed in parallel from a 1 x 3 inch² microscope glass slide. The equivalent of ten 2.5 x 2.5 inch² darkfield and brightfield photomask plates were produced overnight, at a low cost.

Figure 6-8(a) shows the overall pattern of the Au film, including the 4 x 4 array of electrodes and their associated leads and bonding pads, as well as alignment marks, in the form of crosses. The latter were necessary to the accurate positioning of the photomasks over the device in the subsequent photolithographic steps of the fabrication process. In the case of ITO electrodes, the high transparency of ITO required the use of an additional material for the alignment marks; to that end, Au was patterned onto the ITO surface using the photomask shown in Figure 6-8(b). The pattern of Figure 6-8(c) corresponds to that of a photoresist sacrificial layer used to protect the passivating silicon nitride while it was removed by dry etching from over the active area of the electrodes and bonding pads. Three dimensions of electrodes are shown, with diameters of 440 μm , 330 μm and 220 μm . The photomask of Figure 6-8(d) is a negative image of that of Figure 6-8(a) and was used to pattern a layer of photoresist used as a sacrificial layer during wet etching of ITO. The masks of Figure 6-8(e) and Figure 6-8(f) were used to produce masters for the molding of PDMS gaskets with integrated fluidics circuitry; (e) was used to pattern a positive photoresist sacrificial layer on the surface of a Si wafer that was subsequently dry etched, while (f) was used to produce a SU8 master by photolithographic structuring. The channel width was 50 μm in both patterns.

6. 4. 2. 2. 2. Microfabrication of ITO and Au electrode arrays

ITO electrode arrays

25 mm x 75 mm x 0.9 mm float glass slides coated with a 200 nm layer of ITO (resistivity lower than 20 Ω/\square) on one side and an anti-reflection coating on the opposite side were purchased from Delta Technologies Ltd (Stillwater, MN). These substrates were processed according to the following sequence of microfabrication steps.

- (i) The substrates were cleaned by sequential sonication in IPA, acetone and ethanol (5 min each), then blow-dried with N₂.
- (ii) The ITO-glass substrates were spin-coated with S1818 photoresist (4000 rpm for 30 s). Adhesion of S1818 photoresist to ITO was sufficient to make the use of an adhesion primer unnecessary.
- (iii) The photoresist-coated substrates were soft-baked at 90°C for 15 min, immersed in chlorobenzene for 15 min, blow-dried and again soft-baked at 90°C for 15 min. The role of the intermediate chlorobenzene soak was to create overhanging photoresist sidewalls, a feature known to facilitate the subsequent lift-off process.¹⁷²
- (iv) The photoresist layer was photolithographically patterned through the photomask of Figure 6-8(b), using a 10 s exposure time, and subsequent developed in 1:1 Microposit: water for 85 s.

- (v) The substrates were coated with a layer of Ti:Pd:Au (10:10:100 nm) using a Plassys electron-beam evaporator. The sequential evaporation of Ti, Pd and Au was used to compensate the limited adhesion of Au onto glass, as the Ti underlayer greatly enhanced the adhesion to the glass substrate, while the intermediate Pd layer prevented subsequent oxidation of the Ti layer through the Au layer, the latter being microporous.¹⁷²
- (vi) Lift-off of the photoresist was carried out, in acetone at room temperature.
- (vii) The devices were rinsed with RO water and blow-dried with N₂.
- (viii) The side of the substrates featuring the anti-reflection coating was spin-coated with a layer of S1818 photoresist (4000 rpm for 30 s) which was subsequently soft-baked at 90°C for 15 min. The role of this photoresist layer was to protect the anti-reflection coating during the subsequent wet etching of ITO, step (xi).
- (ix) The ITO side of the substrates was spin-coated with S1818; the photoresist layer was then soft-baked at 90°C for 15 min, photolithographically patterned (10 s exposure at 0.52 mW cm⁻²) through the photomask of Figure 6-8(d) and developed in 1:1 Microposit: water for 75 s.
- (x) The patterned photoresist layers (on both sides of the substrate) were post-baked at 120°C for 60 min so as to increase their resistance towards the strongly acidic and oxidising agents used in the next step .
- (xi) The substrates were immersed in 6 M HCl + 0.2 M FeCl₃, at room temperature, for 15 min, under mild agitation.
- (xii) The photoresist was removed from both sides of the devices by 1 minute sonication in acetone.
- (xiii) The devices were rinsed with RO water and blow-dried with N₂.

Au electrodes

Thin film Au electrode arrays with the same pattern as that for the ITO electrodes were microfabricated on 3" x 1" microscope glass slides. Au electrodes and alignment marks were created simultaneously according to steps (ii)-(vii) of the experimental procedure described above. The photomask of Figure 6-8(a) was used instead of that of Figure 6-8(b) in step (iv).

Passivation of the leads with Si₃N₄

A 600 nm thick layer of low-stress Si₃N₄ was deposited by PE-CVD over the ITO and Au devices, using a mixture of SiH₄, NH₃, N₂ and He at 300°C and 1000 mTorr. The deposition time was circa 60 min. Holes corresponding to the electrodes and bonding pads were then

opened up in the silicon nitride layer by dry etching the latter with C_2F_6 gas, using a layer of S1818 photoresist, patterned through the photomask of Figure 6-8(c), as a sacrificial layer.

The complete procedure for the fabrication of ITO electrodes on glass substrates is schematically represented in Figure 6-9. Each processed substrate was then diced into individual 12.5 mm x 25 mm devices using a tungsten carbide cutter.

6. 4. 2. 2. 3. Cleaning of thin film Au electrodes

Two procedures were assessed for the cleaning of thin films Au electrodes: electrochemical cleaning and plasma cleaning. In addition, the possibility to use a protective metallic sacrificial layer of NiCr was investigated.

Cleaning of Au electrodes by potential cycling in acidic solutions

This was achieved by applying a scanning potential to the electrodes immersed in 1 M perchloric acid, between -0.2 V and 1.4 V vs an Ag/AgCl reference electrode. The procedure was restricted to a small number of cycles (3 to 5) so as to alleviate significant etching and roughening of the Au surface, presumably induced by the presence of chloride ions in the cell, released from the silver chloride reference electrode.

Plasma cleaning of thin film Au electrodes

This method was applied to photoresist-covered glass substrates prior to thin-film metallisation, as well as to bare thin-film electrodes prior to insulation with silicon nitride. An O_2 plasma, known to be efficient in the removal of organic contamination, was used. The power (controlled by the bias voltage) had to be kept low to avoid damage to the thin metal film through sputtering. A PlasmaFab ET340 was used with the following settings: 50 mT pressure, 45 sccm flow rate, 180 V bias, 1 minute etching time.

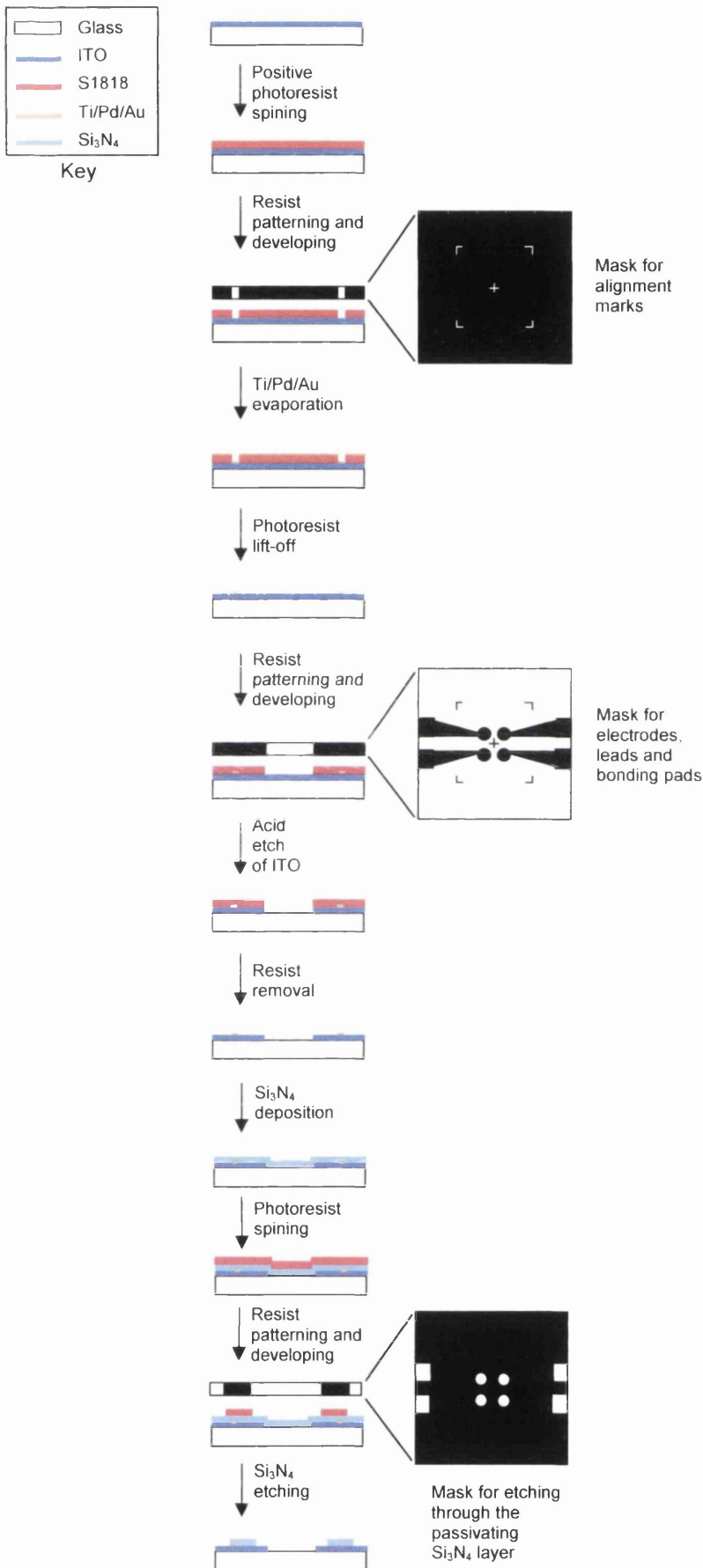


Figure 6-9. Experimental procedure used for the fabrication of an array of ITO electrodes on glass.

Use of NiCr sacrificial layers as a protection for Au thin films

Since Au was found to occasionally undergo damage during the silicon nitride deposition and etching processes, devices were made in which the Ti/Pd/Au metallisation was replaced by Ti/Pd/Au/NiCr. The NiCr layer (60% Ni: 40% Cr, 20 nm thick) was etched after the Si₃N₄ deposition and etching steps (and after the hardbaked S1818 photoresist used as a mask for silicon nitride etching was removed by a 10 s sonication in acetone) by immersion in a solution of 10 g ceric ammonium nitrate and 10 mL HNO₃ (70%) in 100 mL RO water for an appropriate duration, followed by immediate immersion in RO water to stop the process, and rinsing with RO water.

6. 4. 2. 2. 4. Growing of porous Pt black films onto Au electrodes

Pt black was electrochemically grown onto “clean” Au microelectrodes from an electroplating solution containing 0.5 g chloroplatinic acid hexahydrate, 4 mg lead acetate and 15 mL RO water. The set-up shown in Figure 6-10 was used to that end.

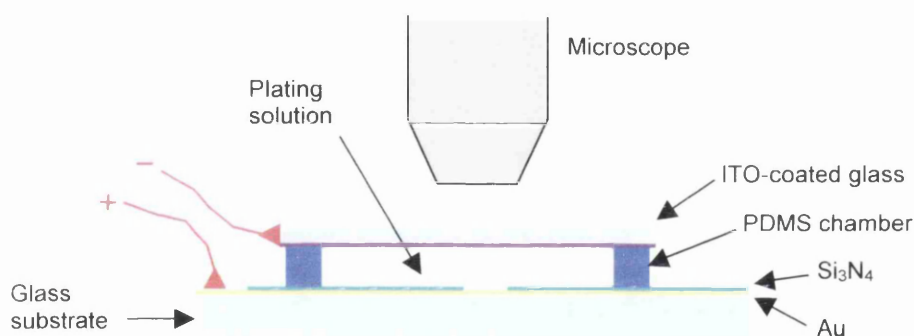


Figure 6-10. Set-up used for the electroplating of Au microelectrodes with Pt black.

A PDMS gasket was placed onto the device to be electroplated, so as to form a circa 100 μ L chamber into which the platinising solution was pipetted. A piece of ITO-coated glass slide placed on top (ITO side down) served as the anode. Electroplating was carried out by applying a potential difference between the ITO anode and the Au cathode, in a galvanostatic mode, at current intensities of 5 μ A to 40 μ A. Different electrodes of the same device were subjected to Pt electroplating at various current intensities and for various durations so as to investigate the effect of these parameters upon the formation of the Pt black film.

The use of a transparent ITO anode permitted optical monitoring of the Pt black growing process by darkfield microscopy. In addition, Pt black films grown in various conditions were characterised by a number of methods including SEM imaging and surface profiling (using a Hitachi S-800 and DekTak ³ST, respectively), and cyclic voltammetry. Cyclic voltammograms were recorded in 1 M H₂SO₄ between -0.18 V and +1.15 V against an Ag/AgCl reference electrode, at 100 mV s⁻¹, with a piece of Pt foil acting as the counter electrode.

6. 4. 2. 3. Results and discussion

6. 4. 2. 3. 1. ITO electrode arrays

The ITO layer had an initial sheet resistance of $16.2 \pm 0.1 \, \Omega/\square$, as determined using a 4-point probe. After production of the Au alignment marks and S1818 patterning (including the post-bake step), the sheet resistance in the non protected areas of the substrates was found to increase to $44.2 \pm 1.1 \, \Omega/\square$, indicating a partial degradation of the conductive properties of ITO, probably due to oxidation during the baking steps. After the wet etch step, the sheet resistance was measured as $45.4 \pm 1.2 \, \Omega/\square$. The transparency of the ITO layer was not affected upon processing.

6. 4. 2. 3. 2. Au electrode arrays

Figure 6-11 shows white light microscopy images of thin-film Au electrode arrays afforded by photolithographic patterning through plastic photomasks.

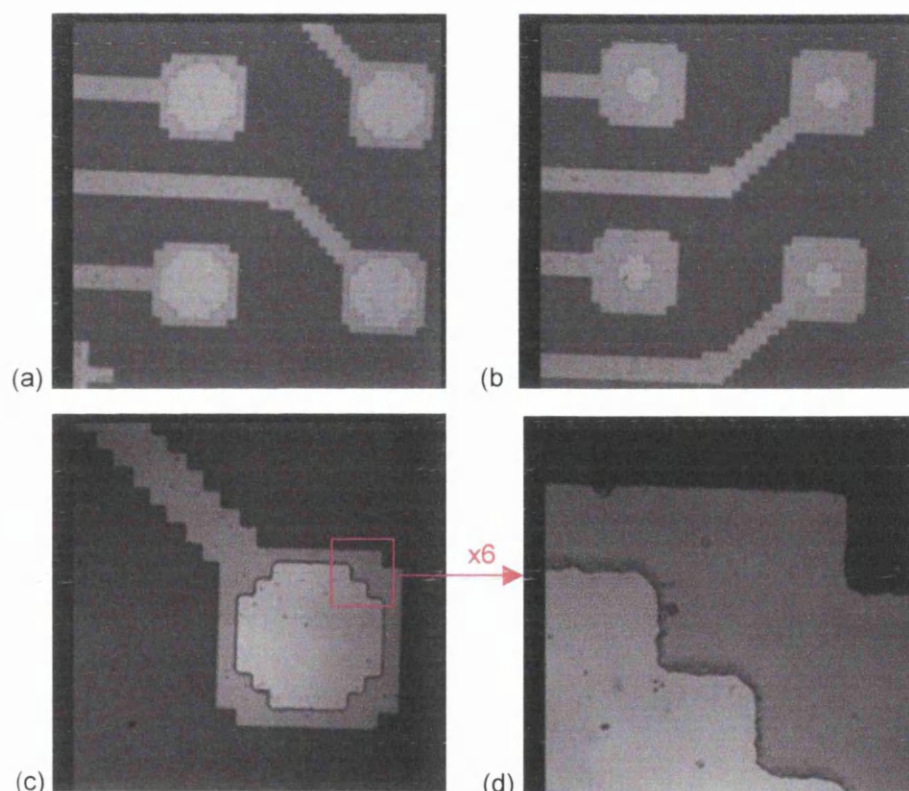


Figure 6-11. White light microscopy images of Au electrode arrays produced by “rapid prototyping” photolithography with plastic photomasks. (a), (b) Darkfield images, after photoresist removal; (c), (d) Nomarski Differential Interference Contrast images, before the photoresist coating was removed.

Figure 6-11 shows the pixelisation of the pattern, resulting from the resolution of the printer used. The dimensions of each pixel were $55 \times 55 \, \mu\text{m}^2$. The lighter areas correspond to bare Au, while the darker areas indicate the presence of the silicon nitride passivation layer. The active

surface area of each electrode was circa $1.7 \times 10^{-1} \text{ mm}^2$ (Figure 6-11(a)) and $3.6 \times 10^{-2} \text{ mm}^2$ (Figure 6-11(b)). $9.7 \times 10^{-2} \text{ cm}^2$ electrodes were also fabricated.

The small dark spots seen in the images of Figure 6-11 represent residues of photoresist which were not been made soluble during the exposure step, due to localised reduced levels of illumination caused by the presence of microbubbles within the acetate sheet. This problem was subsequently partially solved by increasing the exposure time to 28 s and the developing time to 110 s, but a number of these defects remained, as seen later. Figure 6-11(c) and Figure 6-11(d) are Nomarski differential interference contrast (DIC) images of an electrode acquired after the silicon nitride was etched away but before the photoresist was removed. Figure 6-11(d) clearly shows the roughness of the pattern edges. This problem could of course be alleviated by the use of standard ferric oxide or chromium photomasks.

Cleaning of Au electrodes by potential cycling in acidic solutions was found to result in significant etching and roughening of the Au surface, presumably due to the presence in the electrolyte of chloride ions released from the silver chloride reference electrode. Therefore, plasma cleaning was used preferentially. The use of NiCr to protect Au electrodes was somewhat limited by the fact that the NiCr wet etch process is isotropic, making it crucial to precisely control the etching time to avoid lateral overetching, as exemplified in Figure 6-12.

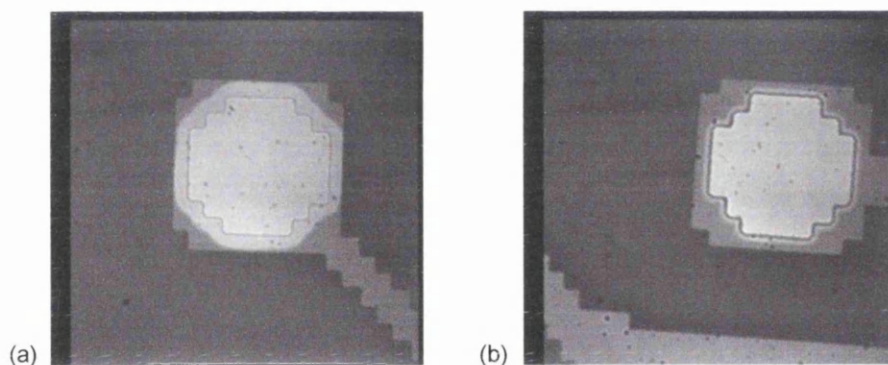


Figure 6-12. Microphotographs of Au electrodes after removal of the NiCr sacrificial layer. (a) 25 s and (b) 14 s etching time.

Figure 6-12(a) shows an excessive lateral overetching of the NiCr layer. The silicon nitride layer, which remained unaffected by the NiCr etch, formed an overhang over the bare Au area. An etching time of 14 s (followed by immediate immersion and rinsing in RO water) was found to be optimum, although some degree of lateral overetching could not be avoided.

6.4.2.3.3. Pt black electrodes

In situ white light microscopy

Figure 6-13 shows white light darkfield microscopy images of an electrode, acquired *in situ* as described in Figure 6-10, before and during the electroplating process.

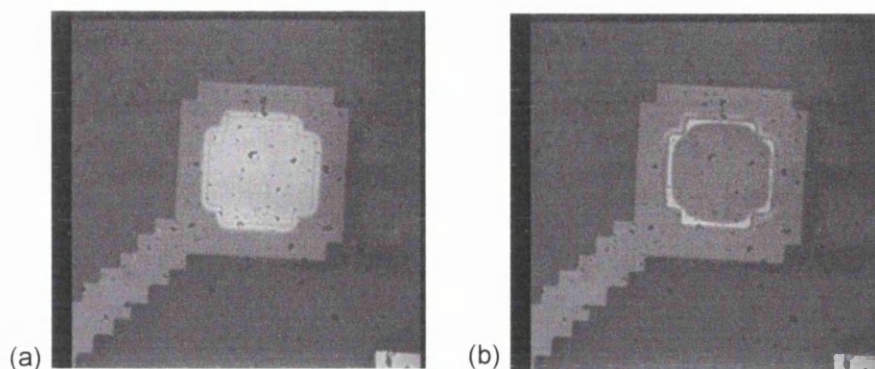


Figure 6-13. White light darkfield microscopy images of a Au microelectrode, (a) prior to electroplating and (b) after electroplating at $5 \mu\text{A}$ (equivalent to 5.1 mA cm^{-2}) for 30 s.

Figure 6-13 clearly shows an increase in optical density over the electrode area, indicating the presence of a Pt black film. A number of particles can be seen in the solution; these were removed in subsequent experiments by filtering the electroplating solution through a $0.45 \mu\text{m}$ filter (Whatman).

Characterisation by SEM imaging

Figure 6-14(a)-(c) shows SEM images of Pt black, grown on Au microelectrodes according to the procedure described in Section 6.4.2.2.4.

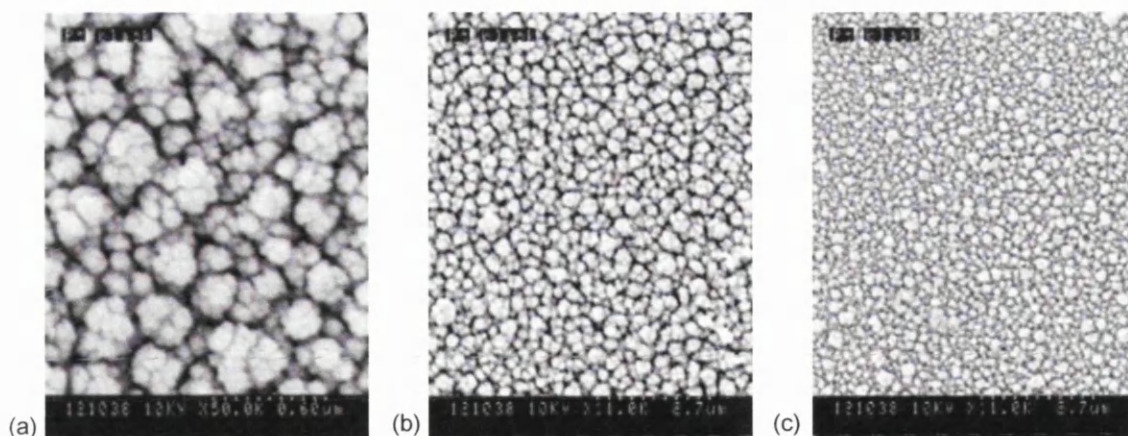


Figure 6-14. Scanning electron microscope images of Pt black grown at (a) and (b) 40 mA cm^{-2} ; (c) 10 mA cm^{-2} .

Figure 6-14(a) clearly shows the porous structure of the Pt black, with sub-micron dendrites perpendicular to the surface. Comparison of the SEM images of Figure 6-14(b) and Figure 6-14(c), which were recorded at the same level of magnification, clearly shows the effect of the current density on the porosity of the structure: in Figure 6-14(c), the use of a lower current intensity resulted in a tighter pore structure than in Figure 6-14(b).

Characterisation by surface profiling

Figure 6-15 shows surface profiles of micro electrodes coated with Pt black grown in various electroplating conditions.

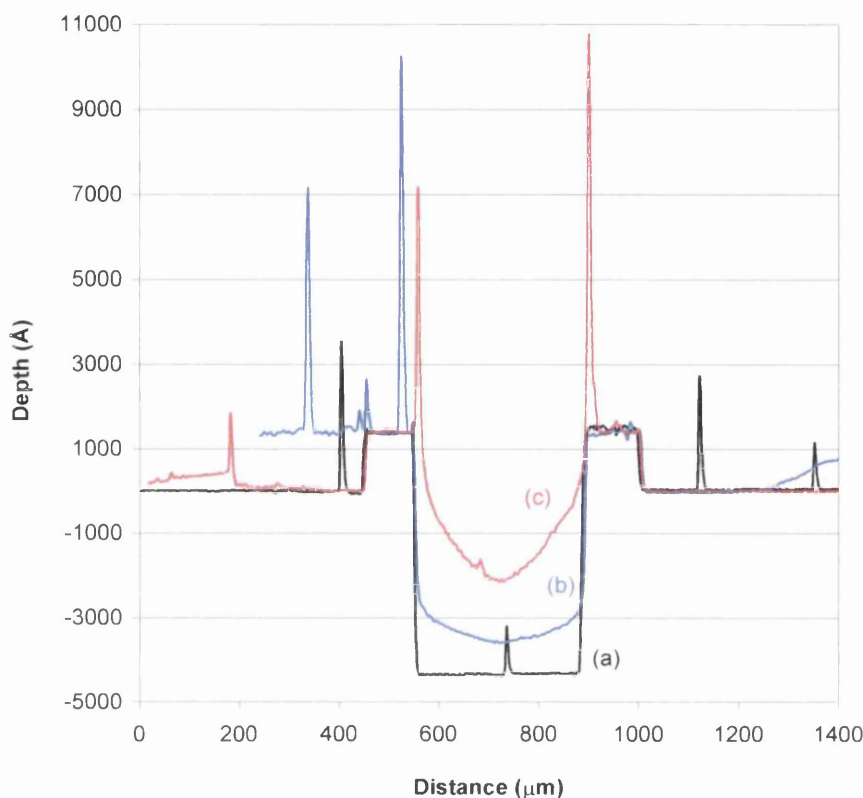


Figure 6-15. Surface profiles of (a) a bare Au microelectrode and (b-c) of Pt black films grown on Au microelectrodes at $20\ \mu\text{A}$ (equivalent to $20.6\ \text{mA cm}^{-2}$) for (b) 30 s and (c) 2 min.

The profile for the bare Au microelectrode, Figure 6-15(a), clearly shows the microwell formed by the $330\ \mu\text{m}$ diameter opening in the $600\ \text{nm}$ thick silicon nitride layer over the $500\ \mu\text{m}$ diameter, $120\ \mu\text{m}$ thick Ti/Pd/Au disk. The profiles for the Pt black-coated electrodes show the effect of the current intensity and biasing duration on the thickness of the Pt black film. Although the latter was not radially uniform, it appeared to be cylindrically symmetrical. The higher thickness obtained near the electrode edges for the films grown at $20\ \mu\text{A}$ reflect the higher electric field strength (hence higher current density) at the electrode edges. The spikes in the surface profiles correspond to photoresist residues, as discussed in Section 6.4.2.3.1.

Characterisation by cyclic voltammetry

Pt black films were also characterised by CV. Figure 6-16 shows the cyclic voltammograms of two Au microelectrodes which had been coated with Pt black grown at different current densities. The voltammograms shown in Figure 6-16 feature peaks characteristic of Pt electrodes,¹⁶⁶ namely peaks due to the oxidation and reduction of Pt at the surface of the

electrode (O_a , formation of adsorbed oxygen and Pt oxide layers; O_c , reduction of oxide layers), and to the inherent reactivity of Pt towards hydrogen oxidation and reduction (H_a and H_c : oxidation and reduction, respectively, of adsorbed hydrogen layers).

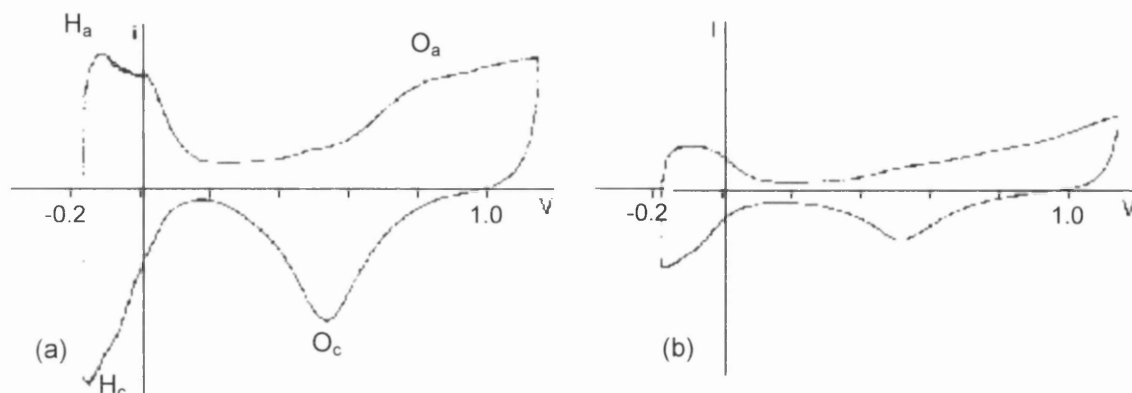


Figure 6-16. Cyclic voltammograms of Pt black electrodes grown at (a) 10 mA cm^{-2} and (b) 40 mA cm^{-2} , both for 10 s. Electrolyte: $1 \text{ M H}_2\text{SO}_4$, reference electrode: Ag/AgCl; scan rate: 100 mV s^{-1} .

The larger value of the integral of the charge under the hydrogen wave in Figure 6-16(a) confirms the larger electrochemically active area of the Pt black film grown at a lower current intensity. This is in agreement with the results of Figure 6-14.

6. 4. 2. 3. 4. Completed device

Figure 6-17(a) shows a completed device featuring a 4×4 array of Au microelectrodes. Connectors were attached to the bonding pads with silver-loaded epoxy glue and further stabilised with epoxy glue. The device is shown here without the PDMS fluidics structure. Figure 6-17(b) is a microphotograph of the central part of the device, showing the array of electrodes, part of the leads and a couple of alignment marks. Eight of the sixteen electrodes have been coated with Pt black grown at 10 mA cm^{-2} for 10 s.

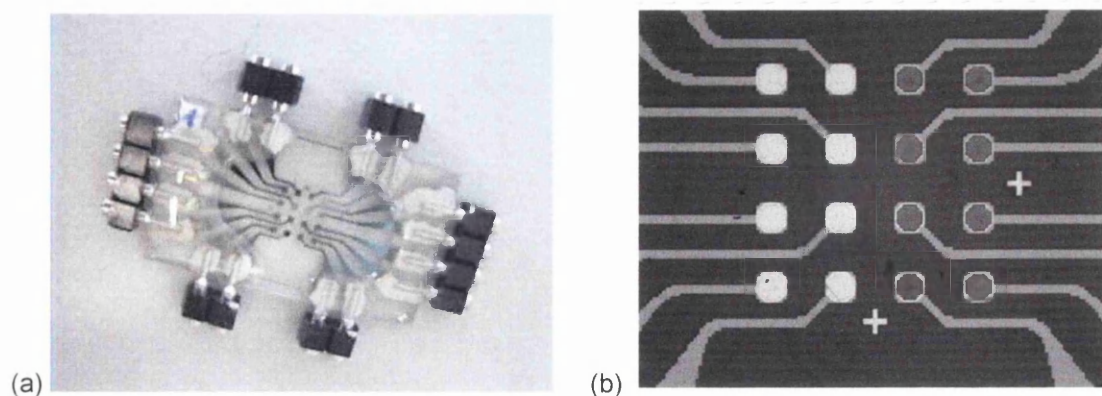


Figure 6-17. (a) Photograph of a complete 4×4 electrode array device with electrical connectors. (b) Microphotograph of a 4×4 array of thin film Au electrodes. The electrodes on the right have been coated with Pt black.

6. 4. 3. Selection of a suitable buffer

6. 4. 3. 1. Introduction

A number of buffers were tested for their combined ability to shield the phosphodiester backbone of nucleic acid molecules while featuring a low conductivity and a sufficient buffering strength. These buffers included standard DNA hybridisation buffers (SSC and SSPE), a buffer commonly used in electrophoresis of nucleic acids (TRIS-borate) and two isoelectric amino acid buffers, L-histidine (His) and γ -aminobutyric acid (GABA). Table 6-3 gives the values for the pK_a, pI and conductivity of these buffers. The conductivity values were determined experimentally.

Isoelectric buffers are aqueous solutions of zwitterionic species which exhibit a weak or no net charge (and consequently a low conductivity) at pH values close to their isoionic point (pI) while exhibiting appreciable buffering properties at this same pI, the latter being close to a pK_a.^{173,174} Table 6-3 indicates that the conductivity of the 100 mM His and GABA solutions is at least two orders of magnitude lower than that of the "salt" buffers, SSC and SSPE. The expected gain in performance provided by this low conductivity in terms of electrophoretic transport was investigated, using a device similar to that shown in Figure 6-17, through a series of experiments in which DNA molecules were electrokinetically transported over an array of patterned electrodes, in a two dimensional configuration.

All the buffers considered here are weak acids and/or bases. At pH values comprised within the range [pK_a-1, pK_a+1], the β value for a weak acid is within 1/3 of its maximum, where K_a is the thermodynamic dissociation constant, *i.e.* the value for the dissociation constant at zero ionic strength; in practice, the effect of the ionic strength of the medium has to be considered. Unlike SSPE, His and GABA, which feature both an acidic and a basic function, SSC and TRIS-borate do not provide buffering in basic and acidic media, respectively.

Buffer	1x SSC			1x SSPE				His, 100 mM	TRIS-borate, 100 mM	GABA, 100 mM
Component	Na ⁺	Cl ⁻	Citrate	Na ⁺	Cl ⁻	Phosphate	EDTA	HIS	TRIS	Borate
Concentration (mM)	165	150	15	149	149	10	1	100	100	100
pH	7.46			7.41				7.65	8.32	
pK _a	3.1			2.12				1.8	8.1	4.0
	4.8			7.21				6.0	9.1	10.6
	6.4			12.7				9.4		
pl	-			-				7.47	-	7.31
Conductivity (mS cm ⁻¹)	> 20			> 20				0.094	0.661	0.006

able 6-3. Buffers tested for flow-through hybridisation with electrokinetic pumping. His: L-histidine; GABA: γ -aminobutyric acid. pK_a: thermodynamic acidity dissociation constant; pl: isoelectric point. The pH and conductivity values of the prepared solutions were determined experimentally, using a HANNA Instruments 8521 pH meter and a RS 180-7127 conductimeter, respectively, at 22±1 °C.

The stability of double-stranded nucleic acid hybrids is commonly characterised by the melting temperature T_m of the duplex, temperature at which half of the hybrids are dissociated. The following empirical equation is commonly used to estimate the T_m for the hybridisation of solution-borne targets to membrane-bound probes of complementary sequence, in "salt" buffers such as SSC and SSPE.³⁸

$$T_m = 81.5 + 16.6 \log ([Na^+]) + 0.41 (G+C \text{ fraction}) - 600 / L \quad (\text{Equation 6-4})$$

where $[Na^+]$ is the molar concentration of salt in the hybridisation medium,

$G+C \text{ fraction}$ is the total percent fraction of guanine and cytosine residues in the hybrid,

L is the length (in number of bases) of the shortest DNA strand in the duplex (usually the probe).

This formula gives a good approximation for the T_m of oligonucleotides as short as 14 bases and as long as 70 bases, for sodium ion concentrations between 10 mM and 400 mM, and for G+C fractions between 30% and 75%. The presence of mismatches within the duplexes leads to a reduction of T_m by 1 to 1.5°C for every percent mismatch, depending on the position of the mismatched bases along the strands.

Equation 6-4 does not apply to buffer solutions containing a low (< 10 mM) amount of small cations, such as the TRIS-borate and isoelectric buffers of interest here. The suitability of these buffers as hybridisation media was thus tested experimentally, and compared to that of SSC and SSPE, through static hybridisation experiments.

6. 4. 3. 2. Experimental

6. 4. 3. 2. 1. Electrokinetic transport of ODNs over an array of microelectrodes

The sample used throughout was a 29-mer ODN, T8, of sequence "R"AGTGGGTGGCGCTGTTGAAGTCAGAGGC, where "R" is a 5'-Texas red label, dissolved at 100 nM in each of the above-mentioned buffers from a 200 μ M stock solution in TE. A device similar to that shown in Figure 6-17 was used in these experiments. A 6 mm x 6 mm window was cut off in a 0.7 mm thick PDMS slab, which was brought into conformal contact with the device, so as to create a 25 μ L open chamber. A corresponding volume of sample was pipetted into the chamber, which was subsequently capped with a thin glass coverslip (80-120 μ m, BDH) so as to prevent sample evaporation. Two adjacent electrodes of the same type (bare Au or Pt black-coated) were used as anode and cathode.

The device was connected to a galvanostat/potentiostat and placed within the field of view of an epifluorescence microscope fitted with a CCD camera (as described in Section 5. 3. 1. 2). Each experiment consisted in applying a galvanostatic bias of 0.5 μ A to 5 μ A (equivalent to 1.6 mA cm⁻² - 16 mA cm⁻²) between the two electrodes for a given period of time, while monitoring the evolution of the potential difference between the electrodes, as well as the

redistribution of target within the chamber by epifluorescence imaging through the glass window. Experiments were conducted in which the polarity of the electrodes was reversed at a fixed frequency. A Zeiss Fluar 10x, NA 0.50 objective lens was used. The sample contained in the chamber was renewed between successive experiments so as to minimise photobleaching of the fluorescent label as well as electrochemical damage of the ODN. In addition, the chamber was rinsed with buffer, ample RO water, and blow-dried between measurements.

6. 4. 3. 2. 2. Testing for hybridisation

The capacity of each buffer to support hybridisation was investigated in a static mode, in an experiment similar to that reported in Section 4. 5. 3. Ten glass substrates were processed as described in Section 4. 5. 3. 2. The ODN target T3 was dissolved at 100 nM in each of the above-mentioned buffers (1x SSC, 1x SSPE, 100 mM TRIS-borate, 100 mM His and 100 mM GABA) from a 200 μ M stock solution in 5x SSPE. Each target solution was hybridised sequentially for 20, 30, 60, 120, 240 and 240 minutes with two substrates. After each sequential hybridisation period, the chips were washed with hybridisation buffer, blow-dried and imaged. A fresh 100 μ L of target solution was used in each successive hybridisation.

6. 4. 3. 3. Results and discussion

6. 4. 3. 3. 1. Electrokinetic transport of ODN over an array of microelectrodes (lateral transport)

Figure 6-18 shows the evolution over time of the potential difference between the anode and the cathode, during continuous galvanostatic biasing at 0.5 μ A and 1 μ A, the cell being filled with a 100 nM solution of Texas Red-labelled 29mer ODN in 100 mM His and 100 mM GABA.

Figure 6-18 shows an increase in the bias voltage with both increasing applied current intensity and decreasing conductivity of the medium. Some capacitive behaviour was observed, a characteristic of the formation of an electrical double layer at the surface of the electrodes. The use of a galvanostatic-, rather than potentiostatic, biasing scheme afforded better control over the level of surface current density at the electrodes, and thus over the extent of electrochemical reaction (in particular water electrolysis) taking place at the electrodes.

Higher levels of current intensity translated into higher levels of electric field strength within the cell; the expected higher rate of ODN transport was verified by monitoring the redistribution of fluorescently-labelled ODNs within the cell, using epifluorescence microscopy. Evidence of ODN transport under galvanostatic biasing is provided by Figure 6-19.

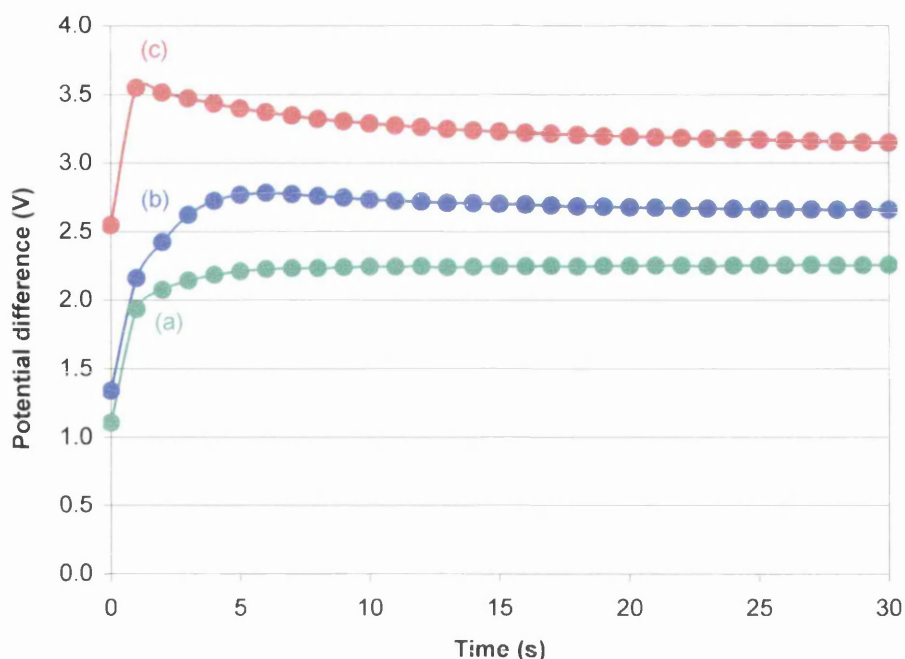


Figure 6-18. Evolution of the potential difference between a Au anode and a Au cathode over time, during continuous galvanostatic biasing, in two different isoelectric buffers. (a) 100 mM His, 0.5 μ A; (b) 100 mM GABA, 1 μ A; (c) 100 mM GABA, 0.5 μ A.

Figure 6-19 shows an overall increase in fluorescence intensity at the surface of the anode over time, while the opposite trend was observed at the cathode (note that the Pt black anode and cathode were not used at this stage). Since the ODN molecules were uniformly distributed within the volume of the chamber before the onset of biasing, the higher brightness of the electrodes and leads as compared to the non-patterned area in Figure 6-19(a) was due to reflection of light at the Au surface rather than to a higher concentration of ODNs at these locations. Rapid redistribution of the ODN molecules around the electrodes upon biasing was evidenced, even though non-confocal optics were used (hence a relatively high level of background fluorescence). The Texas Red label was chosen for the insensitivity of its fluorescence properties toward pH, so as to alleviate any effect of local pH changes at the electrodes on the intensity of fluorescence. At higher current intensities, the formation of bubbles within the cell was observed, as expected from the production of O_2 and H_2 during water electrolysis.

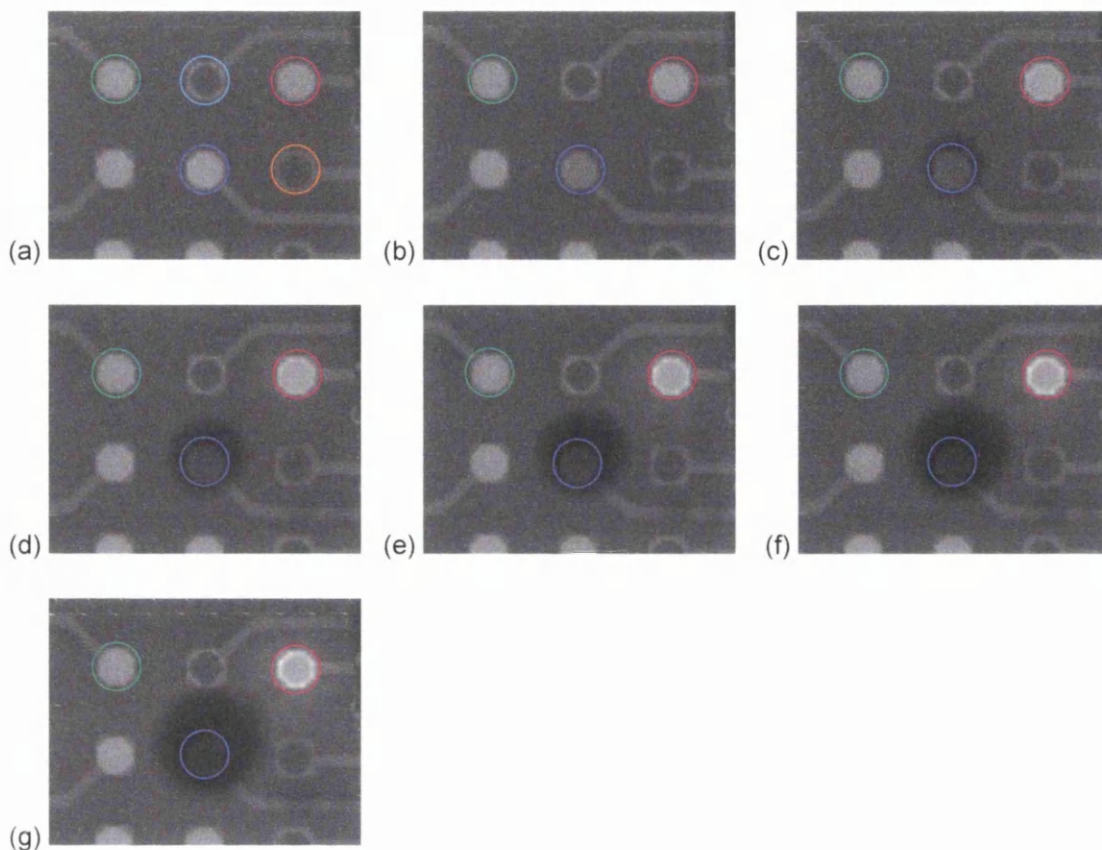


Figure 6-19. Epifluorescence images of a 100 nM solution of a Texas Red-labelled 29-mer ODN target in 100 mM GABA submitted to an electric field generated by the continuous application of a 1 μ A galvanostatic biasing between two Au electrodes of the device shown in Figure 6-17. Blue: cathode; Red: anode; green: floating potential (unbiased) electrode. Images (a) to (g) were acquired at 5 s intervals from the onset of the voltage biasing. Light blue, orange: Pt black anode and cathode, respectively.

Quantitation of the rate of ODN transport was implemented by determining the fluorescence intensity over the whole area of each electrode in the sequence of epifluorescence images. This was performed using IPLab software. Figure 6-20 shows the resulting “kinetics” curves associated with Figure 6-19. The curves of Figure 6-20 illustrate the phenomena of ODN concentration at the anode, curve (a), as well as ODN depletion at the cathode, curve (b). The fluorescence intensity at the floating electrode exhibited a small (< 2%) decrease over 30 s, which might reflect photobleaching.

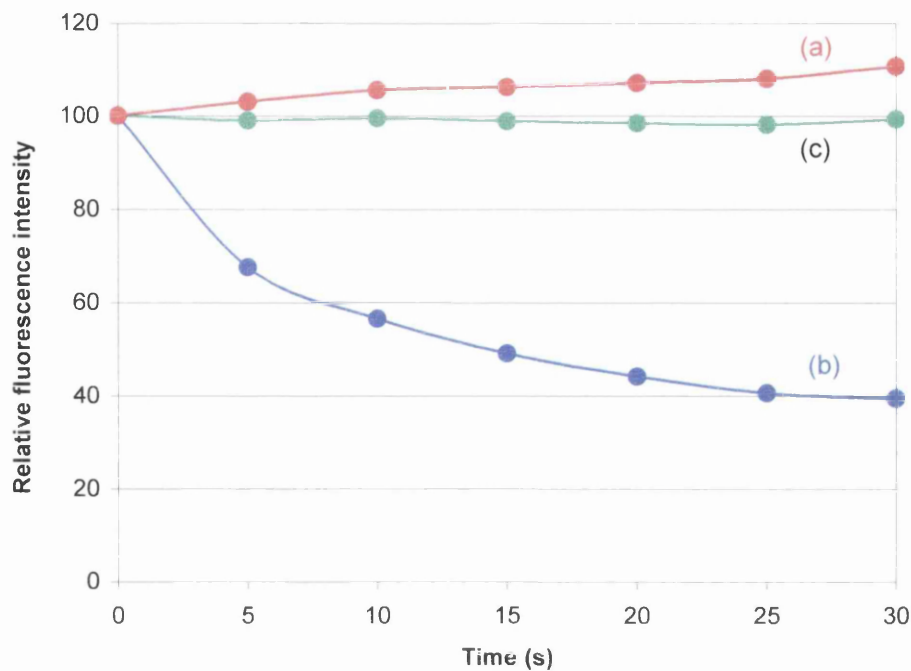


Figure 6-20. Evolution over time of the fluorescence intensity over the area of (a) the anode, (b) the cathode and (c) the floating electrode, measured from the images of Figure 6-19.

Lateral transport of the Texas Red-labelled ODN molecules over the array of microelectrodes was carried out in the five buffers of Table 6-3, at 1 μ A biasing. The increase of fluorescence intensity at the anode over the first five seconds of biasing was used as a measure of the rate of transport. A comparison between the five buffers is provided by Figure 6-21.

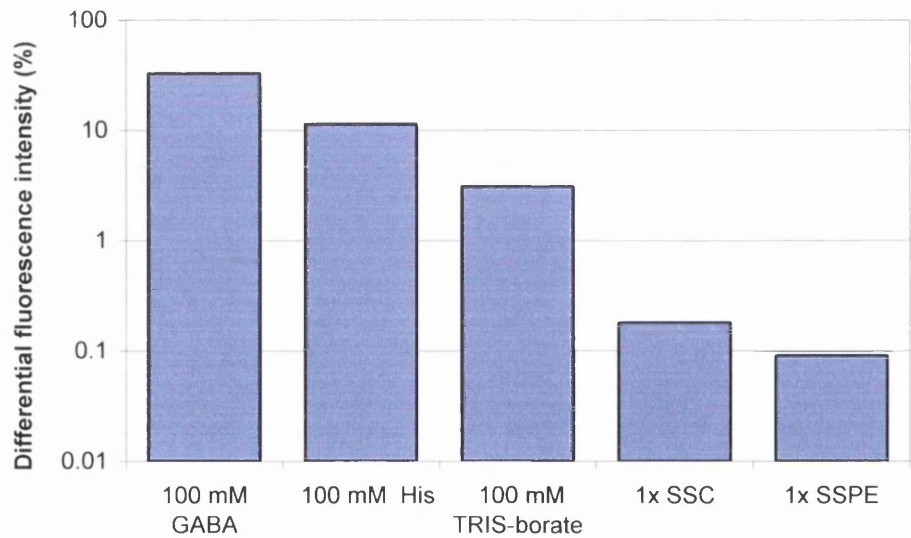


Figure 6-21. Relative increase (in %) of fluorescence intensity at the anode over the first five seconds of galvanostatic biasing (at 1 μ A), in various buffers.

Figure 6-21 shows that the rate of transport was highly dependent on the medium. The isoelectric buffers, His and GABA, provided two orders of magnitude faster transport than the salt buffers, SSC and SSPE, in agreement with the relative conductivity values (Table 6-3).

The production of charged species (H^+ , OH^-) upon redox transfer at the electrodes was expected to increase the conductivity of the buffer, and thus to decrease the electric field strength. This effect was investigated over a period of time during which the polarity of the electrodes was reversed at a fixed frequency. Images were acquired every 10 ms (instead of 5 ms in the previous experiment) to reduce the effects of photobleaching. The results are shown in Figure 6-22, curves (a) and (b).

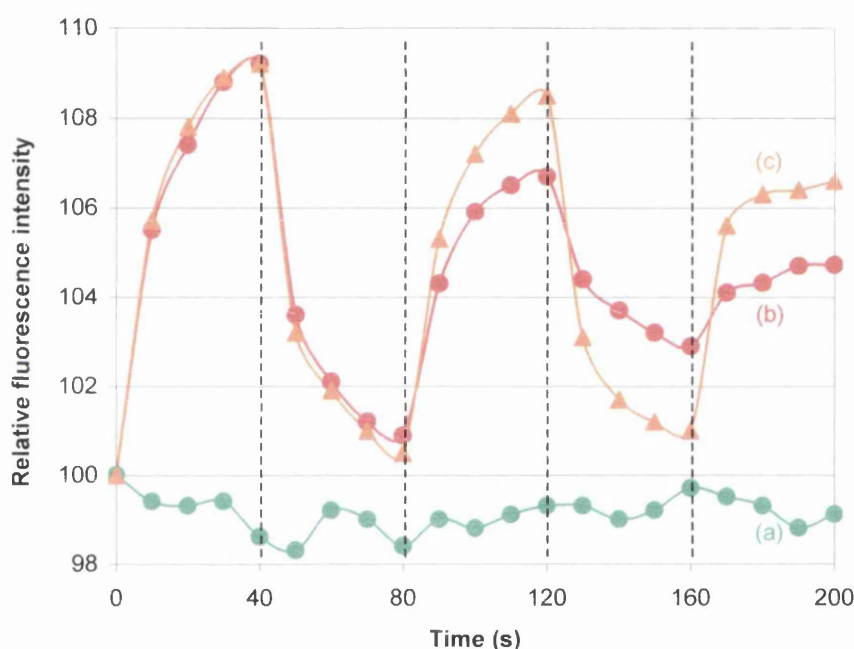


Figure 6-22. Time-dependence of the fluorescence intensity over (a) an unbiased Au electrode, (b) a biased Au electrode and (c) a biased Pt black electrode, during electrokinetic transport of a Texas Red-labelled 29-mer ODN target present at 100 nM in 100 mM GABA buffer. The Au and Pt black electrodes were used separately, in two independent experiments in which each of these electrodes was iteratively biased at +1 μA for 40 s and -1 μA for 40 s against a Au electrode. The vertical dashed lines indicate the time points at which the polarity was reversed.

The low extent of photobleaching over the duration of the experiment (200 s) is illustrated by curve (a), which represents the fluorescence intensity over an unbiased electrode. Curve (b) shows the fluorescence intensity over a Au electrode which was biased at 1 μA against another Au electrode, the direction of the current being reversed every 40 s.

Over the first 40 s, during which the electrode was biased anodically, ODN concentration took place at the electrode, as illustrated by the associated increase in fluorescence intensity. As

soon as the polarity was reversed, the fluorescence intensity decreased over the next 40 s. Over the next cycle (80-160 s), ODN concentration and depletion were again observed, but with a reduced amplitude. The latter effect reflects of a lower transport rate, probably caused by an increase in the conductivity of the medium as a consequence of the production of charged species through water electrolysis, and/or possible electrochemical damage of the ODN at the surface of the electrodes.

Curve (c) of Figure 6-22 shows the results of a similar experiment in which a Pt black electrode was biased at 1 μ A against a Au electrode. The fluorescence intensity values were normalised with those of curve (b) in order to compensate for the lower reflectivity of the Pt black. Curve (c) shows that the decrease in transport rate with time was not as pronounced as that observed for a Au electrode. This can be explained by a reduced extent of water electrolysis at the Pt black electrode, a consequence of the higher effective surface area of the porous Pt black film as compared to that of the thin Au film, whereby the increase in surface area could have led to a lower surface current density, hence a lower level of faradaic current. In this respect, the assumption that the level of porosity of the Pt black film affected the ODN transport rate could not be unequivocally verified, due to the lack of sensitivity of the method used to measure transport rates. In addition, the difference between Au and Pt in terms of water electrolysis overpotential might have contributed to the observed phenomenon.

6. 4. 3. 3. 2. Electrokinetic transport of ODN between two parallel microelectrode arrays (axial transport)

The two-dimensional electrokinetic transport of ODN demonstrated above was directly relevant to the issues of electrokinetic injection and concentration of nucleic acid targets at selected locations, as would be carried out in the bottom chamber of the hybridisation cell, prior to back-and-forth axial pumping through a microchannel chip. Axial transport of ODN between two parallel microelectrode arrays was attempted; however, in this three-dimensional configuration, monitoring the redistribution of ODN within the cell by fluorescence imaging required confocal optics so as to probe a single optical plane. In the absence of a confocal microscope, no conclusive evidence of the axial transport of ODN through a microchannel chip could be obtained.

6. 4. 3. 3. 3. Comparison of various buffers in static, mixed-phase hybridisation assays

Figure 6-23 shows the compared hybridisation kinetic curves in the five different buffers. Each data point represents the average of two independent measurements from two chips.

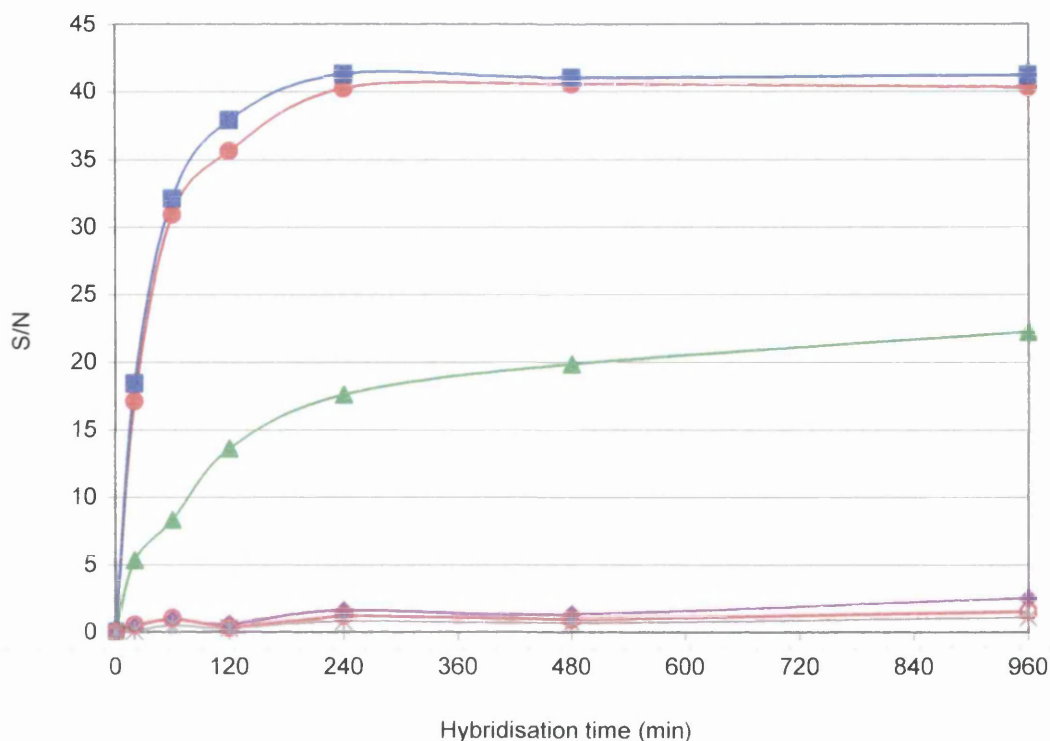


Figure 6-23. Compared kinetics of mixed-phase hybridisation between a planar glass-immobilised 15-mer oligonucleotide capture probe and a 14-mer target present at 100 nM in different buffers: 1x SSC (squares), 1x SSPE (full circles), 100 mM TRIS-borate (triangles), 100 mM His (diamonds), 100 mM GABA (stars). The open circles represent non-specific binding of the target to a non-complementary probe, in 1x SSPE.

As shown in Figure 6-23, the kinetics of hybridisation were found to vary widely with the buffer used. The results obtained for 1x SSC and 1x SSPE were close to each other and in agreement with those of Figure 4-6(a). Saturation was reached after circa 4 hours. A negative control, provided by the presence on the chip of a non-complementary probe, showed the low extent of non-specific hybridisation in 1x SSPE, with S/N values remaining below 5 over a total cumulative hybridisation period of 16 hours. Slower kinetics of hybridisation were obtained in 100 mM TRIS-borate, reflecting the reduced ability of this buffer to stabilise the probe-target duplexes. Hybridisation did not take place to any significant extent in the isoelectric buffers His and GABA.

6. 4. 4. Conclusions

Electrophoretic transport of nucleic acids over an array of photolithographically-defined microelectrodes was demonstrated. Furthermore, the coating of the thin-film Au electrodes with a thick, porous Pt black film was shown to be beneficial to the process, allowing for transport rates to be sustained for longer periods of time. This could be applied to the injection and concentration of nucleic acid targets within integrated, miniaturised bioMEMS devices such as

that of Figure 6-7. However, successful combination of electrophoretic transport of target nucleic acids and probe-target heterogeneous hybridisation could not be achieved due to conflicting requirements for a medium featuring both a high ionic strength and a low electrical conductivity. Possible improvements to the approach remain to be tested, such as the use of peptide nucleic acid (PNA) capture probes¹⁷⁵ which are known to hybridise with DNA in low ionic strength media.

CHAPTER 7. CONCLUSIONS AND FUTURE DIRECTIONS

7. 1. Achievements of this thesis

The realisation of a novel bioanalytical platform from a concept to a functional device necessarily involves a number of different technical issues. Accordingly, the contents of this thesis reflect the multidisciplinary nature of the microarray field. The knowledge gained within the scope of this thesis is believed to be directly transferable to various applications belonging to the rapidly expanding field of bioelectronics, such as lab-on-a-chip technology.

The fabrication of silicon microstructures with feature sizes in the micrometre range and aspect ratios in excess of 30:1 has been achieved, using two different techniques, electrochemical etching and deep dry etching, whose relative merits have been assessed. The most promising technique appears to be deep dry silicon etching, due to its flexibility in the fabrication of substrates with varied morphologies, and its status as a MEMS technique with the associated possibilities for the implementation of quality control and large scale production. Most of the technical issues involved in the fabrication of microchannel substrates, such as the processing of thick ($> 300\ \mu\text{m}$) photoresist layers, pertain to the development of other types of MEMS and bioanalytical devices.

Investigations into the possible use of fluorescence detection in conjunction with microchannel substrates has been the main focus of this thesis. The success of the approach was illustrated by the achievement of detection limits as low as a few attomoles of fluorescent dye, in an imaging mode that provides two levels of multiplexing (spatial and spectral discrimination). This has been made possible by the remarkable optical properties of microchannel glass, in addition to the implementation of a methodology for the optimisation of CCD-based epifluorescence imaging systems. Simulations of the fluorescence imaging process based on ray-tracing procedures have been beneficial in this respect; this approach should be useful to a range of bioanalytical applications involving fluorescence detection in microstructures, such as lab-on-a-chip devices.

A strategy has been developed for the immobilisation of oligonucleotide probes onto silica-rich substrates, in a functional conformation suitable to heterogeneous hybridisation. The approach is versatile in that it is applicable to glass as well as silicon. The particular wetting properties of microchannel substrates were characterised and subsequently taken into account in the development of a microarraying procedure based on non-contact dispensing. This strategy has been used to produce medium-density microchannel oligoarrays, with as many as 256 probe spots over a $< 1\ \text{cm}^2$ area.

A fluidics scheme compatible with microchannel chip-based hybridisation assays has been implemented, in which the sample was mechanically pumped through the chip. This scheme

was used in hybridisation experiments which demonstrated the improved performance of the flow-through microchannel configuration over the conventional planar configuration.

Even at this early stage of development, it has been shown that the flow-through microchannel biochip configuration provides increased sensitivity, speed and throughput to nucleic acid hybridisation assays. A few possible routes for further improving the performance and scope of flow-through microchannel biochips are suggested below.

7. 2. Suggestions for future work

7. 2. 1. Improved optical detection

The performance of the optical detection scheme has been shown in Chapters 3 and 6 to be limited by a relatively high level of background signal which detrimentally affected the detectability and dynamic range of the assay. This background came from the substrate itself, through autofluorescence of the lead glass matrix and surface scattering of light, as well as from non-specifically bound targets that unavoidably adsorbed onto the high surface area of the MCG substrate. Accordingly, possible work aiming at reducing these background levels should focus on two directions. On the one hand, detection schemes that provide enhanced selectivity at the molecular level should be considered, so that only targets involved in duplexes with their cognate probe generate signal; on the other hand, improvement of the optical instrumentation can be envisaged, for example through selective illumination of spots.

7. 2. 1. 1. Fluorescence resonance energy transfer (FRET)-based methodologies

Principle

The non-radiative transfer of excitation energy between a donor fluorophore and a suitable energy acceptor is described by Förster's theory.¹²⁶ The rate of energy transfer to a specific acceptor, k_T , is given by:

$$k_T = \tau_D^{-1} (R_0/r)^6 \quad (\text{Equation 7-1})$$

where τ_D is the luminescence lifetime of the donor, r the average distance between the donor and acceptor molecules, and R_0 the Förster distance. R_0 is sometimes referred to as the distance for half-transfer efficiency. It depends on the fluorescence quantum yield of the donor (ϕ_D), the donor-acceptor dipole orientation factor (κ^2), the index of refraction of the medium (n), and the spectral overlap between donor and acceptor (J), according to the following equation:

$$R_0 = 9.8 \times 10^3 (\phi_D \kappa^2 n^{-4} J)^{1/6} \quad (\text{Equation 7-2})$$

with J being given by

$$J = \int_0^{\infty} \varepsilon_A(\lambda) I_D(\lambda) \lambda^4 d\lambda \quad (\text{Equation 7-3})$$

where ε_A is the extinction coefficient of the acceptor, λ the wavelength, and I_D the fluorescence emission intensity of the donor as a fraction of the total integrated intensity. The energy transfer efficiency, E , varies with the distance r between the donor and acceptor molecules, according to

$$E = \left(\frac{R_0^6}{R_0^6 + r^6} \right) \quad (\text{Equation 7-4})$$

Application to heterogeneous nucleic acid hybridisation assays

FRET is particularly well suited to the selective detection of double-stranded DNA. By labeling a probe and its cognate target with members of an acceptor-donor pair, energy transfer can be made to occur only when a duplex is formed, due to the dependence of the energy transfer on the sixth power of the separation distance. The chain order (single- or double-stranded) of a probe can thus be inferred from the relative fluorescence emissions of the acceptor and the donor.⁹² This is best implemented as a ratiometric measurement through two optical channels, which reduces distortions due to photobleaching and instrumental fluctuations. Alternatively, the target can be labeled with a non-fluorescent acceptor that acts as a quencher for the probe-bound donor.

Benefits to flow-through microchannel chip-based hybridisation assays

The main advantage of the approach as compared to direct fluorescence detection of labeled targets is that no stringent washing step is required to remove non-hybridised targets (either in solution or non-specifically adsorbed to the substrate) from the hybridisation volume during detection. This offers the possibility of performing real-time monitoring of the hybridisation process, e.g. for kinetic studies.⁵⁰ This feature would be invaluable in the optimisation of various experimental parameters involved in flow-through microchannel DNA chip assays, such as the channel diameter and the flow rate. Also, the contribution of non-specifically bound targets to the fluorescence signals would be much reduced, which would improve the detectability and dynamic range of the assay. The main limitation of the approach is the need to label both the probes and targets, which complicates the chip and sample preparation procedures.

7. 2. 1. 2. Molecular beacon technology

Principle

Molecular beacons are oligonucleotide probes with a stem-and-loop (or dumbbell, or hairpin) structure (Figure 7-1) that can selectively report the presence of specific nucleic acids targets.¹⁷⁶ The loop portion of a molecular beacon is a probe sequence complementary to a target of interest. The stem consists of the annealing of two complementary arms located on either side of the probe section. One arm of the stem bears a fluorescent label, while a quenching moiety is attached to the other arm. In the default configuration (*i.e.*, in the absence of a target complementary to the probe), complementary base pairing keeps the fluorophore and the quencher in close proximity, within their Förster radius, ensuring quenching of the fluorescence by energy transfer. Upon specific interaction between the probe and its complementary target, the molecular beacon undergoes a conformational reorganisation in which the loop opens and the two strands of the stem separate, resulting in restoration of the fluorescence activity.

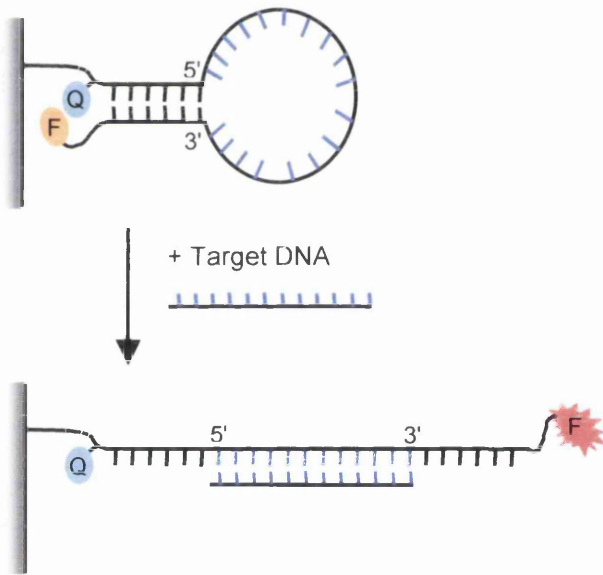


Figure 7-1. Mechanism of action of a surface-bound "molecular beacon" oligonucleotide capture probe. (a) Hairpin probe in a closed conformation, with the fluorescent label *F* being quenched by the quencher *Q*; (b) upon hybridisation with a complementary target, the molecular beacon opens up, and the fluorescence of *F* is restored.

Implementation

Molecular beacon technology has been used successfully in homogeneous^{92,177} and heterogeneous^{178,179} hybridisation assays. The expected benefits to microchannel chip-based hybridisation assays are similar to those discussed for inter-molecular FRET (between probes

and targets), including the possibility of performing real-time monitoring of hybridisation events. The main advantage of the molecular beacon approach over inter-molecular FRET is that the sample does not have to be labelled. Factors which limit the use of hairpin probes include the greater technical difficulty involved in their synthesis and optimisation as compared to linear ODN probes.⁹²

7. 2. 1. 3. Non-organic fluorescent labels

The use of most organic fluorophores as labels in optical bioassays is limited by their low resistance to photobleaching and their environmental sensitivity. Most synthetic organic dyes are large, planar structures that are intrinsically hydrophobic and have a tendency to aggregate in aqueous solutions. In addition, relatively broad emission spectra limit the use of multicolor labelling for multiplexing (small Stokes shifts limit the effectiveness of spectral discrimination for background rejection). Long-wavelength dyes have an increased tendency to stacking due to their increased size and hydrophobicity.

Recently, the possibility of using non-organic particles as fluorescent labels, in place of traditional organic molecules, has been demonstrated.¹⁷⁹⁻¹⁸¹ This novel class of materials consist of nanometer-sized semiconductor crystals. By using mixtures of group 13 and group 15 or group 12 and group 16 elements, a variety of compounds can be formed that have bandgaps ranging from the IR to the UV and can give strong light emission upon illumination, making them functionally similar to organic fluorophores. These materials do not suffer from many of the problems associated with organic dyes. They exhibit high quantum yields (up to 50%) and high resistance to photobleaching, as well as narrow emission spectra (typically 30 nm full width at half maximum) and broad excitation spectra, permitting multiplexed excitation over a single wavelength range and minimal overlap in multicolor assays.

Although the possibility of directly labelling nucleic acid targets with these nanocrystals is not certain as of this writing, non-organic fluorophores would be particularly appropriate as internal reference spots.

7. 2. 1. 4. Chemiluminescence detection

Principle of chemiluminescence and use as an optical detection method in bioanalysis

Chemiluminescence refers to the phenomenon of light emission associated with chemical reactions in which a significant fraction of intermediates or products are produced in excited electronic states; the decay, to the electronic ground state, of the chemically excited molecules is accompanied by the emission of photons, which is measured.^{182,183} Equation 7-5 gives a typical chemiluminescent reaction sequence:



where A is the chemiluminescent precursor, B is a species that influences the chemiluminescent reaction, I is an intermediate species, and P is the product of the reaction. I^* refers to the intermediate in an excited state.

Chemiluminescence is widely used as a detection method in bioanalysis due to its high versatility, sensitivity, and relative ease of implementation.¹⁸⁴ Unlike fluorescence methods, photoexcitation is not involved, which simplifies the instrumentation (no light source is required) and provides high levels of sensitivity, due to the absence of scattering and background photoluminescence signals.¹²⁷ In most cases, it is possible to arrange the conditions in which a chemiluminescent reaction takes place so that the chemiluminescent signal is directly related to the concentration of an analyte of interest. This analyte can be the chemiluminescent precursor (A in Equation 7-5), or most often an activator or inhibitor of the reaction (B in Equation 7-5).

Application to heterogeneous nucleic acid hybridisation assays

Chemiluminescence-based heterogeneous nucleic acid hybridisation assays have been reported which involve the labelling of the nucleic acid target with an enzyme that catalyses the first step of a reaction sequence through which a chemiluminescent precursor is converted into a chemiluminescent species.¹⁸⁵ The most commonly used enzymes are alkaline phosphatase (ALP) and horseradish peroxidase (HRP), whose activity is retained upon attaching to DNA (indirectly, through digoxigenin-antidigoxigenin or biotin-streptavidin coupling).

The chemiluminescence readout of an heterogeneous hybridisation assay is typically performed after the final stringent washing step,¹⁸⁶ although particular chemiluminescent substrates such as acridinium esters provide selectivity between single-stranded and double-stranded DNA, through an alteration of the time-course of the chemiluminescence emission, thereby alleviating the need for stringent washing before readout.¹⁸⁷⁻¹⁸⁹ An appropriate amount of chemiluminescent precursor is added to the medium, whereby this precursor is transformed into a chemiluminescent species by the enzyme attached to the target molecules. The intensity of the measured luminescence emission is indirectly related to the amount of target, through the catalytic turnover of the substrate and the lifetime of the light-producing compound. The performance and flexibility of this type of assay are benefited by the amplification effect afforded by the enzyme label.

Application to multiplexed heterogeneous nucleic acid hybridisation assays

The use of chemiluminescence in multiplexed array-based systems is limited by the difficulty of achieving adequate spatial resolution, due to the fact that the luminescent species is in solution (rather than linked to the substrate, as in fluorescence detection schemes) and thus prone to diffusion outside the spot area. This implies that the readout has to be performed within a time

frame over which spatial redistribution of the chemiluminescent species does not occur to a significant extent.⁴⁸

An assessment of the feasibility of using the enzyme label approach in hybridisation array assays has been reported recently, in low- and medium-density arrays (nylon membranes and glass slides).¹⁹⁰ Chemiluminescent precursor was added to the array and the emitted light detected with a CCD or X-ray film. In the experimental conditions used, spatial spreading of spots was not observed, due to the fast kinetics of the chemiluminescence emission (rapid fading of the chemiluminescence light) which allowed for the readout to be performed within a few minutes. However, the sensitivity of the assay was limited by the rapid exhaustion of the chemiluminescent precursor, since only molecules of the latter present in close proximity of the hybridised targets contributed to the chemiluminescence signal.

Potential advantages of chemiluminescence over fluorescence in flow-through microchannel chip-based hybridisation assays

Chemiluminescence detection appears to be a promising alternative to fluorescence detection in flow-through microchannel chip-based hybridisation assays. As photoexcitation of chemiluminescent labels is not required, optical effects that have been shown to limit the detection efficiency in fluorescence measurements, namely the high levels of background signals generated by MCG and the low levels of photoexcitation obtained in MCS, would be alleviated in chemiluminescence measurements. Considerations regarding the collection of emitted fluorescence radiations from microchannel substrates apply to chemiluminescence radiations as well.

In addition, microchannel substrates would provide confinement of the chemiluminescent species within individual chambers of reduced lateral dimensions; thus, it is expected that fresh chemiluminescent precursor can be actively delivered to the array by convective flowing without degradation of the spatial resolution. The flow rate could be adjusted so as to match the kinetics of chemiluminescence emission and to take full advantage of the signal amplification capability afforded by the enzyme label.

A possible limitation to the use of chemiluminescent reactions within enclosed volumes such as the hybridisation chamber of the flow cell concerns the release of gaseous compounds (N_2 , O_2 or CO_2) that accompanies most of the chemiluminescent reactions, as bubbles trapped within the cell would be detrimental to light collection through the optical window.

7. 2. 2. Optimisation of the morphology of microchannel substrates

The microchannel chips used in this thesis featured a regular, uniform array of near-cylindrical channels. This morphology was dictated by the fabrication processes: bundling of glass capillaries in the case of MCG, photolithographic patterning in the case of MPS. Although

systematic optimisation of the morphology of microchannel substrates was not carried out in this thesis, the importance of the chip thickness on the efficiency of optical detection (Chapter 3) and ODN probe immobilisation (Chapter 5) was clearly evidenced. The effect of the standards of smoothness of the microchannel sidewalls and of the interstitial area were also discussed. The feature size of the microchannels obviously directly impinges upon the wetting properties, bioassay kinetics, fluidics and optical detection efficiency, so that optimisation of the channel dimensions involves a trade-off to between these factors.

Other morphological characteristics that affect the overall performance of microchannel DNA chips are the shape of the microchannels (axial cross-section) as well as their lateral arrangement over the front surface of the chip. Possible optimisation of these two factors would consist in the tapering of the channels, as well as the suppression of non-active channels (*i.e.* channels on the sidewall of which no probe is immobilised), as discussed below.

The use of tapered microchannels, with a larger feature size on the front face, could enhance the efficiency of photoexcitation within MCS chips. However, the effect tapered microchannels would have on the flow-through ability of the structures is also to be considered. In Chapter 2, tapering of the microchannels was observed as an uncontrolled characteristic of the ASE process, but it is likely that this could be controlled. The production of tapered channels would also be feasible by photoelectrochemical etching, through appropriate modulation of the biasing parameters over the course of the etching process.

Non-active channels contribute to increasing the volume of the hybridisation cell, to increasing the surface area over which non-specific binding of targets can take place, and to reducing the effectiveness of target capture by allowing targets to flow through channels where no probes are present. Microchannels silicon chips could be fabricated that feature localised porous areas for reduction in the number of non-active microchannels, as shown schematically in Figure 7-2.

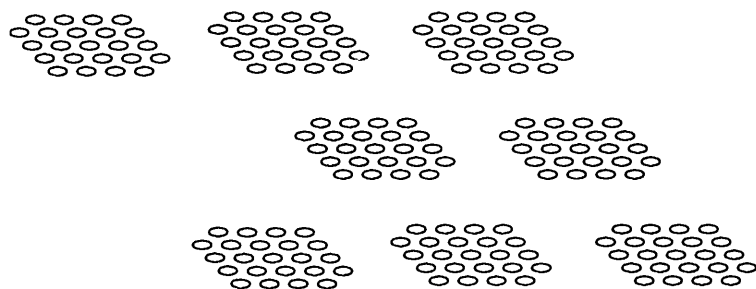


Figure 7-2. Proposed concept of microchannel silicon chips with patches of porous areas matching the capture probe arraying pattern. Microchannels are drawn in black while the footprints of probe spots are represented in yellow.

The patches of porous areas would have to approximately match the size of probe spots, so that the effective surface area over which probes are tethered is not diminished, while the total

non-active surface area is decreased. This type of chip can not readily be made by photoelectrochemical etching, which is limited in lateral design in that it requires a uniform pattern all over the chip surface, but it is achievable by deep dry etching. A constraint associated with the approach is the need to accurately deliver spots at locations corresponding to the porous areas.

7. 3. Further possible applications of the flow-through microchannel biochip platform

At the beginning of the “post-genome” area, increasingly significant academic and industrial research effort is now being directed towards the development of so-called *protein chips*, within the rapidly emerging field of proteomics.^{191,192} Although nucleic acids and proteins are very different in nature, some of the bioanalytical solutions that have been developed to provide high levels of throughput in DNA and RNA analysis are readily applicable to protein assays. This is expected to be the case with the flow-through microchannel biochip platform.

REFERENCES

1. Fodor, S. P. A.; Rava, R. P.; Huang, X. C.; Pease, A. C.; Holmes, C. P.; Adams, C. L. Multiplexed Biochemical assays with biological chips. *Nature* 1993, 364, 555-556.
2. Lemieux, B.; Aharoni, A.; Schena, M. Overview of DNA chip technology. *Mol. Breeding* 1998, 4, 277-289.
3. De Wildt, R. M. T.; Mundy, C. R.; Gorick, B. D.; Tomlinson, I. M. Antibody arrays for high-throughput screening of antibody-antigen interactions. *Nature Biotechnol.* 2000, 18, 989-994.
4. Ekins, R. P. Ligand Assays: From Electrophoresis To Miniaturized Microarrays. *Clin. Chem.* 1998, 44 (9) 2015-2030.
5. Granjeaud, S.; Bertucci, F.; Jordan, B. R. Expression profiling: DNA arrays in many guises. *BioEssays* 1999, 21, 781-790.
6. O'Donnell-Malonay, M. J.; Little, D. P. Microfabrication and Array Technology for DNA Sequencing and Diagnostics. *Gen. Anal.* 1996, 13, 151-157.
7. Beugelsdijk, T. J., ed. Automation Technologies for Genome Characterisation. John Wiley & Sons, Inc., New York, NY, 1997.
8. Fodor, S. P. A.; Read, J. L.; Pirrung, M. C.; Stryer, L.; Lu, A. T.; Solas, D. Light-directed, spatially addressable parallel chemical synthesis. *Science* 1991, 251, 767-773.
9. Maskos, U.; Southern, E. M. Oligonucleotide hybridisations on glass supports: a novel linker for oligonucleotide synthesis and hybridisation properties of oligonucleotides synthesised *in situ*. *Nucl. Ac. Res.* 1992, 20 (7) 1679-1684.
10. McGall, G.; Labadie, J.; Brock, P.; Wallraff, G.; Nguyen, T.; Hinsberg, W. Light directed synthesis of high-density oligonucleotide arrays using semiconductor photoresists. *Proc. Natl. Acad. Sci. USA* 1996, 93, 13555-13560.
11. Daniel, J. H.; Iqbal, S.; Millington, R. B.; Moore, D. F.; Lowe, C. R.; Leslie, D. L.; Lee, M. A.; Pearce, M. J. Silicon Microchambers for DNA Amplification. *Sens. and Actuators A* 1998, 71, 81-88.
12. Northrup, M. A.; Hadley, D.; Landre, P.; Lehew, S.; Richards, J.; Stratton, P. A Miniature DNA-Based Analytical Instrument Based On Micromachined Silicon Reaction Chambers. *Anal. Chem.* 1998, 70 (5) 918-922.
13. Ibrahim, M. S.; Lofts, R. S.; Henchal, E. A.; Jahrling, P.; Weedn, V. W. Northrup, M. A.; Belgrader, P. Real-Time Microchip PCR for Detecting Single-Base Differences in Viral and Human DNA. *Anal. Chem.* 1998, 70 (9) 2013-2017.

14. Zhang, N.; Tan, H.; Yeung, E. S. Automated and Integrated System for High-Throughput DNA Genotyping Directly from Blood. *Anal. Chem.* 1999, 71 (6) 1138-1145.
15. Shoffner, M. A.; Cheng, J.; Hvichia, G. E.; Kricka, L. J.; Wilding, P. Chip PCR. I. Surface passivation of microfabricated silicon-glass chips for PCR. *Nucl. Ac. Res.* 1996, 24 (2) 375-379.
16. Cheng, J.; Shoffner, M. A.; Hvichia, G. E.; Kricka, L. J.; Wilding, P. Chip PCR. II. Investigation of different PCR amplification systems in microfabricated silicon-glass chips. *Nucl. Ac. Res.* 1996, 24 (2) 380-385.
17. Hühmer, A. F. R.; Landers, J. P. Noncontact infrared-mediated thermocycling for effective polymerase chain reaction amplification of DNA in nanoliter volumes. *Anal. Chem.* 2000, 72, 5507-5512.
18. Swerdlow, H. S.; Jones, B. J.; Wittwer, C. T. Fully Automated DNA Reaction and Analysis in a Fluidic Capillary Instrument. *Anal. Chem.* 1997, 69 (5) 848-855.
19. Effenhauser, C. S.; Bruin, G. J. M.; Paulus, A.; Ehrat, M. Integrated capillary electrophoresis on flexible silicone microdevices: analysis of DNA restriction fragments and detection of single DNA molecules on microchips. *Anal. Chem.* 1997, 69, 3451-3457.
20. Jacobson, S. C.; Koutny, L. B.; Hergenröder, R.; Moore, A. W., Jr.; Ramsey, J. M. Microchip Capillary Electrophoresis with an Integrated Postcolumn Reactor. *Anal. Chem.* 1994, 66, 3472-3476.
21. Harrison, D. J.; Fluri, K.; Seiler, K.; Fan, Z.; Effenhauser, C. S.; Manz, A. Micromachining a Miniaturized Capillary Electrophoresis-Based Chemical Analysis System on a Chip. *Science* 1993, 261, 895-897.
22. Jacobson, S. C.; Ramsey, J. M. Integrated Microdevice for DNA restriction Fragment Analysis. *Anal. Chem.* 1996, 68, 720-723.
23. Verpoorte, E. M.; van der Shoot, B. H.; Jeanneret, S.; Manz, A.; Widmer, H. M.; de Rooij, N. F. Three-dimensional micro flow manifolds for miniaturized chemical analysis systems. *J. Micromech. Microeng.* 1994, 4, 246-256.
24. Shoji, S.; Esashi, M. Microflow devices and systems. *J. Micromech. Microeng.* 1994, 4, 157-171.
25. Seiler, K.; Fan, Z. H.; Fluri, K.; Harrison, D. J. Electroosmotic Pumping and Valveless Control of Fluid Flow within a Manifold of Capillaries on a Glass Chip. *Anal. Chem.* 1994, 66, 3485-3491.
26. Kunz, R. E. Miniature integrated optical modules for chemical and biochemical sensing. *Sens. And Actuators B* 1997, 38, 13-28.
27. Vo-Dinh, T.; Alarie, J. P.; Isola, N.; Landis, D.; Wintenberg, A. L.; Ericson, M. N. DNA Biochip Using a Phototransistor Integrated Circuit. *Anal. Chem.* 1999, 71, 358-363.

28. Budach, W.; Abel, A. P.; Bruno, A. E.; Neuschafer, D. Planar Waveguides as High-Performance Sensing Platforms for Fluorescence-Based Multiplexed Oligonucleotide Hybridization Assays. *Anal. Chem.* 1999, 71, 3347-3355.
29. Abel, A. P.; Weller, M. G.; Duveneck, G. L.; Ehrat, M.; Widmer, H. M. Fiber-Optic Evanescent Wave Biosensor for the Detection of Oligonucleotides. *Anal. Chem.* 1996, 68, 2905-2912.
30. Figeys, D.; Pinto, D. Lab-on-a-chip: a revolution in biological and medical sciences. *Anal. Chem.* 2000, 330A-335A.
31. Ruano, J. M.; Benoit, V.; Aitchison, J. S.; Cooper, J. M. Flame hydrolysis deposition of glass on silicon for the integration of optical and microfluidic devices. *Anal. Chem.* 2000, 72 (5) 1093-1097.
32. De Benedetti, V. M. G.; Biglia, N.; Sismondi, P.; De Bortoli, M. DNA chips: the future of biomarkers. *Int. J. Biol. Markers* 2000, 15, 1-9.
33. Nygaard, A. P.; Hall, B. D. A method for the detection of RNA-DNA complexes. *Biochem. Biophys. Res. Commun.* 1963, 12, 98-104.
34. Katafos, F. C.; Jones, C. W. Efstratladis, A. Determination of nucleic acid sequence homologies and relative concentrations by a dot hybridisation procedure. *Nucl. Ac. Res.* 1979, 24, 1541-1552.
35. Gillespie, D.; Spiegelman, S. A. A quantitative assay for DNA-RNA hybrids with DNA immobilised on a membrane. *J. Mol. Biol.* 1965, 12, 829-842.
36. Meinkoth, J.; Wahl, G. Hybridization of Nucleic Acids on Solid Supports. *Anal. Biochem.* 1984, 138, 267-284.
37. Guo, Z.; Guilfoyle, R. A.; Thiel, A. J.; Wang, R.; Smith, L. M. Direct fluorescence analysis of polymorphism by hybridization with oligonucleotide arrays on glass supports *Nucl. Ac. Res.* 1994, 22 (24) 5456-5465.
38. Sambrook, J.; Fritsch, E. F.; Maniatis, T. Molecular cloning: a laboratory manual. 2nd Edition. CSH Laboratory Press, Cold Spring Harbor, NY, 1989.
39. Paddock, S. W. Confocal laser scanning microscopy. *BioTechniques* 1999, 27 (5) 992-1004.
40. Lander, E. A note on nomenclature. Chipping forecast supplement, *Nature Genetics* 1999, 21, 1s.
41. Hoheisel, J. D. Oligomer-Chip Technology. *Tibtech* 1997, 15, 465-469.
42. Anderson, R. C.; McGall, G.; Lipshutz, R. J. Polynucleotide Arrays for Genetic Sequence Analysis. In Manz, A. & Becker, H., eds. *Microsystem Technology in Chemistry and Life Sciences*. Springer-Verlag, Berlin, 1998.

43. Lipshutz, R. J.; Fodor, S. P. A.; Gingeras, T. R.; Lockhart, D. J. High density synthetic oligonucleotide arrays. *Nature Genet.* 1999, 21, 20-24.
44. Matteucci, M. D.; Caruthers, M. H. Synthesis of deoxyoligonucleotides on a polymer support. *J. Am. Chem. Soc.* 1981, 103, 3185-3191.
45. Schena, M.; Shalon, D.; Heller, R.; Chai, A.; Brown, P. O.; Davis, R. W. Parallel Human Genome Analysis: Microarray-Based Expression Monitoring of 1000 Genes. *Proc. Natl. Acad. Sci. USA* 1996, 93, 10614-10619.
46. Southern, E. M.; Case-Green, S. C.; Elder, J. K.; Johnson, M.; Mir, K. U.; Wang, L.; Williams, J. C. Arrays of complementary oligonucleotides for analyzing the hybridization behavior of nucleic acids. *Nucl. Ac. Res.* 1994, 22, 1368-1373.
47. Duggan, D. J.; Bittner, M.; Chen, Y.; Meltzer, P.; Trent, J. Expression profiling using cDNA microarrays. *Nature Genet.* 1999, 21, 10-14.
48. Guiliano, D.; Ganatra, M.; Ware, J.; Parrot, J.; Daub, J.; Moran, L.; Brennecke, H.; Foster, J. M.; Supali, T.; Blaxter, M.; Scott, A. L.; Williams, S. A.; Slatko, B. E. Chemiluminescent detection of sequential DNA hybridizations to high-density, filter-arrayed cDNA libraries: a subtraction method for novel gene discovery. *BioTechniques* 1999, 27 (1) 146-152.
49. Southern, E.; Mir, K.; Shchepinov, M. Molecular interactions on microarrays. *Nature Genet.* 1999, 21, 5-9.
50. Parkhurst, K. M.; Parkhurst, L. J. Kinetic Studies by Fluorescence Energy Transfer employing a double-labeled Oligonucleotide: Hybridization to the Oligonucleotide Complement and to Single-Stranded DNA. *Biochemistry* 1995, 34, 285-292.
51. Okahata, Y.; Kawase, M.; Niikura, K.; Ohtake, F.; Furusawa, H.; Ebara, Y. Kinetic measurements of DNA hybridisation on an oligonucleotide-immobilised 27-MHz quartz crystal microbalance. *Anal. Chem.* 1998, 70, 1288-1296.
52. Chan, V.; Graves, D. J.; McKenzie, S. E. The biophysics of DNA hybridisation with immobilised oligonucleotide probes. *Biophys. J.* 1995, 69 (6) 2243-2255.
53. Chan, V.; Graves, D. J.; Fortina, P.; McKenzie, S. E. Adsorption and surface diffusion of DNA oligonucleotides at liquid/solid interfaces. *Langmuir* 1997, 13 (2) 320-329.
54. Chan, V.; McKenzie, S. E.; Surrey, S.; Fortina, P.; Graves, D. J. Effect of hydrophobicity and electrostatics on adsorption and surface diffusion of DNA oligonucleotides at liquid/solid interfaces. *J. Colloid Interface Sci.* 1998, 203 (1) 197-207.
55. Lane, M. J.; Benight, A. S.; Faldasz, B. D. Nucleic acid capture moieties. *US Patent* 5,770,365; June 23, 1998.
56. Ma, W. L.; Zheng, W. L.; Cui, D.; Song, Y. B.; Wu, Q. H. DNA microarray chips made on surface of ceramic slides. *Acta Bioch. Biophys. Sinica* 2000, 32 (3) 285-289.

57. Cloarec, J. P.; Martin, J. R.; Polychronakos, C.; Lawrence, I.; Lawrence, M. F.; Souteyrand, E. Functionalization of Si/SiO₂ substrates with homooligonucleotides for a DNA biosensor. *Sens. and Actuators B* 1999, 58, 394-398.
58. O'Donnell, M. J.; Tang, K.; Koster, H.; Smith, C. L.; Cantor, C. R. High-density, covalent attachment of DNA to silicon wafers for analysis by MALDI-TOF mass spectrometry. *Anal. Chem.* 1997, 69, 2438-2443.
59. Burger, R. M. & Donovan, R. P., eds. *Fundamentals of Silicon Integrated Device Technology*, Vol. 1. Prentice-Hall, New Jersey, 1967.
60. Soper, S. A.; Ford, S. M.; Qi, S.; McCarley, R. L.; Kelly, K.; Murphy, M. C. Polymeric microelectromechanical systems. *Anal. Chem.* 2000, 72 (19) 643A-651A.
61. McCormick, R. M.; Nelson, R. J.; Alonso-Amigo, M. G.; Benvegnu, D. J.; Hooper, H. H. Microchannel electrophoretic separations of DNA in injection-molded plastic substrates. *Anal. Chem.* 1997, 69, 2626-2630.
62. Hanemann, T.; Piottter, V.; Ruprecht, R. Fabrication of polymeric microcomponents using liga- and related techniques. *Abstr. Pap. Am. Chem. Soc.* 1999, 218 (2) U611.
63. Matson, R. S.; Rampal, J. B.; Coassin, P. J. Biopolymer synthesis on polypropylene supports. I. Oligonucleotides. *Anal. Biochem.* 1994, 217, 306-310.
64. Beier, M.; Hoheisel, J. Versatile derivatisation of solid support media for covalent bonding on DNA-microchips. *Nucl. Ac. Res.* 1999, 27 (9) 1970-1977.
65. Henry, A. C.; Tutt, T. J.; Galloway, M.; Davidson, Y. Y.; McWhorter, S.; Soper, S. A.; McCarley, R. L. Surface modification of poly(methyl methacrylate) used in the fabrication of microanalytical devices. *Anal. Chem.* 2000, 72, 5331-5337.
66. Nikiforov, T. T.; Rendle, R. B.; Goelet, P.; Rogers, Y. H.; Kotewicz, M. L.; Anderson, S.; Trainor, G. L.; Knapp, M. R. Genetic Bit Analysis: a solid phase method for typing single nucleotide polymorphisms. *Nucl. Ac. Res.* 1994, 22 (20) 4167-4175.
67. Proudnikov, D.; Timofeev, E.; Mirzabekov, A. Immobilization of DNA in polyacrylamide gel for the manufacture of DNA and DNA-oligonucleotide microchips. *Anal. Biochem.* 1998, 259, 34-41.
68. Vasiliskov, A. V.; Timofeev, E. N.; Surzhikov, S. A.; Drobyshev, A. L.; Schick, V. V.; Mirzabekov, A. D. Fabrication of microarray of gel-immobilized compounds on a chip by copolymerisation. *BioTechniques* 1999, 27 (3) 592-606.
69. Heller, M. J.; Forster, A. H.; Tu, E. Active microelectronic chip devices which utilize controlled electrophoretic fields for multiplex DNA hybridization and other genomic applications. *Electrophoresis* 2000, 21, 157-164.

70. Pease, A. C.; Solas, D.; Sullivan, E. J.; Cronin, M. T.; Holmes, C. P.; Fodor, S. P. A. Light-generated oligonucleotide arrays for rapid DNA sequence analysis. *Proc. Natl. Acad. Sci. USA* 1994, 91, 5022-5026.
71. Graves, D. J.; Su, H. J.; McKenzie, S. E.; Surrey, S.; Fortina, P. System for preparing microhybridization arrays on glass slides. *Anal. Chem.* 1998, 70, 5085-5092.
72. Yoon, S. H.; Choi, J. G.; Lee, S. Y. Development of DNA chip microarrayer. *J. Microbiol. Biotechnol.* 2000, 10 (1) 21-26.
73. Ducrée, J.; Gruhler, H.; Hey, N.; Müller, M.; Békési, S.; Freygang, M.; Sandmaier, H.; Zengerle, R. Topspot - A new method for the fabrication of microarrays. Thirteen Annual International Conference on Micro Electro Mechanical Systems, Miyazaki, Japan, January 23-27, 2000.
74. Livache, T.; Bazin, H.; Caillat, P.; Roget, A. Electroconducting polymers for the construction of DNA or peptide arrays on silicon chips. *Biosens. Bioelec.* 1998, 13, 629-634.
75. Caillat, P.; David, D.; Belleville, M.; Clerc, F.; Massit, C.; Revol-Cavalier, F.; Peltié, P.; Livache, T.; Bidan, G.; Roget, A.; Crapez, E. Biochips on CMOS: an active matrix address array for DNA analysis. *Sens. and Actuators B* 1999, 61, 154-162.
76. Edman, C. F.; Raymond, D. E.; Wu, D. J.; Tu, E.; Sosnowski, R. G.; Butler, W. F.; Nerenberg, M.; Heller, M. J. Electric field directed nucleic acid hybridization on microchips. *Nucl. Ac. Res.* 1997, 25 (24) 4907-4914.
77. Sosnowski, R. G.; Tu, E.; Butler, W. F.; O'Connell, J. P.; Heller, M. J. Rapid determination of single base mismatch mutations in DNA hybrids by direct electric field control. *Proc. Natl. Acad. Sci. USA* 1997, 94, 1119-1123.
78. Wang, J. From DNA biosensors to gene chips. *Nucl. Ac. Res.* 2000, 28 (16) 3011-3016.
79. Lamture, J. B.; Beattie, K. L.; Burke, B. E.; Eggers, M. D.; Ehrlich, D. J.; Fowler, R.; Hollis, M. A.; Kosicki, B. B.; Reich, R. K.; Smith, S. R.; Varma, R. S.; Hogan, M. E. Direct detection of nucleic acid hybridization on the surface of a charge coupled device. *Nucl. Ac. Res.* 1994, 22 (11) 2121-2125.
80. Piunno, P. A. E.; Krull, U. J.; Hudson, R. H. E.; Damha, M. J.; Cohen, H. Fiber-Optic DNA sensor for fluorometric nucleic acid determination. *Anal. Chem.* 1995, 67, 2635-2643.
81. Steemers, F. J.; Ferguson, J. A.; Walt, D. R. Screening unlabeled DNA targets with randomly ordered fiber-optic gene arrays. *Nature Biotechnol.* 2000, 18 (1) 91-94.
82. Ferguson, J. A.; Steemers, F. J.; Walt, D. R. High-density fiber-optic DNA random microsphere array. *Anal. Chem.* 2000, 72, 5618-5624.
83. Steel, A. B.; Herne, T. M.; Tarlov, M. J. Electrochemical quantitation of DNA immobilised on gold. *Anal. Chem.* 1998, 70, 4670-4677.

84. Kelley, S. O.; Boon, E. M.; Barton, J. K.; Jackson, N. M.; Hill, M. G. Single-base mismatch detection based on charge transduction through DNA. *Nucl. Ac. Res.* 1999, 27 (24) 4830-4837.
85. Bardea, A.; Patolsky, F.; Dagan, A.; Willner, I. Sensing and amplification of oligonucleotide-DNA interactions by means of impedance spectroscopy: a route to a Tay-Sachs sensor. *Chem. Commun.* 1999, 21-22.
86. Saoudi, B.; Despas, C.; Chehimi, M. M.; Jammul, N.; Delamar, M.; Bessière, J.; Walcarius, A. Study of DNA adsorption on polypyrrole: interest of dielectric monitoring. *Sens. and Actuators B* 2000, 62, 35-42.
87. Stomakhin, A. A.; Vasiliskov, V. A.; Timofeev, E.; Schulga, D.; Cotter, R. J.; Mirzabekov, A. D. DNA sequence analysis by hybridisation with oligonucleotide microchips: MALDI mass spectrometry identification of 5mers contiguously stacked to microchip oligonucleotides. *Nucl. Ac. Res.* 2000, 28 (5) 1193-1198.
88. Drmanac, S.; Kita, D.; Labat, I.; Hauser, B.; Schmidt, C.; Burczak, J. D.; Drmanac, R. Accurate sequencing by hybridization for DNA diagnostics and individual genomics. *Nature Biotechnol.* 1998, 16, 54-58.
89. Parinov, S.; Barsky, V.; Yershov, G.; Kirillov, E.; Timofeev, E.; Belgovskiy, A.; Mirzabekov, A. DNA sequencing by hybridization to microchip octa- and decanucleotides extended by stacked pentanucleotides. *Nucl. Ac. Res.* 1996, 24 (15) 2998-3004.
90. Zhang, Y.; Coyne, M. Y.; Will, S. G.; Levenson, C. H.; Kawasaki, E. S. Single-base mutational analysis of cancer and genetic diseases using membrane bound modified oligonucleotides. *Nucl. Ac. Res.* 1991, 19 (14) 3929-3933.
91. Nikiforov, T. T.; Rendle, R. B.; Goelet, P.; Rogers, Y. H.; Kotewicz, M. L.; Anderson, S.; Trainor, G. L.; Knapp, M. R. Genetic Bit Analysis: a solid phase method for typing single nucleotide polymorphisms. *Nucl. Ac. Res.* 1994, 22 (20) 4167-4175.
92. Bernard, P. S.; Wittwer, C. T. Homogeneous Amplification and Variant Detection by Fluorescent Hybridization Probes. *Clin. Chem.* 2000, 46 (2) 147-148.
93. Lashkari, D. A.; DeRisi, J. L.; McCusker, J. H.; Namath, A. F.; Gentile, C.; Hwang, S. Y.; Brown, P. O.; Davis, R. W. Yeast microarrays for genome wide parallel genetic and gene expression analysis. *Proc. Natl. Acad. Sci. USA* 1997, 94, 13057-13062.
94. Stratowa, C.; Wilgenbus, K. K. Gene expression profiling in drug discovery and development. *Current Opinion Mol. Therap.* 1999, 1 (6) 671-679.
95. Bowtell, D. D. L. Options Available – from Start to Finish – for Obtaining Expression Data by Microarray. *Nature Genet.* 1999, 21, 25-32.
96. Gunderson, K. L.; Huang, X. C.; Morris, M. S.; Lipschutz, R. J.; Lockhart, D. J.; Chee, M. S. Mutation detection by ligation to complete n-mer DNA arrays. *Genome Res.* 1998, 8, 1142-1153.

97. Newman, J.S. *Electrochemical Systems*. Prentice Hall, New Jersey, 1991.
98. Beattie, K. L. Microfabricated flow through porous apparatus for discrete detection of binding reactions. *US Patent # 5,843,767* (1996).
99. Tuwiner, S. B. *Diffusion and Membrane Technology*. Chapman and Hall, London, 1962.
100. Howell, J. A.; Sanchez, V.; Field, R. W., eds. *Membranes in Bioprocessing: Theory and Applications*. Chapman and Hall, London, 1993.
101. Falipou, S.; Chovelon, J. M.; Martelet, C.; Margonari, J.; Cathignol, D. Obtention and characterization of bioengineered layers onto silica-based microstructures. *Sens. and Actuators A* 1999, 74, 81-85.
102. Tonucci, R. J.; Justus, B. L.; Campillo, A. J.; Ford, C. E. Nanochannel array glass. *Science* 1992, 258, 783-785.
103. Turner, D. R. *J. Electrochem. Soc.* 1958, 105, 402.
104. Beale, M. I. J.; Chew, N. G.; Uren, M. J.; Cullis, A. G.; Benjamin, J. D. Microstructure and formation mechanism of porous silicon. *Appl. Phys. Lett.* 1985, 46 (1) 86-88.
105. Lehmann, V. and Föll, H. Formation Mechanism and Properties of Electrochemically Etched Trenches in n-Type Silicon. *J. Electrochem. Soc.* 1990, 137 (2) 653-659.
106. Lehmann, V. The Physics of Macropore formation in Low Doped n-Type Silicon. *J. Electrochem. Soc.* 1993, 140 (10) 2836-2843.
107. Lehmann, V. and Grüning, U. The Limits of Macropore Array Fabrication. *Thin Solid Films* 1997, 297, 13-17.
108. Lärmer, F.; Schilp, P. Method of anisotropically etching silicon. *German patent DE 4,241,045* (1994).
109. Ferguson, G. S.; Chaudhury, M. K.; Biebuyck, H. A.; Whitesides, G. M. Monolayers on disordered substrates: self-assembly of alkyltrichlorosilanes on surface-modified polyethylene and poly(dimethylsiloxane). *Macromolecules* 1993, 26, 5870-5875.
110. Stimpson, D. I.; Hoijer, J. V.; Hsieh, W.; Jou, C.; Gordon, J.; Theriault, T.; Gamble, R.; Baldeschwieler, J. D. Real-time detection of DNA hybridization and melting on oligonucleotide arrays by using optical wave guides. *Proc. Natl. Acad. Sci. USA* 1995, 92, 6379-6383.
111. Cheung, V.; Morley, M.; Aguilar, F.; Massimi, A.; Kucherlapti, R.; Childs, G. Making and Reading Microarrays. *Nature Genet.* 1999, 21, 15-19.
112. Church, G. M.; Gilbert, W. Genomic sequencing. *Proc. Natl. Acad. Sci. USA* 1984, 81, 1991-1995.

113. Steel, A. B.; Levicky, R. L.; Herne, T. M.; Tarlov, M. J. Immobilization of nucleic acids at solid surfaces: effect of oligonucleotide length on layer assembly. *Biophys. J.* 2000, 79 (2) 975-981.
114. Demers, L. M.; Mirkin, C. A.; Mucic, R. C.; Reynolds, R. A., III; Letsinger, R. L.; Elghanian, R.; Viswanadham, G. A fluorescence-based method for determining the surface coverage and hybridization efficiency of thiol-capped oligonucleotides bound to gold thin films and nanoparticles. *Anal. Chem.* 2000, 72, 5535-5541.
115. Fan, Z. H.; Mangru, S.; Granzow, R.; Heaney, P.; Ho, W.; Dong, Q.; Kumar, R. Dynamic DNA hybridization on a chip using paramagnetic beads. *Anal. Chem.* 1999, 71, 4851-4859
116. Smith, L. M.; Fung, S.; Hunkapiller, M. W.; Hunkapiller, T. J.; Hood, L. E. The synthesis of oligonucleotides containing an aliphatic amino group at the 5' terminus. *Nucl. Ac. Res.* 1994, 22 (4) 412-416.
117. Dasgupta, P. K.; Liu, S. Electroosmosis: a reliable fluid propulsion system for flow injection analysis. *Anal. Chem.* 1994, 66, 1792-1798.
118. Wang, X. B.; Huang, Y.; Burt, J. P. H.; Markx, G. H.; Pethig, R. Selective dielectrophoretic confinement of bioparticles in potential energy wells. *J. Phys. D: Appl. Phys.* 1993, 26, 1278-1285.
119. Asbury, C. L.; van den Engh, G. Trapping of DNA in nonuniform oscillating electric fields. *Biophys. J.* 1998, 74, 1024-1030.
120. Green, N. G.; Ramos, A.; Morgan, H. AC electrokinetics: a survey of sub-micrometre particle dynamics. *J. Phys. D: Appl. Phys.* 2000, 33, 632-641.
121. Benoit, V.; Steel, A.; Torres, M.; Yu, Y.-Y.; Yang, H.; Cooper, J. Evaluation of Three-Dimensional Microchannel Glass Biochips for Multiplexed Nucleic Acid Fluorescence Hybridization Assays. Accepted for publication in *Analytical Chemistry*.
122. Wu, S.-X., Personal Communication, University of Glasgow, UK; October 2000.
123. Xia, Y.; McClelland, J. J.; Gupta, R.; Qin, D.; Zhao, X.-M.; Sohn, L. L.; Celotta, R. J.; Whitesides, G. M. Replica molding using polymeric materials: a practical step toward nanomanufacturing. *Adv. Mater.* 1997, 9 (2) 147-149.
124. Duffy, D. C.; McDonald, J. C.; Schueller, O. J. A.; Whitesides, G. M. Rapid prototyping of microfluidic systems in poly(dimethylsiloxane). *Anal. Chem.* 1998, 70, 4974-4984.
125. Hosokawa, K.; Fujii, T.; Endo, I. Handling of picoliter liquid samples in a poly(dimethylsiloxane)-based microfluidic device. *Anal. Chem.* 1999, 71, 4781-4785.
126. Pope, A. J.; Haupts, U. M.; Moore, K. J. Homogeneous fluorescence readouts for miniaturized high-throughput screening: theory and practice. *Drug Discovery Today* 1999, 4, 350-362.
127. Ingle, J. D., Jr.; Crouch, S. R. Spectrochemical analysis. Prentice Hall, New Jersey, 1988.

128. Cullander, C. Imaging in the far-red with electronic light microscopy: requirements and limitations. *J. Microscopy* 1994, 176 (3) 281-286.
129. Silzel, J. W.; Cercek, B.; Dodson, C.; Tsay, T.; Obremski, R. J. Mass-sensing, multianalyte microarray immunoassay with imaging detection. *Clin. Chem.* 1998, 44 (9) 2036-2043.
130. Lieberwirth, U.; Arden-Jacob, J.; Drexhage, K. H.; Herten, D. P.; Müller, R.; Neumann, M.; Schultz, A.; Siebert, S.; Sagner, G.; Klingel, S.; Sauer, M.; Wolfrum, J. Multiplex dye DNA sequencing in capillary gel electrophoresis by diode laser-based time-resolved fluorescence detection. *Anal. Chem.* 1998, 70 (22) 4771-4779.
131. Baars, M. J.; Patonay, G. Ultrasensitive detection of closely related angiotensin I peptides using capillary electrophoresis with near-infrared laser-induced fluorescence detection. *Anal. Chem.* 1999, 71, 667-671.
132. Pilevar, S.; Davis, C. C.; Portugal, F. Tapered optical fiber sensor using near-infrared fluorophores to assay hybridization. *Anal. Chem.* 1998, 70, 2031-2037.
133. Jiang, G.; Attiya, S.; Ocvirk, G.; Lee, W. E.; Harrison, D. J. Red diode laser induced fluorescence detection with a confocal microscope on a microchip for capillary electrophoresis. *Biosens. Bioelec.* 2000, 14, 861-869.
134. Dai, Y.; Whittall, R. M.; Li, L. Confocal fluorescence microscopic imaging for investigating the analyte distribution in MALDI matrices. *Anal. Chem.* 1996, 68 (15) 2494-2500.
135. Agard, D. A. Optical sectioning microscopy: cellular architecture in three dimensions. *Ann. Rev. Biophys. Bioeng.* 1984, 13, 191-219.
136. Hiraoka, Y.; Sedat, J. W.; Agard, D. A. The use of a charge-coupled device for quantitative optical microscopy of biological structures. *Science* 1987, 238, 26-31.
137. Hooper, C. E.; Ansorge, R. E. Quantitative luminescence imaging in the biosciences using the CCD camera: analysis of macro and micro samples. *Trends Anal. Chem.* 1990, 9 (8) 269-277.
138. Boldt-Houle, D.; Yan, S.; Olesen, C.; D'Eon, B.; Lee, J.; Liu, B.; Bodziuch, U.; Chiulli, A.; Atwood, J.; Gambini, M.; Voyta, J.; Bronstein, I. A CCD-based integrated platform for accelerated high-throughput screening. *Am. Laboratory* 2000, 32 (3) 60-70.
139. <http://www.hamamatsu.com>.
140. Winston, R. Light collection within the framework of geometrical optics. *J. Opt. Soc. Am.* 1970, 60, 245-247.
141. Benoit, V.; Yappert, M. C. Sensitivity Enhancement in Capillary/Fiber Optical Sensors. *Anal. Chem.* 1996, 68, 183-188.
142. Benoit, V.; Yappert, M. C. Characterization of a Simple Raman Capillary/Fiber Optical Sensor. *Anal. Chem.* 1996, 68, 2255-2258.

143. Welford, W. T.; Winston, R. High collection nonimaging optics. Academic Press, London, 1989; pp 9-13.
144. Pringsheim, P. Fluorescence and phosphorence. Interscience Publishers Inc., New York, 1949; pp 505-507.
145. Palik, E. D., ed. Handbook of Optical Constants of Solids. Academic Press, Orlando, 1998.
146. Piller, H. Microscope photometry. Springer-Verlag, Berlin, 1977.
147. Van Der Voort, P.; Vansant, E. F. Silylation of the silica surface: a review. *J. Liq. Chrom. & Rel. Technol.* 1996, 19(17&18), 273-2752.
148. Cras, J. J.; Rowe-Taitt, C. A.; Nivens, D. A.; Ligler, F. S. Comparison of chemical cleaning methods of glass in preparation for silanization. *Biosens. Bioelec.* 1999, 14, 683-688.
149. Smith, L. M.; Fung, S.; Hunkapiller, M. W.; Hunkapiller, T. J.; Hood, L. E. The synthesis of oligonucleotides containing an aliphatic amino group at the 5' terminus. *Nucl. Ac. Res.* 1994, 22 (4) 412-416.
150. Beattie, W. G.; Meng, L.; Turner, S. L.; Varma, R. S.; Dao, D. D.; Beattie, K. L. Hybridization of DNA targets to glass-tethered oligonucleotide probes. *Mol. Biotechnol.* 1995, 4, 213-225.
151. Bloomfield, V. A.; Crothers, D. M.; Tinoco, I. Physical chemistry of nucleic acids. Harper and Row, New York, 1974.
152. Sambrook, J.; Fritsch, E. F.; Maniatis, T. Molecular cloning: a laboratory manual, 2nd edition. CSH Laboratory Press, Cold Spring Harbor, NY, 1989; pages 9.48-9.49.
153. Eigler, F. S. *et al.* Immobilization of active agents on substrates with a silane and heterobifunctional crosslinking agent. U.S. Patent 5, 077, 210, December 1991.
154. Grovenor, C. R. M. Microelectronic materials. IOP, Bristol, 1989. pp 292-301.
155. Grove, A. S. Physics and technology of semiconductor devices. Wiley, New York, 1967. Chapter 2, pp 22-34.
156. Roberts, G. G.; Morant, M. J. Insulating films on semiconductors. IOP, Bristol, 1979. pp 12-27.
157. Morra, M.; Ochiello, E.; Marola, R.; Garbassi, F.; Humphrey, P.; Johnson, D. On the aging of oxygen plasma-treated polydimethylsiloxane surfaces. *J. Colloid Interface Sci.* 1990, 137 (1) 11-24.
158. Chaudhury, M. K.; Whitesides, G. M. Correlation between surface free energy and surface constitution. *Science* 1991, 255, 1230-1232.
159. Silver, J. H.; Lin, J. C.; Lim, F.; Tegoulia, V. A.; Chaudhury, M. K.; Cooper, S. L. Surface properties and hemocompatibility of alkyl-siloxane monolayers supported on silicon

- rubber: effect of alkyl chain length and ionic functionality. *Biomaterials* 1999, 20, 1533-1543.
160. Halliwell, C. M. Personal communication; Imperial College of Science, Technology and Medicine, London, UK; March 1999.
161. Steel, A. B.; Torres, M. P. Internal report; Gene Logic, Inc., Gaithersburg, MD, USA; September 1999.
162. Jacobson, S. C.; Ermakov, S. V.; Ramsey, J. M. Minimizing the number of voltage sources and fluid reservoirs for electrokinetic valving in microfluidic devices. *Anal. Chem.* 1999, 71, 3273-3276.
163. Jacobson, S. C.; McKnight, T. E.; Ramsey, J. M. Microfluidic devices for electrokinetically driven parallel and serial mixing. *Anal. Chem.* 1999, 71, 4455-4459.
164. Paul, P. H.; Garguilo, M. G.; Rakestraw, D. J. Imaging of pressure- and electrokinetically driven flows through open capillaries. *Anal. Chem.* 1998, 70, 2459-2467.
165. Grossman, P. D.; Colburn, J. C., eds. *Capillary Electrophoresis Theory and Practice*; Academic Press, New York, 1992, p. 127.
166. Lambrechts, M.; Sansen, W. *Biosensors: microelectrochemical devices*. IOP Publishing, London, 1992.
167. Macka, M.; Andersson, P.; Haddad, P. R. Changes in electrolyte pH due to electrolysis during capillary zone electrophoresis. *Anal. Chem.* 1998, 70, 743-749.
168. Fiedler, S.; Shirley, S. G.; Schnelle, T. Dielectrophoretic field cages made from Indium Tin Oxide. *Sensors and Materials* 1997, 9 (3) 141-148.
169. Horányi, G. A novel approach to platinized platinum electrode. *J. Electroanal. Chem.* 1996, 417, 185-188.
170. Lambrechts, M.; Sansen, W. *Biosensors: microelectrochemical devices*. IOP Publishing, London, 1992, p. 184.
171. Heuschkel, M. O.; Guérin, L.; Buisson, B.; Bertrand, D.; Renaud, P. Buried microchannels in polymer for delivering of solutions to neurons in a network. *Sens. and Actuators B* 1998, 48 (1-3) 356-361.
172. Griffith, A. *Applications of Microfabrication in Biotechnology*. PhD Thesis, University of Glasgow, 1996.
173. Chen, N.; Chrambach, A. Enhanced field strength and resolution in gel electrophoresis upon substitution of buffer by histidine at its isoelectric point. *Electrophoresis* 1996, 17, 699-703.
174. Bossi, A.; Olivieri, E.; Castelletti, L.; Gelfi, C.; Hamdan, M.; Righetti, P. G. General experimental aspects of the use of isoelectric buffers in capillary electrophoresis. *J. Chromatography A* 1999, 853, 71-82.

175. Egholm, M.; Buchardt, O.; Christensen, L.; Behrens, C.; Freier, S. M.; Driver, D. A.; Berg, R. H.; Kim, S. K.; Norden, B.; Nielsen, P. E. PNA hybridises to complementary oligonucleotides obeying the Watson-Crick hydrogen-bonding rules. *Nature* 1993, 365, 566-568.
176. Tyagi, S.; Bratu, D. P.; Kramer, F. R. Multicolor molecular beacons for allele discrimination. *Nature Biotechnol.* 1998, 16, 49-53.
177. Liu, X.; Tan, W. A Fiber-Optic Evanescent Wave DNA Biosensor Based on Novel Molecular Beacons. *Anal. Chem.* 1999, 71, 5054-5059.
178. Brown, L. J.; Cummins, J.; Hamilton, A.; Brown, T. Molecular beacons attached to glass beads fluoresce upon hybridisation to target DNA. *Chem. Commun.* 2000, 621-622.
179. Empedocles, S.; Wong, E.; Adams, E.; Bruchez, M.; Phillips, V.; Trent, J.; Bittner, M. Nanocrystals: A new material for high-sensitivity, multicolor bioassays. *Abstr. Pap. Am. Chem. Soc.* 2000, 219 (1) IEC-212.
180. Bruchez, M.; Moronne, M.; Gin, P.; Weiss, S.; Alivisatos, A. P. Semiconductor nanocrystals as fluorescent biological labels. *Science* 1998, 281, 2013-2016.
181. Chan, W. C. W.; Nie, S. Quantum dot bioconjugates for ultrasensitive nonisotopic detection. *Science* 1998, 281, 2016-2020.
182. Campbell, A.K., Kricka, L.J., and Stanley, P.E., eds. *Bioluminescence and Chemiluminescence: Fundamentals and Applied Aspects*. Wiley, 1994.
183. Hastings, J.W., Kricka, L.J., and Stanley, P.E., eds. *Bioluminescence and Chemiluminescence: Molecular Reporting with Photons*. Wiley, 1997.
184. Roda, A.; Pasini, P.; Guardigli, M.; Baraldini, M.; Musiani, M.; Mirasoli, M. Bio- and chemiluminescence in bioanalysis. *Fres. J. Anal. Chem.* 2000, 366, 6-7, 752-759.
185. Nelson, N. C. et al. in *Nonisotopic DNA Probe Techniques*, L.J. Kricka ed., pp. 275-309.
186. Steck, T. R. Improved chemiluminescent detection of DNA. *Biotechniques* 1994, 16 (3) 406-407.
187. Kricka, L. J.; Ji, Q.; Nozaki, O.; Wilding, P. Imaging of Chemiluminescent Reactions in Mesoscale Silicon-Glass Microstructures. *J. Biolumin. Chemilumin.* 1994, 9, 135-138.
188. Brown, R. C.; Weeks, I.; Fisher, M.; Harbron, S.; Taylorson, C. J.; Woodhead, J. S. Employment of a Phenoxy-Substituted Acridinium Ester as a Long-Lived Chemiluminescent Indicator of Glucose Oxidase Activity and its Application in an Alkaline Phosphatase Amplification Cascade Immunoassay. *Anal. Biochem.* 1998, 259, 142-151.
189. Mazumder, A.; Majlessi, M.; Becker, M. M. A High Throughput Method to Investigate Oligodeoxyribonucleotide Hybridisation Kinetics and Thermodynamics. *Nucl. Ac. Res.* 1998, 26 (8) 1996-2000.

190. Akhavan-Tafti, A.; Reddy, L. V.; Siripurapu, S.; Schoenfelner, B. A.; Handley, R. S.; Schaap, A. P. Chemiluminescent detection of DNA in low- and medium-density arrays. *Clin. Chem.* 1998, 44, 2065-2066.
191. Irving, R. A.; Hudson, P. J. Proteins emerge from disarray. *Nature Biotechnol.* 2000, 18, 932.
192. Zhu, H.; Klemic, J. F.; Chang, S.; Bertone, P.; Casamayor, A.; Klemic, K. G.; Smith, D.; Gerstein, M.; Reed, M. A.; Snyder, M. Analysis of yeast protein kinases using protein chips. *Nature Genetics* 2000, 283-289.

